An international peer reviewed journal of science

PHYSICS

MATHEMATICS

BIOLOGY

SCIENCE

CHEMISTRY

Table of Contents (İçindekiler)
Volume (Cilt): 15 Number (Sayı): 1 June (Haziran) 2025

Table of Contents (İçindekiler)
Volume (Cilt): 15 Number (Sayı): 1 June (Haziran) 2025

Synthesis, Characterization of α-Cyanochalcone Compounds and Determination of Their Antibacterial, Antifungal, and Antioxidant Activities

Hakan ASLAN[1,*], Cumhur AVSAR[2]

[1]*Sinop University, Faculty of Science and Arts, Department of Chemistry, 57000, Sinop, Türkiye*
haslan@sinop.edu.tr, ORCID: 0000-0002-5268-7196
[2]*Sinop University, Faculty of Science and Arts, Department of Biology, 57000, Sinop, Türkiye*
cavsar@sinop.edu.tr, ORCID: 0000-0002-4095-0022

Abstract

In this study, the Knoevenagel condensation reactions of 3-(heteroaryl)-3-oxopropanenitriles and various aromatic/heteroaromatic aldehydes via L-proline were performed. In these reactions, α-cyanochalcone compounds were obtained in mid-good yields. Spectroscopic techniques were used to clarify the compounds' structures. Both the well-diffusion method and the minimum inhibitory concentration (MIC) method were used to assess the antibacterial and antifungal properties of all products. Compound 1c, containing the pyridin-3-yl group, exhibited broad-spectrum properties by acting against all bacteria and fungi tested. The antioxidant activities of the compounds were tested by a DPPH radical scavenging assay, and according to the results of antioxidant activities, the most effective compound among all was found to be 1c. It is possible to say that compounds 1b and 1d also have moderate antioxidant activity.

Keywords: α-cyanochalcone; Knoevenagel condensation; Antimicrobial activity; Antioxidant activity.

α-Siyanokalkon Bileşiklerinin Sentezi, Karakterizasyonu ve Antibakteriyel, Antifungal ve Antioksidan Aktivitelerinin Belirlenmesi

Öz

Bu çalışmada, 3-(heteroaril)-3-oksopropannitriller ile çeşitli aromatik/heteroaromatik aldehitlerin L-prolin aracılığında Knoevenagel kondensasyon reaksiyonları gerçekleştirildi. Bu reaksiyonlarda orta-iyi verimlerde α-siyanokalkon bileşikleri elde edildi. Bileşiklerin yapıları spektroskopik yöntemler kullanılarak aydınlatıldı. Tüm ürünlerin antibakteriyel ve antifungal aktiviteleri hem kuyu- difüzyon yöntemi hem de minimum inhibisyon konsantrasyonu (MIC) yöntemiyle belirlendi. Piridin-3-il grubunu içeren bileşik 1c, hem Gram (+) hem de Gram (-) bakteri ve mantarlara karşı etki göstererek geniş spektrumlu özellikler sergiledi. Bileşiklerin antioksidan aktiviteleri DPPH radikal temizleme yöntemi ile test edildi ve antioksidan aktivite sonuçlarına göre en etkili bileşiğin 1c olduğu bulundu. 1b ve 1d bileşiklerinin de orta düzeyde antioksidan aktiviteye sahip olduğunu söylemek mümkündür.

Anahtar Kelimeler: α-Siyanokalkon; Knoevenagel kondensasyonu; Antimikrobiyal aktivite; Antioksidan aktivite.

1. Introduction

Chalcones, which are both found in natural products and are readily synthesized using a multitude of techniques, are an important compound class in organic chemistry because they show a broad and diverse biological activity and are the starting components of many important biologically active compound classes [1-3]. Among the wide range of biological activities shown by chalcones are antimicrobial [4, 5], antimitotic [6], antitumor [7, 8], anti-inflammatory [9], antioxidant [10], antihistamine [11], antidiabetic [12], antihypertensive [13], enzyme inhibition [14, 15], antiparasitic [16], and antiplasmodial [17] properties (Fig. 1).
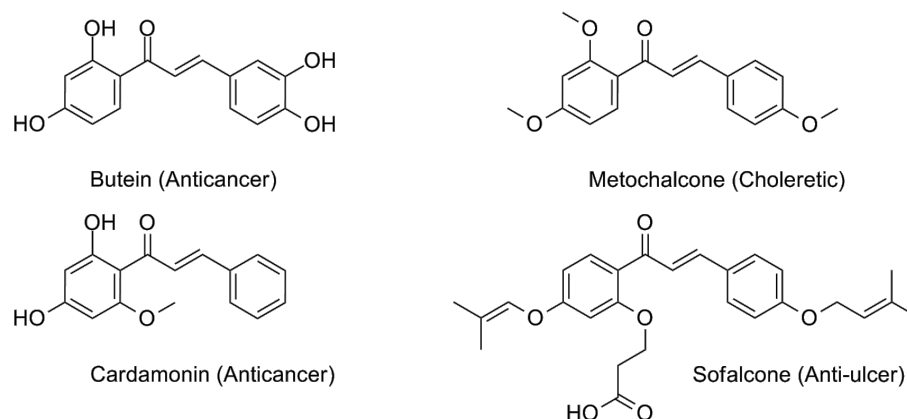
Figure 1: Some of the bioactive chalcone compounds.

Chalcones are mostly synthesized by base-catalyzed Claisen-Schmidt condensation but can also be synthesized by coupling reactions such as Heck, Suzuki, Suzuki-Miyaura, Wittik, and Sonogashira [2]. Additionally, chalcones can be converted to biologically important five-membered (pyrole, furan, benzofuran, pyrazole, imidazole, isoxazole, thiazole, triazole), six-membered (pyridine, pyrimidine), and seven-membered heterocycles (diazepine) [3].

α-Cyanocalcone compounds are mostly synthesized by Knoevenagel condensation and, like chalcones, exhibit a variety of biological functions [18]. For example, Kumar et al. [19] synthesized α-cyano chalcones, including bis(indolyl) groups, and examined the effectiveness of these compounds against lung (A549), prostate (PC3) and pancreas (PaCa2) cancer lines. They reported that the best results were obtained against lung cancer. Fahim and Farag [20] reported that they synthesized various α-cyanochalcone compounds. They also synthesized aminopyrazole compounds and pyrazolopyrimidine compounds, respectively, by reacting these compounds with hydrazine derivatives and various pyrazole derivatives. They examined the antimicrobial effects of both the α-cyanochalcones and the products they obtained from α-cyanochalcones. They found that both α-cyanochalcones and heterocyclic products showed moderate to good activity against bacteria and fungus.

In this study, α-cyanochalcone compounds were obtained by performing the Knoevenagel condensation reaction of 3-oxopropanenitriles and various aromatic/heteroaromatic aldehydes. Spectroscopic techniques were used to clarify the compounds' structures. The biological effects against bacteria, fungi, and antioxidant properties of the substances were investigated.

2. Materials and Methods

3-Oxo-propanenitriles (1-3) were synthesized according to the literature [21]. Aldehydes are commercially available and were not further purified before being used. An electrothermal capillary melting point device (Stuart SMP30) was used to measure melting points (mp). Infrared spectra were acquired using a SHIMADZU IRSpirit QATR-S in the 400-4000 cm^{-1} range. ^{1}H and ^{13}C-NMR spectra were recorded on a Bruker AVANCE III-400 MHz spectrophotometer. The coupling constants (J) are expressed in hertz (Hz), and chemical shifts are reported in parts per million (ppm) concerning Me$_4$Si as the internal standard. The following are the designations for splitting patterns: s stands for singlet, d for doublet, t for triplet, m for multiplet, and bs for broad singlet. An Agilent 6530 and an Agilent 6230 Accurate-Mass Q-TOF LC–MS apparatus were used to measure the mass spectra; m/z (rel. %). Using Merck silica gel 60 (230–400 mesh) as the stationary phase and EtOAc and hexane as eluents, column chromatography (cc) was utilized to purify the products.

2.1. General Procedure for the Synthesis of 3-Oxo-Propanenitriles (1-3)

A three-necked flask with a thermometer, dropping funnel, and condenser with a gas trap at the outlet; 60% sodium hydride (5.6 g; 140 mmol), ester (70 mmol), and 150 mL toluene are added and heated to 90 °C. To the mixture at this temperature, 6 mL of toluene solution of acetonitrile (140 mmol) is added dropwise over 30 minutes. The reaction continues until hydrogen gas is released. After gas evolution ends, the solution is cooled. The resulting solids are filtered and dried. These solids are then dissolved in water in an ice-salt bath and hydrolyzed dropwise with a dilute HCl (1:1) solution, preventing the temperature from rising above 5°C. The resulting crude product is purified by crystallization from methanol [21].

2.2. General Procedure for the Reactions of 3-Oxo-Propanenitriles (1-3) and Aldehydes (a-f) via L-Proline

3-aryl-3-oxo-propanenitrile (1 eq) and the L-proline (0.2 eq) are dissolved in 4 ml of ethanol. Aromatic aldehyde (1 eq) is added to the mixture. The chalcone derivative formed within 1-2 minutes from the solution mixed at room temperature on the magnetic stirrer begins to separate in solid form. The experiment is controlled by thin-layer chromatography and terminated at the appropriate time. Once the starting compounds are completed, cold water is added to the reaction medium. The solid undergoes filtration, a cold ethanol-water mixture wash, and a thorough water wash before drying. The product is purified by crystallization or cc [22].

2.3. Determination of Antimicrobial Activity

In this study, the techniques described in previous studies [23-24] were used to evaluate the compounds' minimal inhibitory concentrations (MIC) and agar well diffusion. In this study, 2 Gram (+) (*Staphylococcus aureus* ATCC 6538 and *Bacillus cereus* ATCC 7064), 3 Gram (-) (*Escherichia coli* ATCC 11293, *Klebsiella pneumonia* ATCC 27889, and *Pseudomonas aeuroginosa* ATCC 27853) and 2 fungi (*Candida krusei* ATCC 6258 and *Candida parapsilosis* 22019) reference microorganisms were used. DMSO, in which the chemicals were dissolved, was used as a negative control. Additionally, Bacteria were grown on Mueller-Hinton Agar (MHA) and Broth (MHB), while fungi were grown on Sabouraud-Dextrose Agar (SDA) and Broth (SDB).

2.4. Agar Well Diffusion Method

After being grown overnight in MHB and SDB, the bacterial and fungal cultures were adjusted using the McFarland 0.5 standard (~1.5×10^8 cfu/mL). Following this, approximately

10^6 cfu/mL of new cultures was added to recently prepared sterile MHA and SDA petri surfaces. Using a sterile cork borer, on the agar surface, wells with a diameter of 6 mm were created. 40 µL of the product's solution to be tested—2 mg of compounds coded 1c, 1d, and 1e and 0.1 mg of chemicals coded 1a, 1b, 2a, and 2b—was added to the wells. The petri dishes were then incubated for 18 to 24 hours at 37±4°C (for bacteria) and at 28±2°C (for fungi). At the end of the period, the zone diameter formed around the wells was measured with the help of a millimetric ruler and then transferred to Excel 2010 to obtain the Standard Deviations (±SD) of the three repeated tests. Commercial antibiotics were used as the positive control (pc), while DMSO was used as the negative control (nc).

2.5. Minimal inhibitory concentrations (MIC)

Minimum inhibition concentrations were determined by the tube dilution method followed by incubation techniques in an agar medium. For this, 1 mL of MHB and SDB was added to each tube, and after the sterilization process, serial dilutions (range 5 – 0.125 mg) of the compounds to be tested were prepared. Then, 50 µL of microorganism culture prepared based on the McFarland standard was inoculated into each tube and incubated at 37±4°C (for bacteria) and at 28±2°C (for fungi) for 18-24 hours. The results were visually inspected, and the dilution at which no growth or turbidity was observed was recorded as the MIC value. The sample taken from the dilution showing the MIC value was inoculated into sterile MHA and SDA petri dishes and incubated at 37±4°C and 28±2°C for 18-24 hours. Results were reported based on whether there was growth in the petri dishes.

2.6. Determination of antioxidant activities

Samples were analyzed for free radical scavenging activity using the DPPH radical scavenging test [25-26]. Different concentrations (1000 – 62.5 µg/mL) of the compounds to be tested were prepared. A 4 mL DPPH-ethanol solution (0.1 mM) was introduced to various component concentration solutions in 1 mL ethanol. Absorbance values at 517 nm were measured after the solutions were left in the dark for half an hour. The following formula was used to determine the DPPH radical's scavenging activity:

$$\% \ Inhibition = \frac{AB - AS}{AB}.100 \tag{1}$$

In this equation, AS represents the absorbance of the test substance, and AB represents the absorbance of the control reaction. IC_{50} stands for the concentration of a chemical needed to

block 50% of free radical scavenging action. The standard was ascorbic acid. Standard-free ethanol was used as a negative control, and the tests were also performed in triplicate.

3. Experimental

3.1. Physical and Spectral Data of the Substrates

3-Oxo-3-(furan-2-yl)-propanenitrile (1): Yield 76 %, brown solid, mp: 74-75 °C (Lit. [27] mp: 66-68 °C); IR (ATR, ν/cm): 3134 (ArH), 2950-2920 (RH), 2256 (C≡N), 1671 (C=O); ^{1}H-NMR (400 MHz, CDCl$_3$, δ): 4.00 (s, 2H), 6.67 (dd, 1H, J = 3.6, 1.6 Hz), 7.42 (dd, 1H, J = 3.6, 0.8 Hz), 7.69 (t, 1H, J = 0.8 Hz). Similar to that previously reported [27].

3-Oxo-3-(thiophene-2-yl)-propanenitrile (2): Yield 81%, brown solid, mp: 114-115°C (Lit. [27] mp: 123-126 °C); IR (ATR, ν/cm): 3113-3091 (ArH), 2949-2918 (RH), 2256 (C≡N), 1664 (C=O); ^{1}H-NMR (400 MHz, CDCl$_3$, δ): 4.00 (s, 2H), 7.20 (dd, 1H, J = 4.8, 4.4 Hz), 7.78-7.80 (m, 2H). Similar to that previously reported [27].

3-Oxo-3-(pyridine-2-yl)-propanenitrile (3): Yield 76%, claret red solid, mp 87-88°C; IR (ATR, ν/cm): 3101-3058 (ArH), 2953-2927 (RH), 2260-2186 (C≡N), 1711 (C=O); $_1$H-NMR (400 MHz, CDCl$_3$, δ): 4.74 (s, 2H), 7.76-7.73 (m, 1H), 8.09-8.00 (m, 2H), 8.75 (d, 1H, J = 3.2 Hz) ; ^{13}C-NMR (100 MHz, CDCl$_3$, δ): 29.73, 116.75, 122.30, 129.14, 138.35, 149.83, 151.27, 191.33; HRMS (m/z): calculated for C$_8$H$_6$N$_2$O [M]$^+$: 146.0475, found: 146.9963.

3.2. Physical and Spectral Data of the Products

2-(furan-2-carbonyl)-3-(furan-2-yl)acrylonitrile (1a) : Yield 92%, yellow solid, mp: 143-144°C; IR (ATR, ν/cm): 3134-3117 (ArH), 2213 (C≡N), 1640 (C=O); ^{1}H-NMR (400 MHz, DMSO-d6, δ): 6.84-6.85 (m, 1H), 6.92-6.93 (m, 1H), 7.60 (d, 1H, J = 3.2 Hz), 7.70 (dd, 1H, J = 4.0, 0.8 Hz), 8.168-8.173 (m, 1H), 8.26 (s, 1H), 8.28 (d, 1H, J = 0.8 Hz); ^{13}C NMR (101 MHz, DMSO-d6, δ): 173.95 (C=O), 150.77 (CH), 150.29 (C), 149.59 (CH), 149.07 (CH), 139.89 (CH), 125.60 (CH), 121.82 (CH), 117.07 (C), 115.07 (CH), 113.52 (C), 103.20 (C); HRMS (m/z): calculated for C$_{12}$H$_7$NO$_3$ [M+H]$^+$: 214.04987, found: 214.9802.

2-(furan-2-carbonyl)-3-(thiophen-2-yl)acrylonitrile (1b) : Yield 90%, yellow solid, mp: 135-136°C; IR (ATR, ν/cm): 3113-3088 (ArH), 2214 (C≡N), 1644 (C=O); ^{1}H-NMR (400 MHz, DMSO-d6, δ): 6.84-6.87 (m, 1H), 7.39-7.42 (m, 1H), 7.70 (dd, 1H, J = 4.0, 0.8 Hz), 8.13 (d, 1H, J = 3.2 Hz), 8.17-8.18 (m, 1H), 8.26 (dd, 1H, J = 4.8, 0.8 Hz), 8.73 (s, 1H); ^{13}C NMR (101 MHz, DMSO-d6, δ) 173.81 (C=O), 150.33 (C), 149.58 (CH), 148.44 (CH), 141.33 (CH),

138.00 (CH), 136.56 (C), 129.41 (CH), 121.80 (CH), 117.61 (C), 113.55 (CH), 104.10 (C); HRMS (m/z): calculated for $C_{12}H_7NO_2S$ $[M+H]^+$: 230.027026, found: 230.9596.

2-(furan-2-carbonyl)-3-(pyridin-3-yl)acrylonitrile (1c) : Yield 62%, yellow solid, mp: 135-136°C; IR (ATR, ν/cm): 3137-3116 (C=CH), 2216 (C≡N), 1641 (C=O); ^{1}H NMR (400 MHz, DMSO-d6, δ) 9.12 (s, 1H), 8.78 (d, J = 4.5 Hz, 1H), 8.55-8.48 (m, 2H), 8.22 (s, 1H), 7.79 (d, J = 3.6 Hz, 1H), 7.67 (dd, J = 8.0, 4.8 Hz, 1H), 6.88 (dd, J = 3.6, 1.5 Hz, 1H); ^{13}C NMR (101 MHz, DMSO-d6, δ) 174.04 (C), 153.48 (CH), 152.51 (CH), 152.49 (CH), 150.27 (CH), 149.89 (C), 136.93 (CH), 128.58 (C), 124.60 (CH), 123.04 (CH), 116.72 (C), 113.73 (CH), 111.36 (C); HRMS (m/z): calculated for $C_{13}H_8N_2O_2$ $[M+H]^+$: 225.065854, found: 225.06576.

3-(4-chlorophenyl)-2-(furan-2-carbonyl)acrylonitrile (1d) : Yield 79%, beige solid, mp: 125-126°C; IR (ATR, ν/cm): 3143 (C=CH), 3034 (ArH), 2207 (C≡N), 1651 (C=O); ^{1}H NMR (400 MHz, DMSO-d6, δ) 8.45 (s, 1H), 8.21 (d, J = 0.9 Hz, 1H), 8.11 (d, J = 8.6 Hz, 2H), 7.75 (d, J = 3.5 Hz, 1H), 7.72 (d, J = 8.6 Hz, 2H), 6.87 (dd, J = 3.6, 1.6 Hz, 1H); ^{13}C NMR (101 MHz, DMSO-d6, δ) 174.28 (C), 154.02 (CH), 150.10 (CH), 150.00 (C), 138.32 (C), 132.94 (CHx2), 131.22 (C), 129.91 (CHx2), 122.75 (CH), 116.91 (C), 113.66 (CH), 109.74 (C); HRMS (m/z): calculated for $C_{14}H_8ClNO_2$ $[M+H]^+$: 258.031633, found: 258.03144.

2-(furan-2-carbonyl)-3-(4-hydroxyphenyl)acrylonitrile (1e) : Yield 63%, orange solid, mp: 181-182°C; IR (ATR, ν/cm): 3304 (OH), 3162 (C=CH), 2212 (C≡N), 1606 (C=O) ; ^{1}H NMR (400 MHz, DMSO-d6, δ) 10.92 – 10.87 (bs, 1H, OH), 8.33 (s, 1H), 8.16 (s, 1H), 8.06 (d, J = 8.5 Hz, 2H), 7.67 (s, 1H), 6.98 (d, J = 8.3 Hz, 2H), 6.83 (s, 1H); ^{13}C NMR (101 MHz, DMSO-d6, δ) 174.75 (C), 163.52 (CH), 155.50 (CH), 150.37 (C), 149.41 (C), 134.74 (CHx2), 123.45 (CH), 121.64 (CH), 118.17 (C), 116.90 (CHx2), 113.42 (CH), 103.85 (C); HRMS (m/z): calculated for $C_{14}H_9NO_3$ $[M+H]^+$: 240.06552, found: 240.06524.

3-(furan-2-yl)-2-(thiophene-2-carbonyl)acrylonitrile (2a): Yield 87%, yellow solid, mp: 138-139°C; IR (ATR, ν/cm): 3085-3031 (ArH), 2210 (C≡N), 1629 (C=O); ^{1}H-NMR (400 MHz, DMSO-d6, δ): 6.92 (dd, 1H, J = 3.6, 1.6 Hz), 7.34 (dd, 1H, J = 5.2, 3.6 Hz), 7.59 (d, 1H, J = 3.6 Hz), 8.15 (dd, 1H, J = 4.0, 1.2 Hz), 8.18 (dd, 1H, J = 4.8, 1.2 Hz), 8.20 (s, 1H), 8.28 (d, 1H, J = 1.2 Hz); ^{13}C NMR (101 MHz, DMSO-d6, δ) 179.47 (C=O), 150.72 (CH), 149.00 (C), 141.52 (C), 140.08 (CH), 137.05 (CH), 135.42 (CH), 129.49 (CH), 125.66 (CH), 117.39 (C), 115.04 (CH), 103.53 (C); HRMS (m/z): calculated for $C_{12}H_7NO_2S$ $[M+H]^+$: 230.26242, found: 230.9593.

3-(thiophen-2-yl)-2-(thiophene-2-carbonyl)acrylonitrile (2b) : Yield 84%, yellow solid, mp: 150-151°C; IR (ATR, ν/cm): 3110-3083 (ArH), 2207 (C≡N), 1628 (C=O); ^{1}H-NMR (400

MHz, DMSO-d6, δ): 7.35 (dd, 1H, *J* = 4.8, 4.0 Hz), 7.40 (dd, 1H, *J* = 4.8, 4.0 Hz), 8.12 (d, 1H, *J* = 4.4 Hz), 8.15 (dd, 1H, *J* = 4.0, 0.8 Hz), 8.18 (dd, 1H, *J* = 4.8, 0.8 Hz), 8.26 (d, 1H, *J* = 4.8 Hz), 8.67 (s, 1H); ^{13}C NMR (101 MHz, DMSO-d6, δ) 179.40 (C=O), 148.60 (CH), 141.55 (C), 141.31 (CH), 137.92 (CH), 137.04 (CH), 136.50 (C), 135.46 (CH), 129.54 (CH), 129.41 (CH), 117.89 (C), 104.56 (C); HRMS (m/z): calculated for $C_{12}H_7NOS_2$ [MH]$^+$: 246.00418, found: 246.0039.

4. Result and Discussion

Initially, the reactions of 3-Oxo-3-(furan-2-yl)-propanenitrile (1) and 2-furancarboxaldehyde (a) via different catalysts were investigated (Table 1). Inorganic bases, organic and inorganic acids, and L-proline were tested as catalysts in these reactions carried out in 80% ethanol solution, and the highest efficiency was obtained when L-proline was used as the catalyst. In reactions where absolute ethanol was used as a solvent, a significant increase in yield was observed due to the solubility of the compounds increased.

Table 1: Optimization conditions of Knoevenagel condensation reactions.
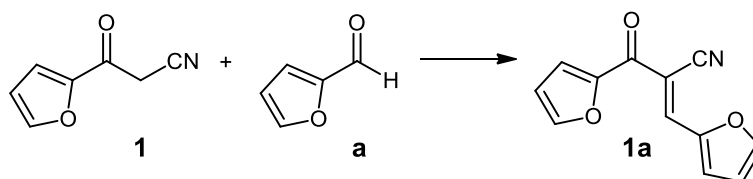
No	Reactive	Solvent	Time	1a Yield (%)[b]
1	Na_2CO_3	EtOH/H_2O[a]	o.n.	25
2	K_2CO_3	EtOH/H_2O[a]	o.n.	38
3	NaOH	EtOH/H_2O[a]	o.n.	45
4	KOH	EtOH/H_2O[a]	o.n.	48
5	der. H_2SO_4	EtOH/H_2O[a]	o.n.	5
6	p-Toluenesulfonic acid	EtOH/H_2O[a]	o.n.	45
7	Silica-Sulfuric acid	EtOH/H_2O[a]	o.n.	51
8	L-Proline	EtOH/H_2O[a]	o.n.	65
9	L-Proline	EtOH	1 h	89
10	L-Proline	EtOH	2.5 h	92

a: 80% Ethanole solution were used. b: All experiments were carried out at room temperature.

α-Cyano chalcone compounds were obtained in mid-good yields by performing L-proline catalyzed Knoevenagel condensation reactions of 3-oxo-propanenitriles (1, 2) and aldehydes (a-e) (Table 2). The structures of the compounds were clarified through the use of spectroscopic methods. However, the targeted α-cyanochalcones could not be synthesized from the reactions of pyridine-2-carbaldehyde with 3-aryl-3-oxo-propanenitriles and the reactions of 3-(pyridin-2-yl)-3-oxo-propanenitriles with aldehydes. In these experiments, compounds that were insoluble

in most solvents, dark colored, and had low light transmission were obtained, and their structures could not be elucidated due to solubility problems.

Table 2: Products of the Knoevenagel condensation reactions of 3-Oxo-propanenitriles (1-3) and aldehydes (a-f) via L-proline[a].

No	R	R[1]	Time	Product	Yield (%)[b]
1	Furan-2-yl	Furan-2-yl	2.5 h	1a	92
2	Furan-2-yl	Thiophene-2-yl	1 h	1b	90
3	Furan-2-yl	Pyridine-3-yl	o.n.	1c	62
4	Furan-2-yl	4-Cl-C_6H_4	o.n.	1d	79
5	Furan-2-yl	4-OH-C_6H_4	o.n.	1e	63
6	Thiophene-2-yl	Furan-2-yl	1 h	2a	87
7	Thiophene-2-yl	Thiophene-2-yl	o.n.	2b	84
8	Furan-2-yl	Pyridine-2-yl	o.n.	1f	-
9	Thiophene-2-yl	Pyridine-2-yl	4 h	2f	-
10	Pyridine-2-yl	Furan-2-yl	o.n.	3a	-
11	Pyridine-2-yl	Thiophene-2-yl	o.n.	3b	-
12	Pyridine-2-yl	Pyridine-2-yl	o.n.	3f	-

a: All the reactions were carried out in a 1: 1: 0.2 molar ratio of 3-Oxo-propanenitrile (1-3), aldehyde (a-f) and L-proline in EtOH at rt.
b: Isolated yield.
o. n. : overnight

When the IR spectra of the products were examined, the vibrations of the aromatic and vinylic hydrogens were observed in the range of 3162-3031 cm^{-1}, the vibrations of the cyano group were observed around 2210 cm^{-1}, and the vibrations of the conjugated carbonyl group were observed around 1640 cm^{-1} and all these vibrations are as expected (Table 3). 1e's phenolic O-H vibration was observed at 3304 cm^{-1}.

Table 3: Some selected IR vibrations.

Compound	O-H	C=C-H	C≡N	C=O
1a		3134-3117	2213	1640
1b		3113-3088	2214	1644
1c		3137-3116	2216	1641
1d		3143-3034	2207	1651
1e	3304	3162	2212	1606
2a		3085-3031	2210	1629
2b		3110-3083	2207	1628

In the ^{1}H-NMR spectra of the products except 1c, aromatic protons resonated at between 6.8 and 8.3 ppm. Due to the presence of the pyridine ring in compound 1c, resonance

occurred in a lower area according to the other compounds, and H-C2 in the pyridine ring gave a signal as a single peak at 9.1 ppm. While vinylic protons adjacent to the thiophene ring resonated at 8.7 ppm, vinylic protons in other compounds resonated in the range of 8.2-8.45 ppm. Similarly, in the ^{13}C-NMR spectrum, the carbon atom in the carbonyl group attached to the thiophene ring gives a peak at 179 ppm, while the carbonyl carbon attached to the furan ring gives a peak at 174 ppm.

Table 4:. Agar well diffusion test results of the samples.

Compound	*Staphylococcus aureus* ATCC 6538	*Bacillus cereus* ATTC 7064	*Escherichia coli* ATCC 11293	*Pseudomonas aeruginosa* ATCC 27853	*Klebsiella pneumonia* ATCC 27889	*Candida parapsilosis* ATCC 22019	*Candida krusei* ATCC 6258
1a	16±0.2	-	-	-	-	-	12±0.43
1b	13±0.05	-	-	-	-	-	-
1c	24±1	17.3±0.5	-	-	20±1	17.3±1.5	14±2
1d	-	-	-	-	-	-	-
1e	-	-	-	-	-	-	-
2a	-	14±0.45	-	-	-	-	-
2b	-	-	-	-	-	-	-
DMSO	-	-	-	-	-	-	*
Ipm 10	28	26	21	*	38	*	*
CL30	27	10	-	9	-	*	*
Te 30	11	21	21	13	16	*	*
Da 2	11	16	-	12	14	*	43
Cyc	*	*	*	*	*	40	*

(-) not effect, (*) not tested; negative control: DMSO; positive control: Imipenem (Ipm 10); Cephalexin (CL-30); Tetracycline (TE 30); Clindamycin (Da-2); Cycloheximide (Cyc); units of measurement are recorded in millimeters

Agar well diffusion test results of 7 different α-cyano chalcones tested are shown in Table 4. According to the results, compounds 1d, 1e, and 2b had no effect against microorganisms, while compound 1c had a significant effect (between 14±2 and 24±1 mm) against Gram-negative, Gram-positive, and fungi (Fig. 2). Based on the findings of the MIC test shown in Table 5, although the effects of 1d and 1e were observed above 2 mg concentration against two Gram-positive isolates and *C. krusei*, the effective result of 1c between 0.25 and 4 mg concentrations was remarkable.

Table 5: Minimal Inhibition Concentration (MIC) test results for the samples

Compound	*Staphylococcus aureus* ATCC 6538	*Bacillus cereus* ATTC 7064	*Escherichia coli* ATCC 11293	*Pseudomonas aeruginosa* ATCC 27853	*Klebsiella pneumonia* ATCC 27889	*Candida parapsilosis* ATCC 22019	*Candida krusei* ATCC 6258
1a	125	-	-	-	-	-	-
1b	125	500	-	500	-	-	-
1c	250	1000	4000	-	500	500	500
1d	2500	2500	-	-	-	-	2500
1e	2500	2500	-	-	-	-	5000
2a	-	-	-	-	-	-	-
2b	-	-	-	-	-	-	-
DMSO	-	-	-	-	-	-	-

(-) not effect; negative control: DMSO

Compounds 1d, 1e and 2b showed no antimicrobial effect against the tested microorganisms in the agar well-diffusion test. While compounds 1a, 1b, and 2a showed moderate to good activity only against Gram (+) bacteria, compound 1c showed a broad spectrum of activity against both Gram (+) and Gram (-) bacteria and fungi. In addition, the antioxidant activities of the compounds were measured by the DPPH method, and the most effective compound was found to be 1c (Table 6). It is possible to say that compounds 1b and 1d also have moderate antioxidant activity. On the other hand, samples coded 1a, 1e, 2a, and 2b were considered as having no activity since they showed antioxidant activity higher than 1000 µg/mL (Table 6).
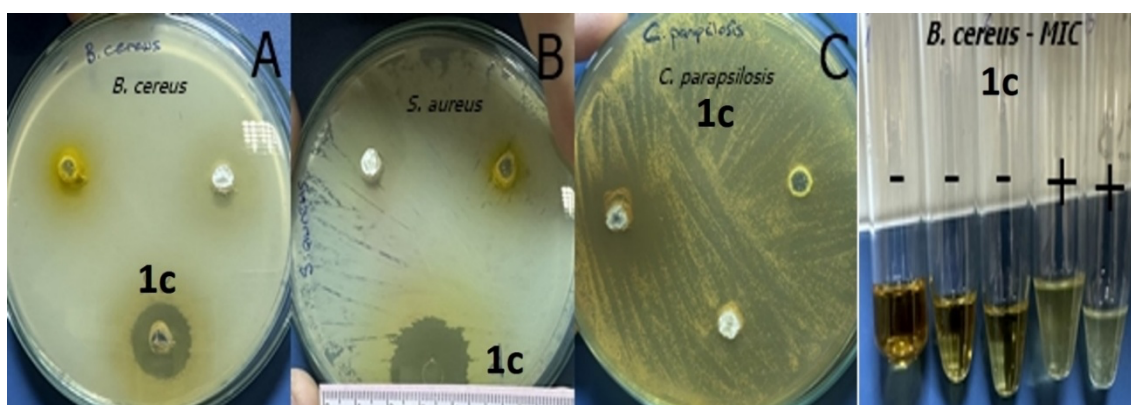
Figure 2: Agar well-diffusion test result images of (A) *B. cereus*, (B) *S. aureus*, (C) *C. parapsilosis* strains, (D) Five different MIC test result images of *B. cereus*, '-' on the tubes means no growth, '+' means growth (turbidity due to growth is seen in the last two concentrations).

Table 6: IC$_{50}$ (µg/mL) antioxidant test results of the samples based on DPPH.

1a	-
1b	765.74±1.77
1c	553.14±2.38
1d	736.10±0.51
1e	-
2a	-
2b	-
A	110.96±0.58

A: Ascorbic acid; (-) no activity

When the antimicrobial and antioxidant activities of the synthesized α-cyanochalcone compounds from this study were examined, it was observed that different compounds had different effects (Tables 4-6). Although it is difficult to evaluate the synthesized α-cyanochalcone compounds among themselves due to their different chemical structures, there are still studies on α-cyanochalcone compounds in the literature. One of them, Fahim and Farag [20], synthesized α-cyanochalcone compounds in their study and reported that the compounds, including bis-substituted phenyl rings, showed antimicrobial activity in the range of 11.0 ± 0.11 - 19.2 ± 0.21 mm against Gram-positive and negative bacteria and some fungi. In another study conducted by El-Shenawy [28], in which the synthesis and antibacterial activities of quinazolinone substituted α-cyanochalcone compound was studied, it was determined that the compound was effective against Gram-positive (*S. epidermidis* and *S. aureus*) and Gram-negative (*P. aeruginosa* and *E. coli*) bacteria in the range of 14-22 mm. Apart from these, α-cyanochalcone compounds were studied not only in terms of antimicrobial activities but also in anticancer research, and it was determined that they have potential in the fight against lung cancer cells [19], colorectal carcinoma [29] and breast cancer cell lines [30]. To the best of our knowledge, there are only two studies involving the antioxidant properties of α-cyanochalcones [30, 31]. In the first of these, indole-pyrazole amalgamated α-cyano-substituted chalcones were synthesized, and it was stated that some of these compounds showed moderate DPPH free radical scavenging activity [30]. In the second study, compounds with α-cyano-substituted bis chalcone structure containing indolyl groups were synthesized, and their antioxidant properties were examined. According to the stated results, the synthesized compounds were found to have good to excellent DPPH free radical scavenging activity [31]. This study we have conducted, to the best of our knowledge, will be the third study involving the synthesis and antioxidant properties of α-cyano chalcones. Due to the scarcity of such studies, when we consider α-cyano chalcones as two different functional groups, chalcone, and acrylonitrile, there are many studies

in the literature showing that compounds with these structures also exhibit antioxidant activity [32-35].

5. Conclusion

In this study, α-cyanochalcone compounds were synthesized in mid-good yields by performing the Knoevenagel condensation reactions of 3-(heteroaryl)-3-oxopropanenitriles and various aromatic/heteroaromatic aldehydes. L-proline was found to be the most effective catalyst among those tested in these reactions. Spectroscopic techniques were used to clarify the compounds' structures. It was also observed that some of the synthesized α-cyanochalcone compounds were effective against Gram-positive and negative bacteria and fungi. In addition, they were evaluated for their antioxidant activity. Although one of the compounds had a five times lower effect than the tested positive control, it was observed to be promising. All these data show that the α-cyanochalcone compounds synthesized in this study are remarkable in terms of their antimicrobial and antioxidant capacities, and their inclusion in the literature shows the importance of this study.

References

[1] Sahu, K.N., Balbhadra, S.S., Choudhary, J., & Kohli, D., *Exploring pharmacological significance of chalcone scaffold: a review*, Current Medicinal Chemistry, 19(2), 209-225, 2012.

[2] Rammohan, A., Reddy, J.S., Sravya, G., Rao, C.N., & Zyryanov, G.V., *Chalcone synthesis, properties and medicinal applications:a review*, Environmental Chemistry Letters, 18, 433-458, 2020.

[3] Nayak, Y.N., Gaonkar, S.L., & Sabu, M., *Chalcones:Versatile intermediates in heterocyclic synthesis*, Journal of Heterocyclic Chemistry, 60(8), 1301-1325, 2023.

[4] Khider, A.K., *In vivo Antimicrobial Activity of 1 (4-(4-chlorobenzyloxy) phenyl)-3-(4-methyl Phenyl)-2-propen-1-ones (Chalcone 2) Against klebsiella pneumoniae Isolated from Pneumonia Patients,* British Journal of Pharmacology and Toxicology, 2(2), 92-96, 2011.

[5] Asiri, A.M., & Khan, S.A., *Synthesis and anti-bacterial activities of a bis-chalcone derived from thiophene and its bis-cyclized products,* Molecules, 16(1), 523-531, 2011.

[6] Edwards, M.L., Stemerick, D.M., & Sunkara, P.S., *Chalcones: a new class of antimitotic agents,* Journal of Medicinal Chemistry, 33(7), 1948-1954, 1990.

[7] Mohamed, M.F., & Abuo-Rahma, G.E.D.A., *Molecular targets and anticancer activity of quinoline–chalcone hybrids: Literature review*, RSC advances, 10(52), 31139-31155, 2020.

[8] Ouyang, Y., Li, J., Chen, X., Fu, X., Sun, S., & Wu, Q., *Chalcone derivatives: role in anticancer therapy*, Biomolecules, 11(6), 894, 2021.

[9] Pereira, R., Silva, A.M., Ribeiro, D., Silva, V.L., & Fernandes, E., *Bis-chalcones: A review of synthetic methodologies and anti-inflammatory effects,* European Journal of Medicinal Chemistry, 252, 115280, 2023.

[10] Siddiqa, A., Tajammal, A., Irfan, A., Azam, M., Munawar, M.A., Hardy, R.S., et al., *Synthesis, molecular docking, bio-evaluation and quantitative structure activity relationship of new chalcone derivatives as antioxidants,* Journal of Molecular Structure, 1277, 134814, 202.

[11] Yamamoto, T., Yoshimura, M., Yamaguchi, F., Kouchi, T., Tsuji, R., Saito, M., et al., *Anti-allergic activity of naringenin chalcone from a tomato skin extract,* Bioscience, Biotechnology, and Biochemistry, 68(8), 1706-1711, 2004.

[12] Mahapatra, D.K., Asati, V., & Bharti, S.K., *Chalcones and their therapeutic targets for the management of diabetes: structural and pharmacological perspectives,* European journal of Medicinal Chemistry, 92, 839-865, 2015.

[13] Kumar, H., Devaraji, V., Joshi, R., Jadhao, M., Ahirkar, P., Prasath, R., et al., *Antihypertensive activity of a quinoline appended chalcone derivative and its site specific binding interaction with a relevant target carrier protein*, RSC Advances, 5(80), 65496-65513, 2015.

[14] Aslan, H., Yetişsin, F., Korkmaz, A., Bursal, E., *Design, Synthesis, Characterization, Enzyme Inhibition, Molecular Docking, and Pharmacological Evaluation of New Chalcone‐Sulfonate Derivatives Bearing Thiophene*, ChemistrySelect, 9(14), e202400053, 2024.

[15] Korkmaz, A., *Design, synthesis, characterization, molecular docking studies, molecular properties, toxicity, and bioactivity score prediction evaluation of novel chalcone-sulfonate hybrid derivatives*, Journal of Molecular Structure, 1286, 135597, 2023.

[16] Singh, G., Arora, A., Kalra, P., Maurya, I.K., Ruizc, C.E., Estebanc, M.A., et al., *A strategic approach to the synthesis of ferrocene appended chalcone linked triazole allied organosilatranes: Antibacterial, antifungal, antiparasitic and antioxidant studies,* Bioorganic & Medicinal Chemistry, 27(1), 188-195, 2019.

[17] Guantai, E.M., Ncokazi, K., Egan, T.J., Gut, J., Rosenthal, P.J., Bhampidipati, R., et al., *Enone–and chalcone–chloroquinoline hybrid analogues: in silico guided design, synthesis, antiplasmodial activity, in vitro metabolism, and mechanistic studies,* Journal of Medicinal Chemistry, 54(10), 3637-3649, 2011.

[18] Al-Rifai, N.M., & Mubarak, M.S., *α-Substituted Chalcones:A Key Review,* ChemistrySelect, 6(46), 13224-13252, 2021.

[19] Kumar, D., Kumar, N.M., Tantak, M.P., Ogura, M., Kusaka, E., & Ito, T., *Synthesis and identification of α-cyano bis (indolyl) chalcones as novel anticancer agents*, Bioorganic & Medicinal Chemistry Letters, 24(22), 5170-5174, 2014.

[20] Fahim, A.M., & Farag, A.M. *Synthesis, antimicrobial evaluation, molecular docking and theoretical calculations of novel pyrazolo [1,5-a] pyrimidine derivatives,* Journal of Molecular Structure, 1199, 127025, 2020.

[21] Yilmaz, M., Uzunalioğlu, N., Yakut, M., & Pekel, A.T.*, Oxidative cyclisation of 3-oxopropanenitriles mediated manganese (III) acetate with 2-thienyl substituted alkenes,* Turkish Journal of Chemistry, 32(4), 411-422, 2008.

[22] Amancha, P.K., Lai, Y.C., Chen, I.C., Liu, H.J., & Zhu, J.L., *Diels–Alder reactions of acyclic α-cyano α, β-alkenones: a new approach to highly substituted cyclohexene system*, Tetrahedron, 66(4), 871-877, 2010.

[23] Stagos, D., Soulitsiotis, N., Tsadila, C., Papaeconomou, S., Arvanitis, C., Ntontos, A., et al., *Antibacterial and antioxidant activity of different types of honey derived from Mount Olympus in Greece,* International Journal of Molecular Medicine, 42(2), 726-734, 2018.

[24] Mama, M., Teshome, T., & Detamo, J., *Antibacterial Activity of Honey against Methicillin-Resistant Staphylococcus aureus: A Laboratory-Based Experimental Study,* International Journal of Microbiology, 2019, 7686130, 2019.

[25] Blois, M.S., *Antioxidant determinations by the use of a stable free radical*, Nature, 181(4617), 1199-1200, 1958.

[26] Kumar, L.S., Prasad, K.S., & Revanasiddappa, H.D., *Synthesis, characterization, antioxidant, antimicrobial, DNA binding and cleavage studies of mononuclear Cu (II) and Co (II) complexes of 3-hydroxy-N'-(2-hydroxybenzylidene)-2-naphthohydrazide,* European Journal of Chemistry, 2(3), 394-403, 2011.

[27] Ma, L., Yuan, L., Xu, C., Li, G., Tao, M., & Zhang, W., *An efficient synthesis of 2-aminothiophenes via the Gewald reaction catalyzed by an N-methylpiperazine-functionalized polyacrylonitrile fiber,* Synthesis, 45(01), 45-52, 2013.

[28] El-Shenawy, A.I., *Synthesis and in vitro antibacterial evaluation of some novel annulated quinazolinone derivatives*, Russian Journal of General Chemistry, 88, 1712-1719, 2018.

[29] Mohamed, M.F., Ibrahim, N.S., Saddiq, A.A., & Abdelhamid, I.A., *Novel 3-(pyrazol-4-yl)-2-(1 H-indole-3-carbonyl) acrylonitrile derivatives induce intrinsic and extrinsic apoptotic death mediated P53 in HCT116 colon carcinoma*, Scientific Reports, 13(1), 22486, 2023.

[30] Bhale, P.S., Shringare, S.N., Khade, A.B., Chavan, H.V., S*ynthesis, Characterization and Biological Evaluation of Indole-Pyrazole Amalgamated α-Cyano Substituted Chalcones,* Anti-Cancer Agents in Medicinal Chemistry, 21(16), 2216-2223, 2021.

[31] Bhale, P.S., Chavan, H.V., Endait, R.S., Kadam, A.T., Bopalkar, R.J., & Gaikwad, M.S., *Synthesis and Biological Evaluation of Indolyl Bis-chalcones as Anti-Breast Cancer and Antioxidant Agents*, Croatica Chemica Acta, 94(1), 35-41, 2021.

[32] Zlotnikov, I.D., Krylov, S.S., Belogurova, N.G., Blinnikov, A.N., Kalugin, V.E., & Kudryashova, E.V., *New Derivatives of Chalcones, Chromens and Stilbenoids, Complexed with Methyl-β-Cyclodextrin, Show Antioxidant Properties and Antibacterial Synergism with Antibiotics,* Biophysica*, 4(4), 667-694, 2024.

[33] Sallam, H.A., Elgubbi, A.S., & El-Helw, E.A.E., *Synthesis and antioxidant screening of new 2-cyano-3-(1,3-diphenyl-1H-pyrazol-4-yl)acryloyl amide derivatives and some pyrazole-based heterocycles*, Synthetic Communications, 50(13), 2066–2077, 2020.

[34] Gacche, R.N., Dhole, N.A., Kamble, S.G., & Bandgar, B.P., *In-vitro evaluation of selected chalcones for antioxidant activity*, Journal of Enzyme Inhibition and Medicinal Chemistry, 23(1), 28–31, 2008.

[35] Kim, B.T., Chun, J.C., & Hwang, K.J., *Synthesis of dihydroxylated chalcone derivatives with diverse substitution patterns and their radical scavenging ability toward DPPH free radicals*, Bulletin of the Korean Chemical Society, 29(6), 1125-1130, 2008.

Discovery of Potential PD-1 and PD-L1 Interaction Inhibitors Using Combined Molecular Modeling Approaches

Özlem ULUCAN[1,*]

[1]*İstanbul Bilgi University, Faculty of Engineering and Natural Sciences, Department of Genetics and Bioengineering, 34060, İstanbul, Türkiye*
ozlem.ulucan@bilgi.edu.tr, ORCID: 0000-0002-7442-5728

Abstract

Immune checkpoints are regulators of the immune system that maintain immune homeostasis and prevent autoimmunity. Cancer cells often manipulate immune checkpoint mechanisms to escape anti-tumor immune response by overexpressing the immune checkpoint ligands. Thus, the interactions between the immune checkpoint receptors and ligands attracted attention and were proven to be effective targets in treating cancer. In this study, combining several computational approaches, we discovered small molecules that effectively bind to the ligand Programmed Cell Death Ligand 1 (PD-L1) and have the potential to hamper its interaction with the negative immune checkpoint receptor Programmed Cell Death Protein-1 (PD-1). Different pharmacophore models were constructed using triple and quadruple combinations of the interface residues on PD-1, which were used later for scanning the ZINC15 database. 12714 small molecules were retrieved and virtually screened using molecular docking calculations. The complexes of promising small molecules with PD-L1 were further evaluated using energetic and structural analyses. Our results suggest that the three small molecules ZINC21075815, ZINC70692276, and ZINC64031730 retrieved from the ZINC15 database establish stable and energetically favorable interactions with PD-L1 at the hot region consisting of the residues Tyr

56, Glu 58, Arg 113, Met 115, and Tyr 123. These molecules can be used as a starting point to develop more effective and selective anti-PD-1/PD-L1 inhibitors.

Keywords: Inhibitory T cell receptors, immunomodulation; PD-1 receptor; computer-aided drug design; Molecular docking; Molecular dynamic simulations.

Moleküler Modelleme Yaklaşımları Kullanılarak Potansiyel PD-1 ve PD-L1 Etkileşim İnhibitörlerinin Keşfi

Öz

Bağışıklık kontrol noktaları, bağışıklık homeostazını sürdüren ve otoimmüniteyi önleyen bağışıklık sistemi düzenleyicileridir. Kanser hücreleri, anti-tümör bağışıklık yanıtından kaçmak için sıklıkla bağışıklık kontrol noktası ligandlarını aşırı ifade ederek bağışıklık kontrol noktası mekanizmalarını manipüle eder. Bu nedenle, bağışıklık kontrol noktası reseptörleri ve ligandları arasındaki etkileşimler araştırmacıların dikkatini çekmiş ve bu etkileşimin kanser tedavisinde etkili hedefler olduğu gösterilmiştir. Bu çalışmanın temel amacı, çeşitli hesaplamalı yaklaşımları birleştirilerek, ligand PD-L1'e etkili bir şekilde bağlanan ve negatif bağışıklık kontrol noktası reseptörü PD-1 ile etkileşimini engelleme potansiyeli taşıyan küçük moleküller keşfetmektir. Bu amaç doğrultusunda PD1/PD-L1 ara yüzünde PD-1 üzerindeki amino asitlerin üçlü ve dörtlü kombinasyonları kullanılarak farklı farmakofor modelleri oluşturuldu. Farmakofor modelleri kullanılarak ZINC15 veri tabanı tarandı. ZINC15 veri tabanından indirilen 12714 küçük molekül moleküller için moleküler kenetleme çalışmaları gerçekleştirildi. Moleküler kenetleme çalışmalarında öne çıkan küçük moleküllerin PD-L1 ile komplekslerinin moleküler dinamik simülasyonları gerçekleştirildi ve bu kompleksler enerjik ve yapısal analizler kullanılarak detaylıca incelendi. Bulgularımız, ZINC15 veri tabanından alınan ZINC21075815, ZINC70692276 ve ZINC64031730 adlı üç küçük molekülün, Tyr 56, Glu 58, Arg 113, Met 115 ve Tyr 123 amino asitlerinden oluşan sıcak bölgede PD-L1 ile kararlı ve enerjik açıdan uygun etkileşimler kurduğunu göstermektedir. Bu moleküller, daha etkili ve seçici anti-PD-1/PD-L1 inhibitörleri geliştirmek için bir başlangıç noktası olarak kullanılabilir.

Anahtar Kelimeler: İnhibitör T hücre reseptörleri; İmmünomodülasyon; PD-1 reseptörü; Bilgisayar destekli ilaç tasarımı; Moleküler kenetleme; Moleküler dinamik simülasyonları.

1. Introduction

The immune system's role in controlling tumor growth and spread is now well established. However, tumor cells may evolve mechanisms to escape immune surveillance and suppress immune response. One of the frequently used mechanisms by tumor cells is the exploitation of

co-inhibitory immune checkpoints via overexpression of immune checkpoint ligands such as PDL-1[1], CD155[2], and CD112[3]. Revealing how immune checkpoints work has paved the way for new strategies to fight against cancer. The primary focus in the rapidly emerging field of cancer immunotherapy is to control and redirect the host immune response to recognize and eliminate cancer cells. Developing immune checkpoint inhibitors, mainly antibodies, has provided a remarkable advancement in this field. Those inhibitors exhibit their effects by interrupting co-inhibitory signals and reactivating antitumor immune responses. PD-1/PD-L1 and CTLA-4 inhibitors have shown promising effects among the immune checkpoint inhibitors. Some have been approved for treating different types of cancers, while clinical trials for others are ongoing [4–6]. PD-1 (CD279), one of the well-studied immune checkpoint receptors, delivers a co-inhibitory signal when it binds to one of its ligands, PD-L1 and PD-L2. Several monoclonal antibodies targeting PD-1/PD-L1 interaction have been approved for monotherapy or combinatorial therapy with other therapeutic agents, such as other immune checkpoint inhibitors, radiation, and chemotherapy against different cancer types [7, 8].

Despite the success of monoclonal antibodies in immunotherapy against cancer, some of their disadvantages have led researchers to seek small-molecule or peptide alternatives [7, 9]. The production cost of monoclonal antibodies remains exceptionally high. While their high molecular weight prevents them from diffusing into the tumor, their high affinity for the target keeps them on the outer edge of the tumor. Additionally, their unintended interactions with various cell surface receptors prolong their retention in circulation and delay their arrival at the target site or excretion from the body [10, 11]. When administered as a monotherapy, monoclonal antibodies reported common side effects are fatigue, rash, diarrhea, colitis, endocrine and hepatic toxicities, pneumonitis, neurological syndromes, and ocular toxicities [12]. For the anti-PD-1 monoclonal antibodies, severe and sometimes fatal lung-related autoimmune adverse effects have been reported [13, 14]. This is partly due to PD-1 inhibition simultaneously disrupting the binding of both ligands, PD-L1 and PD-L2, which play an essential role in maintaining immune homeostasis in the lung. Targeting PD-L1 has some advantages over targeting PD-1[15]. When PD-L1 is targeted, PD-L2 remains active, reducing the risk of developing severe inflammatory toxicity in organs such as the lungs [16]. Moreover, targeting PD-L1 also disrupts the interaction of PD-L1 with B7-1, the function of which is to inhibit T-cell activation and cytokine production [17, 18].

Small molecules have numerous key advantages, such as being cheap, being administered orally, having low immunogenic potential, and kinetic advantages over significant antibodies [19]. However, the discovery process for these molecules faces several difficulties, especially for protein-protein interaction inhibitors [20]. This is due to the lack of natural small-molecule

binders that can be used as starting points, the relatively large surface area buried by both protein partners, the flatness of the interfaces, and the absence of narrow, deep cavities at the interfaces. Fortunately, we also know that the small-molecule effectors do not need to cover the entire interface due to the small number of interface residues that contribute substantially to binding affinity [21]. Yet, the protein-protein interaction modulators have been reported to be larger on average than classical drug molecules and tend to be more hydrophobic and rigid. They have fewer hydrogen bonding groups than classical drug-like molecules [22]. PD-1/PD-L1 interaction forms a typical example of protein-protein interfaces. Zak et al. [23] reported that the relatively flat interface involves polar and nonpolar interactions and has a moderately large, buried surface area. Their structural analysis showed three major hotspots on PD-L1 that can be important for drug design. The first hotspot is a pocket of predominantly hydrophobic character that accommodates Ile 134 of PD-1. The second hotspot is a neighbor of the first one and accommodates Ile 126 of PD-1. Finally, the third hot spot is an extended groove where the PD-1 residues Tyr 68, Gln 75, and Thr 76 of PD-1 bind.

In this study, we combined several computational approaches to discover new small-molecule candidates that target the PD-1/PD-L1 interaction. We scanned the ZINC15 database and retrieved 12714 small molecules that were further evaluated using molecular docking and molecular dynamic (MD) simulations. Detailed energetic and structural analyses suggested three molecules that form stable and energetically favorable interactions with PD-L1 at the region consisting of the residues Tyr 56, Glu 58, Arg 113, Met 115, and Tyr 123.

2. Materials and Methods

2.1. Generation of Small Molecule Set

The atomic coordinates of the PD-1/PD-L1 complex were retrieved from the PDB databank with the PDB ID 4ZQK. PD-1 (chain B) was used to generate structure-based pharmacophore models, whereas PD-L1 (chain A) was used as the target protein in docking calculations.

All possible triple combinations of the interfacial residues were generated. Then, the triple combinations with a distance larger than 7 Å between any of their two residues were eliminated, resulting in 63 triple combinations in total. These triple residue combinations were used to construct pharmacophores, which were used later to screen the ZINC15 database [24]. 12714 small molecules were retrieved from the ZINC15 database using these pharmacophores. The pharmacophore models that resulted in a vast number of hits in the ZINC15 database were reconstructed by including another residue within 7 Å distance to the original residues. Thus, 8 more pharmacophore models were constructed using quadruple combinations of interface

residues. PocketQuery was combined with ZINCPharmer to construct pharmacophore models and search the ZINC15 database [25].

2.2. Molecular Docking Calculations

We carried out two sets of molecular docking simulations using the molecular docking software AutoDock 4.2 [26]. In the first set of calculations, we docked 12714 small molecules to the target protein PD-L1 using the standard Lamarckian genetic algorithm protocol, where the size of the initial population and the maximum number of energy evaluations were set to 300 and 5 million, respectively. Afterward, we ranked the small molecules based on their free binding energies to PD-L1. The top 600 molecules were selected and evaluated further in the second set of docking calculations. In the second set of calculations, the maximum number of energy evaluations and the number of independent runs were increased gradually. Here, we aimed to generate a single densely populated cluster with low energy to achieve convergence in the results. The results are based on 100 independent runs, with a maximum of 30 million energy evaluations set for each run.

The target protein PD-L1 and the small molecules were prepared for docking using the AutoDock Tools version 1.5.6 [26]. The torsions of the small molecules were determined by employing the AutoTors function of AutoDock Tools. Amide and ring torsions were kept rigid, while all other torsions were treated as flexible. Gasteiger atomic charges were assigned to both the protein and the small molecules. The non-polar hydrogen atoms were treated implicitly. Grid maps were generated with 0.375Å spacing by the AutoGrid program. The grid dimensions were chosen to ensure that all of the residues on PD-L1 at the PD-1/PD-L1 interface were included. Thus, the grid dimensions were 60Å x 80Å x 60Å. The initial position of the ligand was set randomly in both sets of docking calculations.

We assumed that a docking calculation was converged when 20% of the 100 independent runs resulted in the same binding conformation. Subsequently, we ranked the molecules that fulfill the convergence criterion according to their binding free energies and selected the top 20 molecules for further analysis.

2.3. Parameterization of Small Molecules

Topologies and parameters for the small molecules selected for molecular dynamic (MD) simulations were obtained using the Antechamber Python Parser Interface (ACPYPE) [27]. The spatial coordinates of each small molecule were obtained from the top-ranked conformation within the dominant cluster. The AM1-BCC charges were derived after the optimization of the

structure [28]. Force constants and equilibrium values for the bond lengths, angles, and dihedrals of the compounds were borrowed from the General Amber Force Field (GAFF) [29].

2.4. Molecular Dynamics (MD) Simulations

In this work, we performed 11 ns conventional MD simulations of 20 protein-ligand complexes solvated in explicit water, utilizing Gromacs version 5.1.2 [30]. For the MD simulation of each complex, we used the highest-ranking conformation within the dominant cluster derived from molecular docking runs as starting structures. The complex was inserted in a cubic box filled with TIP3P water molecules, and the whole system was neutralized by adding counterions. The Amber force field ff99sb-ildn [31] was utilized for modeling the interactions of protein and ions. The short-range non-bonded interactions were cut at 1.2 nm. The electrostatic interactions were treated using the particle mesh Ewald method. A dispersion correction was implemented for pressure and energy, while periodic boundary conditions were enforced in every direction.

Energy minimization was performed using a combination of algorithms, performing 1000 steps of the conjugate gradient method, with one steepest descent step inserted every 10 steps. After minimization, we equilibrated each system by running 100 ps of molecular dynamics (MD) in the NVT ensemble. During equilibration, the non-hydrogen atoms of the protein were harmonically restrained with a force constant of 1000 kJ mol^{-1} nm^{-2}. Solute and solvent atoms were independently coupled to temperature baths where the temperature was maintained at 300 K with a coupling time of 0.5 ps. A leap-frog algorithm was used to integrate Newton's motion equations, with a time step set to 2 fs. We used an NPT ensemble for the production phase without applying any restraints. The pressure was kept at 1 bar with the help of the Parrinello-Rahman barostat [32], setting the time constant to 0.5 ps. To regulate the temperature, we employed the Nose-Hoover temperature coupling method [33, 34], setting the reference temperature to 300 K and the time constant to 0.5 ps. The generated trajectories were used for free energy calculations.

2.5. Binding Free Energy Calculations

The end-point MM(PB/GB)SA method integrates gas-phase and solvation energy contributions derived using an implicit solvent model for the ligand, receptor, and complex. Additionally, solute entropy contributions are included to refine the total free energy.

In this work, we used the single trajectory approach to derive the binding free energies for the selected compounds. We treated the first 1 ns of each trajectory as the equilibrium phase. Before the free energy calculations, water molecules and ions were removed from the trajectory files. The computations were performed with the MMPBSA.py script of AmberTools18 [35]. For

the calculation of the gas phase free energy contributions, the Sander program in AmberTools18 was utilized.

The polar contribution of solvation-free energy was derived using the continuum solvent model GB-OBC introduced by Onufriev et al. [36]. The values 1.0, 0.8, and 4.85 were used for the parameters α, β, and γ. As Onufriev et al. [37] suggested, we utilized mbondi2 radii for effective Born radii. The LCPO method [38] was used to approximate the nonpolar components of solvation-free energy. Translational, rotational, and vibrational entropies were calculated individually and then summed to estimate the solute configurational entropy.

We computed the translational and rotational entropies from their gas phase partition functions. Frequencies for the vibrational modes were derived by normal-mode analysis following energy minimization. The entropy was averaged using 200 equally spaced snapshots taken from the trajectory.

To calculate the standard error of the binding free energy, we combined the standard errors for the effective energy from the MMGBSA method and the solute entropy using quadrature. The resulting standard error was then used to create a 95% Welch-Satterthwaite confidence interval for the binding free energy.

As positive controls, two well-characterized PD-L1 dimerizers (BMS-202 [39] and A1D9R [40]) and two compounds that bind PD-L1 in its monomeric form (CA-170 [41] and the cyclic peptide, Peptide 104, [42]) were used. For BMS-202 (5J89, chain C) and A1D9R (9INU, chain A), docked models and available crystal structures were used as starting structures for the simulations. For Peptide 104, only the crystal structure (PDB ID: 7OUN) was used, as the number of torsions exceeded the maximum allowed for docking. In the case of CA-170, a representative docked conformation was obtained as explained in the Materials and Methods, as no crystal structure was available.

3. Results and Discussion

3.1. Generation of Small-molecule Dataset

The interface residues of the PD-1/PD-L1 complex were retrieved from the PDBsum database. PD-1 and PD-L1 contribute to the interface with 17 residues, corresponding to an interface area of 1557 Å^2 that forms 2 salt bridges, 11 hydrogen bonds, and many other non-bonded close contacts. Using the interface residues on PD-1, 71 different pharmacophore models were constructed to be used later for scanning the ZINC15 database. Some of the pharmacophores did not match with any small molecules, while others resulted in millions of molecules. We

modified the pharmacophore models, which resulted in millions of molecules, including another nearby residue that fulfilled our distance criterion. More than 12000 small molecules were retrieved from the ZINC15 database using the pharmacophore models constructed from the PD-1 interfacial residues. Based on the residue combinations used for pharmacophore modeling, the number of retrieved molecules ranges from 1 to 4367.

3.2. Virtual Screening by Molecular Docking

We selected the molecules based on their binding free energies in the first set of docking calculations. This calculation set resulted in 600 promising small molecules further evaluated in the second set of calculations, where a more extensive search was performed. The molecules were filtered based on the convergence criterion (see the Methods Section) and ranked according to their binding free energies. Table 1 lists the top 20 molecules together with some of their molecular properties and their binding free energies obtained from molecular docking. As seen in Table 1, the most promising 20 molecules have quite different molecular properties. Among those molecules, there exists one tripeptide (ZINC83308150) and 2 macrocycles (ZINC94303267 and ZINC94303139). The molecular weight, logP values, and the charges for those molecules range from 350.5 to 765, -6.9 to 7.1, and 0 to 5, respectively (see Table 1).

We examined the docked conformations of the top 20 molecules and found that all of them, although they are of different molecular characters, were bound to the same site on PD-L1 (see Fig. 1b). This site covers two of the three hotspots reported before by Zak et al. (see Fig. 1a). Even though the grid box used in docking calculations spanned the whole interface on PD-L1, the site preference of the top 20 molecules suggests that the two hotspots (HS-1 and HS-2) may, in fact, be druggable.

Table 1: The top 20 promising molecules came out of molecular docking calculations. The reported binding free energies were obtained from the second set of molecular docking calculations. The molecular weight and logP values were taken from the ZINC15 database.

Molecule ID	Molecular Weight	LogP	Charge	Binding free energy (kcal/mol)
ZINC77271764	539.6	-6.9	5	-17.3
ZINC77271775	539.6	-6.9	5	-15.8
ZINC67910521	666.8	1.8	0	-14.2
ZINC83308150	426.6	-1.7	0	-12.1
ZINC94303267	720.9	1.3	2	-11.9
ZINC67903231	682.8	0.4	0	-11.7
ZINC77257248	678.9	3.3	0	-11.4
ZINC22048461	449.7	2.2	2	-11.2
ZINC36047071	433.4	-1.8	0	-11.2
ZINC39500620	412.5	1.2	1	-11.0

ZINC39362507	378.5	0.9	1	-10.8
ZINC21075815	464.6	4.7	0	-10.6
ZINC70692276	536.6	0.4	0	-10.5
ZINC20832674	487.6	2.1	0	-10.5
ZINC59676745	632.8	7.1	0	-10.4
ZINC40173059	505.5	5.8	0	-10.3
ZINC64031730	350.5	0.4	1	-10.3
ZINC77257358	620.8	3.1	0	-10.2
ZINC35456718	520.5	0.1	0	-10.1
ZINC94303139	765	1.9	1	-10.1
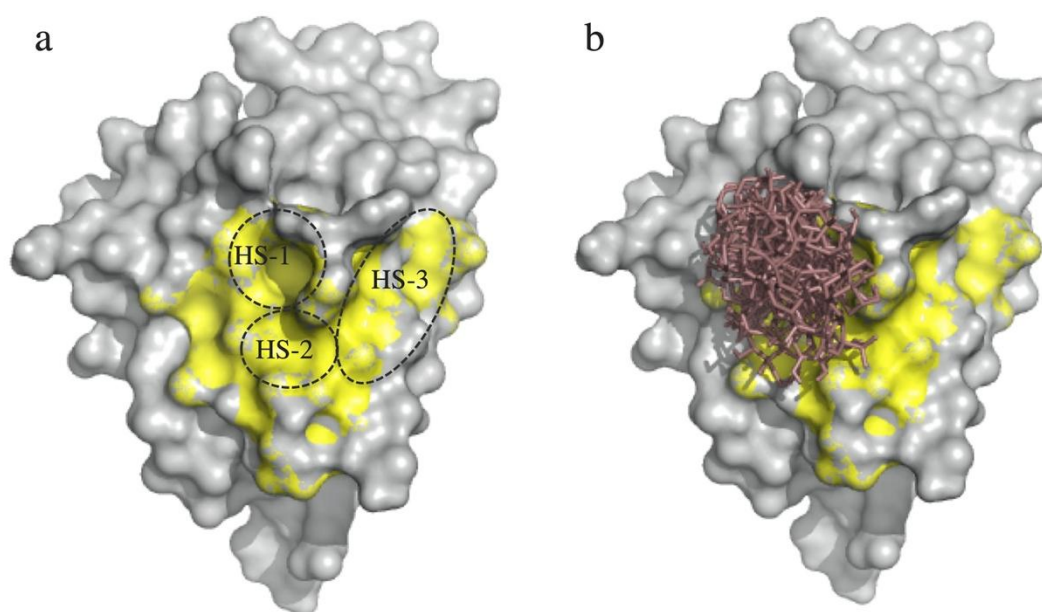
Figure 1: Site preference of the top 20 molecules on PD-L1. a) The 3 hotspots (HS-1, HS-2, and HS-3) on PD-L1 reported by Zak et al. b) Docked top 20 molecules shown with stick representation. The PD-L1 residues that contribute to the PD-1/PD-L1 interface are depicted in the yellow surface.

3.3. Energetic and Structural Evaluation of PD-L1/Small-molecule Complexes

We performed 11 ns MD simulations of 20 protein-ligand complexes derived from molecular docking calculations. For all analyses performed using MD simulation trajectories, the first 1 ns was treated as the equilibrium phase and discarded.

Table 2 summarizes the energy contributions of each term obtained from MMGBSA and entropy calculations. Free energy calculations put forward 6 molecules (ZINC77271775, ZINC67910521, ZINC67903231, ZINC21075815, ZINC70692276, and ZINC64031730) whose free energies of binding vary from -7.1 to -18.1 kcal/mol (see Table 2). Binding free energies for the other 14 molecules are higher than -5 kcal/mol, which indicates nonspecific binding or no binding. Therefore, we decided to further assess the complexes for the 6 promising small molecules using detailed structural analysis.

Table 2: MMGBSA and entropy contributions to the binding free energies for the top 20 molecules. VdW and EEL refer to the average Van der Waals and electrostatic interaction energies, respectively, while EGB and ESURF represent the average polar and nonpolar solvation-free energies. TOTAL indicates the MMGBSA effective energy, which includes the contribution of solute entropy. The values in parentheses represent the standard deviations, and the brackets indicate the 95% Welch-Satterthwaite confidence interval for the binding free energy.

Molecule ID	MMGBSA					Entropy	Binding free energy (kcal/mol)
	VdW	EEL	EGB	ESURF	TOTAL		
ZINC77271764	-16.1	-283.2	279.3	-3.1	-23.1 (3.9)	-19.8 (3.6)	-3.3 [-3.8, -2.8]
ZINC77271775	-2.5	-392.0	360.8	-2.7	-36.4 (6.5)	-18.3 (3.4)	-18.1 [-18.7, -17.5]
ZINC67910521	-32.9	-15.5	24.0	-4.1	-28.5 (3.9)	-19.3 (3.0)	-9.2 [-9.7, -8.7]
ZINC83308150	-22.2	-10.2	21.9	-3.2	-13.7(4.1)	-18.6 (3.9)	4.9 [4.3, 5.5]
ZINC94303267	-12.6	-80.0	81.6	-2.2	-13.2 (5.4)	-18.2 (3.1)	5.0 [4.5, 5.5]
ZINC67903231	-34.5	-12.1	24.9	-4.5	-26.2 (3.8)	-18.0 (3.4)	-8.5 [-8.7, -7.7]
ZINC77257248	-26.4	-16.6	22.1	-3.7	-24.6 (6.2)	-20.1 (3.3)	-4.5 [-5.0, -4.0]
ZINC22048461	-12.1	-162.3	153.3	-2.5	-23.6 (6.5)	-19.6 (3.7)	-4.0 [-4.6, -3.4]
ZINC36047071	-25.0	-36.7	45.1	-3.4	-20.0 (3.9)	-19.5 (2.5)	-0.5 [-0.9, -0.1]
ZINC39500620	-25.5	-32.4	43.2	-3.1	-17.8 (3.8)	-19.7 (2.9)	1.9 [1.5, 2.3]
ZINC39362507	-16.4	-76.7	78.3	-2.2	-17.0 (4.3)	-19.5 (3.4)	2.5 [2.0, 3.0]
ZINC21075815	-25.1	-37.9	39.3	-3.8	-27.5 (4.0)	-18.9 (3.0)	-8.6 [-9.1, -8.1]
ZINC70692276	-25.0	-40.4	43.9	-3.4	-24.9 (3.8)	-17.8 (2.1)	-7.1 [-7.4, -6.7]
ZINC20832674	-30.8	-13.2	25.5	-4.4	-22.9 (4.9)	-21.9 (4.2)	-1.0 [-1.6, -0.4]
ZINC59676745	-33.3	-8.9	21.4	-4.1	-24.9 (4.5)	-22.6 (3.0)	-2.3 [-2.8, -1.8]
ZINC40173059	-26.7	-9.5	18.3	-3.1	-21.0 (3.4)	-18.3 (2.2)	-2.7 [-3.0, -2.4]
ZINC64031730	-21.9	-75.0	72.6	-2.4	-26.7 (3.0)	-18.8 (2.8)	-7.9 [-8.3, -7.5]
ZINC77257358	-34.2	-10.2	22.7	-4.5	-26.2 (4.2)	-21.9 (3.2)	-4.3 [-4.8, -3.8]
ZINC35456718	-27.3	-20.3	29.3	-3.7	-22.0 (8.3)	-21.9 (3.5)	-0.1 [-0.7, 0.5]
ZINC94303139	-22.0	-26.8	39.0	-3.1	-12.9 (2.9)	-21.3 (3.5)	8.4 [7.9, 8.9]
Peptide 104	-49.9	-144.0	158.2	-7.9	-43.6 (10.5)	-31.0 (3.9)	-12.6 [-13.4, -11.8]

Table 3 depicts some structural properties of the complexes formed by PD-L1 and 6 small molecules. The root mean square deviation (RMSD) values were computed using the docked

conformations of the molecules as reference structures after aligning the protein conformations. While RMSD values show how the molecular conformations during the simulations differed from the docked conformations, the standard deviations show how stable the binding conformations were throughout the simulations (See Table 3). Fig. 2 shows how the RMSD values for the promising 6 small molecules change over time. The compounds ZINC77271775 and ZINC67910521 adopted conformations that were different from their docked conformations during the simulations. The compound ZINC67903231 did not adopt a stable conformation over time (see Fig. 2). However, ZINC21075815, ZINC70692276, and ZINC64031730 preserved conformations close to their docked conformations throughout the simulations (see Fig. 2). The average RMSD values were 2.4 Å, 2.5 Å, and 3.1 Å for ZINC21075815, ZINC70692276, and ZINC64031730, respectively (see Table 3).
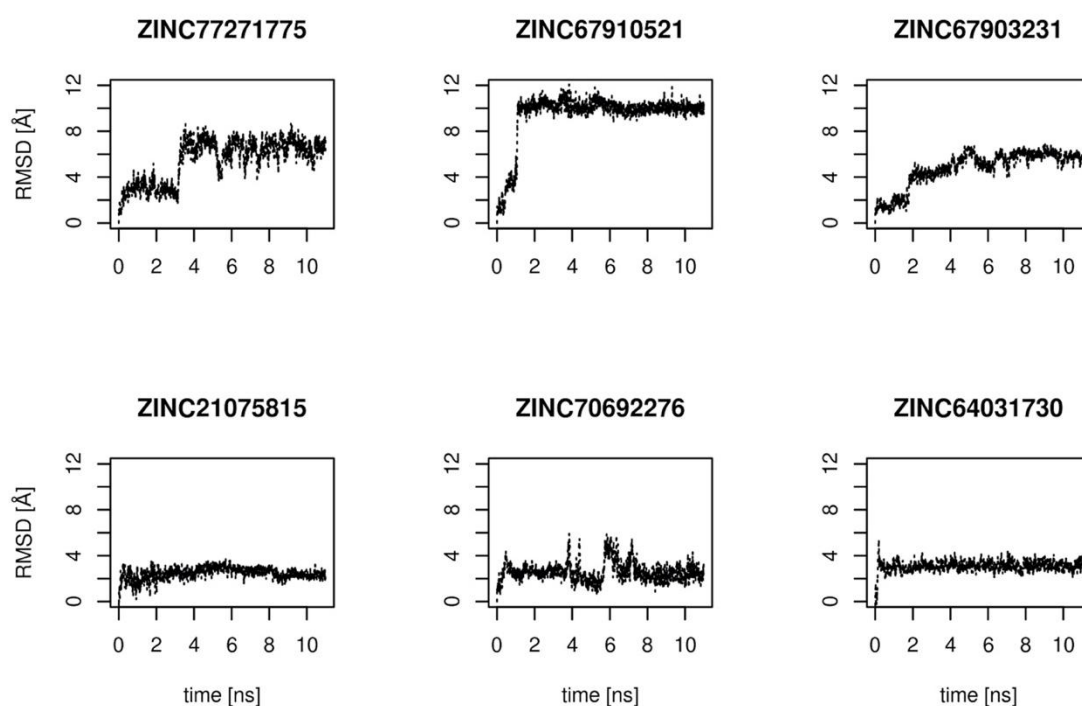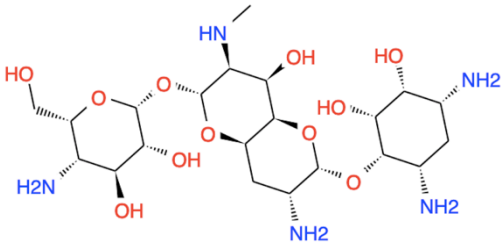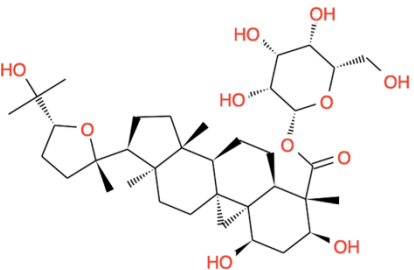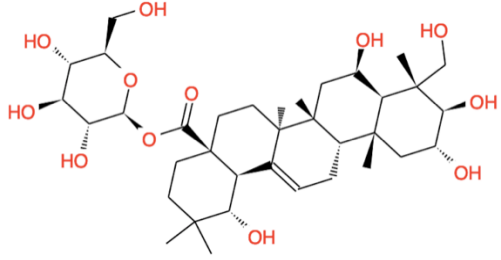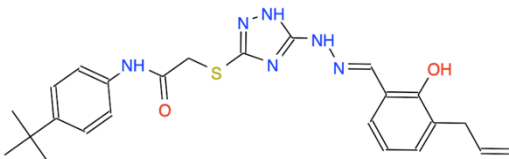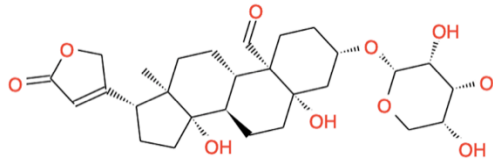
Figure 2: RMSD values for 6 promising molecules over time. The RMSD values were computed using the docked conformations of the molecules as reference structures after aligning the protein conformations.

The buried solvent-accessible surface area (BSASA) was calculated as the sum of the solvent-accessible surface area of PD-L1 and the small molecule minus the solvent-accessible surface area of the complex. Note that we did not assume interface symmetry and did not divide the total buried solvent accessible surface area by two. Hence, the values in Table 3 involve the surface contributions of both binding partners. The smallest (ZINC64031730) and the largest (ZINC77271775) BSASA values given in Table 3 account for 43% and 63% of the solvent-accessible surface area buried upon complexation of PD-1 and PD-L2 (1557 Å^2). Except for

ZINC77271775, our small molecules tend to form fewer hydrogen-bonding contacts than average drug-like molecules. The average BSASA values and the number of hydrogen-bonding contacts the molecules formed are comparable to those previously reported for TIMBAL molecules [22].

Table 3: Structural properties of 6 promising molecules and their complexes. The docked conformations of the molecules served as the reference points for RMSD calculations following the alignment of the protein conformations. Values given in parentheses stand for standard deviations. BSASA values and several hydrogen bonds were computed using the Gromacs routines gmx-sasa and gmx-hbond, respectively, with default settings.

Molecule ID	Chemical Structure	RMSD	H-bonds	BSASA ($Å^2$)
ZINC77271775		5.5 (1.8)	6.2 (1.0)	979.0 (63.0)
ZINC67910521		9.4 (2.3)	1.6 (0.6)	922.3 (52.2)
ZINC67903231		4.7 (1.6)	0.7 (0.8)	950.9 (56.4)
ZINC21075815		2.4 (0.5)	1.6 (1.2)	772.0 (50.4)
ZINC70692276		2.5 (0.8)	2.3 (0.8)	942.4 (48.3)

ZINC64031730   3.1 (0.5)   1.9 (0.8)   670.5 (40.2)
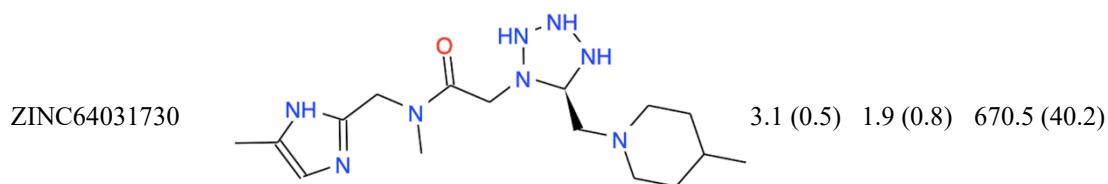
Figure 3 depicts the binding conformations of the three molecules (ZINC21075815, ZINC70692276, and ZINC64031730) that preserved conformations close to their docked conformations. As evident from Fig. 3, the PD-L1 surface exhibits high structural plasticity; therefore, the three hotspots shown in Fig.1a are no longer readily distinguishable. The rearrangement of the side chains of the contact residues (the RMSD value for the backbone of PD-L1 was smaller than 2 Å throughout the simulations) enabled stable interactions with the small molecules. We utilized the program LigPlot+ [43] to identify the PD-L1 residues forming contact with the small molecules. Even though the binding region on PD-L1 adopts a different conformation for each molecule, the contact residues are common (Tyr 56, Glu 58, Arg 113, Met 115, and Tyr 123) for all molecules. The common contact residues Tyr 56, Glu 58, Arg 113, Met 115, and Tyr 123 constitute the first hotspot, a pocket of predominantly hydrophobic character, and accommodates the PD-1 residue Ile 134 [23]. It is well-established that the free energy of binding is not evenly distributed across the interface; instead, a small subset of interface residues (enriched in tryptophan, tyrosine, and arginine) contributes substantially to the free energy of binding [21].
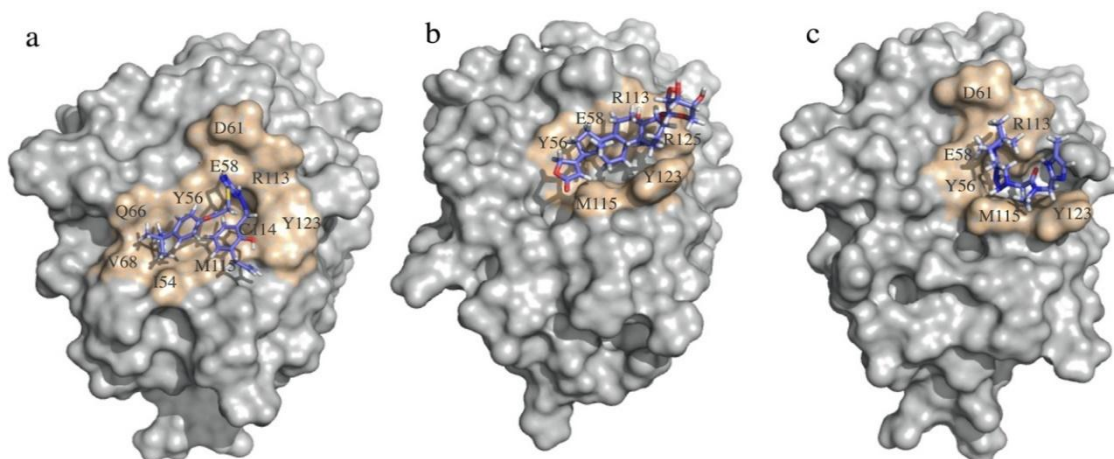
Figure 3: Conformations adopted by the small-molecules ZINC21075815 (a), ZINC70692276 (b), and ZINC64031730 (c) on PD-L1. The small molecules are shown in stick representation. The PD-L1 residues that contribute to binding are depicted in the orange surface. The conformations represent the last snapshots of the corresponding MD trajectories.

Moreover, it was shown that those energetically critical residues are not randomly distributed but rather form clusters termed hot regions [44]. A recent study that addresses hot regions at the PD-1/PD-L1 interfaces defined two hot regions, which comprise the residues Tyr

56, Glu 58, and Asn 66 and the residue Met 115, respectively. The first region (Tyr 56, Glu 58, and Asn 66) was important in antibody and small-molecule binding. In contrast, the second region (Met 115) was found to be necessary only in small-molecule binding [45]. Considering the site preference of the top 20 molecules in molecular docking calculations and the structural and energetic analysis of the MD trajectories of the PD-L1/Small-molecule complexes together with previously reported findings suggests that the PD-L1 residues Tyr 56, Glu 58, Arg 113, Met 115 and Tyr 123 comprise the hot region on PD-L1 at the PD-1/PD-L1 interface and this hot region is the most likely region to accommodate a small-molecule inhibitor of protein-protein interactions.

3.4. Comparisons with Known PD-L1 Inhibitors

Most well-known small-molecule PD-L1 inhibitors like BMS-202, A1D9R, and their analogs work by inducing PD-L1 dimerization, which sterically blocks PD-1 binding [46]. However, our aim in this study was to discover non-dimerizing small molecules that inhibit PD-1 binding. There are limited non-dimerizing PD-L1 inhibitors with well-defined structural and mechanistic evidence, and all are either antibodies or larger peptide/macrocyclic compounds that fall outside the typical small-molecule criteria. In fact, an analysis of all 67 human PD-L1 structures deposited in the Protein Data Bank further supported this, revealing the lack of well-characterized non-dimerizing small molecules.

Since no non-dimerizing small molecule with strong structural or mechanistic evidence for PD-L1 binding was available, we performed simulations of several reported compounds to evaluate their stability and binding behavior. Simulations of BMS-202 and A1D9R with monomeric PD-L1 showed unstable binding. None of the ligands kept their initial conformations, whether starting from docking poses or crystal structures. The average RMSD values exceeded 12 Å and 8 Å for BMS-202 and A1D9R, respectively, indicating substantial deviation from crystal structures. This is not surprising as these compounds bind to the dimeric form of PD-L1 in their crystal structures and interact with residues from both monomers.

CA-170 is an orally available small-molecule antagonist targeting PD-L1/PD-L2 and VISTA, proposed to disrupt PD-1/PD-L1 interaction without inducing PD-L1 dimerization. Although it has advanced to Phase I clinical trials, its direct binding to PD-L1 remains debated [41, 47]. CA-170 detached from PD-L1 within the first 3 ns of simulation, suggesting a lack of stable interaction. This observation aligns with the study reporting no direct interaction with PD-L1, supporting the view that CA-170 may act through an indirect or alternative mechanism [46].

Since well-known small molecules do not form stable interactions with monomeric PD-L1, we used the cyclic Peptide 104 as a positive control. This peptide maintained stable binding to monomeric PD-L1 throughout the simulation, with an average RMSD below 2.0 Å. The binding free energy computed using our protocol was −12.6 kcal/mol, consistent with the reported moderate binding affinity (120 nM) of the peptide [42], considering that MM/GBSA calculations often overestimate binding affinity [48]. Peptide 104 keeps its key interactions with residues Ile 54, Tyr 56, Met 115, and Tyr 123 in the simulation, which aligns with the binding regions observed for our most promising compounds, emphasizing the importance of this surface region for non-dimerizing PD-L1 binding.

4. Conclusion

In this study, using triple and quadruple combinations of the interface residues on PD-1, we constructed several pharmacophore models to scan the ZINC15 database. More than 12000 small molecules were retrieved from the ZINC15 database. The retrieved small molecules were virtually screened using molecular docking calculations. We further evaluated the complexes of promising small molecules energetically and structurally. Overall, our results suggest that the three small molecules ZINC21075815, ZINC70692276, and ZINC64031730 establish stable and energetically favorable interactions with PD-L1 at the hot region consisting of the residues Tyr 56, Glu 58, Arg 113, Met 115, and Tyr 123. This surface region undergoes local structural rearrangements and provides sufficient space and interaction surface to accommodate relatively large ligands such as ours. The positive control, Peptide 104, forms also key interactions with this surface region, underscoring the relevance of this region for non-dimerizing binding.

Our study highlights the relevance of incorporating molecular dynamics in drug discovery, as it provides a deeper understanding of the interactions and behavior of molecules in a dynamic environment. The molecules ZINC21075815, ZINC70692276, and ZINC64031730 have moderate estimated binding affinities (-8.6, -7.1, and -7.9 kcal/mol, respectively) for PD-L1 and can be used as starting points to develop more effective and selective non-dimerizing anti-PD-1/PD-L1 inhibitors.

References

[1] Wang, X., Teng, F.F., Kong, L., Yu, J.M., *PD-L1 expression in human cancers and its association with clinical outcomes*, Oncotargets and Therapy, 9, 5023–5039, 2016.

[2] Li, Y.C., Zhou, Q., Song, Q.K., Wang, R.B., Lyu, S.Z., Guan, X.D., et al., *Overexpression of an Immune Checkpoint (CD155) in Breast Cancer Associated with Prognostic Significance and Exhausted Tumor-Infiltrating Lymphocytes: A Cohort Study,* Journal of Immunology Research, 3948928, 2020.

[3] Pardoll, D.M., *The blockade of immune checkpoints in cancer immunotherapy*, Nature Reviews Cancer, 12, 252–264, 2012.

[4] Gong, J., Chehrazi-Raffle, A., Reddi, S., Salgia, R., *Development of PD-1 and PD-L1 inhibitors as a form of cancer immunotherapy: a comprehensive review of registration trials and future considerations*, Journal for Immunotherapy of Cancer, 6, 8, 2018.

[5] Darvin, P., Toor, S.M., Nair, V.S., Elkord, E., *Immune checkpoint inhibitors: recent progress and potential biomarkers*, Experimental and Molecular Medicine, 50, 1–11, 2018.

[6] Ai, L., Chen, J., Yan, H., He, Q., Luo, P., Xu, Z., et al., *Research Status and Outlook of PD-1/PD-L1 Inhibitors for Cancer Therapy*, Drug Design, Development and Therapy, 14, 3625–3649, 2020.

[7] Guzik, K., Tomala, M., Muszak, D., Konieczny, M., Hec, A., Blaszkiewicz, U., et al., *Development of the Inhibitors That Target the PD-1/PD-L1 Interaction: A Brief Look at Progress on Small Molecules, Peptides and Macrocycles*, Molecules, 24, 2071, 2019.

[8] Guo, L.B., Wei, R., Lin, Y., Kwok, H.F., *Clinical and Recent Patents Applications of PD-1/PD-L1 Targeting Immunotherapy in Cancer Treatment-Current Progress, Strategy, and Future Perspective*, Frontiers in Immunology, 11, 1508, 2020.

[9] Konstantinidou, M., Zarganes-Tzitzikas, T., Magiera-Mularz, K., Holak, T.A., Dömling, A., *Immune Checkpoint PD-1/PD-L1: Is There Life Beyond Antibodies ?,* Angewandte Chemie-International Edition, 57, 4840–4848, 2018.

[10] Chames, P., Van Regenmortel, M., Weiss, E., Baty, D., *Therapeutic antibodies: successes, limitations and hopes for the future,* British Journal of Pharmacology, 157, 220–233, 2009.

[11] Ryman, J.T., Meibohm, B., *Pharmacokinetics of Monoclonal Antibodies,* CPT Pharmacometrics and Systems Pharmacology, 6, 576–588, 2017.

[12] Hansel, T.T., Kropshofer, H., Singer, T., Mitchell, J.A., George, A.J.T., *The safety and side effects of monoclonal antibodies,* Nature Reviews Drug Discovery, 9, 325–338, 2010.

[13] Topalian, S.L., Hodi, F.S., Brahmer, J.R., Gettinger, S.N., Smith, D.C., McDermott, D.F., et al., *Safety, Activity, and Immune Correlates of Anti-PD-1 Antibody in Cancer,* New England Journal of Medicine, 366, 2443–2454, 2012.

[14] McDermott, J., Jimeno, A., *Pembrolizumab: PD-1 Inhibition as a Therapeutic Strategy in Cancer*, Drugs of Today, 51, 7–20, 2015.

[15] Chen, D.S., Irving, B.A., Hodi, F.S., *Molecular Pathways: Next-Generation Immunotherapy-Inhibiting Programmed Death-Ligand 1 and Programmed Death-1*, Clinical Cancer Research, 18, 6580–6587, 2012.

[16] Brahmer, J.R., Tykodi, S.S., Chow, L.Q.M., Hwu, W.J., Topalian, S.L., Hwu, P., et al., *Safety and Activity of Anti-PD-L1 Antibody in Patients with Advanced Cancer*, New England Journal of Medicine, 366, 2455–2465, 2012.

[17] Yang, J., Riella, L.V., Chock, S., Liu, T., Zhao, X., Yuan, X., et al., *The Novel Costimulatory Programmed Death Ligand 1/B7.1 Pathway Is Functional in Inhibiting Alloimmune Responses In Vivo,* Journal of Immunology, 187, 1113–1119, 2011.

[18] Paterson, A.M., Brown, K.E., Keir, M.E., Vanguri, V.K., Riella, L.V., Chandraker, A., et al., *The Programmed Death-1 Ligand 1: B7-1 Pathway Restrains Diabetogenic Effector T Cells In Vivo,* Journal of Immunology, 187, 1097–1105, 2011.

[19] Dranitsaris, G., Amir, E., Dorward, K., *Biosimilars of Biological Drug Therapies Regulatory, Clinical and Commercial Considerations,* Drugs, 71, 1527–1536, 2011.

[20] Wells, J.A., McClendon, C.L., *Reaching for high-hanging fruit in drug discovery at protein-protein interfaces,* Nature, 450, 1001–1009, 2007.

[21] Bogan, A.A., Thorn, K.S., *Anatomy of hot spots in protein interfaces,* Journal of Molecular Biology, 280, 1–9, 1998.

[22] Higueruelo, A.P., Schreyer, A., Bickerton, G.R.J., Pitt, W.R., Groom, C.R., Blundell, T.L., *Atomic Interactions and Profile of Small Molecules Disrupting Protein-Protein Interfaces: the TIMBAL Database,* Chemical Biology and Drug Design, 74, 457–467, 2009.

[23] Zak, K.M., Kitel, R., Przetocka, S., Golik, P., Guzik, K., Musielak, B., et al., *Structure of the Complex of Human Programmed Death 1, PD-1, and Its Ligand PD-L1,* Structure, 23, 2341–2348, 2015.

[24] Sterling, T., Irwin, J.J., *ZINC 15-Ligand Discovery for Everyone,* Journal of Chemical Information and Modeling, 55, 2324–2337, 2015.

[25] Koes, D.R., Camacho, C.J., *PocketQuery: protein-protein interaction inhibitor starting points from protein-protein interaction structure,* Nucleic Acids Research, 40, W387–W392, 2012.

[26] Morris, G.M., Huey, R., Lindstrom, W., Sanner, M.F., Belew, R.K., Goodsell, D.S., et al., *AutoDock4 and AutoDockTools4: Automated Docking with Selective Receptor Flexibility,* Journal of Computational Chemistry, 30, 2785–2791, 2009.

[27] Sousa da Silva, A.W., Vranken, W.F., *ACPYPE - AnteChamber PYthon Parser interfacE*, BMC Res Notes, 5, 367, 2012.

[28] Jakalian, A., Bush, B.L., Jack, D.B., Bayly, C.I., *Fast, efficient generation of high-quality atomic Charges. AM1-BCC model: I. Method,* Journal of Computational Chemistry, 21, 132–146, 2000.

[29] Wang, J., Wolf, R., Caldwell, J., Kollman, P., Case, D., *Development and testing of a general amber force field,* Journal of Computational Chemistry, 25, 1157–1174, 2004.

[30] Pronk, S., Pall, S., Schulz, R., Larsson, P., Bjelkmar, P., Apostolov, R., et al., *GROMACS 4.5: a high-throughput and highly parallel open-source molecular simulation toolkit,* Bioinformatics, 29, 845–854, 2013.

[31] Lindorff-Larsen, K., Piana, S., Palmo, K., Maragakis, P., Klepeis, J.L., Dror, R.O., et al., *Improved side-chain torsion potentials for the Amber ff99SB protein force field,* Proteins-Structure Function and Bioinformatics, 78, 1950–1958, 2010.

[32] Parrinello, M., Rahman, A., *Polymorphic Transitions in Single-Crystals - A New Molecular-Dynamics Method,* Journal of Applied Physics, 52, 7182–7190, 1981.

[33] Nose, S., *A Unified Formulation of the Constant Temperature Molecular-Dynamics Methods.* Journal of Chemical Physics, 81, 511–519, 1984.

[34] Hoover, W.G., *Canonical Dynamics - Equilibrium Phase-Space Distributions.* Physical Review A, 31, 1695–1697, 1985.

[35] Case, D.A., Betz, R.M., Cerutti, D.S., Cheatham, T.E. III, Darden, T.A., Duke, R.E., et al., *Amber 18,* University of California, San Francisco, 2018.

[36] Onufriev, A., Bashford, D., Case, D.A., *Modification of the generalized Born model suitable for macromolecules,* Journal of Physical Chemistry B, 104, 3712–3720, 2000.

[37] Onufriev, A., Bashford, D., Case, D.A., *Exploring protein native states and large-scale conformational changes with a modified generalized born model,* Proteins-Structure Function and Bioinformatics, 55, 383–394, 2004.

[38] Weiser, J., Shenkin, P.S., Still, W.C., *Approximate atomic surfaces from linear combinations of pairwise overlaps (LCPO),* Journal of Computational Chemistry, 20, 217–230, 1999.

[39] Zak, K.M., Grudnik, P., Guzik, K., Zieba, B.J., Musielak, B., Dömling, A., et al., *Structural basis for small molecule targeting of the programmed death ligand 1 (PD-L1),* Oncotarget, 7, 30323–30335, 2016.

[40] Sun, C., Cheng, Y., Dong, J., Hu, L., Zhang, Y., Shen, H., et al., *Novel PD-L1/VISTA Dual Inhibitor as Potential Immunotherapy Agents,* Journal of Medicinal Chemistry, 68, 156–173, 2025.

[41] Sasikumar, P.G., Sudarshan, N.S., Adurthi, S., Ramachandra, R.K., Samiulla, D.S., Lakshminarasimhan, A., et al., *PD-1 derived CA-170 is an oral immune checkpoint inhibitor that exhibits preclinical anti-tumor efficacy,* Communications Biology, 4, 699, 2021.

[42] Zyla, E., Musielak, B., Holak, T.A., Dubin, G., *Structural Characterization of a Macrocyclic Peptide Modulator of the PD-1/PD-L1 Immune Checkpoint Axis*, Molecules, 26, 4848, 2021.

[43] Laskowski, R.A., Swindells, M.B., *LigPlot+: multiple ligand-protein interaction diagrams for drug discovery,* Journal of Chemical Information and Modeling, 51, 2778-86, 2011.

[44] Cukuroglu, E., Gursoy, A., Keskin, O., *HotRegion: a database of predicted hot spot clusters,* Nucleic Acids Research, 40, D829–D833, 2012.

[45] Lim, H., Chun, J., Jin, X., Kim, J., Yoon, J., No, K.T., *Investigation of protein-protein interactions and hot spot region between PD-1 and PD-L1 by fragment molecular orbital method*, Scientific Reports, 9, 16727, 2019.

[46] Wu, Q., Jiang, L., Li, S.C., He, Q.J., Yang, B., Cao, J., *Small molecule inhibitors targeting the PD-1/PD-L1 signaling pathway,* Acta Pharmacologica Sinica, 42, 1–9, 2021.

[47] Musielak, B., Kocik, J., Skalniak, L., Magiera-Mularz, K., Sala, D., Czub, M., et al., *CA-170 - A Potent Small-Molecule PD-L1 Inhibitor or Not ?,* Molecules, 24, 2804, 2019.

[48] Alibay, I., Magarkar, A., Seeliger, D., Biggin, P.C., *Evaluating the use of absolute binding free energy in the fragment optimisation process,* Communications Chemistry, 5, 105, 2022.

Investigation the Exopolysaccharide Production Potential of Newly Isolated

Trametes versicolor during Repeated-Batch Fermentation

Gonca TORUN[1], Özfer YEŞİLADA[2,*], Filiz BORAN[3]

[1]Department of Biology, Faculty of Art and Science, İnönü University, 44280, Malatya, Türkiye
torun.gnc@gmail.com, ORCID: 0000-0001-6570-9748
[2]Department of Biology, Faculty of Art and Science, İnönü University, 44280, Malatya, Türkiye
ozfer.yesilada@inonu.edu.tr, ORCID: 0000-0003-0038-6575
[3]Department of Biology, Faculty of Art and Science, İnönü University, 44280, Malatya, Türkiye
filiz.kuru@inonu.edu.tr, ORCID: 0000-0002-8801-7987

Abstract

White rot fungi can produce exopolysaccharides (EPS) and these EPSs have the potential to be used in various applications. *Trametes versicolor*, a white rot fungus, can also produce high amount of EPS. EPS production varies depending on fermentation method, production conditions, nutrient sources (especially glucose concentration) in the medium, and also the strain used. Therefore, in this study, EPS production ability of *T. versicolor* strain collected from Hatay/Turkey was firstly investigated during the repeated-batch fermentation (RBF) process. *T. versicolor* was incubated under RBF condition. After investigating the EPS production in different media during repeated-batch process, the effect of medium retention time on EPS production was determined. Then; the effects of agitation, temperature, pH, amount of pellets used and amount of glucose on EPS production were determined. The results of the study showed that both production conditions and glucose concentration affect the EPS production of this strain during the RBF process.

Keywords: Exopolysaccharide; Repeated-batch fermentation; *Trametes versicolor*; White rot fungus.

Yeni İzole Edilmiş *Trametes versicolor*'un Tekrarlı-Kesikli Fermentasyon Sürecinde Ekzopolisakkarit Üretme Potansiyelinin Araştırılması

Öz

Beyaz çürükçül funguslar ekzopolisakkarit (EPS) üretebilir ve bu EPS'lerin çeşitli uygulamalarda kullanılma potansiyeli vardır. Beyaz çürükçül fungus olan *Trametes versicolor* da yüksek miktarda EPS üretebilir. EPS üretimi fermentasyon metodu, üretim koşulları, ortamdaki besin kaynakları (özellikle glukoz konsantrasyonu) ve ayrıca kullanılan suşa bağlı olarak değişir. Bu nedenle, bu çalışmada öncelikle Hatay/Türkiye'den toplanan *T. versicolor* suşunun EPS üretim yeteneği tekrarlı-kesikli fermentasyon (TKF) sürecinde araştırılmıştır. *T. versicolor*, TKF koşulunda inkübe edildi. Tekrarli-kesikli süreç sırasında farklı ortamlarda EPS üretimi araştırıldıktan sonra, besiyeri alıkonma süresinin EPS üretimi üzerindeki etkisi belirlendi. Daha sonra da çalkalama, sıcaklık, pH, kullanılan pelet miktarı ve glukoz konsantrasyonun EPS üretimi üzerindeki etkileri belirlendi. Çalışmanın sonuçları, hem üretim koşullarının hem de glukoz konsantrasyonun bu suşun TKF sürecinde EPS üretimini etkilediğini göstermiştir.

Anahtar Kelimeler: Beyaz çürükçül fungus; Ekzopolisakkarit; Tekrarlı-kesikli fermentasyon; *Trametes versicolor*.

1. Introduction

Exopolysaccharides (EPS) are polysaccharides secreted by microorganism into the extracellular medium. The biological activities of EPSs (long chain and molecular weight polymers composed of especially sugar units) including anti-inflammatory, antioxidative, antitumoral and antidiabetic have led to their increasing interest in various fields and especially in medicine [1, 2].

White rot fungi are efficient EPS producers. It was reported that the EPS from *Pleurotus pulmonarius* has potential antioxidant capacity and therefore, it can be used for functional food and medicine production [3]. Similarly, EPS from *Pleurotus eryngii* have antitumoral and antioxidative activities [1]. *Trametes versicolor* is a biotechnologically important medicinal white rot fungus. It can be used in bioremediation and for producing various enzymes such as laccase and peroxidases. Another important characteristic of this fungus is its ability to produce EPS [4-6]. The anti-inflammatory and prebiotic potential of crude EPS obtained from submerged culture liquid of *T. versicolor* was also reported [7].

EPS production potential varies depending on microorganism and even the strain used, physical conditions of the microorganism such as agitation, pH and temperature, and also inorganic/organic sources in the growth medium [8].

Fermentation method is also important for EPS production. Repeated-batch fermentation (RBF) method is an alternative method to batch method, and it allows maintenance long term activity of fungal pellets for a long period of time [9]. This method can also be used for production of metabolites and it improves the productivity of fungal products [10-13]. In this method, the mycelia of the fungus are in free pellet form and free pellets are self-immobilized mycelia [10, 14]. It is possible to store and reuse these pellets and retain their long-term activity [10]. For example, it is an easy and simple process for production of high amounts of laccase enzyme by whole fungal pellets. RBF process was reported as the efficient method for obtaining high amount of EPS [2]. This method provides an easy operation for EPS production by free and immobilized pellets of *Ganoderma lucidum* [15, 16]. Highly stable *Ganoderma pfeifferi* pellets can be used in extended fermentation cycles for production of EPS efficiently [14]. It is possible to produce EPS with antioxidant activity by immobilized Chinese medicinal mushroom *Cordyceps militaris* [17]. However, there are limited studies on EPS production under RBF conditions [13, 15, 16] and according to our literature knowledge, there is no study on EPS production potential of repeated-batch culture of *T. versicolor* and this strain. The aim of this study is to investigate the EPS production potential of newly isolated *T. versicolor* pellets during RBF process.

2. Materials and Methods

2.1. Fungus

The white rot fungus *Trametes versicolor* was used in this study. This fungus was isolated as a pure culture after being collected from Hatay/Turkey and stored in Biotechnology laboratory in Inonu University. It was maintained at 4 °C on Sabouraud dextrose agar (SDA) plates.

2.2. Production of Stock Inoculum and Pellets

T. versicolor cultured on SDA plates was inoculated on slant SDA and incubated statically at 30 °C for 5 days. After incubation, distilled water was added, and a conidial suspension of the culture was prepared. Four mL of this suspension was transferred into 250 mL flask containing 100 mL Sabouraud dextrose broth (SDB) and the culture was incubated at 30 °C and 150 rpm for 5 days. After incubation, the whole culture was gently homogenized and 1.5 mL of this homogenized culture inoculated into fresh SDB. This culture was incubated and then homogenized in the same conditions as above. This homogenized culture was used as stock

inoculum culture. For fungal pellet production, 7.5 mL from this stock inoculum culture was inoculated into 600 mL SDB/1000 mL flask. It was incubated 30 °C and 150 rpm for 5 days and the pellets obtained [18].

2.3. Repeated-Batch Fermentation with Fungal Pellets

The fungal pellets prepared as stated above were harvested and used for RBF studies. Appropriate amounts of the prepared pellets were transferred to fresh medium to be used in RBF studies and incubated. After incubation, the culture was filtered under sterile condition, and fresh medium was added onto the pellets remaining in the flask [18].

2.4. Selecting the Most Appropriate Culture Medium for EPS Production

Firstly, the RBF studies were conducted in two different culture media. These media were

A) Commercial SDB medium (g/L): Peptone 10, glucose 20

B) Complex medium (CM) (g/L): KH_2PO_4 0.5, $MgSO_4.7H_2O$ 0.5, peptone 2, yeast extract 2, glucose 22.

In RBF experiments, the pellets were, firstly, transferred into 100 ml medium/250 mL. After incubation for appropriate time, the culture was filtered without removing the pellets. The medium was discharged and was exchanged with fresh medium. In these experiments the pellets were repeatedly used in these two media for 3 times with medium retention time of 1 h, 2 h, 24 h or 72 h and then, the most appropriate medium and retention time were selected.

2.5. Optimization the EPS Production of Repeated-Batch Cultures

These studies were performed in the most appropriate medium. After the most appropriate medium selected, studies were conducted to determine the optimum conditions for exopolysaccharide production in this medium. The medium and medium retention time used in these studies were the Complex medium and 24 h, respectively.

2.5.1. Effect of Agitation on EPS Production of Repeated-Batch Cultures

Effect of agitation on EPS production of pellets during RBF was investigated within the agitation rate of 0-200 rpm. The temperature and pellet amount used were 30 °C and 20 g, respectively.

2.5.2. Effect of Incubation Temperature on EPS Production of Repeated-Batch Cultures

To test the effect of incubation temperature on EPS production of pellets during RBF, the cultures were incubated within the temperature range of 20-40 °C. The agitation rate and pellet amount used were 150 rpm and 20 g, respectively.

2.5.3. Effect of Initial pH on EPS Production of Repeated-Batch Cultures

Effect of initial pH on EPS production of pellets during RBF was investigated within the pH range of 3.0-7.0. The incubation temperature, agitation rate and pellet amount used were 30 °C, 150 rpm and 20 g, respectively.

2.5.4. Effect of Pellet Amount on EPS Production of Repeated-Batch Cultures

Different pellet amounts (5, 10, 20 and 30 g) were tested to determine the effect of pellet amount on EPS production during RBF studies. The incubation temperature, agitation rate and initial pH used were 30 °C, 150 rpm and 7.0, respectively.

2.5.5. Effect of Glucose Concentration on EPS Production of Repeated-Batch Cultures

To determine the effect of glucose concentration on EPS production 0, 11, 22, 44, 88 g/L of glucose (final concentrations) were used, and RBF were conducted under the optimum culture parameters detected.

2.6. Isolation of Exopolysaccharide

To isolate the EPS from culture broth of repeated-batch cultures, the culture was centrifuged at 9000 rpm for 15 min. to separate the supernatant from pellets. The supernatant obtained was mixed with cold ethanol and kept overnight at 4 °C. Then, it was filtered using filter paper (pre-dried at 65 °C for overnight/pre-weighed) and the filter paper with EPS was kept again at 65 °C for overnight, placed in desiccator and dried to a constant weight. After that, the dry weight of the EPS was calculated [14, 19]. The macroscopic image of EPS obtained under optimal condition during RBF is shown in Fig. 1.

Figure 1: Macroscopic image of EPS.

3. Results and Discussion

Both the isolation of new microorganisms/strains and increasing the capacity of EPS production attract the attention of researchers [17, 20]. *Trametes versicolor* is one of the most frequently studied medicinal mushroom [7]. Therefore, in this study, the EPS production ability of *T. versicolor* strain collected and isolated from Hatay/Turkey was investigated under repeated-batch fermentation conditions. This fermentation method has various advantages such as storage and reuse of the pellets and use of fungal pellets for a long period of time with long-term activity [9, 10]. The effects of various production conditions and glucose concentration on EPS production of this strain was also tested.

3.1. Selecting the Most Appropriate Culture Medium

EPS production by *T. versicolor* pellets under RBF was investigated in two different media (SDB and CM). These pellets were used for 3 times with various medium retention times of 1 h, 2 h, 24 h and 72 h. Low amounts of EPS could be produced at the retention times of 1 h and 2 h. On the other hand, when the medium retention time of 24 h was used, the amounts of EPS detected at third cycle were 2.14±0.36 and 2.75±0.33 g/L in SDB and CM media, respectively (Table 1).

Table 1: EPS production (g/L) by *T. versicolor* pellets in SDB and CM media at 24 h and 72 h medium retention times.

| Number of Times Pellets Used | Medium Retention Time | | | |
| | 24 h | | 72 h | |
	SDB	CM	SDB	CM
First cycle	1.88±0.16	1.67±0.07	2.02±0.10	1.74±0.23
Second cycle	1.80±0.27	3.06±0.17	1.13±0.23	1.99±0.32
Third cycle	2.14±0.36	2.75±0.33	1.32±0.31	2.41±0.10

When 1 h and 2 h medium retention times used the cumulative total EPS amounts obtained after three cycles were below 2.5 g/L. However, when medium retention of 24 h and 72 h were used for SDB cultures, the cumulative total EPS amounts after three cycles were 5.82 and 4.47 g/L, respectively. These values were 7.48 and 6.14 g/L for CM cultures (Fig. 2). The fungal pellets could produce low amounts of EPS at short retention times. However, when medium retention times of 24 h and 72 h were conducted, higher EPS amounts were obtained by the pellets (Fig. 2). As a result of the studies, CM medium and 24 h medium retention time were selected and used throughout the studies.
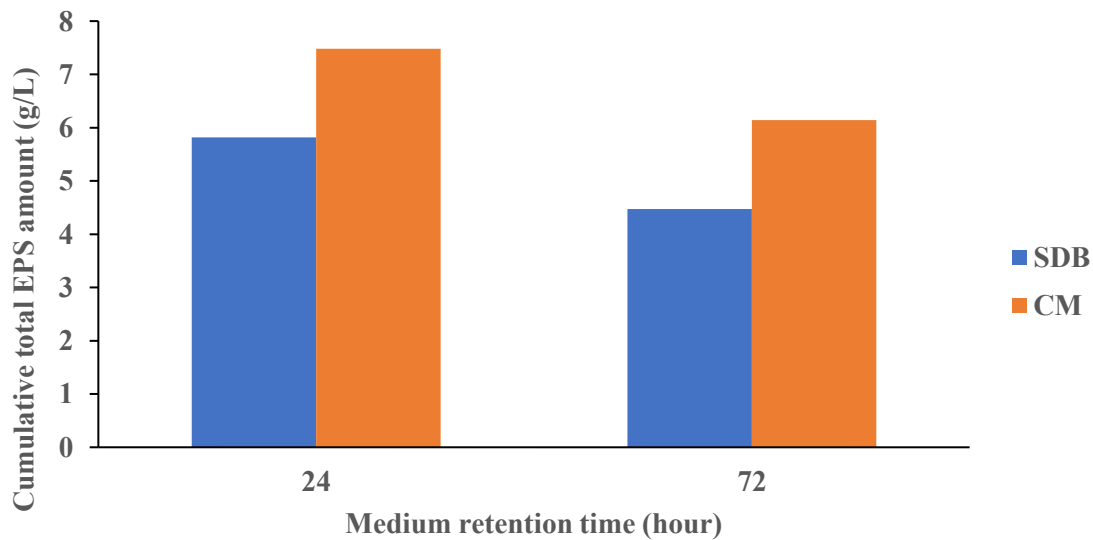
Figure 2: EPS production (g/L) by *T. versicolor* pellets at 24 h and 72 h medium retention times after three cycles in SDB and CM media.

3.2. Effect of Agitation Rate on EPS Production of Pellets During Repeated-Batch Fermentation

Agitation and aeration ensure good mixing of liquid, solid and gas phases in the medium. However, high agitation rates can also cause the pellets to break down. Therefore, the effect of agitation on EPS production during RBF mode was tested. Agitation affected the EPS production of the pellets. As can be seen from Table 2, the EPS production of the RB cultures at each cycle remained low when the culture was mixed at low agitation speed such as 50 ppm or without mixing. However, higher levels of EPS could be produced at 100 (2.15±0.19 at third cycle) and 150 rpm (3.06±0.17 at second cycle) and the production decreased at 200 rpm.

Table 2: Effect of agitation on EPS (g/L) production of pellets during RBF.

	Number of Times Pellets Used		
Agitation (rpm)	**1**	**2**	**3**
0	0.34±0.13	0.62±0.05	0.63±0.06
50	0.19±0.09	0.64±0.15	0.78±0.09
100	0.65±0.04	1.81±0.52	2.15±0.19
150	1.67±0.07	3.06±0.17	2.75±0.33
200	0.83±0.30	1.20±0.28	1.79±0.26

The cumulative total EPS amounts at 0, 50, 100, 150 and 200 rpm after three cycles were 1.59, 1.61, 4.61, 7.48 and 3.82 g/L, respectively (Fig.3). Oxygen transfer rate is reduced at low agitation and therefore, it affects the cell growth and metabolism. On the other hand, high agitation rate can cause shear stress and lead the cell (pellet) damage [2, 10]. In this study, the best agitation rate for EPS production was determined as 150 rpm. It was reported that 150 rpm is the best agitation rate for EPS production of white rot fungal cultures [21].
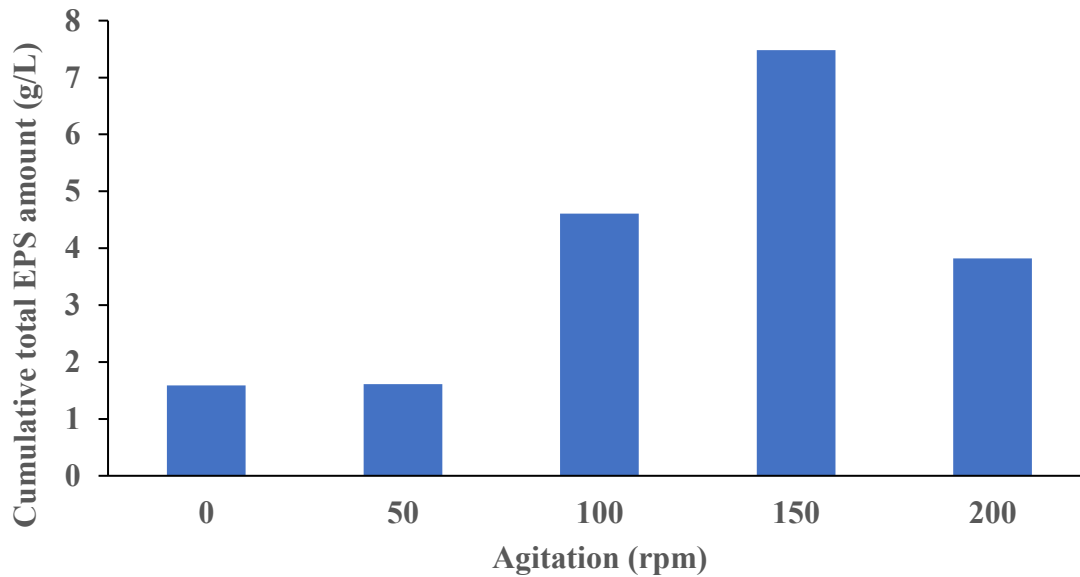
Figure 3: The cumulative total EPS amounts obtained at various agitation speeds after three cycles.

3.3. Effect of Temperature on EPS Production of Pellets During Repeated-Batch Fermentation

EPS production by pellets was carried out at various temperatures such as 20-40 °C and 150 rpm. The pellets were able to produce EPS at all temperatures tested. However, more EPS was produced between 20-30 °C than between 35 and 40 °C. 30 °C was detected as the best temperature for EPS production and the EPS amounts obtained at second and third cycles were 3.06±0.17 and 2.75±0.33, respectively (Table 3).

Table 3: Effect of temperature on EPS (g/L) production of pellets during RBF.

Temperature (°C)	Number of Times Pellets Used		
	1	**2**	**3**
20	1.88±0.48	2.26±0.13	2.01±0.41
25	1.56±0.07	3.03±0.44	2.28±0.14
30	1.67±0.07	3.06±0.17	2.75±0.33
35	1.41±0.10	1.76±0.39	1.12±0.11
40	1.42±0.15	1.26±0.16	1.13±0.07

The cumulative total EPS amounts at 20, 25, 30, 35 and 40 °C after three cycles were 6.15, 6.87, 7.48, 4.29 and 3.81g/L, respectively (Fig. 4). Most fungi can produce EPS within a temperature range of 22-30 °C [22].
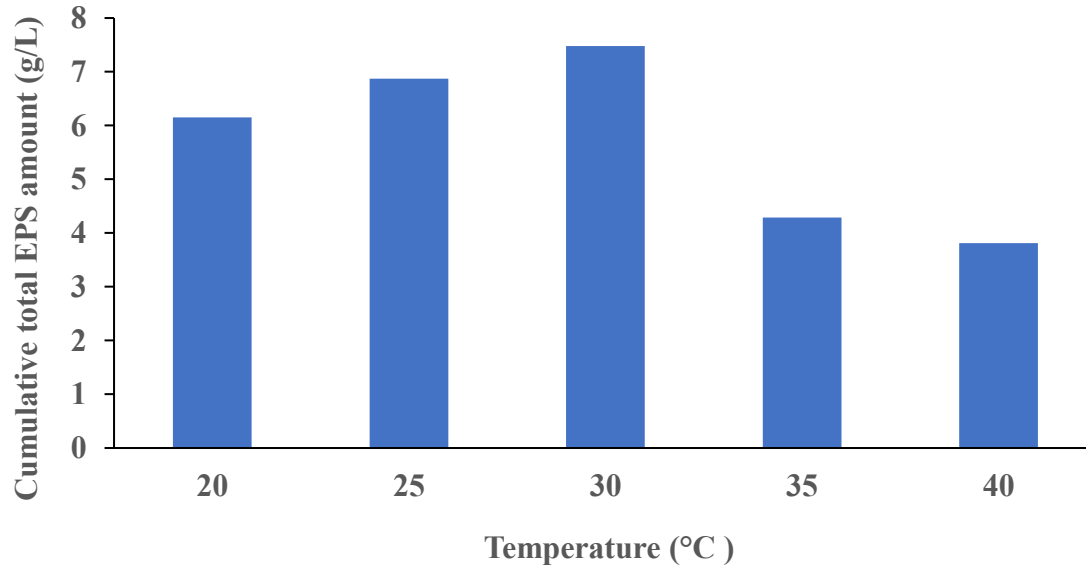
Figure 4: The cumulative total EPS amounts obtained at various temperatures after three cycles.

3.4. Effect of pH on EPS Production of Pellets During Repeated-Batch Fermentation

The effect of initial pH values (pH 3.0-7.0) on EPS production activity of the pellets was also tested with 20 g wet pellet amounts at 30 °C and 150 rpm. All initial pH values supported the EPS production of the pellets. At pH 3.0, the EPS amounts were 2.49±0.32 g/L and 3.18±0.38 g/L at second and third cycles. When initial pH 7.0 was used, it was 3.58±0.46 g/L at the third cycle (Table 4).

Table 4: Effect of pH on EPS (g/L) production of pellets during RBF.

	Number of Times Pellets Used		
pH	**1**	**2**	**3**
3	1.57±0.32	2.49±0.32	3.18±0.38
4	1.53±0.05	1.75±0.19	2.20±0.25
5	1.62±0.18	2.12±0.20	1.79±0.07
6	1.55±0.35	1.58±0.04	2.08±0.11
7	1.51±0.11	1.99±0.35	3.58±0.46

The cumulative total EPS amounts detected after three cycles for pH values of 3, 4, 5, 6, and 7 were 7.24, 5.48, 5.53, 5.21 and 7.08 g/L, respectively (Fig. 5). It was reported that the best initial pH values for EPS production of shake flask cultures of *C. versicolor*, *Grifola umbellata* and *Grifola frondosa* are pH 5.5, pH 5.0 and 5.5, respectively [23-25]. *Aspergillus* sp. DHE6 produces the highest amount of EPS at pH 6.0 under submerged fermentation conditions [26]. *L. edodes* can produce high amount of EPS at initial pH of 4.5 under submerged culture condition [27].
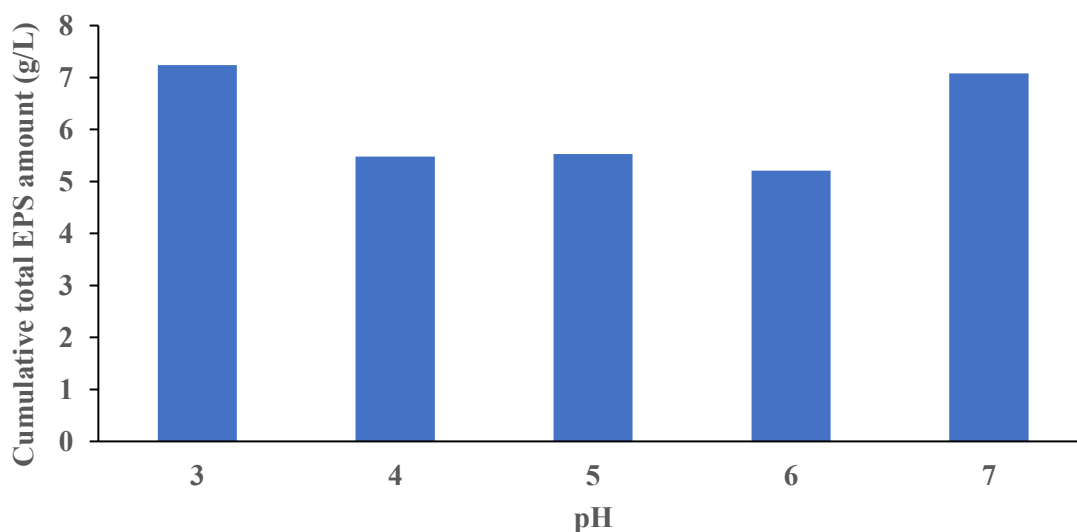
Figure 5: The cumulative total EPS amounts obtained at various pH values after three cycles.

3.5. Effect of Pellet Amounts on EPS Production of Pellets During Repeated-Batch Fermentation

It was reported that an increase in pellet amounts makes a positive effect on activity of pellets during RBF [10, 28]. In our study, pellets were used for three times under optimum conditions (Table 5).

Table 5: Effect of pellet amounts on EPS (g/L) production.

Pellet Amounts	Number of Times Pellets Used		
(g/100 mL)	1	2	3
5	1.59±0.10	1.80±0.05	2.67±0.24
10	1.74±0.13	2.11±0.32	2.59±0.08
20	1.67±0.07	3.06±0.17	2.75±0.33
30	1.44±0.27	2.98±0.39	2.79±0.24

When 5 and 10 g pellet amounts used, the cumulative total EPS amounts after three cycles were 6.06 and 6.44 g/L, respectively. However, these values were 7.48 and 7.21 g/L for pellet amounts of 20 and 30 g/L (Fig. 6). The results showed that higher pellet amounts positively affected the EPS production.
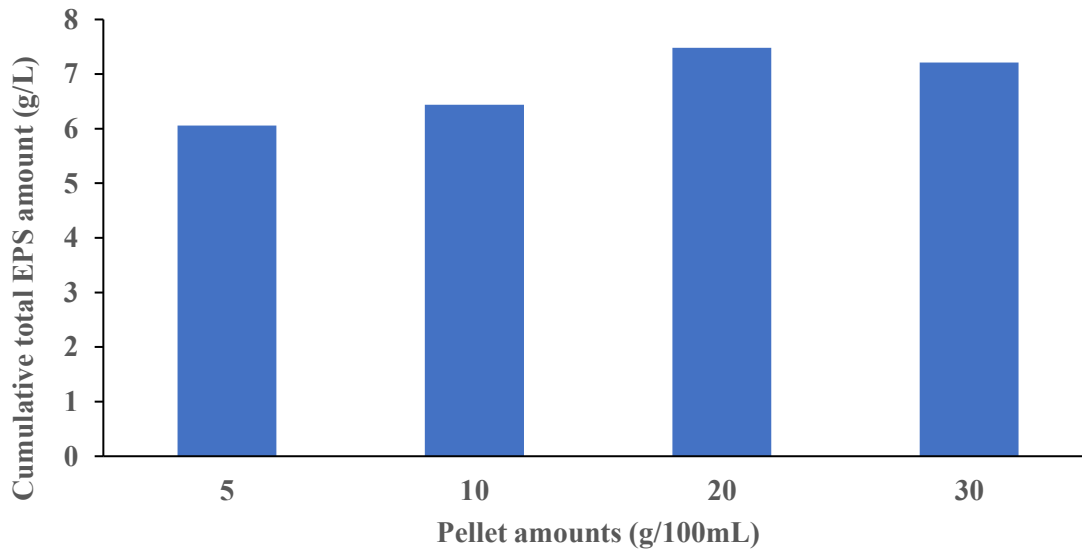
Figure 6: The cumulative total EPS amounts obtained by various pellets amounts after three cycles.

3.6. Effect of Glucose Concentration on EPS Production During Repeated-Batch Fermentation

Glucose is a principal carbon and energy source for most of the microorganisms. Therefore, the effect of glucose amount on EPS production potential of the pellets was tested. As shown in Table 6, an increase in the glucose amount had a positive effect on the EPS production potential of the pellets and EPS production activity increased at each cycle.

Table 6: Effect of glucose concentration on EPS (g/L) production of pellets during RBF.

Glucose (g/L)	Number of Times Pellets Used		
	1	**2**	**3**
22	1.67±0.07	3.06±0.17	2.75±0.33
44	3.26±0.35	5.75±1.08	6.87±0.20
88	3.27±0.44	6.22±0.51	9.68±0.74

The cumulative total EPS amounts obtained after three cycles for the glucose concentrations of 22, 44, 88 g/L were 7.48, 15.88 and 19.17, respectively (Fig. 7). This shows the critical role of glucose for EPS production. Glucose is a favorable nutrient for EPS production of *G. formosanum* [29] and the best carbon source for EPS production of submerged cultures of *P. sajor-caju* [30]. α-phosphoglucomutase gene was reported as an important gene for EPS production of *G. lucidum* [31].
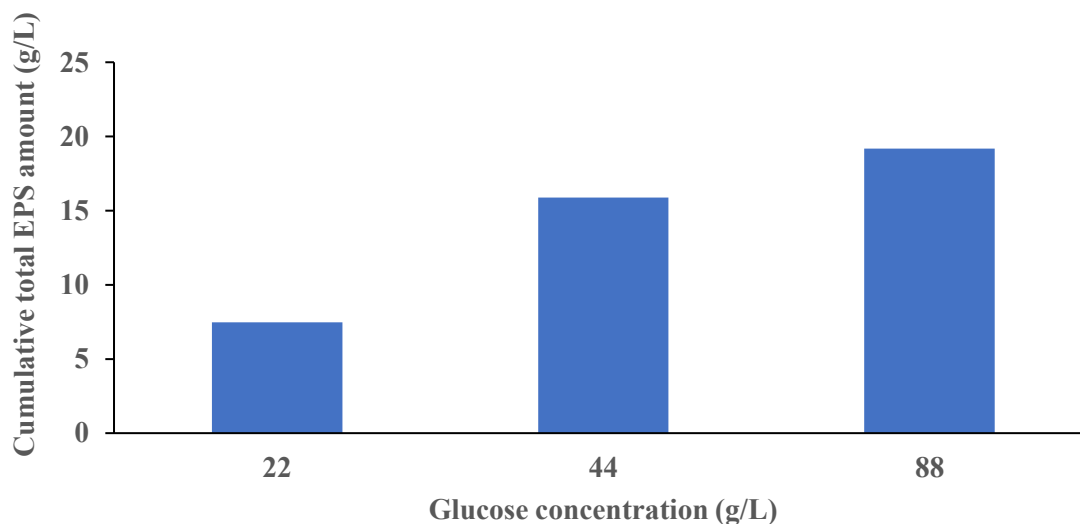
Figure 7: The cumulative total EPS amounts obtained at various glucose concentrations after three cycles.

4. Conclusion

This biotechnologically important *T. versicolor* strain used in our study was able to produce significant amounts of exopolysaccharide (EPS) under repeated-batch condition. The EPS production potential of this microorganism varied depending on the agitation speed, temperature, pellet amount, medium type and glucose concentration. It was observed that the concentration of glucose, which is a carbon and energy source, was very effective in the EPS production of these pellets in RBF process. Our results show that this strain and RBF method can be used for production of high amounts of EPS repeatedly.

References

[1] Jing, X.Y., Mao, D.B., Geng, L.J., Xu, C.P., *Medium optimization, molecular characterization, and bioactivity of exopolysaccharides from Pleurotus eryngii*, Archives of Microbiology, 195, 749–757, 2013.

[2] Wang, C.C., Wu, J.Y., Chang, C.Y., Yu, S.T., Liu, Y.C., *Enhanced exopolysaccharide production by Cordyceps militaris using repeated batch cultivation*, Journal of Bioscience and Bioengineering, 127(4), 499–505, 2019.

[3] Shen, J.W., Shi, C.W., Xu, C.P., *Exopolysaccharides from Pleurotus pulmonarius: fermentation optimization, characterization and antioxidant activity*, Food Technology and Biotechnology, 51(4), 520–527, 2013.

[4] Bolla, K., Gopinath, B., Shaheen, S.Z., Charya, M.S., *Optimization of carbon and nitrogen sources of submerged culture process for the production of mycelial biomass and exopolysaccharides by Trametes versicolor*, International Journal for Biotechnology and Molecular Biology Research, 1(2), 15–21, 2010.

[5] Que, Y.X., Sun, S.J., Xu, L.P., Zhang, Y.Y., Zhu, H., *High-level coproduction, purification and characterisation of laccase and exopolysaccharides by Coriolus versicolor*, Food Chemistry, 159, 208–213, 2014.

[6] Kachrimanidou, V., Alexandri, M., Papapostolou, H., Papadaki, A., Kopsahelis, N., *Valorization of grape pomace for Trametes versicolor mycelial mass and polysaccharides production*. Sustainability, 15(20), 1–18, 2023.

[7] Angelova, G., Brazkova, M., Mihaylova, D., Slavov, A., Petkova, N., Blazheva, D., et al., *Bioactivity of biomass and crude exopolysaccharides obtained by controlled submerged cultivation of medicinal mushroom,* Journal of Fungi, 8(7), 1–22, 2022.

[8] Hamidi, M., Okoro, O.V., Milan, P.B., Khalili, M.R., Samadian, H., Nie, L., et al., *Fungal exopolysaccharides: Properties, sources, modifications, and biomedical applications*, Carbohydrate Polymers, 284, 1–23, 2022.

[9] Yesilada, O., Yildirim, S.C., Birhanli, E., Apohan, E., Asma, D., Kuru, F., *The evaluation of pre-grown mycelial pellets in decolorization of textile dyes during repeated batch process*. World Journal of Microbiology & Biotechnology, 26(1), 33–39, 2010.

[10] Birhanli, E., Yesilada, O., *Enhanced production of laccase in repeated-batch cultures of Funalia trogii and Trametes versicolor*, Biochemical Engineering Journal, 52(1), 33–37, 2010.

[11] Rywinska, A., Rymowicz, W., *High-yield production of citric acid by Yarrowia lipolytica on glycerol in repeated-batch bioreactors,* Journal of Industrial Microbiology & Biotechnology, 37(5), 431–435, 2010.

[12] Chen, Y., Liu, Q.G., Zhou, T., Li, B.B., Yao, S.W., Wu, J.L., et al., *Ethanol production by repeated batch and continuous fermentations by Saccharomyces cerevisiae immobilized in a fibrous bed bioreactor*, Journal of Microbiology and Biotechnology, 23(4), 511-517, 2013.

[13] Wan-Mohtar, W.A., Ab Kadir, S., Saari, N., *The morphology of Ganoderma lucidum mycelium in a repeated-batch fermentation for exopolysaccharide production*, Biotechnology Reports, 11, 2–11, 2016.

[14] Supramani, S., Jailani, N., Ramarao, K., Zain, N.A.M., Klaus, A., Ahmad, R., et al., *Pellet diameter and morphology of European Ganoderma pfeifferi in a repeated-batch fermentation for exopolysaccharide production*, Biocatalysis and Agricultural Biotechnology, 19, 101118, 2019.

[15] Wan-Mohtar, W.A., Malek, R.A., Harvey, L.M., McNeil, B., *Exopolysaccharide production by Ganoderma lucidum immobilised on polyurethane foam in a repeated-batch fermentation,* Biocatalysis and Agricultural Biotechnology, 8, 24–31, 2016.

[16] Wan-Mohtar, W.A., Latif, N.A, Harvey, L.M., McNeil, B., *Production of exopolysaccharide by Ganoderma lucidum in a repeated-batch fermentation,* Biocatalysis and Agricultural Biotechnology, 6, 91–101, 2016.

[17] Lin, S.P., Sung, T.H., Angkawijaya, A.E., Go, A.W., Hsieh, C.W., Hsu, H.Y., Santoso, S.P., Cheng, K.C., *Enhanced exopolysaccharide production of Cordyceps militaris via mycelial cell immobilization on plastic composite support in repeated-batch fermentation*, International Journal of Biological Macromolecules, 250, 1–10, 2023.

[18] Yesilada, O, Birhanli, E., Ozmen, N., Ercan, C., *Highly stable laccase from repeated-batch culture of Funalia trogii ATCC 200800,* Applied Biochemistry and Microbiology, 50(1), 65–71, 2014.

[19] Ma, Y.P., Mao, D.B., Geng, L.J., Wang, Z., Xu, C.P., *Production, fractionation, characterization of extracellular polysaccharide from a newly isolated Trametes gibbosa and its hypoglycemic activity,* Carbohydrate Polymers, 96(2), 460–465, 2013.

[20] Yuan, B.J., Chi, X.Y., Zhang, R.J., *Optimization of exopolysaccharides production from a novel Ganoderma lucidum strain of cau5501 in submerged culture*, Brazilian Journal of Microbiology, 43(2), 490–497, 2012.

[21] Asadi, F., Barshan-Tashnizi, M., Hatamian-Zarmi, A., Davoodi-Dehaghani, F., & Ebrahimi Hosseinzadeh, B., *Enhancement of exopolysaccharide production from Ganoderma lucidum using a novel submerged volatile co-culture system*, Fungal Biology, 125(1), 25–31, 2021.

[22] Mahapatara, S., Banerjee, D., *Fungal exopolysaccharide: production, composition and applications*, Microbiology Insights, 6, 1–16, 2013.

[23] Lee, B.C., Bae, J.T., Pyo, H.B., Choe, T.B., Kim, S.W., Hwang, H.J., et al., *Submerged culture conditions for the production of mycelial biomass and exopolysaccharides by the edible Basidiomycete Grifola frondosa*, Enzyme *and* Microbial Technology, 35(5), 369–376, 2004.

[24] Tavares, A.P.M., Agapito, M.S.M., Coelho, M.A.Z., da Silva, J.A.L., Barros-Timmons, A., Coutinho, J.A.P., et al., *Selection and optimization of culture medium for exopolysaccharide production by Coriolus (Trametes) versicolor*, World Journal of Microbiology & Biotechnology, 21(8-9), 1499–1507, 2005.

[25] Huang, H.C., Liu, Y.C., *Enhancement of polysaccharide production by optimization of culture conditions in shake flask submerged cultivation of Grifola umbelalta*, Journal of the Chinese Institute of Chemical Engineers, 39(4), 307–311, 2008.

[26] El-Ghonemy, D.H., *Antioxidant and antimicrobial activities of exopolysaccharides produced by a novel Aspergillus sp. DHE6 under optimized submerged fermentation conditions,* Biocatalysis and Agricultural Biotechnology, 36, 1–8, 2021.

[27] García-Cruz, F., Durán-Páramo, E., Garín-Aguilar, M.A., del Toro, G., Chairez, I., *Parametric characterization of the initial pH effect on the polysaccharides production by Lentinula edodes in submerged culture*, Food and Bioproducts Processing, 119, 170–178, 220.

[28] Yesilada, O., Asma, D., Cing, S., *Decolorization of textile dyes by fungal pellets,* Process Biochemistry, 38(6), 933–938, 2003.

[29] Hsu, K.D., Wu, S.P., Lin, S.P., Lum, C.C., Cheng, K.C., *Enhanced active extracellular polysaccharide production from Ganoderma formosanum using computational modeling*, Journal of Food and Drug Analysis, 25(4), 804–811, 2017.

[30] Ozturk, U.R., Ilgın, S., *Production and partial characterization of the exopolysaccharide from Pleurotus sajor caju*, Annals of Microbiology, 69, 1201-1210, 2019.

[31] Xu, J.W., Ji, S.L., Li, H.J., Zhou, J.S., Duan, Y.Q., et al., *Increased polysaccharide production and biosynthetic gene expressions in a submerged culture of Ganoderma lucidum by the overexpression of the homologous α-phosphoglucomutase gene*, Bioprocess and Biosystems Engineering, 38(2), 399–405, 2015.

First Ringing Station in Cyprus, Karpaz Bird Ringing Station: Results of Autumn Migration Season in 2024

Hakan KARAARDIÇ[1,*], Esat KIZILKAYA[2,3], Mustafa Güray BUKAN[3]

[1]*Department of Math and Science Education, Education Faculty, Alanya Alaaddin Keykubat University, Alanya, Antalya, Türkiye*
hkaraardic@gmail.com, ORCID: 0000-0001-9839-4201
[2]*Department of Forestry, Sütçüler Prof. Dr. Hasan Gürbüz Vocational School, Isparta University of Applied Science, Isparta, Türkiye*
kizilkayaesat@gmail.com, ORCID: 0000-0002-3557-5440
[3]*Cyprus Wildlife Research Institute, Taşkent Nature Park Way 1, Taşkent 9390, Kyrenia District, Cyprus*
guray.bukan@cwri.net, ORCID: 0009-0002-8878-4585

Abstract

Cyprus is one of the important islands in the Western Palearctic for bird migration routes, especially on the eastern Mediterranean route. In contrast to Western Europe, research on bird migrations in Eastern Europe and the Eastern Mediterranean remains limited. Due to its geographical location and surface area, Cyprus hosts millions of migratory birds in the Eastern Mediterranean region during the Eastern European bird migrations. The Karpaz Bird Ringing Station, established in Northern Cyprus, has the potential to fill many gaps. Regular ringing activities started in the autumn season of 2024 at the station, a total of 157 meters of mist nets were used, and 1,436 birds from 39 species were ringed. The most frequently ringed species were the Eurasian blackcap, common chiffchaff, European robin, Sardinian warbler, willow warbler, song thrush, stonechat, Spanish sparrow, black redstart, and common redstart. According to the results, the long-distance migrants, such as willow warblers, common redstarts, and blackcap individuals, have higher fat scores. These preliminary data reveal the importance of the role of

Cyprus in bird migrations. Although there is only one control bird (Hungarian control), increasing the recapture data (especially between Israel, Türkiye and Cyprus) will significantly contribute to the determination of migration dynamics (migration phenology, stopover ecology, migration routes, individual physiological changes and more) in the Eastern Mediterranean part of bird migrations under the western Palearctic migration route.

Keywords: Bird migration; Bird ringing; Ecological barrier; Eastern Mediterranean; North Cyprus; Stopover.

Kıbrıs'ın İlk Halkalama İstasyonu, Karpaz Kuş Halkalama İstasyonu: 2024 Sonbahar Göç Sezonu Sonuçları

Öz

Kıbrıs, özellikle Doğu Akdeniz rotası olmak üzere, Batı Palearktik kuş göç yolları için önemli adalardan biridir. Batı Avrupa'nın aksine, Doğu Avrupa ve Doğu Akdeniz'deki kuş göçleri üzerine yapılan araştırmalar sınırlı kalmaktadır. Kıbrıs, coğrafi konumu nedeniyle Doğu Avrupa kuş göçleri sırasında Doğu Akdeniz bölgesinde milyonlarca göçmen kuşa ev sahipliği yapmaktadır. Kuzey Kıbrıs'ta kurulan Karpaz Kuş Halkalama İstasyonu birçok boşluğu dolduracak potansiyele sahiptir. İstasyonda 2024 sonbahar sezonunda düzenli halkalama faaliyetlerine başlanmış, toplam 157 metre sis ağı kullanılmış ve 39 türe ait 1.436 kuş halkalanmıştır. En sık halkalanan türler karabaşlı ötleğen, çıvgın, kızılgerdan, maskeli ötleğen, söğüt bülbülü, öter ardıç, söğüt serçesi, kara kızılkuyruk ve kızılkuyruk olmuştur. Elde edilen sonuçlara göre, karabaşlı ötleğen, kızılkuyruk ve söğüt bülbülü gibi uzun mesafe göçmenler daha fazla yağ miktarına sahiptir. Bu ön veriler, Kıbrıs'ın kuş göçlerindeki rolünün önemini ortaya koymaktadır. Sadece bir kontrol kuşu (Macar geribildirimi) olmasına rağmen, yeniden yakalama verilerinin artması (özellikle İsrail, Türkiye ve Kıbrıs arasında) Batı Palearktik göç rotası altındaki kuş göçlerinin Doğu Akdeniz bölümünde göç dinamiklerinin (göç fenolojisi, durak ekolojisi, göç rotaları, bireysel fizyolojik değişiklikler ve daha fazlası) belirlenmesine büyük katkı sağlayacaktır.

Anahtar Kelimeler: Kuş göçleri; Kuş halkalama; Ekolojik engel; Doğu Akdeniz; Kuzey Kıbrıs; Konaklama.

1. Introduction

Bird migration has been one of the most important research topics throughout human history. With the acceptance of bird ringing methodology in the early 20th century [1,2], very

comprehensive, and long-term studies have been carried out in cooperation between countries [3]. Bird ringing stations have played a significant role in determining the mysteries of the journeys of species between breeding and wintering areas in Western Palearctic bird migrations [4]. In the last few decades, with the development of technology, detailed data on bird migrations, times, migration routes, and wintering areas have been obtained by using geographical positioning devices (satellite transmitter, GPS, geolocator, etc.) [5,6]. Numerous studies conducted in Europe have produced comprehensive results on Western Europe-Western Mediterranean migration routes [7,8]. In contrast, significant deficiencies are observed in Eastern Europe-Eastern Mediterranean bird migrations.

The key roles of Türkiye (wetlands and coastal stopovers against geographical-ecological barriers) and Cyprus (terrestrial area in the Eastern Mediterranean) in Eastern Europe-Eastern Mediterranean bird migrations are revealed. Control data obtained from ringing studies in southern Türkiye reveal that Central and Eastern European bird populations migrate between breeding and wintering areas via this route [9,10]. Due to its geographical location and surface area, Cyprus hosts millions of migratory birds in the Eastern Mediterranean region during Eastern European bird migrations. However, to date, although irregular studies or short-term research have been conducted to identify diseases carried by birds [11], there is no station in Cyprus where regular bird ringing studies are carried out. To fill this gap and investigate the migration ecology and behavior of birds, the Karpaz Bird Ringing Station (Northern Cyprus) was established in Dipkarpaz, northeast of the island, by the Taşkent Nature Park and the Cyprus Wildlife Research Institute. Studies for the 2024 autumn migration period have begun. This study aimed to determine the diversity and phenology of migratory species in the autumn period of 2024.

2. Materials and Methods

2.1. Study Area

The Karpaz Bird Ringing Station is located near Dipkarpaz Town in the İskele District, northeastern Cyprus. The station is situated close to Ronnas Beach at the Taşkent Nature Park Karpaz Research Station (35°36'01" N; 34°19'50" E) (Fig. 1). The following plant species are dominant in the area: *Juniperus phoenicea*, *Pistacia lentiscus*, *Thymus capitatus*, *Myrtus communis*, *Lithodora hispidula*, and *Rhamnus oleioides*. In addition, *Fumana thymifolia*, *Rubia laurae*, *Asparagus acutifolius*, *Cistus sp.*, *Helichrysum conglobatum*, *Genista fasselata*, *Olea europea*, *Allium sp.*, *Hyperhenia hirta*, and *Ceratonia siliqua* species are also found in the region.
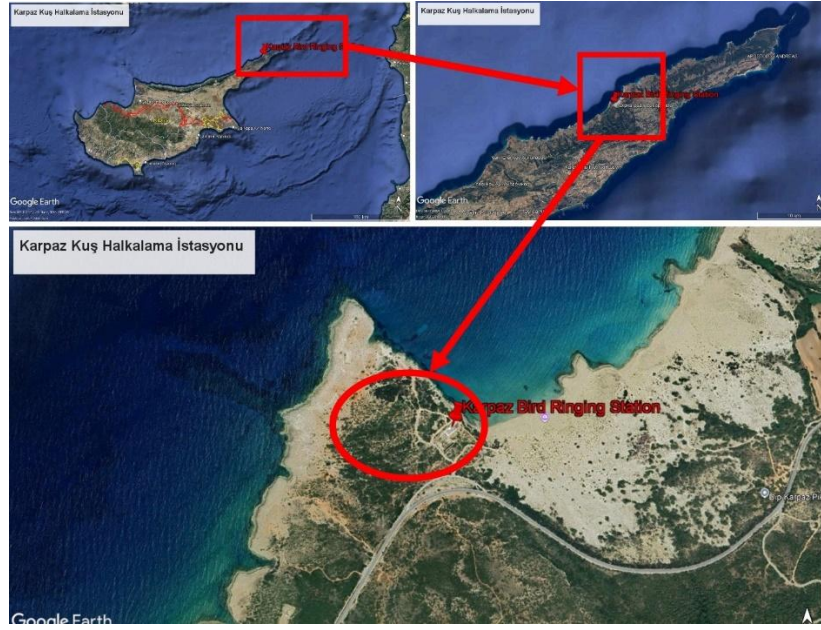
Figure 1: The location of the Karpaz Bird Ringing Station (modified from Google Earth).

2.2. Fieldworks

The study was conducted during the autumn migration period (October-November 2024) to examine the migration movements of bird species and determine their migration phenology. During the autumn season, a total of 157 meters of mist nets were used, including one 18-meter net, ten 12-meter nets, two 9-meter nets, and one 6-meter net. The nets were set parallel to the vegetation in the area, which primarily consisted of juniper and lentisk (Fig. 2). All birds were aged and sexed by plumage coloration [12], measured (maximum wing length to the nearest 0.5 mm) [12], and weighed to the nearest 0.1 g. The fat score was estimated on a nine-class scale [13], and the size of the breast muscle was assessed on a four-class scale [4]. The individuals were ringed using metal rings sourced from "cwri.net," each coded individually and suitable for the leg size of the bird.
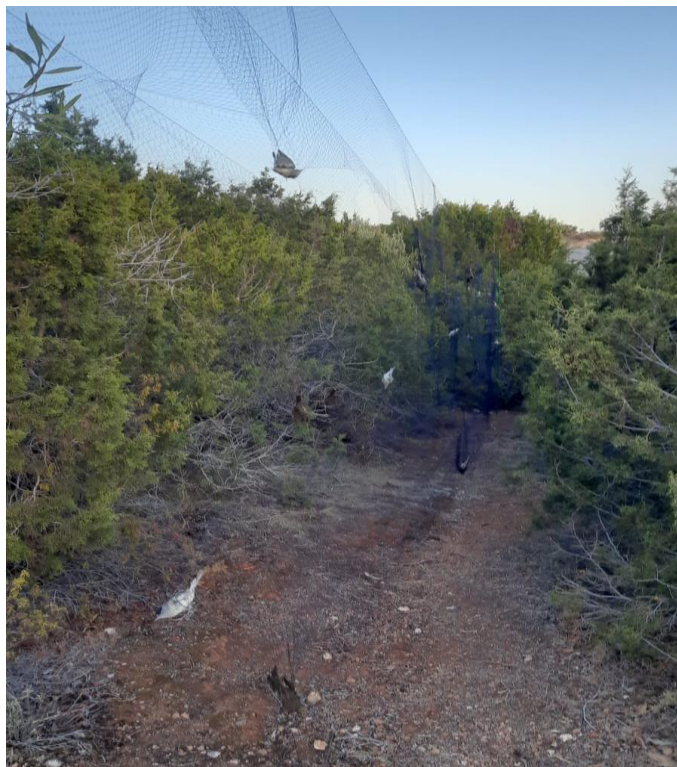
Figure 2: Mist nets used for capturing birds, set parallel to the vegetation.

3. Results and Discussion

During the autumn ringing season in 2024, 1.434 birds from 39 species were captured at the Karpaz Bird Ringing Station. Among these, 1.401 birds were ringed for the first time, one was a control bird, and 32 were recaptures. The ringed bird species and numbers during the autumn period of 2024 are presented in Table 1.

The most frequently ringed species during the autumn period were the Eurasian blackcap (*Sylvia atricapilla*), common chiffchaff (*Phylloscopus collybita*), European robin (*Erithacus rubecula*), Sardinian warbler (*Curruca melanocephala*), willow warbler (*Phylloscopus trochilus*), Song thrush (*Turdus philomelos*), stonechat (*Saxicola torquatus*), Spanish sparrow (*Passer hispaniolensis*), black redstart (*Phoenicurus ochruros*), and common redstart (*Phoenicurus phoenicurus*) **(**Fig. 3). According to the results, the long-distance migrants, such as willow warblers, common redstarts, and blackcap individuals, have higher fat scores. The mean values of the weight, fat scores, and muscle scores of these species are presented in Table 2.

During the autumn period, two scarce species for Cyprus, the red-breasted flycatcher (*Ficedula parva*) and little bunting (*Emberiza pusilla*), were captured and ringed (Figs. 4-5).

Table 1: Summary of bird ringing results at Karpaz Bird Ringing Station in 2024 (*I*: "First capture," *R*: "Recaptured during the period," and *C*: "Control").

Species	Autumn			Total	Species	Autumn			Total
	I	**R**	**C**			**I**	**R**	**C**	
Acrocephalus melanopogon	3	1	0	4	*Luscinia svecica*	12	1	0	13
Acrocephalus schoenobaenus	1	0	0	1	*Oenanthe oenanthe*	1	0	0	1
Acrocephalus scirpaceus	2	0	0	2	*Otus cyprius*	1	0	0	1
Alcedo atthis	1	0	0	1	*Passer domesticus*	14	0	0	14
Athene noctua	1	0	0	1	*Passer hispaniolensis*	37	0	0	37
Cettia cetti	4	1	0	5	*Phoenicurus ochruros*	18	2	0	20
Curruca communis	2	0	0	2	*Phoenicurus phoenicurus*	17	0	0	17
Curruca curruca	14	0	0	14	*Phylloscopus collybita*	149	4	0	153
Curruca melanocephala	99	2	0	101	*Phylloscopus trochilus*	94	0	0	94
Emberiza pusilla	1	0	0	1	*Prunella modularis*	1	0	0	1
Erithacus rubecula	111	14	0	125	*Saxicola maurus*	1	0	0	1
Falco tinnunculus	2	0	0	2	*Saxicola torquatus*	41	2	0	43
Ficedula parva	1	0	0	1	*Serinus serinus*	1	0	0	1
Fringilla coelebs	4	0	0	4	*Spilopelia senegalensis*	1	0	0	1
Galerida cristata	2	0	0	2	*Sylvia atricapilla*	690	5	1	696
Hirundo rustica	1	0	0	1	*Sylvia borin*	3	0	0	3
Jynx torquilla	1	0	0	1	*Troglodytes troglodytes*	3	0	0	3
Lanius collurio	1	0	0	1	*Turdus merula*	5	0	0	5
Linaria cannabina	1	0	0	1	*Turdus philomelos*	58	0	0	58
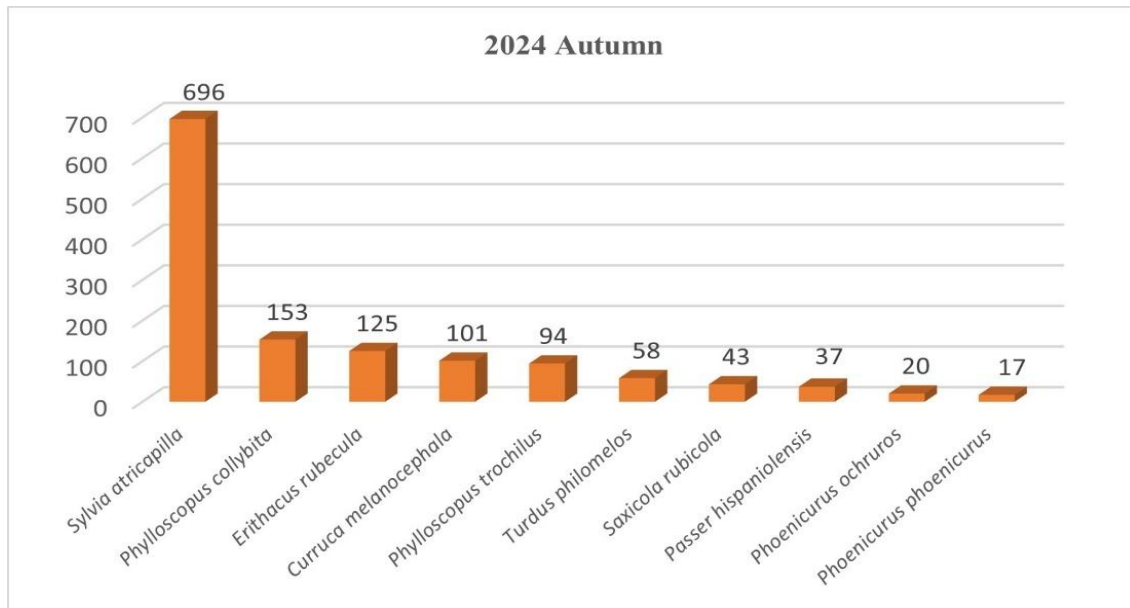
Figure 3: The most frequently captured migratory species.

Table 2: Body condition values of the most frequently captured migratory species during the autumn season (2024).

Species	Weight				Fat Score			Muscle Score		
	n	mean	min-max	SD	mean	min-max	SD	mean	min-max	SD
Curruca melanocephala	100	11,10	9,6-13,5	0,704	0,81	0-4	1,080	1,51	0-3	0,674
Erithacus rubecula	111	15,06	12,6-18,6	1,097	0,73	0-3	0,863	1,50	0-3	0,686
Luscinia svecica	12	14,97	12,8-17,4	1,667	1,58	0-3	1,084	1,08	1-2	0,289
Passer hispaniolensis	37	25,99	22,9-30,3	1,669	1,43	0-3	0,728	1,43	1-2	0,502
Phoenicurus ochruros	18	15,08	13,8-17	0,949	0,67	0-2	0,594	1,33	0-3	0,767
Phoenicurus phoenicurus	17	15,23	12,6-19,4	1,729	1,76	0-4	1,091	1,06	0-2	0,556
Phylloscopus collybita	148	7,22	4,8-11,4	1,370	1,61	0-5	1,450	1,14	0-3	0,791
Phylloscopus trochilus	94	10,10	7-12,7	1,246	2,60	0-4	1,221	0,87	0-2	0,660
Saxicola rubicola	41	13,68	10,9-15,3	0,854	1,12	0-3	1,077	1,59	0-3	0,670
Sylvia atricapilla	688	18,20	14,2-28,5	2,026	2,27	0-6	1,343	1,58	0-3	0,682
Turdus philomelos	58	62,83	47,8-75,7	4,985	0,67	0-2	0,803	0,91	0-2	0,601

Figure 4: One of the rare species for Cyprus, the red-breasted flycatcher (*Ficedula parva*).

Figure 5: Extremely rare species for Cyprus, little bunting (*Emberiza pusilla*).

During the 2024 bird ringing season at the Karpaz Bird Ringing Station, recovery data for one control bird were obtained. The Eurasian blackcap (*Sylvia atricapilla*) was originally ringed at the Sumony Bird Ringing Station (Baranya, Hungary) on September 23, 2024. After 51 days and covering an aerial distance of 1,795 kilometers, it was recaptured at the Karpaz Bird Ringing Station on November 13, 2024.

4. Conclusion

Cyprus has a strategic location on the bird migration routes of Eastern Europe, particularly in the Eastern Mediterranean. Birds spend most of their time in stopover areas during their long-distance migration journeys [6], and the Mediterranean is one of the ecological barriers during the migration [14], with the importance of almost all of Cyprus and the south coastline of Türkiye as stopover areas.

Bird ringing stations contribute to determining the bird diversity of a region [15,16]. Moreover, it can clearly reveal the spread of rare species in the area [17]. Although there is no regular ringing station in Cyprus to date, species diversity has been primarily revealed through bird observation records. However, the little flycatcher and little bunting captured in the first

season of the study (autumn 2024) were important indicators of the level of contribution level of the bird ringing station where regular work had started. On the other hand, long-term ringing studies are effective in determining the migration phenology [18] and the behavior of species [19] over time and in response to changing environmental conditions, particularly climate change. In addition, islands in ecological barriers serve as stopover areas for species during their long and dangerous migration journeys, and data can be obtained to reveal the migration strategies of species (fat depot, muscle score, weight, etc.). Birds increase their fat stores to successfully complete long-distance migrations and cross ecological barriers such as the Mediterranean [6]. Among the species captured in the first season of the study, the weights, fat and muscle scores of long-distance migrants (such as willow warblers, blackcaps, common redstarts, chiffchaffs) were higher compared to other species (Table 2, Figs. 6-8). These preliminary data reveal the importance of the role of Cyprus in bird migrations. Although there is only one control bird for now (Hungarian control), increasing the recapture data (especially between Israel, Türkiye and Cyprus) will significantly contribute to the determination of migration dynamics (migration phenology, stopover ecology, migration routes, individual physiological changes and more) in the Eastern Mediterranean part of bird migrations under the western Palearctic.

As a result, the start of the studies at the Karpaz Bird Ringing Station will contribute to bird migration research in the Western Palearctic. Future studies at this station will support the planning of conservation measures, the acquisition of information required for the protection of bird migration, and biodiversity monitoring due to both climatic and environmental changes. Additionally, it will facilitate the establishment of new stations and the development of international cooperation projects on this island, where millions of migratory birds stop over each year.
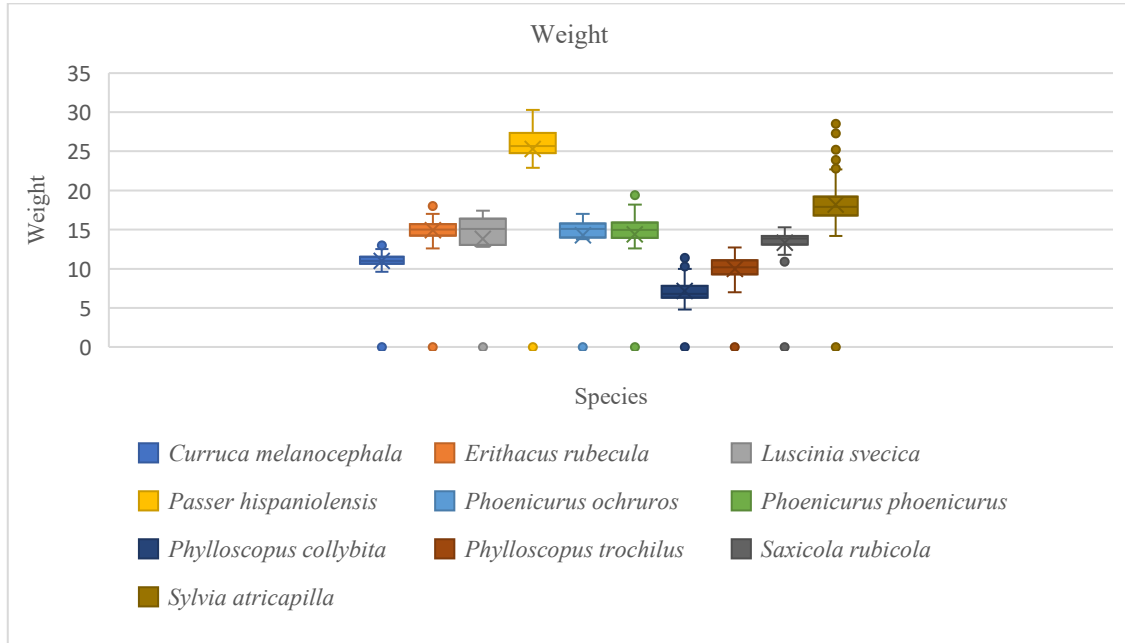
Figure 6: Distribution values of weight from the most frequently captured migratory species during the autumn season (2024).
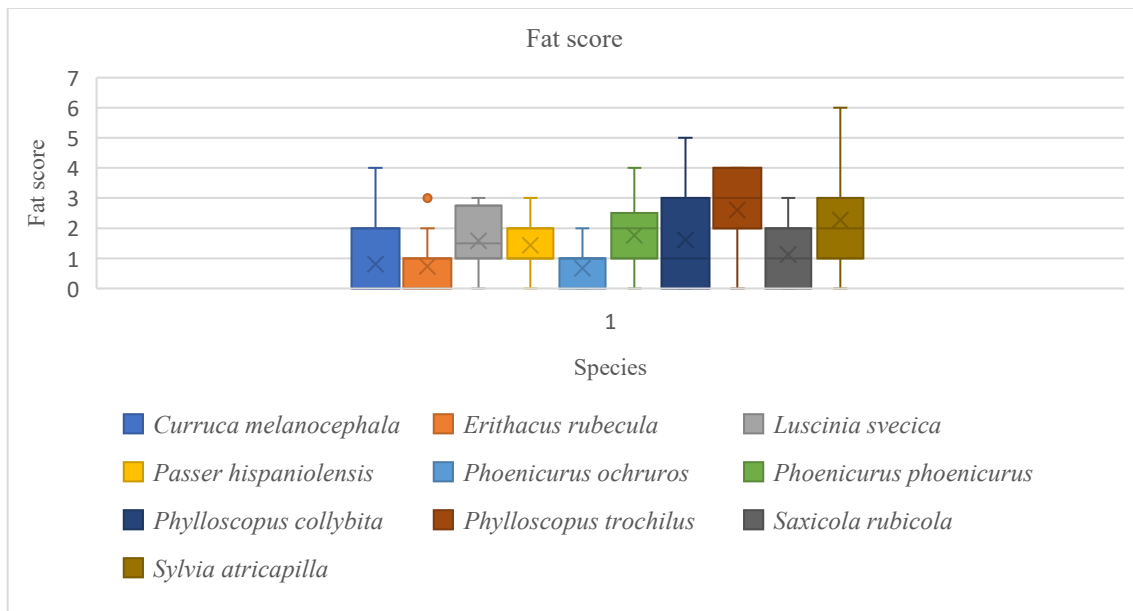
Figure 7: Distribution values of fat scores from the most frequently captured migratory species during the autumn season (2024).
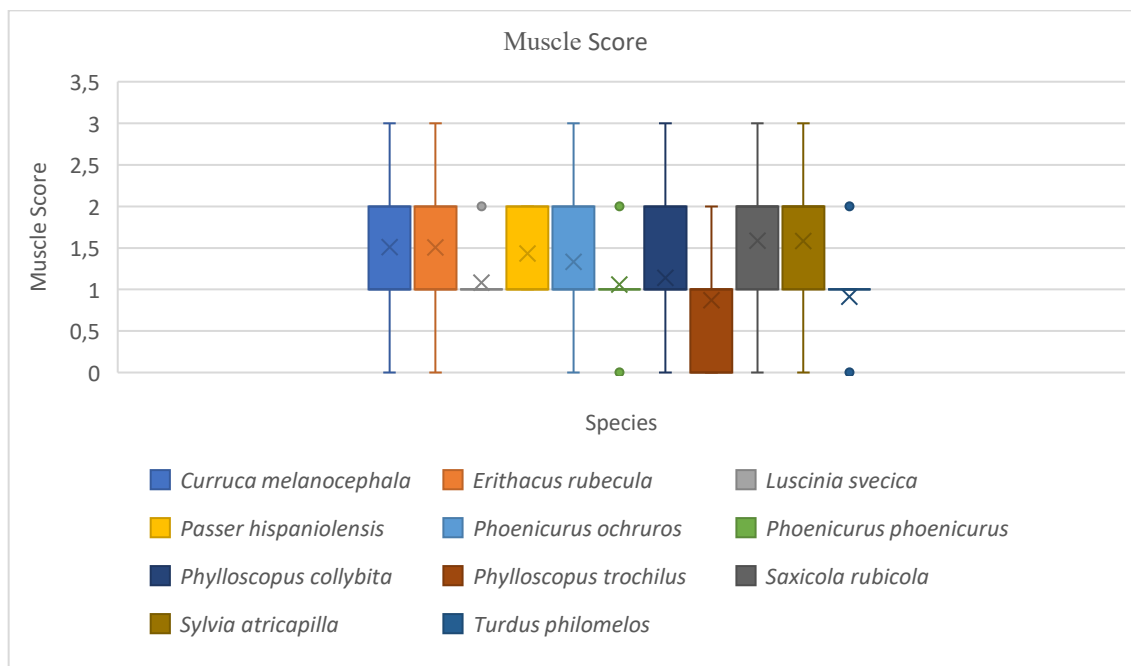
Figure 8: Distribution values of muscle scores from the most frequently captured migratory species during the autumn season (2024).

Acknowledgements

References

[1] Preuss, N.O., *Hans Christian Cornelius Mortensen: Aspects of his life and of the history of bird ringing,* Ardea, 89(special issue), 1–6, 2001.

[2] Bairlein, F., *Results of bird ringing in the study of migration routes,* Ardea, 89(special issue), 7–19, 2001.

[3] Bairlein, F., *Ökologie der Vogel. Physiologische Ökologie- Populationsbiologie-Vogelgemeinschaften- Naturschutz,* Gustav Fischer Verlag, Stutgart, 149p., 1996.

[4] Bairlein, F., *Manual of field methods. European-African Songbird Migration Network*, Wilhelmshaven, 48p., 1994.

[5] Meier, C.M., Karaardıç, H., Aymi, R., Peev, S.G., Witvliet, W., Liechti, F., *Population-specific adjustment of the annual cycle in a super-swift trans-Saharan migrant,* Journal of Avian Biology, 51(11), 2020.

[6] Schmaljohann, H., Eikenaar, C., Sapir, N., *Understanding the ecological and evolutionary function of stopover in migrating birds,* Biological Reviews, 99, 1231–1252, 2022.

[7] Lisovski, S., Bauer, S., Biriedis, M., Davidson, S.C., Dhanjal-Adams, K.L., Hallworth, M.T., et al., *Light-level geolocator analysis: A user's guide,* Journal of Animal Ecology, 89, 221–236, 2020.

[8] Hedenström, A., Norevik, G., Boano, G., Andersson, A., Backman, J., Akesson, S., *Flight activity in pallid swifts Apus pallidus during the non-breeding period,* Journal of Avian Biology, 50, e01972, 2019.

[9] Karaardıç, H., Erdoğan, A., Vohwinkel, R., Prünte, W., *The relationship between biometry and migration time among nine species of warblers in southern Turkey,* Journal of Ornithology, 147 (5), 191, 2006.

[10] Erdoğan, A., Karaardıç, H., Sert, H., Özkan, L., Vohwinkel, R., Prünte, W., *Manavgat/Titreyengöl Kuş Halkalama Çalışması,* Tabiat ve İnsan, Eylül, 23–33, 2008.

[11] Kaiser, M.N., Hoogstraal, H., Watson, G.E., *Ticks (Ixodoidea) on migrating birds in Cyprus, fall 1967 and spring 1968, and epidemiological considerations,* Bulletin of Entomological Research, 64: 97–110, 1974.

[12] Svensson, L., *Identification guide to European passerines,* 4th ed., Stockholm, 367 p. 1992.

[13] Kaiser, A., *A new multi-category classification of subcutaneous fat deposits of songbirds,* Journal of Field Ornithology, 64, 246–255, 1993.

[14] Karaardıç, H., Erdoğan, A., *Spring migration phenology of wheatear species in southern Turkey,* Acta Biologica Turcica, 32(2), 65–69, 2019.

[15] Karaardıç, H., Özkan, L., Erdoğan, A., *Antalya Boğazkent'in Göçmen Kuş Türleri,* Tabiat ve İnsan, 51(200), 40-48, 2017.

[16] Özkan, L., Karaardıç, H., Erdoğan, A., *Antalya Boğazkent'in Üreyen Kuş Türleri.* Tabiat ve İnsan, 51(198), 27–33, 2017.

[17] Prünte, W., Vohwinkel, R., Karaardıç, H., Erdoğan, A., *First record of Blyth's pipit, Anthus godlewskii (Taczanowski, 1876), from Turkey (Aves: Motacillidae),* Zoology in the Middle East, 50(1), 129–131, 2010.

[18] Karaardıç, H., Yavuz, M., Erdoğan, A., Prünte, W., Vohwinkel, R., *Results of bird banding in spring at Titreyengöl, Manavgat, Turkey, since 2002,* Journal of Ornithology, 147(5), 191, 2006.

[19] Karaardıç, H., *Wintering phenology and site fidelity of European Robins (Erithacus rubecula) in an eastern Mediterranean wintering area (Aves: Passeriformes),* Zoology in the Middle East, 68(1), 22–25, 2022.

Synthesis and Dielectric-Antimicrobial Properties of Poly(n-Butyl Methacrylate) with Chalcone Initiator

Demet COŞKUN[1],*

[1]*Firat University, Faculty of Science, Department of Chemistry, 23200, Elazığ, Türkiye*
dcoskun@firat.edu.tr, ORCID: 0000-0001-7141-6909

Abstract

In this study, in the first stage, the chalcone compound was synthesized in accordance with the literature. Then, the synthesized chalcone compound was reacted with bromine acetylbromide and the initiator used in the ATRP method was synthesized. The characterization of the synthesized compound was carried out by FT-IR and NMR spectrometers. The number average molecular weight (Mn) of the polymer was measured as 11780 and the heterogeneity index (HI) was measured as 1.32 by Gel Permeation Chromatography (GPC). In the second stage, the synthesized chalcone compound was used as an initiator and the polymerization of n-butyl methacrylate monomer was provided by the ATRP method. In the last stage, the dielectric and antimicrobial properties of the polymer were investigated. The Agar well method was used in the antimicrobial study. Dielectric properties were investigated as a function of frequency between 100 Hz and 5000 Hz at room temperature.

Keywords: Chalcone; ATRP; Antimicrobial properties; Dielectric properties.

Poli(n-Bütil Metakrilat)'ın Kalkon Başlatıcısı ile Sentezi ve Dielektrik-Antimikrobiyal Özellikleri

Öz

Bu çalışmada, ilk aşamada, literatüre uygun şekilde kalkon bileşiği sentezlenmiştir. Daha sonra sentezlenen kalkon bileşiği ile brom asetilbromür ile tepkimeye sokularak ATRP metodunda kullanılan başlatıcı sentezi gerçekleştirilmiştir. Sentezlenen bileşiğin karakterizasyonu, FT-IR ve NMR spektrometreleri ile yapılmıştır. Jel Geçirgenlik Kromatografisi (GPC) ile polimerin sayıca ortalama molekül ağırlığı (Mn) 11780 ve heterojenlik indisi (HI) ise 1.32 ölçülmüştür. İkinci aşamada, sentezlenen kalkon bileşiği başlatıcı olarak kullanılarak ATRP metodu ile n-bütil metakrilat monomerinin polimerleşmesi sağlanmıştır. Son aşamada ise polimerin dielektrik ve antimikrobiyal özelliği incelenmiştir. Antimikrobiyal çalışmada Agar kuyu yöntemi kullanılmıştır. Dielektrik özellikleri, oda sıcaklığında 100 Hz ile 5000 Hz aralığında frekansın bir fonksiyonu olarak incelenmiştir.

Anahtar Kelimeler: Kalkon; ATRP; Antimikrobiyal özellik; Dielektrik özellik.

1. Introduction

Polymers are high molecular weight compounds formed by the regular bonding of many molecules with chemical bonds [1]. Polymers are used as basic materials in many areas such as toy materials, textile materials, insulation materials, space vehicles, automobile parts, waste and clean water pipes, door and window materials, elastomers, foams, adhesives and many packaging materials. Many of the materials containing polymers have been the subject of research in many areas because they are cheap, lightweight, non-corrosive and durable materials [2]. Synthesis of functional polymers is very important in terms of technological developments. Synthesis of functional polymers is possible by polymerization of monomers with functional groups or by chemical modifications.

Chalcone compounds are one of the members of the flavonoid family that do not have a heterocyclic C ring. The presence of an α,β-unsaturated carbonyl group on the propane chain in the main structure of flavonoids, or in other words, the presence of a double bond and a ketone group, forms chalcones. Chalcone is used for all compounds with the structure of 1,3-diaryl-2-propen-1-one [3]. It is known that chalcones are found in edible plants and fruits in nature and are very beneficial compounds for health. They can be obtained from plants and fruits by methods such as extraction and can also be synthesized chemically. Cyclic compounds and their derivatives containing heteroatoms are used in many areas such as agriculture and medicine.

Polymers containing chalcone as a functional group have good thermal stability, solubility, photosensitivity and film formation capacity [4-6]. Polymers containing reactive functional groups are of great industrial and academic importance. The reason is that their synthesis is basically compatible with modification of the polymer structure to have the desired macromolecules in specific applications. Photopolymers are used to consider the properties of photosensitizers and macromolecular groups. Polymers with photocrosslinkable functional groups such as chalcones, thymine, and coumarin have become an active research area in the polymer world due to their technological importance in the fields of photolithography, non-linear optical materials, microelectronics, liquid crystal materials, and electrophotographic coating [7,8]. Chalcones and their derivatives possess various potent biological activities, such as antimicrobial [9,10], antihypertensive [11], anticancer [12], antioxidant [13], antidiabetic [14], anti-inflammatory [15], antiulcer [16], antimalarial [17], antiviral [18] and anti-gout [19].

AC conductivity measurements of materials are very important. When a dielectric material is placed between opposite poles, it reduces the force acting between the electric charges as if they were separated. Therefore, the dispersion and dielectric constant factor help us to obtain more information about the properties of the polymer. There are many studies on the electrical behavior of methacrylate and styrene derivatives [20-22]. In our study, the polymer containing the chalcone group in the end group was synthesized, and its dielectric properties were investigated.

In this study, it has been proven to be used in the polymerization reaction by synthesizing the previously synthesized but not used in the ATRP method, according to the literature. Thus, it has been determined that it could lead to new studies. investigating how the departure groups at the ends of the polymer chain will affect the polymers has a very high potential to lead new studies

2. Materials and Methods

2.1. Synthesis of 4-[3-(1-benzofuran-2-yl)-3-oxoprop-1-en-1-yl]phenyl bromoacetate

It was synthesized in accordance with the literature [23]. The synthesis reaction is shown in Fig. 1.
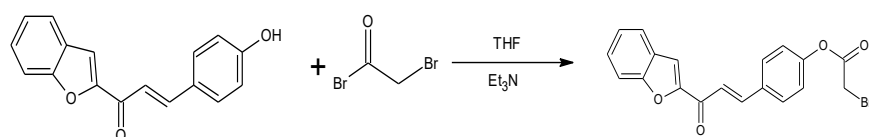
Figure 1: Initiator synthesis.

2.2. Polymer synthesis by ATRP method

0.07 mmol CuBr, 0.14 mmol Bpy and 0.07 mmol synthesized initiator were added to a rubber capped polymerization tube. Then, 1 drop of 1,4-dioxane solvent was dropped into this mixture. After the complex formation, 7 mmol of n-butylmethacrylate monomer was added to the polymerization tube and 0.5 ml of 1,4-dioxane solvent was added. The prepared polymer tube was passed through argon gas for ten minutes and then placed in an oil bath set at 110 °C and kept for 24 hours. The polymerization was terminated after the polymer solution thickened. Then, the thickened polymer solution was dissolved in dichloromethane and precipitated in methyl alcohol. The precipitation process was repeated three times. The precipitated polymer was dried first at room temperature and then under vacuum at 40 °C for 24 hours. The polymer reaction is shown in Fig. 2.
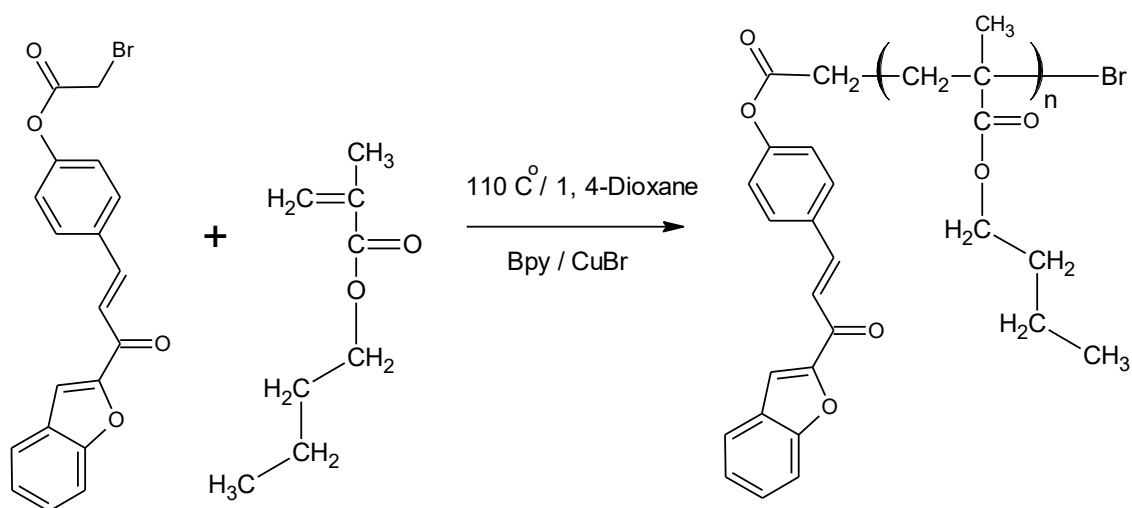
Figure 2: Polymer synthesis.

2.3. Dielectric measurements of polymer

The dielectric properties of the synthesized polymer were investigated. The polymer was converted into pellets by applying approximately 4 tons of pressure and the pellet thickness was measured. The pellet surfaces were painted with silver paint. The dielectric properties of the polymer were investigated as a function of frequency between 100 Hz and 5000 Hz at room temperature with the impedance analyzer.

2.4. Biological studies

In this study, the gram-negative bacteria Escherichia coli ATCC 25322 and Klebsiella pneumaniae ATCC 700603, Gram-positive bacteria Bacillus megaterium DSM32 and

Staphylococcus aureus ATCC 25923 and a fungus Candida albicans FMC17 were used. These microorganisms were obtained from Elazığ Fethi Sekin City Hospital Central Laboratory.

2.4.1. Antimicrobial Studies

An Agar well diffusion method was used to test the antimicrobial effects of the polymer on bacterial strains. Each bacterium was inoculated onto Sabouraud dextrose agar (SDA) and Nutrient Broth (Biolife Lot: HE2602) using a loop and adjusted to the McFarland turbidity standard of 0.5 to obtain a bacterial density of approximately 1-2 x 108 CFU/ml. The fungal strain was inoculated onto petri dishes containing SDA and incubated for 48 hours (31°C). Yeast colonies were suspended in 0.9% sodium chloride (saline) solution and incubated at 45°C to reach a concentration of 2x107 cells/ml. Diluted and sterilized in autoclave (121°C for 15 min) MHA was distributed in an 15-20 ml amounts into petri dishes and allowed to cool. 100 µl of microorganism suspension was added to the solidified MHA and spread evenly on the agar using a drigalski spatula. Wells of the desired diameter were opened with an agar piercer (corkborer). Samples were prepared at four concentrations (125, 250, 500 and 1000 mg/ml) and mixed under aseptic conditions at 100 µl per well. Incubation for bacteria and fungi inoculated plates was 24 h (37±0.1ºC) and 48 h (25±0.1ºC), respectively. 100% DMSO (Merc-Lot K51154243 948) was used as a negative control and a standard disk containing 2 mcg clindamycin (Lot 171127A) was used as a positive control. At the end of incubation, inhibition diameters were measured [24,25].

2.4.2. Determination of antioxidant activity

2,2-Diphenyl-1-picrylhydrazyl (DPPH) radical scavenging activity method was used to evaluate the antioxidant activity of the synthesized polymer. The stock solution of the polymer was prepared and then serially diluted with 0.005% methanolic DPPH solution at concentrations of 125, 250, 500, 1000 µM. 100% ascorbic acid was used as positive control, and 100% methanol was used as negative control. After the mixtures were incubated at 37±0.1°C for 30 min, their absorbances were measured by spectrophotometer at 517 nm wavelength. The following formula was used to determine the scavenging rate of DPPH radicals for each mixture [26]:

$$\text{Antioxidant activity } (\%) = [(Ac - As) \div Ac] \times 100 \tag{1}$$

Ac: Control absorbance; As: Sample absorbance.

3. Results and Discussion

3.1. Characterization of 4-[3-(1-benzofuran-2-yl)-3-oxoprop-1-en-1-yl]phenyl bromoacetate

The IR spectrum of the synthesized initiator is given in Fig. 3, the ^{1}H-NMR spectrum in Fig. 4 and its evaluation in Table 1.
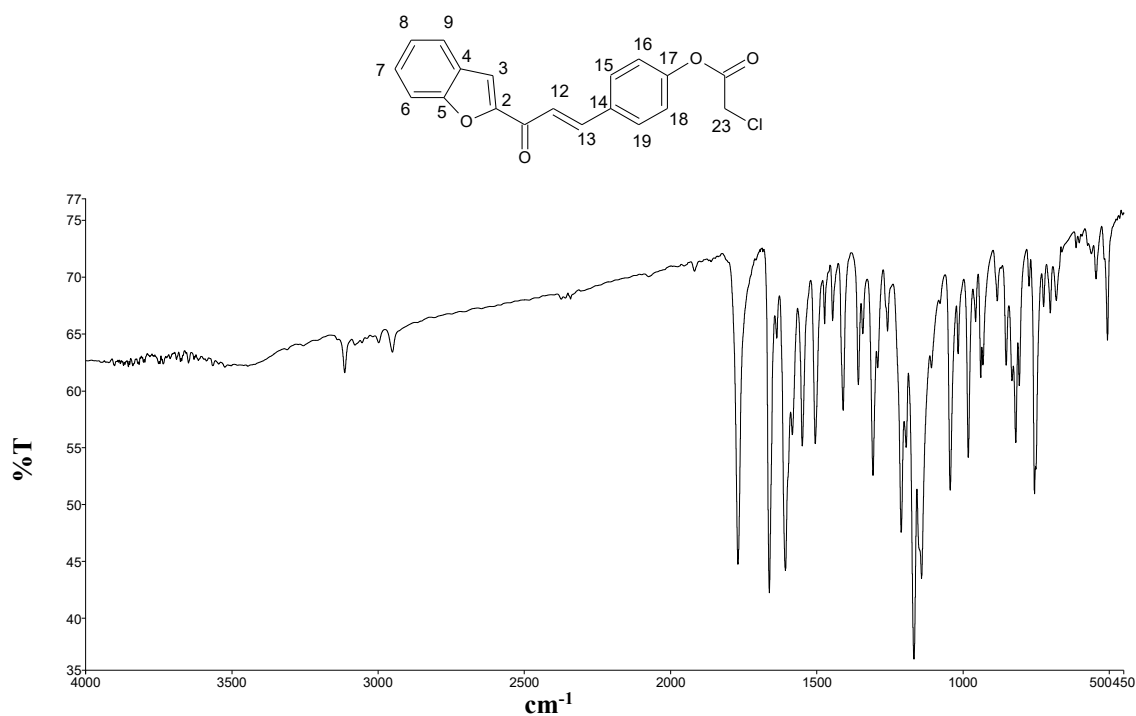
Figure 3: IR spectrum of the initiator.
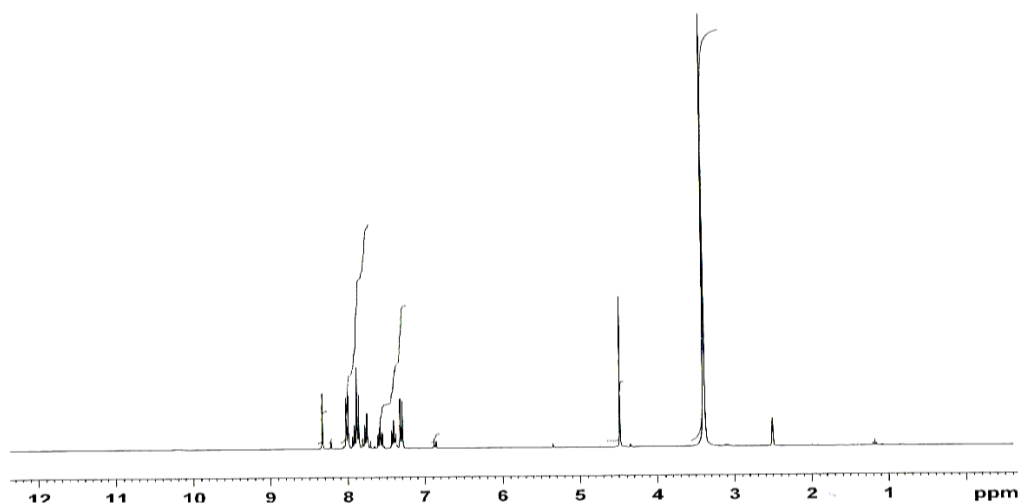
Figure 4: ^{1}H-NMR spectrum of the initiator.

Table 1: Spectrum evaluation of the initiator.

FT-IR (cm⁻¹)			
3114-3000	Aro. C-H	1609	Aro. C=C
1761	C=O	1165	C-O-C asym.
1660	C=O (C=C-C=O)	1133	C-O-C sym.

¹H-NMR (ppm) DMSO-d₆									
H_3	H_{19}	H_{13}	H_9	H_{12}	H_6	H_7	H_8	H_{18}	H_{23}
8,31	8,02	7,92	7,89	7,83	7,75	7,55	7,41	7,31	4,49

3.2. Characterization of Polymer

The IR spectrum of the synthesized polymer is given in Fig. 5, the ¹H-NMR spectrum in Fig. 6, the GPC spectrum in Fig. 7 and its evaluation in Table 2.
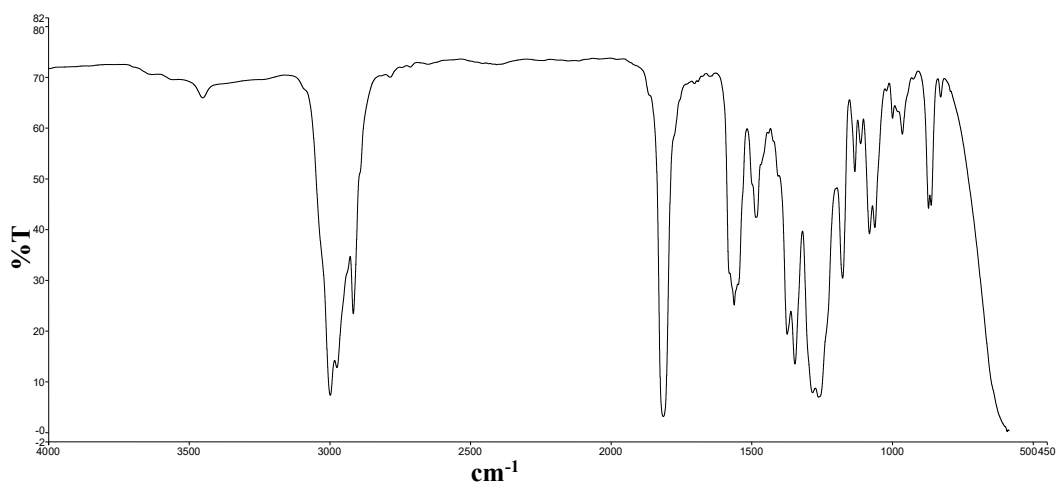
Figure 5: IR spectrum of the polymer.
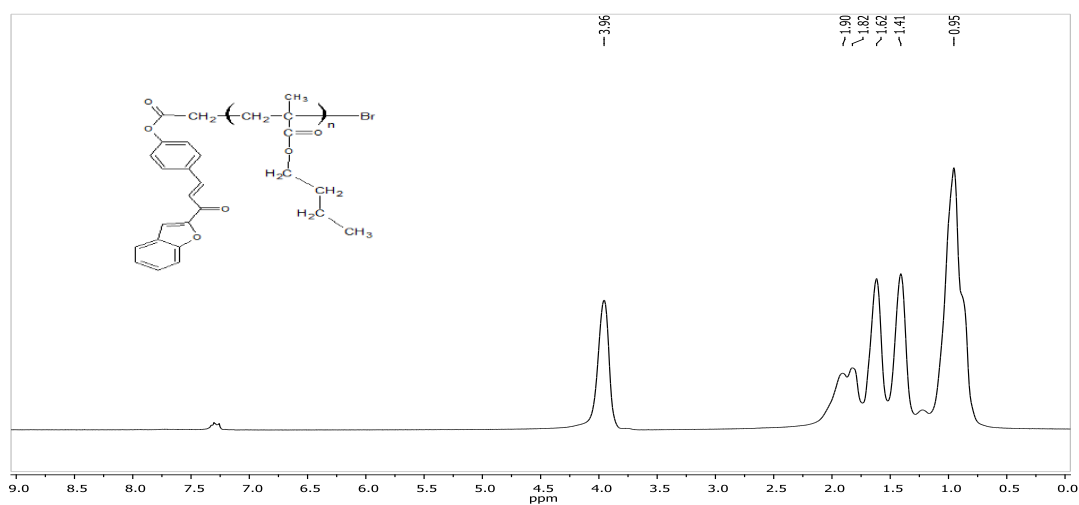
Figure 6: ¹H-NMR spectrum of the polymer.
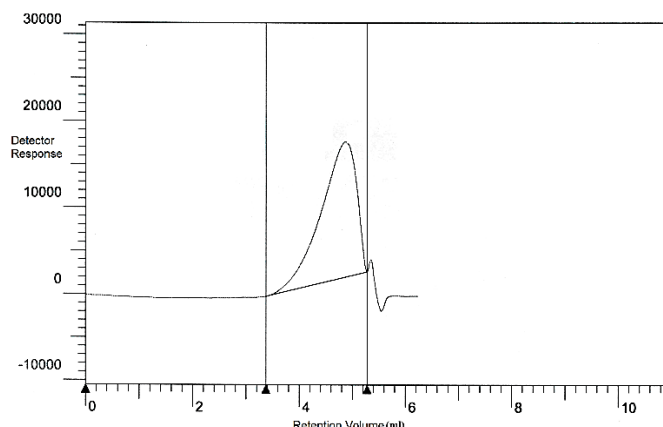
Figure 7: GPC spectrum of the polymer.

In the IR spectrum of the polymer synthesized by the ATRP method; aliphatic C-H stretching at 2945-2845 cm-1, ester C=O stretching at 1736 cm-1, C-H stretching at 1371-1393 cm-1 and C-O-C symmetric stretching in the range of 1148-1050 cm-1 and C-Br stretching at 670-500 cm-1 are the characteristic bands. In the ^{1}H-NMR spectrum; signals at 7.51-7.10 ppm characterize aromatic ring protons and solvent signals, signals at 3.96 ppm characterize O-CH$_2$ protons, signals at 1.90 ppm characterize CH$_2$ protons in the main chain and signals at 1.82-0.95 ppm characterize CH$_2$-CH$_3$ protons. Since aromatic protons are only at the ends of the chain, the signals are weak.

Table 2: Spectrum evaluation of the polymer.

FT-IR (cm^{-1})			
2945-2845	Ali. C-H	1148-1050	-C-O-C
1736	C=O	670-500	C-Br gerilmesi
1371-1393	C-H		

^{1}H-NMR (ppm) CDCl$_3$			
H	**H**	**H**	**H**
Aromatic	OCH$_2$	CH$_2$ (Main chain)	CH$_3$
7,51-7,10	3.96	1.90	1.82-0.95

3.3. Dielectric Results

The dielectric properties of the synthesized polymer were investigated. The polymer was converted into pellets by applying 4 tons of pressure and the pellet thickness was measured. The pellet surfaces were painted with silver paint. Measurements were taken at different frequencies with the impedance analyzer. Dielectric measurements of the polymer against frequency are

shown in Fig. 8, Fig. 9 and Fig. 10. The dielectric values of the polymer at 1 kHz and room temperature are given in Table 3.
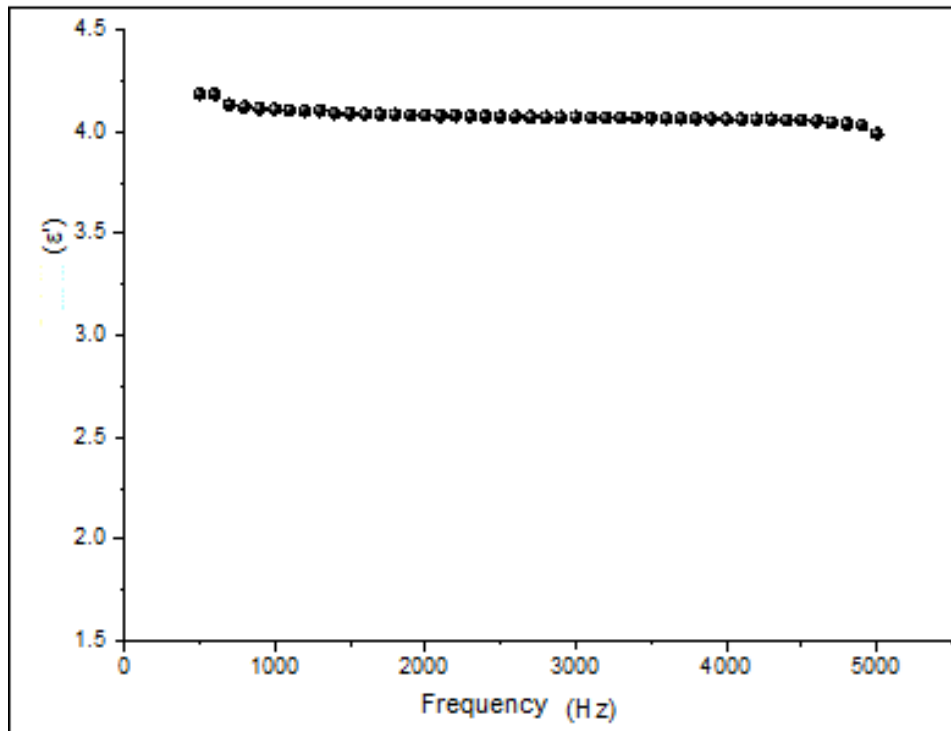
Figure 8: Variation of dielectric constant versus frequency.
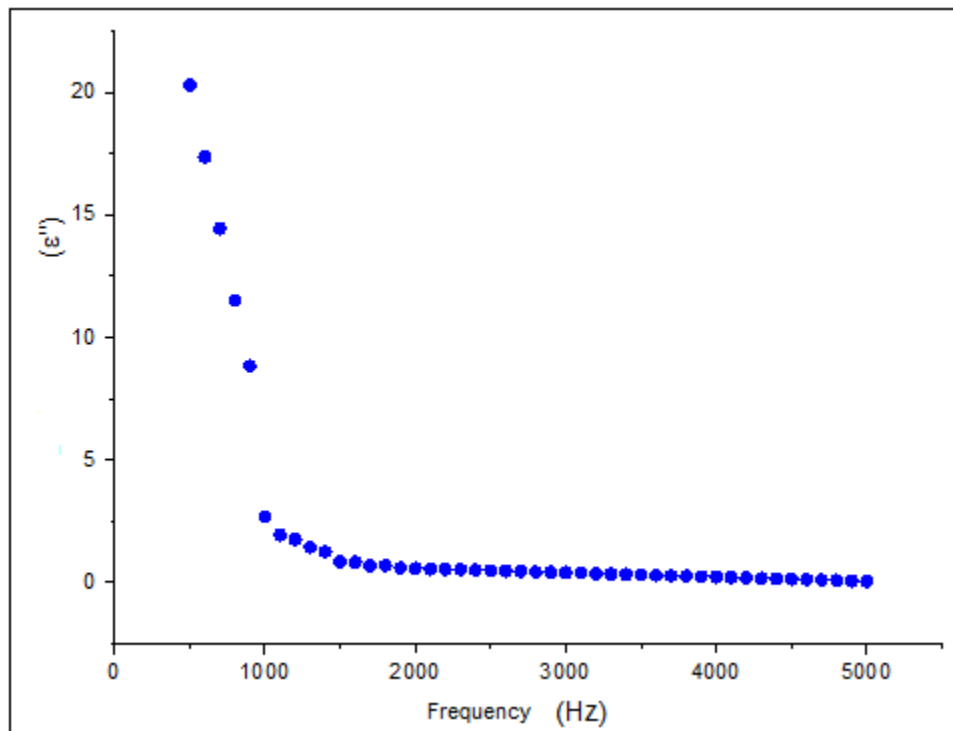
Figure 9: Variation of dielectric loss factor versus frequency.

71
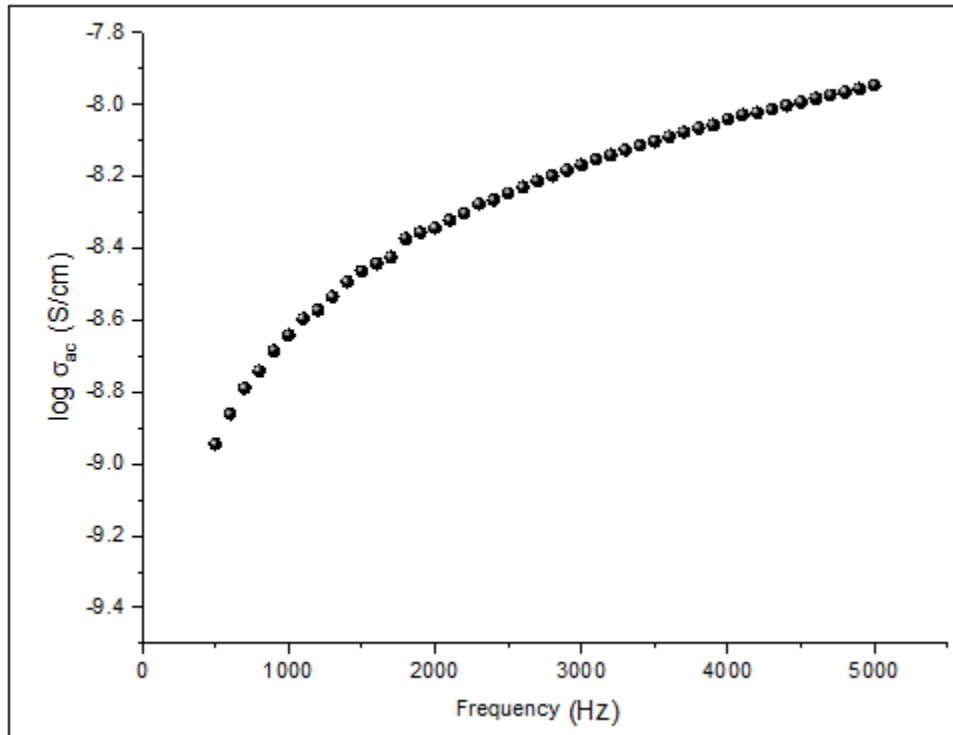
Figure 10: Change of logarithm of conductivity value with frequency.

Table 3: Dielectric values of the polymer at 1 kHz and room temperature.

	Dielectric constant	Dielectric loss	σ_{ac}	Log σ_{ac}
P(nBMA)	4.1113	2.6023	$2.28133E^{-9}$	-8.64181

It has been observed that the dielectric constant and dielectric loss factor of the polymer decrease with increasing frequency. The dielectric constant and dielectric loss factor tend to decrease noticeably in the low frequency range. As high frequency values are approached, the tendency of the dielectric constant decreases, but the decrease continues, albeit slightly. The reason for the sudden decreases in the low frequency regions is that the charged dipoles in the polymer have a higher tendency to move in the direction of their own field than in the direction of the applied electric field in this frequency region [27]. It has been observed that the logarithm of the conductivity value of the polymer increases with increasing frequency. Since the conductivity values are less than 10^{-06}, we can say that these polymers exhibit insulating properties.

3.4. Biological Results

In the study, the antimicrobial activity of the synthesized polymer on five different microorganisms was investigated. Antimicrobial effects were measured as a function of the

inhibition zone diameter (mm) in Table 4, DMSO was used as a negative control and compared with Clindamycin antibiotic disk.

Table 4: Antimicrobial effects of the polymer on 5 different microorganism strains (Zone diameters in mm)

	E.coli				*B. megaterium*				*S. aureus*				*C.albicans*				*K. pneumoniae*			
	125 μM	250 μM	500 μM	1000 μM	125 μM	250 μM	500 μM	1000 μM	125 μM	250 μM	500 μM	1000 μM	125 μM	250 μM	500 μM	1000 μM	125 μM	250 μM	500 μM	1000 μM
P(nBMA)	11± 0,2	11± 0,2	11± 0,2	12± 0,7	11± 1,5	12± 0,5	13± 0,5	14± 1,5	12± 0,7	12± 0,7	13± 0,2	14± 1,2	14± 1,5	13± 0,5	11± 1,5	12± 0,5	13± 1,2	14± 0,2	15± 0,7	15± 0,7
Clindamycin	20±1,4				22±0,6				23±1,6				20±1,4				22±0,6			

According to the results shown in Fig. 11, the Polymer showed good scavenging activity with 94% DPPH scavenging activity at all concentrations. Based on these results, it was determined that the Polymer in general and the concentrations used had a significant effect on the DPPH scavenging activity.
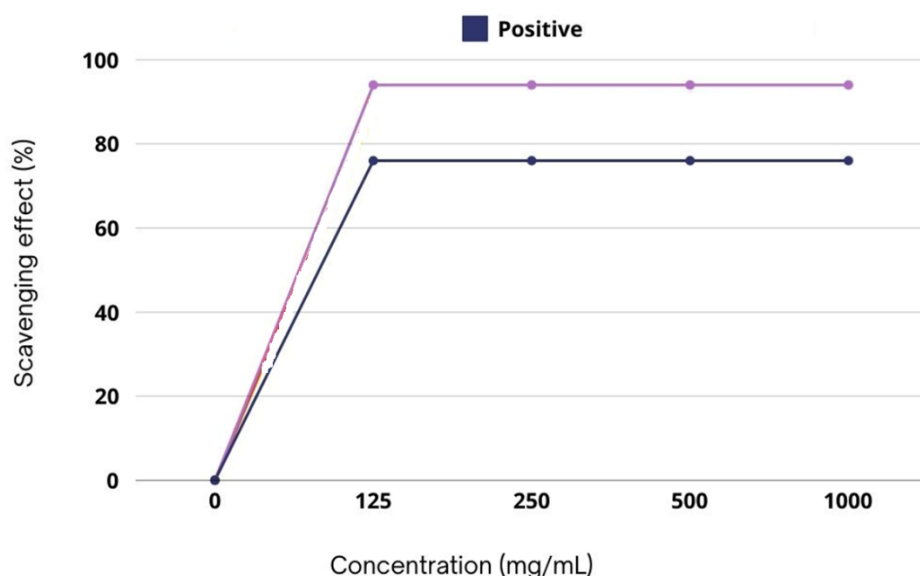
Figure 11: Percent inhibition of DPPH free radical scavenging activity of the polymer.

4. Conclusion

There are many methods for the synthesis of polymers. One of the most important of these methods is the ATRP method. The synthesis of new initiators that can be used in the ATRP method is very important for the scientific world. This study has proven that the initiator we synthesized can be used in the ATRP method. In this study, an initiator containing a chalcone group was synthesized in accordance with the literature. For this purpose, a benzofuran chalcone

compound containing a hydroxy group was reacted with bromocetylbromide. The characterization of the synthesized compound was carried out by FT-IR and NMR spectrometers. Then, the synthesized initiator was polymerized with n-butyl methacrylate monomer. The ATRP method was used as the polymerization method. The average molecular weight and molecular weight distribution of the synthesized polymer were measured with a gel permeation chromatography (GPC) device at 25 °C using a refractive index (RI) detector at a solvent flow rate of 1 mL/min. Polystyrene was used as the standard substance and THF was used as the solvent. In the last stage, the dielectric and antimicrobial properties of the polymer were investigated. The Agar well method was used in the antimicrobial study. Dielectric properties were investigated as a function of frequency between 100 Hz and 5000 Hz at room temperature. In our study, it was determined that the polymer showed the best zone diameter (17 mm) against E. coli. When the antioxidant activity of the polymer was examined, it was seen that it had approximately 94% DPPH scavenging activity. In line with these results, it was determined that the polymer and the concentrations used had a significant effect on the DPPH scavenging activity. When the dielectric properties of the polymer were examined, it was observed that the dielectric constant and dielectric loss factor generally decreased with increasing frequency. It remained almost constant at high frequency values. When the conductivity value was examined, it was seen that the synthesized polymer had insulating properties.

References

[1] Saçak, M., *Polymer Chemistry*, Gazi Bookstore, Ankara, Turkey, 2004.

[2] Köroğlu, A.M., *Synthesis, characterization and copolymerization of new methacrylate monomers and polymers carrying oxime esters in the minor branch*, Afyon Kocatepe University, Master Thesis, Afyon, 2006.

[3] Opletalova, V., Hartl, J., Palat, K.Jr., Patel, A., *Conformational analysis of 2-hydroxy-2',5'-diazachalcones*, Journal of Pharmaceutical and Biomedical Analysis, 23, 55–59, 2020.

[4] Indira, J., Karat, P.P., Sarojini, B.K., *Growth, characterization, and nonlinear optical property of chalcone derivative*, Journal of Crystal Growth, 242, 209–214. 2002.

[5] He, Z., Li, D., Hensley, D.K., Rondione, A.J., Chen, J., *Switching phase separation mode by varying the hydrophobicity of polymer additives in solution-processed semiconducting small-molecule/polymer blends*, Applied Physics Letters, 103, 113301, 2013.

[6] He, Z., Chen, J., Keum, J.K., Szulczewski, G., Li, D., *Improving performance of TIPS pentacene-based organic thin film transistors with small-molecule additives*, Org Electron 15, 150–155, 2014.

[7] Şentürk, A., *The Synthesis and Characterization of Methacrylate Polymers Bearing Chalcone*, Master's Thesis, Firat University, Elazig, Turkey, 2011.

[8] Ekbote, A.N., Maidur, S.R., Jahagirdar, J.R., Patil, P.S., Soma, V.R., *Femtosecond nonlinear optical investigations of nitro chalcones-doped PMMA thin films for optical limiting and photonic applications*, Materials Today Communications, 37, 107240, 2023.

[9] Fang, X., Yang, B., Cheng, Z., Zhang, P., Yang, M., *Synthesis and antimicrobial activity of novel chalcone derivatives,* Research on Chemical Intermediates, 40, 1715–1725, 2014.

[10] Sudhakar, C., Suresh, J., Valarmathi, N., Sumathi, S., Karthikeyan, A., et al., *Synthesis, characterization of acrylate polymer having chalcone moiety: evaluation of antimicrobial, anticancer and drug release study*, Journal Of Biomaterials Science-Polymer Edition, 32(4), 438–453, 2020.

[11] Bonesi, M., Loizzo, M.R., Statti, G.A., Michel, S., Tillequin, F., Menichini, F., *The synthesis and Angiotensin Converting Enzyme (ACE) inhibitory activity of chalcones and their pyrazole derivatives*, Bioorganic & Medicinal Chemistry Letters, 20(6), 1990–1993, 2010.

[12] Burmaoglu, S., Algul, O., Anıl, D.A., Gobek, A., Duran, G.G., Ersan, R.H., et al., *Synthesis and anti-proliferative activity of fluoro-substituted chalcones*, Bioorganic & Medicinal Chemistry Letters, 26(13), 3172–3176, 2016.

[13] Shenvi, S., Kumar, K., Hatti, K.S., Rijesh, K., Diwakar, L., Reddy, G.C., *Synthesis, anticancer and antioxidant activities of 2,4,5-trimethoxy chalcones and analogues from asaronaldehyde: Structure-activity relationship,* European Journal of Medicinal Chemistry, 62, 435–442, 2013.

[14] Hsieh, C.T., Hsieh, T.J., El-Shazly, M., Chuang, D.W., Tsai, Y.H., Yen, C.T., et al., *Synthesis of chalcone derivatives as potential anti-diabetic agents*. Bioorganic & Medicinal Chemistry Letters, 22(12), 3912–3915, 2012.

[15] Iqbal, H., Prabhakar, V., Sangith, A., Chandrika, B., Balasubramanian, R., *Synthesis, anti-inflammatory and antioxidant activity of ring-A-monosubstituted chalcone derivatives*, Medicinal Chemistry Research, 23, 4383–4394, 2014.

[16] Sashidhara, K.V., Avula, S.R., Mishra, V., Palnati, G.R., Singh, L.R., Singh, N., Chhonker, et al., *Identification of quinoline-chalcone hybrids as potential antiulcer agents*, European journal of medicinal chemistry, 89, 638–653, 2015.

[17] Pingaew, R., Saekee, A., Mandi, P., Nantasenamat, C., Prachayasittikul, S., Ruchirawat, S., et al., *Synthesis, biological evaluation and molecular docking of novel chalcone–coumarin hybrids as anticancer and antimalarial agents*, European Journal of Medicinal Chemistry, 85, 65–76, 2014.

[18] Shi, F., Fang, H., Xu, W., *Design, synthesis and biological activity of novel chalcone derivatives as anti-influenza agents,* Chemical Research in Chinese Universities, 32(1), 28–34, 2016.

[19] Mahapatra, D., Asati, V., Bharti, S.K., *Recent therapeutic progress of chalcone scaffold bearing compounds as prospective anti-gout candidates,* Journal of Critical Reviews, 6(1), 1–5, 2019.

[20] Demirelli, K., Kaya, E., Coşkun, M., Bagci, E., *Thermal degradation of two different polymers bearing amide pendant groups prepared by ATRP method*, Journal of Thermal Analysis and Calorimetry, 114(2), 917–926, 2013.

[21] Jobish, J., Charoen, N., Praveen, P., *Dielectric properties and AC conductivity studies of novel NR/PVA full-interpenetrating polymer networks*, Journal of Non-Crystalline Solids, 358(8), 1113–1119, 2012.

[22] Kamath, A., Devendrappa, H., *Concentration-dependent ionic conductivity and dielectric relaxation of methyl blue-dyed polyethylene oxide films*, Polymer Bulletin, 72(10), 2705–2724, 2015.

[23] Coşkun D., *The Synthesis of Benzofurane Substituted α,β-Unsaturated Ketones and Their Derivatives*, PhD Thesis, Firat University, Elazig, Turkey, 2008.

[24] Arslan Ateşşahin, D., Kadioğlu Dalkiliç, L., Özeren, Y., Dalkiliç, S., Çakmak, K., et al., *Investigation of Cytotoxic, Antimicrobial and Antioxidant Activity of Echium vulgare L. Seed*, International Journal of Nature and Life Sciences, 7(2), 129–135, 2023.

[25] Dalkılıç, S., Kadıoğlu Dalkılıç, L., Korkmaz, İ., *Antimicrobial Effect of Traditional Breakfast Zahter*, Gumuşhane University Science Institute Journal, 10(1), 128–133, 2020.

[26] Baliyan, S., Mukherjee, R., Priyadarshini, A., Vibhuti, A., Gupta, A., Pandey, R. P., et al., *Determination of Antioxidants by DPPH Radical Scavenging Activity and Quantitative Phytochemical Analysis of Ficus religiosa*, Molecules, 27(4), 1326, 2022.

[27] Çavuş, M.S., *Defect-Assisted Fractional Stochastic Ising Model of Dielectric Relaxation*, Çukurova University, PhD Thesis, Adana, 2010.

Intuitionistic Fuzzy Partial Metric Spaces

Abdullah KARGIN[1],*

[1]*Gaziantep University, Faculty of Art and Sciences, Department of Mathematics, 27000, Gaziantep, Türkiye*
kargin@gantep.edu.tr, ORCID:0000-0003-4314-5106

Abstract

Fuzzy logic is a theory used as an alternative to classical structures in both application and algebraic fields. In particular, there are fuzzy structures in metric spaces and partial metric spaces. The most widely used of these structures are fuzzy metric spaces, fuzzy partial metric spaces and intuitionistic fuzzy metric spaces. In this paper, intuitionistic fuzzy partial metric spaces are defined, their basic properties and examples are obtained. For it, open ball, convergent sequence, and Cauchy sequence are defined and their basic properties are introduced. Furthermore, the relations between intuitionistic fuzzy partial metric spaces, classical metric spaces, fuzzy metric spaces, fuzzy partial metric spaces, and intuitionistic fuzzy metric spaces are analyzed. As a result of this investigation, it is shown that from each classical metric, classical partial metric, and intuitionistic fuzzy metric, an intuitionistic fuzzy partial metric can be obtained. Moreover, it is achieved that an intuitionistic fuzzy metric is also an intuitionistic fuzzy partial metric space. Thus, a new structure is given by transferring the partial metric structure to intuitionistic fuzzy metric spaces.

Keywords: Metric spaces; Partial metric spaces; Fuzzy metric spaces; Fuzzy partial metric spaces; Intuitionistic fuzzy metric spaces; Intuitionistic fuzzy partial metric spaces.

Sezgisel Bulanık Kısmi Metrik Uzaylar

Öz

Bulanık mantık, hem uygulama hem de cebirsel alanlarda klasik yapılara alternatif olarak kullanılan bir teoridir. Özellikle metrik uzaylarda ve kısmi metrik uzaylarda bulanık yapılar yer almaktadır. Bu yapılardan en yaygın olarak kullanılan bulanık metrik uzaylar, bulanık kısmi metrik uzaylar ve sezgisel bulanık metrik uzaylardır. Bu çalışmada, sezgisel bulanık kısmi metrik uzaylar tanımlanmış, temel özellikleri ve örnekleri elde edilmiştir. Bunun için açık yuvar, yakınsak dizi ve Cauchy dizisi tanımlanmış ve temel özellikleri tanıtılmıştır. Ayrıca, sezgisel bulanık kısmi metrik uzaylar, klasik metrik uzaylar, bulanık metrik uzaylar, bulanık kısmi metrik uzaylar ve sezgisel bulanık metrik uzaylar arasındaki ilişkiler incelenmiştir. Bu inceleme sonucunda, her bir klasik metrik, klasik kısmi metrik ve sezgisel bulanık metrikten bir sezgisel bulanık kısmi metrik elde edilebileceği gösterilmiştir. Ayrıca, bir sezgisel bulanık metriğin aynı zamanda bir sezgisel bulanık kısmi metrik uzay olduğu elde edilmiştir. Böylece kısmi metrik yapısı sezgisel bulanık metrik uzaylara aktarılarak yeni bir yapı verilmiştir.

Anahtar Kelimeler: Metrik uzaylar; Kısmi metrik uzaylar; Bulanık metrik uzaylar; Bulanık kısmi metrik uzaylar; Sezgisel bulanık metrik uzaylar; Sezgisel bulanık kısmi metrik uzaylar.

1. Introduction

Partial metric spaces [1] were defined by Matthews in 1994. The most important feature that distinguishes this metric from the classical metric is that the distance of a point to itself is not always zero. This property leads to important properties in fixed point theories (FPTs).

Zadeh defined fuzzy logic (FL) and fuzzy sets (FS) [2] in 1965 to explain uncertainties more precisely mathematically. In FS, the degree of membership of each element of set takes a value in the range [0, 1]. Thus, unlike classical logic, the membership of each element is graded. For example, the weather can be specified with expressions such as hot, cold, warm, cool, very hot, very cold, etc., and with different degrees of membership. Thus, a more precise type of logic, including classical logic, has been defined to explain uncertainties. FL is one of the most widely used types of logic in almost every field of science, including decision-making applications and algebraic fields. Recently, Emniyet and Şahin obtained fuzzy normed rings [3] in 2018. Kum et al. studied an alternative method for determining erosion risk based on FL [4] in 2022; Wang et al. introduced a new distance measure for q-Rung Orthopair FSs [5] in 2024; Xu and Wang introduced a novel fuzzy bi-clustering algorithm for Co-Regulated Genes [6] in 2024; Plebankiewicz and Karcińska studied supporting construction using to the FSs theory [7] in 2024.

In 1975, Kramosil and Michálek defined fuzzy metric space (FMS) [8]. Also, Grabiec obtained fixed points in FMSs [9] in 1989. This new type of metric, defined as an alternative to classical metric spaces, brings the advantages of FL to the theory of metric spaces. Thus, the distance between two points is graded with the help of a fuzzy membership function. Many classical metric types have been similarly redefined according to FL. Recently, Shukla et al. studied vector-valued FMS [10] in 2024; Gregori et al. achieved completeness FPT based on FMSs [11] in 2024; Huang introduced properties for some metric spaces based on FSs [12] in 2024.

Moreover, fuzzy partial metric space (FPMS) has been defined differently in three different works [13-15] in different years. Olgun et al. introduced the basic definition and properties were given and provided an FPT for FPMS [13]. Recently, Aygün et al. studied FPTs based on FPMS [16] in 2022; Gregori et al. studied relationship between FPMS and fuzzy quasi-metrics [17] in 2020.

In 1986, Atanassov [18] defined intuitionistic fuzzy sets (IFS) by including the degree of uncertainty in addition to the degree of membership and non-membership in FL. In this type of logic, the degree of uncertainty is defined depending on the degree of membership and the degree of non-membership so that the sum of the degree of membership, degree of non-membership, and degree of uncertainty is 1. Thus, a new type of logic that can give more precise results than FL has emerged. Intuitionistic fuzzy logic is frequently used in areas where FL is insufficient. Recently, Ngan studied creating operators and functions based on IFSs [19] in 2024; Gerogiannis et al. obtained an approach for IFSs [20] in 2024; Rajafillah et al. defined intuitionistic fuzzy pooling [21] in 2024.

In 2004, Park defined intuitionistic fuzzy metric spaces (IFMS) [22]. In this study, open balls, convergent sequence, Cauchy sequence, and complete space are defined for IFMS and given an FPT. Also, thanks to this metric space, the advantage of using IFSs is brought to the theory of metric spaces. While defining this metric space, the relationship between FL and intuitionistic FL was transferred to metric spaces. Thus, many researchers are working on IFMS [23-26]. Recently, Wong et al. studied complex-valued IFMS [27] in 2024; Singh et al. defined fuzzy differential equations based on IFMS [28] in 2024.

In this paper, we define intuitionistic fuzzy partial metric spaces (IFPMS) for the first time and give their basic properties. These definitions and properties are obtained by considering the basic definitions and properties given for FPMS in the study [13] of Olgun et al. and in the study [22] of Park. The IFPMS defined in Section 3 have new properties different from the other

structures, but they also provide some basic properties of FMS, FPMS, and IFMS. For this reason, to make the definitions, properties, and results obtained in Section 3 more comprehensible and to easily show which definitions, properties, and results are given by making use of which definitions, properties, and results, the basic information in Section 2 is included. In Section 3, IFPMS are defined and some examples are given. It is also shown that every IFMS is also an IFPMS. It is also shown that one can obtain an IFPMS from every classical partial metric and every IFMS. For IFPMS, basic properties are given. Also, open balls, convergent sequence, Cauchy sequence, and complete space are defined for IFPMS. The basic properties of these structures are given. Thus, existence of IFPMS is proved for each classical, classical partial, and IFMS. In the last section, the conclusions of this study are given and suggestions are made to researchers about the structures that they can obtain by using this study.

2. Preliminaries

In this section, the basic definitions, examples, lemmas, and properties are given based on FS, IFS, FMS and IFMS. These basic contractures are used in Section 3.

Definition 1. [2] Let E be a non-empty set. Fuzzy set K is denoted by

$$K = \{\langle \gamma, \mu_K(\gamma) \rangle : \gamma \in E\}.$$

where

$$\mu_K : E \to [0,1]$$

is the membership function of K. For example, $\mu_K(\gamma)$ is the membership value of $\gamma \in E$.

Definition 2. [18] Let E be a non-empty set. Intuitionistic fuzzy set L is denoted by

$$L = \{\langle \gamma, \mu_L(\gamma), \nu_L(\gamma) \rangle : \gamma \in E\}.$$

where

$$\mu_L : E \to [0,1]$$

is the membership function of L and

$$\nu_L : E \to [0,1]$$

is the non-membership function of L such that

$$0 \le \mu_L(\gamma) + \nu_L(\gamma) \le 1.$$

Also, $\mu_L(\gamma)$ and $\nu_L(\gamma)$ are membership values of γ and non-membership values of γ; respectively.

Definition 3. [29] Let $\oplus$ be a binary operation such that

$$\oplus : [0,1] \times [0,1] \to [0,1].$$

If the following properties are satisfied, then $\oplus$ is called a continuous t-norm (CTN). For $\gamma_1, \gamma_2, \gamma_3, \gamma_4 \in [0,1]$,

i. $\gamma_1 \oplus 1 = \gamma_1,$

ii.   If $\gamma_1 \leq \gamma_2$ and $\gamma_3 \leq \gamma_4$, then $\gamma_1 \oplus \gamma_3 \leq \gamma_2 \oplus \gamma_4,$

iii. $\oplus$ is continuous,

iv. $\oplus$ is commutative and associative.

Definition 4. [29] Let $\odot$ be a binary operation such that

$$\odot : [0,1] \times [0,1] \to [0,1].$$

If the following properties are satisfied, then $\odot$ is called a continuous t-conorm (CTCN). For $\gamma_1, \gamma_2, \gamma_3, \gamma_4 \in [0,1]$,

i. $\gamma_1 \odot 0 = \gamma_1,$

ii.   If $\gamma_1 \leq \gamma_2$ and $\gamma_3 \leq \gamma_4$, then $\gamma_1 \odot \gamma_3 \leq \gamma_2 \odot \gamma_4,$

iii. $\odot$ is continuous,

iv. $\odot$ is commutative and associative.

Definition 5. [13] Let $\mathcal{X}$ be a non-empty set, $\oplus$ be a CTN and $\mathcal{R}$ be FS on $\mathcal{X}^2 \mathrm{x}(0, \infty)$. A 3-tuple $(\mathcal{X}, \mathcal{R}, \oplus)$ is said to be an FPMS if the following conditions are satisfied. For each $\gamma_1, \gamma_2, \gamma_3 \in \mathcal{X}$; $\rho, p_1, p_2 > 0$,

i. $0 \leq \mathcal{R}(\gamma_1, \gamma_2, \rho) \leq 1,$

ii. $\mathcal{R}(\gamma_1, \gamma_1, \rho) \geq \mathcal{R}(\gamma_1, \gamma_2, \rho),$

iii. $\mathcal{R}(\gamma_1, \gamma_2, \rho) = \mathcal{R}(\gamma_2, \gamma_1, \rho),$

iv. $\mathcal{R}(\gamma_1, \gamma_2, \rho) = \mathcal{R}(\gamma_1, \gamma_1, \rho) = \mathcal{R}(\gamma_2, \gamma_2, \rho)$ if and only if $\gamma_1 = \gamma_2,$

v. $\mathcal{R}(\gamma_1, \gamma_3, p_1) \oplus \mathcal{R}(\gamma_3, \gamma_2, p_2) \leq \mathcal{R}(\gamma_1, \gamma_3, p_1 + p_2) \oplus \mathcal{R}(\gamma_3, \gamma_3, \rho), \rho \geq p_1$ and $\rho \geq p_2,$

vi. $\mathcal{R}(\gamma_1, \gamma_2, .): [0, \infty) \to [0,1]$ is continuous,

The function $\mathcal{R}(\gamma_1, \gamma_2, \rho)$ denotes the degrees of nearness, between γ_1 and γ_2 with respect to ρ.

Definition 6. [13] Each FPMS $\mathcal{R}(\gamma_1, \gamma_2, \rho)$ on $\mathcal{X}^2$x(0, ∞) generates a topology τ on $\mathcal{X}$ with the family of open M-balls

$$\{B_M(\gamma_1, \varepsilon): \gamma_1 \in X, 0 < \varepsilon < \mathcal{R}(\gamma_1, \gamma_1, p_1)\}$$

as a base, where for all $\gamma_1 \in \mathcal{X}$,

$$B_M(\gamma_1, \varepsilon) = \{\gamma_2 \in \mathcal{X}: \mathcal{R}(\gamma_1, \gamma_2, \rho) \oplus \mathcal{R}(\gamma_{1_1}, \gamma_1, p_1) > \mathcal{R}(\gamma_{1_1}, \gamma_1, p_1) - \varepsilon, p_1 \geq \rho\}.$$

Definition 7. [13] A sequence $\{\gamma_n\}$ in an FPMS $\mathcal{R}(\gamma_1, \gamma_2, \rho)$ converges to $\gamma_1 \in \mathcal{X}$ with respect to T if and only if

$$\lim_{n \to \infty} \mathcal{R}(\gamma_1, \gamma_n, \rho) = \mathcal{R}(\gamma_1, \gamma_1, \rho).$$

Definition 8. [13] A sequence $\{\gamma_n\}$ in an FPMS $\mathcal{R}(\gamma_1, \gamma_2, \rho)$ is called Cauchy if

$$\lim_{n,m \to \infty} \mathcal{R}(\gamma_m, \gamma_n, \rho)$$

exists and finite.

Lemma 1. [13] Let $(\mathcal{X}, \mathcal{R}, \oplus)$ be an FPMS. Then,

i.   If $\mathcal{R}(\gamma_1, \gamma_2, \rho) = 1$, then $\gamma_1 = \gamma_2$.
ii. If $\gamma_1 \neq \gamma_2$, then $\mathcal{R}(\gamma_1, \gamma_2, \rho) < 1$.
iii. If $\gamma_n \to \gamma_3$ with $\mathcal{R}(\gamma_3, \gamma_3, \rho) = 1$, then $\lim_{n \to \infty} \mathcal{R}(\gamma_2, \gamma_n, \rho) = \mathcal{R}(\gamma_2, \gamma_3, \rho)$ for all $\gamma_2 \in \mathcal{X}$.

Definition 9. [22] Let $\mathcal{X}$ be a non-empty set, $\oplus$ be a CTN, $\odot$ be a CTCN and $\mathcal{R}, \mathcal{S}$ be FS on $\mathcal{X}^2$x(0, ∞). A 5-tuple $(\mathcal{X}, \mathcal{R}, \mathcal{S}, \oplus, \odot)$ is said to be an IFMS if the following conditions are satisfied. For all $\gamma_1, \gamma_2, \gamma_3 \in \mathcal{X}$; $\rho, p_1, p_2 > 0$,

i. $0 \leq \mathcal{R}(\gamma_1, \gamma_2, \rho) \leq 1, 0 \leq \mathcal{S}(\gamma_1, \gamma_2, \rho) \leq 1$ and $0 \leq \mathcal{R}(\gamma_1, \gamma_2, \rho) + \mathcal{S}(\gamma_1, \gamma_2, \rho) \leq 1$,
ii. $\mathcal{R}(\gamma_1, \gamma_2, \rho) = 1$ if and only if $\gamma_1 = \gamma_2$,
iii. $\mathcal{R}(\gamma_1, \gamma_2, \rho) = \mathcal{R}(\gamma_2, \gamma_1, \rho)$,
iv.   iv. $\mathcal{R}(\gamma_1, \gamma_2, p_1) \oplus \mathcal{R}(\gamma_2, \gamma_3, \rho) \leq \mathcal{R}(\gamma_1, \gamma_3, \rho + p_1)$,
v. $\mathcal{R}(\gamma_1, \gamma_2, .): [0, \infty) \to [0,1]$ is continuous,
vi.   vi. $\lim_{\varepsilon \to \infty} \mathcal{R}(\gamma_1, \gamma_2, \rho) = 1$,
vii. $\mathcal{S}(\gamma_1, \gamma_2, \rho) = 0$ if and only if $\gamma_1 = \gamma_2$,
viii. $\mathcal{S}(\gamma_1, \gamma_2, \rho) = \mathcal{S}(\gamma_2, \gamma_1, \rho)$,
ix. $\mathcal{S}(\gamma_1, \gamma_2, p_1) \odot \mathcal{S}(\gamma_2, \gamma_3, \rho) \geq \mathcal{S}(\gamma_1, \gamma_3, \rho + p_1)$,

The functions $\mathcal{R}(\gamma_1, \gamma_2, \rho)$ and $\mathcal{S}(\gamma_1, \gamma_2, \rho)$ denote the degrees of nearness, the degrees of non-nearness between γ_1 and γ_2 with respect to ρ; respectively.

Example 1. [22] Let d be a metric such that $d: \mathcal{X}^2 \to [0, \infty)$, $\mathcal{R}$ and $\mathcal{S}$ be two functions on $\mathcal{X}^2 \times [0, \infty)$ such that

$$\mathcal{R}(\gamma_1, \gamma_2, \rho) = \frac{\rho}{\rho + d(\gamma_1, \gamma_2)} \text{ and } \mathcal{S}(\gamma_1, \gamma_2, \rho) = \frac{d(\gamma_1, \gamma_2)}{\rho + d(\gamma_1, \gamma_2)}.$$

Also, if we take $\gamma_1 \oplus \gamma_2 = \min\{\gamma_1, \gamma_2\}$ and $\gamma_1 \odot \gamma_2 = \max\{\gamma_1, \gamma_2\}$. Thus, $(\mathcal{X}, \mathcal{R}, \mathcal{S}, \oplus, \odot)$ satisfies the conditions of IFMS.

Definition 10. [22] Let $(\mathcal{X}, \mathcal{R}, \mathcal{S}, \oplus, \odot)$ be an IFMS and $0 < r < 1$, $\rho > 0$ and $\gamma_1 \in \mathcal{X}$. The set

$$B(\gamma_1, r, \rho) = \{\gamma_2 \in \mathcal{X}: \mathcal{R}(\gamma_1, \gamma_2, \rho) > 1 - r, \mathcal{S}(\gamma_1, \gamma_2, \rho) < r\}$$

is called the open ball with center γ_1 and radius r with respect to ρ.

Remark 1. [22] Let $(\mathcal{X}, \mathcal{R}, \mathcal{S}, \oplus, \odot)$ be an IFMS. Define

$$\tau(\mathcal{R}, \mathcal{S}) = \{A \subset \mathcal{X}: \text{ for each } \gamma_1 \in A, \text{ there exists } \rho > 0 \text{ and } 0 < r < 1 \text{ such that } B(\gamma_1, r, \rho) \subset A\}.$$

Then, $\tau(\mathcal{R}, \mathcal{S})$ is a topology on $\mathcal{X}$.

Lemma 2. [22] Let $(\mathcal{X}, \mathcal{R}, \mathcal{S}, \oplus, \odot)$ be an IFMS. Then, $\mathcal{R}(\gamma_1, \gamma_2, .)$ is non-decreasing and $\mathcal{S}(\gamma_1, \gamma_2, .)$ is non-increasing for all $\gamma_1, \gamma_2 \in \mathcal{X}$.

Theorem 1. [22] Let $(\mathcal{X}, \mathcal{R}, \mathcal{S}, \oplus, \odot)$ be an IFMS. Every open ball $B(\gamma_2, r, \rho)$ in this space is an open set.

Theorem 2. [22] Let $(\mathcal{X}, \mathcal{R}, \mathcal{S}, \oplus, \odot)$ be an IFMS and $\tau(\mathcal{R}, \mathcal{S})$ be a topology on $\mathcal{X}$ induced by the $(\mathcal{X}, \mathcal{R}, \mathcal{S}, \oplus, \odot)$. Then for a sequence $\{\gamma_n\}$ in $(\mathcal{X}, \mathcal{R}, \mathcal{S}, \oplus, \odot)$,

$$\gamma_n \to \gamma_1$$

if and only if

$$\lim_{n \to \infty} \mathcal{R}(\gamma_1, \gamma_n, \rho) = 1 \text{ and } \lim_{n \to \infty} \mathcal{S}(\gamma_1, \gamma_n, \rho) = 0.$$

Definition 11. [22] Let $(\mathcal{X}, \mathcal{R}, \mathcal{S}, \oplus, \odot)$ be an IFMS and $\tau(\mathcal{R}, \mathcal{S})$ be a topology on $\mathcal{X}$ induced by the $(\mathcal{X}, \mathcal{R}, \mathcal{S}, \oplus, \odot)$. Then a sequence $\{\gamma_n\}$ in $(\mathcal{X}, \mathcal{R}, \mathcal{S}, \oplus, \odot)$ is said to be a Cauchy sequence with respect to $\tau(\mathcal{R}, \mathcal{S})$ if for $\rho > 0$, $r \in (0, 1)$, there exists $n_0 \in \mathbb{N}$, n, m $> n_0$ such that

$$\mathcal{R}(\gamma_m, \gamma_n, \rho) \oplus \mathcal{R}(\gamma_m, \gamma_m, \rho) > 1 - r$$

and

$$\mathcal{S}(\gamma_m, \gamma_n, \rho) \odot \mathcal{S}(\gamma_m, \gamma_m, \rho) < r.$$

3. Results

In this section, IFPMS are defined and their basic properties and examples are given. For IFPMS, open ball, convergent sequence, and Cauchy sequence are defined and their basic properties are achieved using the basic definitions and basic properties in Section 2. Furthermore, the relations between IFPMS and classical metric spaces, FMSs, FPMS, and IFMS are analyzed.

Definition 12. Let $\mathcal{X}$ be a non-empty set, $\oplus$ be a CTN, $\odot$ be a CTCN, $\mathcal{R}$ and $\mathcal{S}$ be FSs on $\mathcal{X}^2$x$(0, \infty)$. A 5-tuple $(\mathcal{X}, \mathcal{R}, \mathcal{S}, \oplus, \odot)$ is said to be an IFPMS if the following conditions are satisfied. For all $\gamma_1, \gamma_2, \gamma_3 \in \mathcal{X}$; $\rho, p_1, p_2 > 0$,

i. $0 \leq \mathcal{R}(\gamma_1, \gamma_2, \rho) \leq 1, 0 \leq \mathcal{S}(\gamma_1, \gamma_2, \rho) \leq 1$ and $0 \leq \mathcal{R}(\gamma_1, \gamma_2, \rho) + \mathcal{S}(\gamma_1, \gamma_2, \rho) \leq 1$,

ii. $\mathcal{R}(\gamma_1, \gamma_1, \rho) \geq \mathcal{R}(\gamma_1, \gamma_2, \rho)$,

iii. $\mathcal{R}(\gamma_1, \gamma_2, \rho) = \mathcal{R}(\gamma_2, \gamma_1, \rho)$,

iv. $\mathcal{R}(\gamma_1, \gamma_2, \rho) = \mathcal{R}(\gamma_1, \gamma_1, \rho) = \mathcal{R}(\gamma_2, \gamma_2, \rho)$ if and only if $\gamma_1 = \gamma_2$,

v. $\mathcal{R}(\gamma_1, \gamma_3, p_1) \oplus \mathcal{R}(\gamma_3, \gamma_2, p_2) \leq \mathcal{R}(\gamma_1, \gamma_3, p_1 + p_2) \oplus \mathcal{R}(\gamma_3, \gamma_3, \rho), \rho \geq p_1$ and $\rho \geq p_2$,

vi. $\mathcal{R}(\gamma_1, \gamma_2, .) : [0, \infty) \rightarrow [0,1]$ is continuous,

vii. $\lim_{\rho \to \infty} \mathcal{R}(\gamma_1, \gamma_1, \rho) = 1$,

viii. $\mathcal{S}(\gamma_1, \gamma_1, \rho) \leq \mathcal{S}(\gamma_1, \gamma_2, \rho)$,

ix. $\mathcal{S}(\gamma_1, \gamma_2, \rho) = \mathcal{S}(\gamma_2, \gamma_1, \rho)$,

x. $\mathcal{S}(\gamma_1, \gamma_2, \rho) = \mathcal{S}(\gamma_1, \gamma_1, \rho) = \mathcal{S}(\gamma_2, \gamma_2, \rho)$ if and only if $\gamma_1 = \gamma_2$,

xi. $\mathcal{S}(\gamma_1, \gamma_3, p_1) \odot \mathcal{S}(\gamma_3, \gamma_2, p_2) \geq \mathcal{S}(\gamma_1, \gamma_3, p_1 + p_2) \odot \mathcal{S}(\gamma_3, \gamma_3, \rho), \rho \geq p_1$ and $\rho \geq p_2$,

xii. $\mathcal{S}(\gamma_1, \gamma_2, .) : [0, \infty) \rightarrow [0,1]$ is continuous,

xiii. $\lim_{\rho \to \infty} \mathcal{S}(\gamma_1, \gamma_1, \rho) = 0$,

The functions $\mathcal{R}(\gamma_1, \gamma_2, \rho)$ and $\mathcal{S}(\gamma_1, \gamma_2, \rho)$ denote the degrees of nearness, the degrees of non-nearness between γ_1 and γ_2 with respect to ρ, respectively.

Example 2. Let p be a partial metric such that $p\colon \mathcal{X}^2 \to [0, \infty)$, $\mathcal{R}$ and $\mathcal{S}$ be two functions on $X^2 \times [0, \infty)$ such that

$$\mathcal{R}(\gamma_1, \gamma_2, \rho) = \frac{\rho}{\rho + p(\gamma_1, \gamma_2)} \text{ and } \mathcal{S}(\gamma_1, \gamma_2, \rho) = \frac{p(\gamma_1, \gamma_2)}{\rho + p(\gamma_1, \gamma_2)}.$$

Also, we take $a \oplus b = \min\{\gamma_1, \gamma_2\}$ and $a \odot b = \max\{\gamma_1, \gamma_2\}$. Thus, $(\mathcal{X}, \mathcal{R}, \mathcal{S}, \oplus, \odot)$ satisfies the conditions of IFPMS.

Corollary 1. In Example 2, if we take for all $\gamma_1, \gamma_2 \in \mathcal{X}$,

$$\mathcal{R}(\gamma_1, \gamma_2, \rho) = 1 \text{ and } \mathcal{S}(\gamma_1, \gamma_2, \rho) = 0.$$

then, $(\mathcal{X}, \mathcal{R}, \mathcal{S}, \oplus, \odot)$ satisfies the conditions of IFMS. Thus, from Definition 13 and Definition 9, every IFMS is also an IFPMS.

Corollary 2. From Example 2, we can obtain an IFPMS from every partial metric space.

Example 3. In Example 1, if we take for all $p_1 \in [0, \infty)$,

$$\mathcal{R}(\gamma_1, \gamma_2, \rho) = \frac{\rho + p_1}{\rho + p_1 + d(\gamma_1, \gamma_2)} \text{ and } \mathcal{S}(\gamma_1, \gamma_2, \rho) = \frac{d(\gamma_1, \gamma_2)}{\rho + p_1 + d(\gamma_1, \gamma_2)}$$

instead of

$$\mathcal{R}(\gamma_1, \gamma_2, \rho) = \frac{\rho}{\rho + d(\gamma_1, \gamma_2)} \text{ and } \mathcal{S}(\gamma_1, \gamma_2, \rho) = \frac{d(\gamma_1, \gamma_2)}{t + d(\gamma_1, \gamma_2)}$$

then, $(\mathcal{X}, \mathcal{R}, \mathcal{S}, \oplus, \odot)$ satisfies the conditions of IFPMS.

Corollary 3. From Example 3, we can obtain an IFPMS from every IFMS.

Definition 13. Let $(\mathcal{X}, \mathcal{R}, \mathcal{S}, \oplus, \odot)$ be an IFPMS and

$$0 \leq \mathcal{S}(\gamma_1, \gamma_1, \rho) < r < \mathcal{R}(\gamma_1, \gamma_1, \rho), p_1 \geq \rho > 0 \text{ and } \gamma_1 \in \mathcal{X}.$$

The set

$$B(\gamma_1, \gamma_2, \rho) = \{\gamma_1 \in \mathcal{X} : \mathcal{R}(\gamma_1, \gamma_2, \rho) \oplus \mathcal{R}(\gamma_1, \gamma_1, \rho) > \mathcal{R}(\gamma_1, \gamma_1, \rho) - r,$$
$$\mathcal{S}(\gamma_1, \gamma_2, \rho) \odot \mathcal{S}(\gamma_1, \gamma_1, \rho) < \mathcal{S}(\gamma_1, \gamma_1, \rho) + r\}$$

is called the open ball with center γ_2 and radius r with respect to ρ.

Corollary 4: In Definition 13, if we take for all $\gamma_1, \gamma_2 \in \mathcal{X}$,

$$\mathcal{R}(\gamma_1, \gamma_2, \rho) = 1 \text{ and } \mathcal{S}(\gamma_1, \gamma_2, \rho) = 0$$

then, $(\mathcal{X}, \mathcal{R}, \mathcal{S}, \oplus, \odot)$ satisfies the conditions in Definition 10 for IFMS.

Remark 2. Let $(\mathcal{X}, \mathcal{R}, \mathcal{S}, \oplus, \odot)$ be an IFPMS. Define

$\tau(\mathcal{R}, \mathcal{S}) = \{A \subset \mathcal{X}: \text{for each } \gamma_1 \in A, \text{ there exists } \rho > 0 \text{ and}$

$0 \leq \mathcal{S}(\gamma_1, \gamma_1, \rho) < r < \mathcal{R}(\gamma_1, \gamma_1, \rho) \text{ such that } B(\gamma_1, \gamma_2, \rho) \subset A\}$.

Then, $\tau(\mathcal{R}, \mathcal{S})$ is a topology on $\mathcal{X}$.

Lemma 3. Let $(\mathcal{X}, \mathcal{R}, \mathcal{S}, \oplus, \odot)$ be an IFPMS. Then, $\mathcal{R}(\gamma_1, \gamma_2, .)$ is non-decreasing and $\mathcal{S}(\gamma_1, \gamma_2, .)$ is non-increasing for all $\gamma_1, \gamma_2 \in \mathcal{X}$.

Proof.

Assume that $\mathcal{R}$ is strictly decreasing. Then,

$$\mathcal{R}(\gamma_1, \gamma_2, p_1) < \mathcal{R}(\gamma_1, \gamma_2, p_2) \text{ for } 0 < p_2 < p_1 \text{ and } \mathcal{R}(\gamma_2, \gamma_2, p_1) < \mathcal{R}(\gamma_2, \gamma_2, p_1 - p_2). \quad (1)$$

From Definition 12, we get

$$\mathcal{R}(\gamma_1, \gamma_2, p_1) \oplus \mathcal{R}(\gamma_2, \gamma_2, p_1) \geq \mathcal{R}(\gamma_1, \gamma_2, p_2) \oplus \mathcal{R}(\gamma_2, \gamma_2, p_1 - p_2). \quad (2)$$

From Definition 3 and (1), we have

$$\mathcal{R}(\gamma_1, \gamma_2, p_1) \oplus \mathcal{R}(\gamma_2, \gamma_2, p_1) \leq \mathcal{R}(\gamma_2, \gamma_2, p_2) \oplus \mathcal{R}(\gamma_2, \gamma_2, p_1 - p_2). \quad (3)$$

where there is a contradiction because of (1), (2), and (3).

Hence, $\mathcal{R}(\gamma_1, \gamma_2, .)$ is non-decreasing.

Assume that $\mathcal{S}$ is strictly increasing. Then

$$\mathcal{S}(\gamma_1, \gamma_2, p_1) > \mathcal{S}(\gamma_1, \gamma_2, p_2) \text{ for } 0 < p_2 < p_1 \text{ and } \mathcal{S}(\gamma_2, \gamma_2, p_1) > \mathcal{S}(\gamma_2, \gamma_2, p_1 - p_2). \quad (4)$$

From Definition 12, we obtain

$$\mathcal{S}(\gamma_1, \gamma_2, p_1) \odot \mathcal{S}(\gamma_2, \gamma_2, p_1) \leq \mathcal{S}(\gamma_1, \gamma_2, p_2) \odot \mathcal{S}(\gamma_2, \gamma_2, p_1 - p_2). \quad (5)$$

From Definition 4 and (5), we obtain

$$\mathcal{S}(\gamma_1, \gamma_2, p_1) \odot \mathcal{S}(\gamma_2, \gamma_2, p_1) \geq \mathcal{S}(\gamma_1, \gamma_2, p_2) \odot (\gamma_2, \gamma_2, p_1 - p_2). \quad (6)$$

where there is a contradiction because of (4), (5), and (6).

Hence, $\mathcal{S}(\gamma_1, \gamma_2, .)$ is non-increasing.

Theorem 3. Let $(\mathcal{X}, \mathcal{R}, \mathcal{S}, \oplus, \odot)$ be an IFPMS. Every open ball $B(\gamma_2, r, \rho)$ in this space is an open set.

Proof. We assume that

$$\gamma_1 \in B(\gamma_2, r, \rho).$$

Since $B(\gamma_2, r, \rho)$ is an open ball in $(\mathcal{X}, \mathcal{R}, \mathcal{S}, \oplus, \odot)$, then

$$\mathcal{R}(\gamma_1, \gamma_2, \rho) \oplus \mathcal{R}(\gamma_1, \gamma_1, \rho_1) > \mathcal{R}(\gamma_1, \gamma_1, \rho_1) - r$$

and

$$\mathcal{S}(\gamma_1, \gamma_2, \rho) \odot \mathcal{S}(\gamma_1, \gamma_1, \rho_1) < \mathcal{S}(\gamma_1, \gamma_1, \rho_1) + r$$

for $\rho_1 \geq \rho > 0$. From Lemma 3, since $\mathcal{R}(\gamma_1, \gamma_2, .)$ is non-decreasing, $\mathcal{S}(\gamma_1, \gamma_2, .)$ is non-increasing, there exists $\rho_2 \in (0, \rho)$ such that

$$\mathcal{R}(\gamma_1, \gamma_2, \rho_2) \oplus \mathcal{R}(\gamma_1, \gamma_1, \rho_1) > \mathcal{R}(\gamma_1, \gamma_1, \rho_1) - r$$

and

$$\mathcal{S}(\gamma_1, \gamma_2, \rho_2) \odot \mathcal{S}(\gamma_1, \gamma_1, \rho_1) < \mathcal{S}(\gamma_1, \gamma_1, \rho_1) + r.$$

We assume that $r_1 = \mathcal{R}(\gamma_1, \gamma_2, \rho_2) \oplus \mathcal{R}(\gamma_1, \gamma_1, \rho_1)$. Since $r_1 > \mathcal{R}(\gamma_1, \gamma_1, \rho_1) - r$, there exist $r_2 \in (0, 1)$ such that

$$r_1 > \mathcal{R}(\gamma_1, \gamma_1, \rho_1) - r_2 > \mathcal{R}(\gamma_1, \gamma_1, \rho_1) - r.$$

Thus, there exist $r_3, r_4 \in (0, 1)$ such that

$$r_1 \oplus r_3 > \mathcal{R}(\gamma_1, \gamma_1, \rho_1) - r_2 \text{ and } (\mathcal{S}(\gamma_1, \gamma_1, \rho_1) - r_1)\odot(\mathcal{S}(\gamma_1, \gamma_1, \rho_1) - r_4) \leq r_2.$$

We assume that $r_5 = \max\{r_3, r_4\}$ and $B(\gamma_1, \mathcal{R}(\gamma_1, \gamma_1, \rho_1) - r_5, \rho - \rho_2)$ is an open ball. We claim that

$$B(\gamma_1, \mathcal{R}(\gamma_1, \gamma_1, \rho_1) - r_5, \rho - \rho_2) \subset B(\gamma, r, \rho).$$

We assume that $\gamma_3 \in B(\gamma_1, \mathcal{R}(\gamma_1, \gamma_1, \rho_1) - r_5, \rho - \rho_2)$. Hence, we obtain

$$\mathcal{R}(\gamma_3, \gamma_2, \rho - \rho_2) > r_5 \text{ and } \mathcal{S}(\gamma_3, \gamma_2, \rho_2) < 2\mathcal{R}(\gamma_1, \gamma_1, \rho - \rho_2) - r_5.$$

Thus, we get

$$\mathcal{R}(\gamma_3,\gamma_2,\rho) \oplus \mathcal{R}(\gamma_1,\gamma_1,\rho_1) \geq \mathcal{R}(\gamma_3,\gamma_1,\rho_2) \oplus \mathcal{R}(\gamma_1,\gamma_2,\rho-\rho_2)$$

$$\geq r_1 \oplus r_5$$

$$\geq r_1 \oplus r_3$$

$$\geq \mathcal{R}(\gamma_1,\gamma_1,\rho_1) - r_2$$

$$> \mathcal{R}(\gamma_1,\gamma_1,\rho_1) - r$$

and

$$\mathcal{S}(\gamma_3,\gamma_2,\rho) \odot \mathcal{S}(\gamma_1,\gamma_1,\rho_1) \leq \mathcal{S}(\gamma_3,\gamma_1,\rho_2) \odot \mathcal{S}(\gamma_1,\gamma_2,\rho-\rho_2)$$

$$\leq (\mathcal{S}(\gamma_1,\gamma_1,\rho_1) - r_1) \odot (\mathcal{S}(\gamma_1,\gamma_1,\rho_1) - r_5)$$

$$\leq (\mathcal{S}(\gamma_1,\gamma_1,\rho_1) - r_1) \odot (\mathcal{S}(\gamma_1,\gamma_1,\rho_1) - r_4)$$

$$\leq r_2$$

$$< r$$

$$< \mathcal{S}(\gamma_1,\gamma_1,\rho_1) + r.$$

Therefore, we obtain

$$\gamma_3 \in B(\gamma_2, r, \rho).$$

Hence, we get

$$B(\gamma_1, \mathcal{R}(\gamma_1,\gamma_1,\rho_1) - r_5, \rho - \rho_2) \subset B(\gamma, r, \rho).$$

Corollary 5. Let $(\mathcal{X}, \mathcal{R}, \mathcal{S}, \oplus, \odot)$ be an IFPMS. The set

$$\tau(\mathcal{R}, \mathcal{S}) = \{A \subset \mathcal{X} : \text{for each } \gamma_1 \in A, \text{ there exists } \rho > 0 \text{ and } 0 \leq \mathcal{S}(\gamma_1,\gamma_1,\rho) < r < \mathcal{R}(\gamma_1,\gamma_1,\rho)$$

such that $B(\gamma_2, r, \rho) \subset A\}.$

is a topology on $\mathcal{X}$.

Theorem 4. Let $(\mathcal{X}, \mathcal{R}, \mathcal{S}, \oplus, \odot)$ be an IFPMS and $\tau(\mathcal{R}, \mathcal{S})$ be a topology on $\mathcal{X}$ induced by the $(\mathcal{X}, \mathcal{R}, \mathcal{S}, \oplus, \odot)$. Then for a sequence $\{\gamma_n\}$ in $(\mathcal{X}, \mathcal{R}, \mathcal{S}, \oplus, \odot)$,

$\gamma_n \rightarrow \gamma_1$

if and only if

$$\lim_{n \to \infty} \mathcal{R}(\gamma_1, \gamma_n, \rho) = \mathcal{R}(\gamma_1, \gamma_1, \rho) \text{ and } \lim_{n \to \infty} \mathcal{S}(\gamma_1, \gamma_n, \rho) = \mathcal{S}(\gamma_1, \gamma_1, \rho).$$

Proof. We assume that for $\rho > 0$,

$$\gamma_n \rightarrow \gamma_1.$$

Then for $r \in (0, 1)$, there exists $n_0 \in \mathbb{N}$, $n > n_0$ such that

$$\gamma_n \in \mathrm{B}(\gamma_1, r, \rho).$$

Hence, we get

$$\mathcal{R}(\gamma_1, \gamma_n, \rho) \oplus \mathcal{R}(\gamma_1, \gamma_1, \rho) > \mathcal{R}(\gamma_1, \gamma_1, \rho) - r$$

and

$$\mathcal{S}(\gamma_1, \gamma_n, \rho) \odot \mathcal{S}(\gamma_1, \gamma_1, \rho) < \mathcal{S}(\gamma_1, \gamma_1, \rho) + r.$$

Thus, we obtain

$$\mathcal{R}(\gamma_1, \gamma_1, \rho) - \mathcal{R}(\gamma_1, \gamma_n, \rho) \oplus \mathcal{R}(\gamma_1, \gamma_1, \rho) < r$$

and

$$\mathcal{S}(\gamma_1, \gamma_n, \rho) \odot \mathcal{S}(\gamma_1, \gamma_1, \rho) - \mathcal{S}(\gamma_1, \gamma_1, \rho) < r.$$

From Definition 12, clearly

$$\mathcal{R}(\gamma_1, \gamma_n, \rho) \leq \mathcal{R}(\gamma_1, \gamma_1, \rho) \leq 1$$

and from Definition 12, clearly

$$\mathcal{R}(\gamma_1, \gamma_n, \rho) \oplus \mathcal{R}(\gamma_1, \gamma_1, \rho) \leq \mathcal{R}(\gamma_1, \gamma_1, \rho).$$

Hence, we have

$$\mathcal{R}(\gamma_1, \gamma_1, \rho) - \mathcal{R}(\gamma_1, \gamma_n, \rho) \oplus \mathcal{R}(\gamma_1, \gamma_1, \rho) < \mathcal{R}(\gamma_1, \gamma_1, \rho) - \mathcal{R}(\gamma_1, \gamma_n, \rho) < r.$$

Since $\gamma_n \rightarrow \gamma_1$, we obtain

$$\mathcal{R}(\gamma_1, \gamma_1, \rho) - \mathcal{R}(\gamma_1, \gamma_n, \rho) = 0.$$

Hence,

$$\mathcal{R}(\gamma_1, \gamma_1, \rho) \rightarrow \mathcal{R}(\gamma_1, \gamma_n, \rho).$$

From Definition 12, clearly

$$\mathcal{S}(\gamma_1, \gamma_n, \rho) \leq \mathcal{S}(\gamma_1, \gamma_n, \rho),$$

$$0 \leq (\gamma_1, \gamma_1, \rho),$$

and from Definition 12, clearly

$$\mathcal{S}(\gamma_1, \gamma_n, \rho) \leq \mathcal{S}(\gamma_1, \gamma_n, \rho) \odot \mathcal{S}(\gamma_1, \gamma_1, \rho).$$

Hence, we have

$$\mathcal{S}(\gamma_1, \gamma_n, \rho) \odot \mathcal{S}(\gamma_1, \gamma_1, \rho) - \mathcal{S}(\gamma_1, \gamma_1, \rho) < \mathcal{S}(\gamma_1, \gamma_n, \rho) - \mathcal{S}(\gamma_1, \gamma_1, \rho) < r.$$

Since $\gamma_n \rightarrow \gamma_1$, we obtain

$$\mathcal{S}(\gamma_1, \gamma_n, \rho) - \mathcal{S}(\gamma_1, \gamma_1, \rho) = 0.$$

Hence,

$$\mathcal{S}(\gamma_1, \gamma_n, \rho) \rightarrow \mathcal{S}(\gamma_1, \gamma_1, \rho).$$

Conversely, we assume that

$$\lim_{n \to \infty} \mathcal{R}(\gamma_1, \gamma_n, \rho) = \mathcal{R}(\gamma_1, \gamma_1, \rho), \ \lim_{n \to \infty} \mathcal{S}(\gamma_1, \gamma_n, \rho) = \mathcal{S}(\gamma_1, \gamma_1, \rho)$$

and

$$\lim_{n \to \infty} \mathcal{H}(\gamma_1, \gamma_n, \rho) = \mathcal{H}(\gamma_1, \gamma_1, \rho).$$

Thus, for r ∈ (0, 1), there exists there exists $n_0 \in \mathbb{N}$, n > n_0 such that

$$\mathcal{R}(\gamma_1, \gamma_1, \rho) - \mathcal{R}(\gamma_1, \gamma_n, \rho) < r \text{ and } < \mathcal{S}(\gamma_1, \gamma_n, \rho) - \mathcal{S}(\gamma_1, \gamma_1, \rho) < r.$$

Since

$$\mathcal{R}(\gamma_1, \gamma_n, \rho) \oplus \mathcal{R}(\gamma_1, \gamma_1, \rho) \leq \mathcal{R}(\gamma_1, \gamma_1, \rho) \text{ and } (\gamma_1, \gamma_n, \rho) \leq \mathcal{S}(\gamma_1, \gamma_n, \rho) \odot \mathcal{S}(\gamma_1, \gamma_1, \rho),$$

we obtain

$$\mathcal{R}(\gamma_1, \gamma_1, \rho) - \mathcal{R}(\gamma_1, \gamma_n, \rho) \oplus \mathcal{R}(\gamma_1, \gamma_1, \rho) < r$$

and

$$\mathcal{S}(\gamma_1,\gamma_n,\rho) \odot \mathcal{S}(\gamma_1,\gamma_1,\rho) - \mathcal{S}(\gamma_1,\gamma_1,\rho) < r.$$

Thus, from Definition 13, we get

$$\gamma_n \in \mathrm{B}(\gamma_1,r,\rho) \text{ and } \gamma_n \to \gamma_1.$$

Lemma 4. Let $(\mathcal{X}, \mathcal{R}, \mathcal{S}, \oplus, \odot)$ be an IFPMS. Then,

i. If $\mathcal{R}(\gamma_1,\gamma_2,\rho) = 1$ and $\mathcal{S}(\gamma_1,\gamma_2,\rho) = 0$, then $\gamma_1 = \gamma_2$.

ii. If $\gamma_1 \neq \gamma_2$, then $\mathcal{R}(\gamma_1,\gamma_2,\rho) < 1$ and $\mathcal{S}(\gamma_1,\gamma_2,\rho) > 0$

iii. If $\gamma_n \to \gamma_3$ with $\mathcal{R}(\gamma_3,\gamma_3,\rho) = 1$ and $\mathcal{S}(\gamma_3,\gamma_3,\rho) = 0$, then
$$\lim_{n\to\infty} \mathcal{R}(\gamma_n,\gamma_2,\rho) = \mathcal{R}(\gamma_3,\gamma_2,\rho) \text{ and } \lim_{n\to\infty} \mathcal{S}(\gamma_n,\gamma_2,\rho) = \mathcal{S}(\gamma_3,\gamma_2,\rho)$$

for all $\gamma_2 \in \mathcal{X}$.

Proof.

i) From Definition 12, clearly,

$$\mathcal{R}(\gamma_1,\gamma_2,\rho) \leq 1, \mathcal{R}(\gamma_1,\gamma_1,\rho) \geq \mathcal{R}(\gamma_1,\gamma_2,\rho) \text{ and } \mathcal{R}(\gamma_2,\gamma_2,\rho) \geq \mathcal{R}(\gamma_1,\gamma_2,\rho).$$

If $\mathcal{R}(\gamma_1,\gamma_2,\rho) = 1$, then

$$\mathcal{R}(\gamma_1,\gamma_1,\rho) \geq \mathcal{R}(\gamma_1,\gamma_2,\rho) = 1.$$

Hence, we get

$$\mathcal{R}(\gamma_1,\gamma_1,\rho) = 1.$$

Similarly,

If $\mathcal{R}(\gamma_1,\gamma_2,\rho) = 1$, then

$$\mathcal{R}(\gamma_2,\gamma_2,\rho) \geq \mathcal{R}(\gamma_1,\gamma_2,\rho) = 1.$$

Thus, we obtain

$$\mathcal{R}(\gamma_2,\gamma_2,\rho) = 1.$$

Therefore,

$$\mathcal{R}(\gamma_1,\gamma_2,\rho) = \mathcal{R}(\gamma_1,\gamma_1,\rho) = \mathcal{R}(\gamma_2,\gamma_2,\rho) = 1.$$

From Definition 12, we obtain

$$\gamma_1 = \gamma_2.$$

Similarly, we get

$$0 \leq \mathcal{S}(\gamma_1, \gamma_2, \rho), \mathcal{S}(\gamma_2, \gamma_2, \rho) \leq \mathcal{S}(\gamma_1, \gamma_2, \rho) \text{ and } \mathcal{S}(\gamma_1, \gamma_1, \rho) \leq \mathcal{S}(\gamma_1, \gamma_2, \rho).$$

If $\mathcal{S}(\gamma_1, \gamma_2, \rho) = 0$, then

$$\mathcal{S}(\gamma_1, \gamma_1, \rho) \leq \mathcal{S}(\gamma_1, \gamma_2, \rho) = 0.$$

Thus,

$$\mathcal{S}(\gamma_1, \gamma_1, \rho) = 0.$$

If $\mathcal{S}(\gamma_1, \gamma_2, \rho) = 0$, then

$$\mathcal{S}(\gamma_2, \gamma_2, \rho) \leq \mathcal{S}(\gamma_1, \gamma_2, \rho) = 0.$$

Thus,

$$\mathcal{S}(\gamma_2, \gamma_2, \rho) = 0.$$

Therefore,

$$\mathcal{S}(\gamma_1, \gamma_2, \rho) = \mathcal{S}(\gamma_1, \gamma_1, \rho) = \mathcal{S}(\gamma_2, \gamma_2, \rho) = 0.$$

From Definition 12, we obtain

$$\gamma_1 = \gamma_2.$$

ii) Let $\gamma_1 \neq \gamma_2$. We assume that

$$\mathcal{R}(\gamma_1, \gamma_2, \rho) \geq 1 \text{ and } \mathcal{S}(\gamma_1, \gamma_2, \rho) \leq 0.$$

Thus, From Definition 12,

$$\mathcal{R}(\gamma_1, \gamma_2, \rho) = 1 \text{ and } \mathcal{S}(\gamma_1, \gamma_2, \rho) = 0 \tag{7}$$

since $\mathcal{R}(\gamma_1, \gamma_2, \rho), \mathcal{S}(\gamma_1, \gamma_2, \rho) \in [0, 1]$.

From (7) and i), we obtain $\gamma_1 = \gamma_2$. $\tag{8}$

where there is a contradiction because of (7) and (8).

Hence,

$$\mathcal{R}(\gamma_1,\gamma_2,\rho) <1 \text{ and } \mathcal{S}(\gamma_1,\gamma_2,\rho) > 0.$$

iii) From Theorem 4, if $\gamma_n \rightarrow \gamma_3$, then

$$\lim_{n\rightarrow\infty} \mathcal{R}(\gamma_3,\gamma_n,\rho) = \mathcal{R}(\gamma_3,\gamma_3,\rho) \text{ and } \lim_{n\rightarrow\infty} \mathcal{S}(\gamma_3,\gamma_n,\rho) = \mathcal{S}(\gamma_3,\gamma_3,\rho).$$

Thus, since

$$\mathcal{R}(\gamma_3,\gamma_3,\rho) = 1 \text{ and } \mathcal{S}(\gamma_3,\gamma_3,\rho) = 0,$$

we obtain

$$\lim_{n\rightarrow\infty} \mathcal{R}(\gamma_3,\gamma_n,\rho) = 1 \text{ and } \lim_{n\rightarrow\infty} \mathcal{S}(\gamma_3,\gamma_n,\rho) = 0. \tag{9}$$

From Definition 12, we obtain

$$\mathcal{R}(\gamma_n,\gamma_3,\rho) \oplus \mathcal{R}(\gamma_3,\gamma_n,\rho) \leq \mathcal{R}(\gamma_n,\gamma_n,2\rho) \oplus \mathcal{R}(\gamma_3,\gamma_3,\rho). \tag{10}$$

Also, from (9) and (10), it is held that

$$1 \oplus 1 \leq \mathcal{R}(\gamma_n,\gamma_n,2\rho) \oplus 1.$$

From Definition 3, clearly

$$\mathcal{R}(\gamma_n,\gamma_n,2\rho) = 1. \tag{11}$$

Also, from Definition 12 and for $p_1 - \rho \leq \rho$ and $0 <\rho < p_1$, we have

$$\mathcal{R}(\gamma_2,\gamma_3,p_1 - \rho) \oplus \mathcal{R}(\gamma_3,\gamma_n,\rho) \leq \mathcal{R}(\gamma_2,\gamma_n,\rho) \oplus \mathcal{R}(\gamma_3,\gamma_3,\rho)$$

and

$$\mathcal{R}(\gamma_2,\gamma_n,\rho) \oplus \mathcal{R}(\gamma_n,\gamma_3,\rho) \leq \mathcal{R}(\gamma_2,\gamma_3,2\rho) \oplus \mathcal{R}(\gamma_n,\gamma_n,2\rho). \tag{12}$$

From (9), (11) and (12), we obtain

$$\mathcal{R}(\gamma_2,\gamma_3,p_1 - \rho) \leq \mathcal{R}(\gamma_2,\gamma_n,\rho)$$

and

$$\mathcal{R}(\gamma_2,\gamma_n,\rho) \leq \mathcal{R}(\gamma_2,\gamma_3,2\rho) \tag{13}$$

since $\mathcal{R}(\gamma_1,\gamma_2,.): [0,\infty) \rightarrow [0,1]$ is continuous. From (13), we obtain

$$\mathcal{R}(\gamma_3, \gamma_2, \rho) \leq \lim_{n \to \infty} \mathcal{R}(\gamma_n, \gamma_2, \rho)$$

and

$$\lim_{n \to \infty} \mathcal{R}(\gamma_n, \gamma_2, \rho) \leq \mathcal{R}(\gamma_3, \gamma_2, \rho).$$

Hence, we get

$$\lim_{n \to \infty} \mathcal{R}(\gamma_n, \gamma_2, \rho) = \mathcal{R}(\gamma_3, \gamma_2, \rho).$$

Also, similarly, we have

$$\lim_{n \to \infty} \mathcal{S}(\gamma_n, \gamma_2, \rho) = \mathcal{S}(\gamma_3, \gamma_2, \rho)$$

for all $\gamma_2 \in \mathcal{X}$.

Corollary 6. In Lemma 4, if we take for all $\gamma_1, \gamma_2 \in \mathcal{X}$,

$$\mathcal{R}(\gamma_1, \gamma_2, \rho) = 1 \text{ and } \mathcal{S}(\gamma_1, \gamma_2, \rho) = 0$$

then, $(\mathcal{X}, \mathcal{R}, \mathcal{S}, \oplus, \odot)$ satisfies the conditions for IFMS.

Definition 14. Let $(\mathcal{X}, \mathcal{R}, \mathcal{S}, \oplus, \odot)$ be an IFPMS and $\tau(\mathcal{R}, \mathcal{S})$ be a topology on $\mathcal{X}$ induced by the $(\mathcal{X}, \mathcal{R}, \mathcal{S}, \oplus, \odot)$.

a) Then a sequence $\{\gamma_n\}$ in $(\mathcal{X}, \mathcal{R}, \mathcal{S}, \oplus, \odot)$ is said to be a Cauchy sequence with respect to $\tau(\mathcal{R}, \mathcal{S})$ if for $\rho > 0$, $r \in (0, 1)$, there exists $n_0 \in \mathbb{N}$; n, m $> n_0$ such that

$$\mathcal{R}(\gamma_m, \gamma_n, \rho) \oplus \mathcal{R}(\gamma_m, \gamma_m, \rho) > \mathcal{R}(\gamma_m, \gamma_m, \rho) - r$$

and

$$\mathcal{S}(\gamma_m, \gamma_n, \rho) \odot \mathcal{S}(\gamma_m, \gamma_m, \rho) < \mathcal{S}(\gamma_m, \gamma_m, \rho) + r.$$

b) $(\mathcal{X}, \mathcal{R}, \mathcal{S}, \oplus, \odot)$ is called complete if every Cauchy sequence is convergent in this space.

Corollary 7. Let $(\mathcal{X}, \mathcal{R}, \mathcal{S}, \oplus, \odot)$ be an IFPMS and $\tau(\mathcal{R}, \mathcal{S})$ be a topology on $\mathcal{X}$ induced by the $(\mathcal{X}, \mathcal{R}, \mathcal{S}, \oplus, \odot)$. Then a sequence $\{\gamma_n\}$ in $(\mathcal{X}, \mathcal{R}, \mathcal{S}, \oplus, \odot)$ is said to be a Cauchy with respect to $\tau(\mathcal{R}, \mathcal{S})$ if

$$\lim_{n,m \to \infty} \mathcal{R}(\gamma_m, \gamma_n, \rho) \text{ and } \lim_{n,m \to \infty} \mathcal{S}(\gamma_m, \gamma_n, \rho)$$

exists and finite.

4. Conclusion

In this paper, IFPMS are defined and their basic properties and examples are achieved. For IFPMS, open ball, convergent sequence, and Cauchy sequence are defined and their basic properties are obtained. Furthermore, the relations between IFPMS and classical metric spaces, FMSs, FPMS, and IFMS are analyzed.

Thanks to this paper, researchers can define some partial metric spaces based on IFS. For example, researchers can define intuitionistic fuzzy partial G-metric spaces, intuitionistic fuzzy partial m-metric spaces, and intuitionistic fuzzy partial b-metric spaces. Also, Researchers can introduce new fixed point theories for these new types of metrics. Furthermore, researchers can define intuitionistic fuzzy partial normed space and neutrosophic partial metric space by taking advantage of IFPMS.

Abbreviations

Continuous t-conorm: CTCN

Continuous t-norm: CTN

Intuitionistic Fuzzy Partial Metric Spaces: IFPMS

Intuitionistic Fuzzy Metric Spaces: IFMS

Fuzzy Partial Metric Spaces: FPMS

Fuzzy Metric Spaces: FMS

Intuitionistic Fuzzy Sets: IFS

Fuzzy Sets: FS

Fuzzy Logic: FL

Fixed Point Theorem: FPT

References

[1] Matthews, S.G., *Partial metric topology*, Annals of the New York Academy of Sciences, 728(1), 183–197, 1994.

[2] Zadeh, L.A., *Fuzzy sets*, Information and Control, 8(3), 338–353, 1965.

[3] Emniyet, A., & Şahin, M., *Fuzzy normed rings*, Symmetry, 10(10), 515, 2018.

[4] Kum, G., Sönmez, M.E., & Kargın, A., *An Alternative Process for Determining Erosion Risk: The Fuzzy Method*, Coğrafya Dergisi, 44, 219–229, 2022.

[5] Wang, D., Yuan, Y., Liu, Z., Zhu, S., & Sun, Z., *Novel Distance Measures of q-Rung Orthopair Fuzzy Sets and Their Applications*, Symmetry, 16(5), 574, 2024.

[6] Xu, K., & Wang, Y., *A Novel Fuzzy Bi-Clustering Algorithm with Axiomatic Fuzzy Set for Identification of Co-Regulated Genes*, Mathematics, 12(11), 1659, 2024.

[7] Plebankiewicz, E., & Karcińska, P., *Model for supporting construction workforce planning based on the theory of fuzzy sets*, Applied Sciences, 14(4), 1655, 2024.

[8] Kramosil, I., & Michálek, J., *Fuzzy metrics and statistical metric spaces*, Kybernetika, 11(5), 336–344, 1975.

[9] Grabiec, M., *Fixed points in fuzzy metric spaces*, Fuzzy Sets and Systems. 27, 385–389, 1989.

[10] Shukla, S., Dubey, N., & Miñana, J.J., *Vector-Valued Fuzzy Metric Spaces and Fixed Point Theorems*, Axioms, 13(4), 252, 2024.

[11] Gregori, V., Miñana, J.J., Roig, B., & Sapena, A., *On Completeness and Fixed Point Theorems in Fuzzy Metric Spaces*, Mathematics, 12(2), 287, 2024.

[12] Huang, H., *Properties of several metric spaces of fuzzy sets*. Fuzzy Sets and Systems. 475, 108745, 2024.

[13] Olgun, N., Şahin, M., Kargın, A., and Uluçay, V., *"Fuzzy generalized Meir-Keeler-type contraction on fuzzy partial metric space"*, in Proceedings of the Eighth International Conference on Soft Computing, Computing with Words and Perceptions in System Analysis, Decision and Control, 2015.

[14] Gregori, V., Minana, J.J., Miravet, D. *Fuzzy partial metric spaces*, International Journal of General Systems, 48, 260–279, 2019.

[15] Amer, F. J., *"Fuzzy partial metric spaces"*, in Proceedings of the Computational Analysis:AMAT, Selected Contributions, Springer International Publishing, 185–191, 2016.

[16] Aygün, H., Güner, E., Miñana, J.J., & Valero, O., *Fuzzy partial metric spaces and fixed point theorems*, Mathematics, 10(17), 3092, 2022.

[17] Gregori, V., Miñana, J.J., & Miravet, D., *A duality relationship between fuzzy partial metrics and fuzzy quasi-metrics*, Mathematics, 8(9), 1575, 2020.

[18] Atanassov, T.K., *Intuitionistic Fuzzy Sets*, Fuzzy Sets and Systems, 20, 87–96, 1986.

[19] Ngan, S.C., *An extension framework for creating operators and functions for intuitionistic fuzzy sets*, Information Sciences, 666, 120336, 2024.

[20] Gerogiannis, V. C., Tzimos, D., Kakarontzas, G., Tsoni, E., Iatrellis, O., Son, L.H., et al., *An Approach Based on Intuitionistic Fuzzy Sets for Considering Stakeholders' Satisfaction, Dissatisfaction, and Hesitation in Software Features Prioritization*, Mathematics, 12(5), 680, 2024.

[21] Rajafillah, C., El Moutaouakil, K., Patriciu, A.M., Yahyaouy, A., & Riffi, J., *INT-FUP: Intuitionistic Fuzzy Pooling*, Mathematics, 12(11), 1740, 2024.

[22] Park, J.H., *Intuitionistic fuzzy metric spaces*, Chaos, Solitons Fractals, 22(5), 1039–1046, 2004.

[23] Alaca, C., Turkoglu, D., & Yildiz, C., *Fixed points in intuitionistic fuzzy metric spaces*, Chaos, Solitons Fractals, 29(5), 1073–1078, 2006.

[24] Gregori, V., Romaguera, S., & Veeramani, P., *A note on intuitionistic fuzzy metric spaces*, Chaos, Solitons Fractals, 28(4), 902–905, 2006.

[25] Rahmat, R.S., & Noorani, S.M., *Fixed point theorem on intuitionistic fuzzy metric spaces*, Iranian Journal of Fuzzy Systems, 3(1), 23–29, 2006.

[26] Saadati, R., Sedghi, S., & Shobe, N., *Modified intuitionistic fuzzy metric spaces and some fixed point theorems*, Chaos, Solitons Fractals, 38(1), 36–47, 2008.

[27] Wong, K. S., Salleh, Z., & Akhadkulov, H., *Exploring Fixed Points and Common Fixed Points of Contractive Mappings in Complex-Valued Intuitionistic Fuzzy Metric Spaces*, International Journal of Analysis and Applications, 22, 91–91, 2024.

[28] Singh, R.M., Singh, D., & Gourh, R., *Approach to fuzzy differential equations in Intuitionistic fuzzy metric spaces using generalized contraction theorems*, Journal of Hyperstructures, 13(1), 109-123, 2024.

[29] Schweizer B, Sklar A., *Statistical metric spaces*, Pacific Journal of Mathematics, 10, 314–340, 1960.

Quantitative Modeling of Treatment and Vaccination Effects on the Dynamics of Cholera Transmission

Kazeem Abidoye ODEYEMI[1,*], Mutairu Kayode KOLAWOLE [2]

[1]*Osun State University, Faculty of Basic and Applied Sciences, Department of Mathematical Sciences, 4490, Osogbo, Nigeria*
abidoyekazeem1@gmail.com, ORCID: 0009-0008-0345-5664
[2]*Osun State University, Faculty of Basic and Applied Sciences, Department of Mathematical Sciences, 4490, Osogbo, Nigeria*
mutairu.kolawole@uniosun.edu.ng, ORCID: 0000-0003-1500-2060

Abstract

This study presents a mathematical analysis of the SVEITR model, which incorporates susceptible (s), vaccinated (v), exposed (e), infected (i), treated (t), and recovered (r) populations to evaluate the dynamics of cholera spread. By integrating treatment and vaccination rates into the model, we aim to understand their impact on disease transmission and the development of immunity. Our findings reveal that combining rapid treatment and vaccination significantly reduces the spread of cholera disease, highlighting the importance of these interventions in public health strategies. The model demonstrates that timely and widespread implementation of vaccination and treatment can effectively control outbreaks and mitigate the disease's impact. Through a numerical simulation of the Laplace Adomian Decomposition Method, the results reveal that treatment rate reduces the spread of the disease, and vaccination plays a vital role in curbing the aftermath of widespread disease. Hence, there is a need for robust healthcare policies that prioritize these measures to achieve substantial progress in managing and eventually eradicating cholera, particularly in vulnerable regions. The SVEITR model offers a valuable framework for policymakers and healthcare professionals to develop effective strategies for cholera control, contributing to improved public health outcomes.

Kolera Bulaşımının Dinamikleri Üzerinde Tedavi ve Aşılama Etkilerinin Kantitatif Modellemesi

Öz

Bu çalışma, kolera yayılımının dinamiklerini değerlendirmek amacıyla duyarlı (s), aşılı (v), maruz kalmış (e), enfekte (i), tedavi edilen (t) ve iyileşen (r) popülasyonları içeren SVEITR modelinin matematiksel analizini sunmaktadır. Modele tedavi ve aşılama oranlarının entegre edilmesiyle, bu önlemlerin hastalığın bulaşması ve bağışıklık üzerindeki etkilerini anlamayı amaçlıyoruz. Bulgularımız, hızlı tedavi ve aşının birleştirilmesinin kolera hastalığının yayılmasını önemli ölçüde azalttığını ortaya koyarak, bu müdahalelerin halk sağlığı stratejilerindeki önemini vurgulamaktadır. Model, aşılama ve tedavinin zamanında ve yaygın olarak uygulanmasının salgınları etkili bir şekilde kontrol edebileceğini ve hastalığın etkilerini azaltabileceğini göstermektedir. Laplace-Adomian Ayrıştırma Yöntemi ile yapılan sayısal simülasyon sonucunda, tedavi oranının hastalığın yayılımını azalttığı ve aşının hastalığın yaygın etkilerini azaltmada hayati bir rol oynadığı ortaya çıkmıştır. Bu nedenle, bu önlemleri önceliklendiren sağlam sağlık politikalarına duyulan ihtiyaç, özellikle savunmasız bölgelerde koleranın yönetilmesi ve nihayetinde ortadan kaldırılması için önemli ilerlemeler sağlamak açısından gereklidir. SVEITR modeli, politika yapıcılar ve sağlık uzmanları için kolera kontrolüne yönelik etkili stratejiler geliştirmede değerli bir çerçeve sunarak, halk sağlığı sonuçlarının iyileştirilmesine katkıda bulunmaktadır.

Anahtar Kelimeler: Kolera kontrolü; Tedavi etkinliği; Aşılama oranı; Kararlılık analizi; Kantitatif analiz; Simülasyon.

1. Introduction

Cholera is a highly infectious disease caused by the bacterium Vibrio cholerae, which remains a public health challenge, particularly in regions with inadequate water and sanitation infrastructure. Characterized by severe diarrhea and dehydration, cholera can lead to death within hours if untreated, as in [1-2]. The disease primarily spreads through the consumption of contaminated water and food, making its control closely linked to the quality of water supply, sanitation, and hygiene practices in [3]. Despite advancements in medical sciences and public health strategies, cholera outbreaks continue to pose a substantial health risk in developing countries. The focus of contemporary cholera research includes treatment efficacy, vaccination,

water and environmental cleanliness, regional enlightenment, regular hand washing, proper waste disposal, and community awareness by [4-5]. These components of sensitization and treatment are crucial in developing a comprehensive approach to control and prevent the disease effectively [6]. Effective treatment of cholera involves prompt rehydration, which can be lifesaving as discussed in [7]. Oral rehydration salts (ORS) are the cornerstone of treatment for most patients, while intravenous fluids are necessary for severe cases [8]. Antibiotics can also reduce the diarrhea and the volume of rehydration fluids needed can be increased instantaneously with researching into optimizing the treatment ongoing in endemic African regions such as Sudan, Ethiopia, Nigeria, Niger and Somalia, aiming to enhance their efficacy and accessibility to healthy water supply and hygienic environmental settings as in [9-10].

The goal is to ensure that treatment protocols are both efficient and adaptable to various healthcare infrastructures, thus reducing mortality and morbidity rates associated with cholera disease [11-12]. Oral cholera vaccines (OCVs) have proven effective in providing immunity and reducing the incidence of the disease as well [13]. The integration of vaccination into public health strategies, especially in high-risk areas, can prevent outbreaks and provide long-term protection [14]. Recently, researchers have focused on improving the efficacy and duration of vaccine-induced immunity, as well as logistics to enhance vaccine distribution and administration to endemic regions, where the success of vaccination campaigns depends on the timely and widespread coverage, particularly before and during cholera outbreaks, as in [15]. Clean water and proper sanitation are fundamental in preventing cholera transmission, where contaminated water sources are the primary vectors for the bacterium, highlighting the need for robust water treatment and safe water storage practices by [16].

Additionally, environmental cleanliness, including the maintenance of clean living conditions and proper sanitation facilities, is essential in [17-18]. Public health initiatives must focus on infrastructure development and community education to promote sustainable practices that ensure water and environmental cleanliness. Educating communities about cholera prevention and control is vital. Regional enlightenment campaigns can significantly impact public health by raising awareness about the disease, its transmission, and preventive measures, as in [19]. These campaigns should focus on informing individuals about the importance of using safe water, practicing good hygiene, and recognizing the symptoms of cholera for prompt treatment. Tailored educational programs that consider local customs and practices can enhance community engagement and compliance with preventive measures [20]. Hand washing technique with soap, disinfectants, and clean water is one of the simplest and most effective ways to prevent the spread of cholera. Regular hand washing, particularly before eating and after using the toilet, can

significantly reduce the transmission of the bacterium [21]. Public health campaigns must emphasize the importance of this practice and ensure that communities have access to soap and clean water. Installing hand-washing stations in public places and schools can also promote this essential hygiene practice. Proper waste disposal is crucial in preventing cholera outbreaks. Improperly disposed of human waste can contaminate water sources, facilitating the spread of Vibrio cholerae [22]. Implementing effective waste management systems, including the use of latrines and sewage treatment facilities, is vital. Public health initiatives should focus on constructing and maintaining these facilities, as well as educating communities about the importance of proper waste disposal [23]. Safe disposal practices help break the transmission cycle and reduce the risk of outbreaks. Awareness campaigns play a crucial role in cholera prevention, informing the public about the deadly disease, its symptoms, and the importance of seeking immediate treatment can save lives [24]. Awareness efforts should also highlight the preventive measures individuals can take to protect themselves and their communities, as in [25]. Utilizing various media platforms, including radio, television, social media platforms, and community outreach programs, can effectively disseminate information and reach a broad audience [26].

However, this research focuses on controlling the spread of cholera, which requires a multifaceted approach. This involves developing a mathematical model that incorporates both effective treatment and vaccination rates, along with various control measures, including water and environmental cleanliness, regional education, regular hand washing, proper waste disposal, and public awareness. By addressing these areas, public health initiatives can significantly reduce the incidence and impact of cholera, ultimately aiming for its eradication. Proper and continuous investment in these strategies is essential to overcoming the persistent threat posed by cholera, particularly in vulnerable regions.

2. Materials and Methods

2.1. Model Formulation

The total population N (t) is distinctly divided into six sub-compartments of population sizes of are susceptible S(t), vaccinated V(t), exposed E(t), infected I(t), hospitalized/treated T(t) and recovered population R(t), The rate of migration π or inflow into the population resulting to the spread of cholera is β as human population are exposed through contaminated water and the hygienic measure put into practice to avoid ingestion and reduce the contact rate of the disease. Logistic coverage of public awareness of infected individuals at a rate of δ, where exposed individuals are subjected to contracting cholera at k, and the rate of recovery is denoted with γ

The treatment rate of the hospitalized individuals ϕ_2. More than 75% of contamination risk of vibro-cholerae results in the spread of the disease and ϕ_1 vaccination rate of susceptible individuals, with ε representing the vaccine efficacy and shedding rate of infected human population, coupled with natural mortality rate for human and vibro-cholerae are φ and μ. The above parameters can be demonstrated with schematic flow in Fig. 1 and a system of nonlinear differential equations in Eqn. (1) below, respectively.
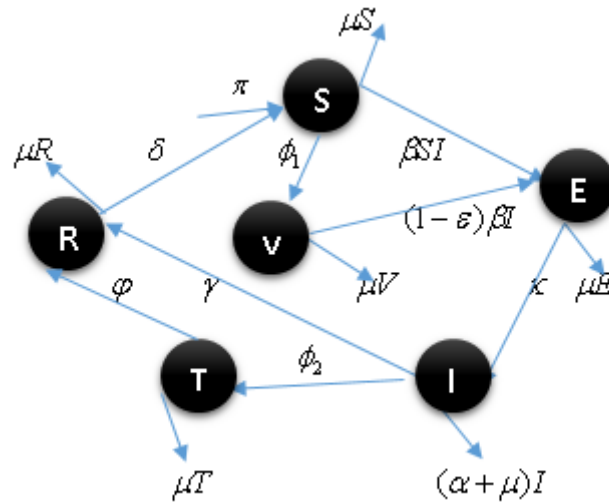
Figure 1: Schematic diagram of the model.

2.2. Model Analysis

From the schematic diagram above, an equation of the model is obtained in Eqn. (1) below:

$$\frac{dS}{dt} = \pi - \beta SI - (\phi_1 + \mu)S + \delta R$$

$$\frac{dV}{dt} = \phi_1 S - (1 - \varepsilon)\beta IV - \mu V$$

$$\frac{dE}{dt} = (1 - \varepsilon)\beta IV + \beta SI - (k + \mu)E$$

$$\frac{dI}{dt} = kE - (\alpha + \mu + \gamma + \phi_2)I$$

$$\frac{dT}{dt} = \phi_2 I - (\varphi + \mu)T$$

$$\frac{dR}{dt} = \varphi T + \gamma I - (\delta + \mu)R \tag{1}$$

Subjected to the initial condition

$$S(0) = s_0, V(0) = v_0, E(0) = e_0, I(0) = r_0, T(0) = t_0, R(0) = r_0 \geq 0. \qquad (2)$$

Parameters of the model solution, descriptions, and references are displayed in Table 1 and Table 2 with values that are time-dependent for cholera spread.

Table 1: Description of model state variables.

Variables	Description
S(t)	Susceptible population
V(t)	Vaccinated population
E(t)	Exposed population
I(t)	Infected population
T(t)	Treated population
R(t)	Recovered population

Table 2: Description of model parameter, values and references

Parameter	Description	Values	References
N	Total population	80,000	[10]
φ	Recovery rate of hospitalized individuals	0.001	[11]
ε	Vaccination efficacy	0.5	[1]
ϕ_2	Treatment rate of hospitalized individuals	0.2	[18]
ϕ_1	Vaccination rate of infected individuals	0.03	[2]
μ	Natural death	1.0	[5]
δ	İmmunity waning rate	0.0016	[20]
π	Recruitment rate	0.113	[3]
β	Rate of cholera transmission	1.0126	[14]
α	Disease induced death rate	0.33182	[21]
γ	Natural recovery rate	0.16524	[17]
k	Progression rate between exposed and infected class of individuals	0.25533	[9,16]

2.3. Existence and Uniqueness of Model

The system of Eqn. (1) above, which describes an epidemic disease within a human population, should have parameters that are non-negative. To ensure that the system of differential Eqn. (1) is both mathematically and epidemiologically well-posed, it is essential to demonstrate that the state variables in the model are nonnegative. Therefore, the system of Eqn. (1) is bounded by an initial condition of $S(0) = s_0$, $V(0) = v_0$, $E(0) = e_0$, $I(0) = i_0$, $T(0) = t_0$, $R(0) = r_0$, in which the solution will persist in being non-negative throughout their evolution, i.e., $t > 0$ and that these positive solutions are bounded in this region. We thus apply the theorem (1) below.

Theorem 2.3.1. Let (x, y) be distinct points of normed linear space $\left(X, \|\cdot\cdot\|\right)$ over $\Re$. Then the map of $p : [0,1] \subseteq \Re \rightarrow \left(X, \|\cdot\cdot\|\right)$ such that $p(\lambda) = \lambda x + (1 - \lambda) y$ is continuous on $[0,1]$.

Proof. Let $\lambda_0 \in [0,1]$ then $p(\lambda_0) = \lambda_0 x + (1 - \lambda_0) y$ for any $\lambda_0 \in [0,1]$,

$$\left\| p(\lambda) - p(\lambda_0) \right\| = \left\| (\lambda - \lambda_0) x + (\lambda - \lambda_0) y \right\| \leq \left| \lambda - \lambda_0 \right| \left(\|x\| + \|y\| \right) \tag{3}$$

If $\varepsilon > 0$ is given, let $\delta = \dfrac{\varepsilon}{\|x\| + \|y\|}$. If $\left| \lambda - \lambda_0 \right| < \delta$, then the $\left\| p(\lambda) - p(\lambda_0) \right\| < \varepsilon$.

Therefore, p is continuous at λ_0. Since λ_0 is an arbitrary point in $[0,1]$. then p is continuous on $[0,1]$. Let X be a linear space over $\Re$. If x,y are distinct points of X, the set $\lambda x + (1 - \lambda) y$ lies in $0 \leq \lambda \leq 1$.

Hence, the solutions of system of Eqn. (1) are bounded if we consider the total population

$$N(t) = S(t) + V(t) + E(t) + I(t) + T(t) + R(t)$$

The variation in the total population concerning time is given by:

$$\frac{dN(t)}{dt} = \frac{dS(t)}{dt} + \frac{dV(t)}{dt} + \frac{dE(t)}{dt} + \frac{dI(t)}{dt} + \frac{dT(t)}{dt} + \frac{dR(t)}{dt} \tag{4}$$

Such that $\dfrac{dN(t)}{dt} = \pi - \mu(S + V + E + I + T + R) - \alpha I \quad \rightarrow \quad \dfrac{dN(t)}{dt} \leq \pi - \mu N$. When there is no outbreak of cholera, $\delta = 0$. Thus, substituting Eqn. (1) into Eqn. (4) as time progressively yields:

$$\lim_{t\to\infty} N(t) \le \lim_{t\to\infty}\left[\frac{\pi}{\mu}+\left(N(0)-\frac{\pi}{\mu}\right)e^{-\mu t}\right]=\frac{\pi}{\mu} \tag{5}$$

If so $N(0) \le \dfrac{\pi N}{\mu}$, as $N(t) \le \dfrac{\pi N}{\mu}$. This is a positive invariant set under the flow described

by Eqn. (2) so that no solution path leaves through any boundary $\mathfrak{R}^6_+$. However, it is sufficient to

consider the dynamics of the model in the domain $\mathfrak{R}^6_+$. In this region, the model can be considered

mathematically and epidemiologically well-posed.

2.4. Positivity and Boundedness of Model

This shows that the total population N(t), and the subpopulations S(t), V(t), E(t), I(t), T(t), R(t) of the model are bounded and are a unique solution. Hence, its applicability to study physical systems is feasible.

Theorem 2.4.1. Suppose $X = x_0$ is a space of consecutive real numbers, and that are defined as

$$L(x,y) = \left(\sum_{i=1}^{n}|x_i|^{\Omega}\right)^{\frac{1}{\Omega}} \qquad \Omega \ge 1 \tag{6}$$

X with the metric is called ξ_n^{Ω} space. If $\sum_{i=1}^{N}|x|^i < \infty$ or absolutely convergent and

$$L(x,y) = \left(\sum_{i=1}^{\infty}|x_i - y_i|^{\Omega}\right)^{\frac{1}{\Omega}}, \text{ then X with this metric is called an } \xi^{\Omega} \text{ space.}$$

Proof. It can be checked that for each n:

$$0 \le x_1^2 + x_2^2 + x_3^2 + \ldots + x_n^2 \le (|x_1| + |x_2| + |x_3| + \ldots + |x_n|)^2 \tag{7}$$

This will result to;

$$x_1^2 + x_2^2 \le (|x_1| + |x_2|)^2 \tag{8}$$

Therefore,

$$0 \le (x_1^2 + x_2^2 + x_3^2 + \ldots + x_n^2)^{\frac{1}{2}} \le |x_1| + |x_2| + |x_3| + \ldots + |x_n|,$$

If $\sum_{n=1}^{\infty}|x_n|$ converges, that is $\sum_{n=1}^{\infty}|x_n|$ is absolutely convergent, then

$$0 \le \left(x_1^2+x_2^2+x_3^2+...+x_n^2\right)^{\frac{1}{2}} \le |x_1|+|x_2|+|x_3|+...+|x_n| = \sum_{n=1}^{\infty}|x_n| < \infty \tag{9}$$

Therefore,

$$0 \le x_n = x_1^2 + x_2^2 + x_3^2 + ... + x_n^2 \le \left[\sum_{n=1}^{\infty}|x_n|\right] < \infty \tag{10}$$

The sequence x_n is monotone increasing and bounded above, it therefore converges. Thus $\sum_{n=1}^{\infty}x_n$ converges absolutely, i. E if $x_n \in \xi^1$, then $x_n \in \xi^2$ where $\xi^1 \le \xi^2$. In case of ξ^1 denote the set of all sequences of x_n of real numbers such that $\sum_{n=1}^{\infty}x_n$ is convergent absolutely. i.e $\sum_{n=1}^{\infty}|x_n| < \infty$ where as ξ^2 denote the set of all sequence x_n of real numbers such that $\sum_{n=1}^{\infty}x_n^2 < \infty$ converges. From the proceeding $x_n \in \xi^1 \Leftrightarrow x_n \in \xi^2$ i.e $\xi^1 \subseteq \xi^2$. Further, if $x_n = \dfrac{1}{n^{\frac{3}{4}}}$, then $\sum_{n=1}^{\infty}|x_n|$ diverges and thus $x_n \notin \xi^1$. But $\sum_{n=1}^{\infty}x_n^2 = \sum_{n=1}^{\infty}\dfrac{1}{n^{\frac{3}{4}}}$ converges, implying that $x_n \in \xi^2$. We conclude that $\xi^1 \subseteq \xi^2$ and thus $\xi^1 \ne \xi^2$. If (x_n, y_n) are sequences of real numbers, then;

$$\sum_{n=1}^{\infty}(x_i - y_i)^2 \le \sum_{n=1}^{\infty}x_i^2 + \sum_{n=1}^{\infty}y_i^2 + 2\left[\sum_{n=1}^{\infty}x_i^2\right]^{\frac{1}{2}}\left[\sum_{n=1}^{\infty}y_i^2\right]^{\frac{1}{2}} \tag{11}$$

Therefore if $\sum_{n=1}^{\infty}x_i^2 < \infty$ and $\sum_{n=1}^{\infty}y_i^2 < \infty$ then $\sum_{n=1}^{\infty}(x_i - y_i)^2 < \infty$ for all n. The monotone increasing sequence $\left[\sum_{n=1}^{\infty}(x_i - y_i)^2\right]$ is then bounded above and hence converges i.e $\sum_{n=1}^{\infty}(x_i - y_i)^2 < \infty$. Thus $(x_i - y_i)^2 \in \xi^2$ if $(x_n, y_n) \in \xi^2$ as in [18]. Given that the

$S(0) = s_0 > 0,\ V(0) = v_0 > 0,\ E(0) = e_0 > 0,\ I(0) = i_0 > 0,\ T(0) = t_0 > 0,\ R(0) = r_0 > 0$

and $t > 0$, then the solution of S(t), V(t), E(t), I(t), T(t), R(t) of the Eqn. (1) will always be nonnegative.

$$\text{Let: } \Psi = \left\{ \left(S(t), V(t), E(t), I(t), T(t), R(t) \right) \in \mathfrak{R}_+^6 : N(t) \leq \frac{\pi}{\mu} \right\} \tag{12}$$

If $f_i, i = 1, 2 \dots 6$ where f is a constant. Then;

$$\left| \frac{df_1}{dS} \right| = |(\beta + \phi_1 + \mu + \delta)| < \infty, \quad \left| \frac{df_1}{dV} \right| = |0| < \infty, \quad \left| \frac{df_1}{dE} \right| = |0| < \infty, \quad \left| \frac{df_1}{dI} \right| = |\alpha| < \infty,$$

$$\left| \frac{df_1}{dT} \right| = |\alpha| < \infty$$

$$\left| \frac{df_1}{dR} \right| = |\delta| < \infty, \left| \frac{df_2}{dS} \right| = |\phi_1| < \infty, \left| \frac{df_2}{dV} \right| = |(1-\varepsilon)\beta + \mu| < \infty, \left| \frac{df_2}{dE} \right| = |0| < \infty,$$

$$\left| \frac{df_2}{dI} \right| = |(1-\varepsilon)\beta| < \infty \left| \frac{df_2}{dT} \right| = |0| < \infty, \quad \left| \frac{df_2}{dR} \right| = |0| < \infty, \quad \left| \frac{df_3}{dS} \right| = |\beta| < \infty,$$

$$\left| \frac{df_3}{dV} \right| = |(1-\varepsilon)\beta| < \infty, \quad \left| \frac{df_3}{dE} \right| = |(k+\mu)| < \infty, \quad \left| \frac{df_3}{dI} \right| = |(1-\varepsilon)\beta| < \infty, \left| \frac{df_3}{dT} \right| = |0| < \infty,$$

$$\left| \frac{df_3}{dR} \right| = |0| < \infty, \left| \frac{df_4}{dS} \right| = |0| < \infty, \left| \frac{df_4}{dV} \right| = |0| < \infty \left| \frac{df_4}{dE} \right| = |k| < \infty,$$

$$\left| \frac{df_4}{dI} \right| = |(\alpha + \gamma + \mu + \phi_2)| < \infty, \quad \left| \frac{df_4}{dT} \right| = |0| < \infty, \quad \left| \frac{df_4}{dR} \right| = |0| < \infty, \quad \left| \frac{df_5}{dS} \right| = |0| < \infty,$$

$$\left| \frac{df_5}{dV} \right| = |0| < \infty, \quad \left| \frac{df_5}{dE} \right| = |0| < \infty, \quad \left| \frac{df_5}{dI} \right| = |\phi_2| < \infty, \quad \left| \frac{df_5}{dT} \right| = |(\varphi + \mu)| < \infty, \quad \left| \frac{df_5}{dR} \right| = |\mu| < \infty,$$

$$\left| \frac{df_6}{dS} \right| = |0| < \infty, \quad \left| \frac{df_6}{dV} \right| = |0| < \infty, \quad \left| \frac{df_6}{dE} \right| = |0| < \infty, \quad \left| \frac{df_6}{dI} \right| = |\gamma| < \infty, \quad \left| \frac{df_6}{dT} \right| = |\varphi| < \infty,$$

$$\left| \frac{df_5}{dR} \right| = |(\mu + \delta)| < \infty \tag{13}$$

Eqn. (13) above confirms that system of Eqn. (1) is bounded, invariantly and attractively influential on the bounded region of $\mathfrak{R}_+^6$.

2.5. Disease Free Equilibrium

The cholera non-infected equilibrium state represents a scenario in which Eqn. (1) is entirely free from Vibrio cholerae spread as in [1]. Consequently, when the number of disease

population of infected, exposed individuals is at equilibrium, i.e I = E = 0. This context brings about the solution for the cholerae free equilibrium oint which is derived as follows in Eqn. (14)

$$\frac{dS}{dt} = \frac{dV}{dt} = \frac{dE}{dt} = \frac{dI}{dt} = \frac{dT}{dt} = \frac{dR}{dt} = 0 \tag{14}$$

At no outbreak of measles infection, the diseases class, at $t > 0$, from Eqn. (8),

$$(S_0, V_0, E_0, I_0, T_0, R_0) = \left(\frac{\pi}{(\phi_1 + \mu)}, \frac{\pi\phi_1}{(\phi_1 - \delta + \mu)(1-\varepsilon)\beta + \mu}, 0, 0, 0, 0 \right) \tag{15}$$

2.6. Disease Endemic Equilibrium

Examining cholera endemicity spread, we focus on strategic interventions of treatment and vaccination of infected individuals with the aim of long-term eradication. The frequency of choleraon (S,V,E,I,T,R) at $t \neq 0$, stressing the dynamic aspect of it to gauge on the crucial role in its infectious disease and protection on the populace. Let the endemic nature of Eqn. (1) be $E_e = (S^*, V^*, E^*, I^*, T^*, R^*)$ at steady state, $I \neq 0$, hence the equation for its endemicity at equilibrium is obtained in Eqn. (16) below;

$$S^* = \frac{\pi(1-\varepsilon)^2[\phi_2 + \mu + \alpha] + \beta[\mu + \gamma + \varphi]}{[(\mu + \gamma + (1-\varepsilon)\phi_1) + \delta]\sqrt{\beta(\gamma + (1-\varepsilon) + (\mu + \gamma + \varphi)}},$$

$$V^* = \frac{(1-\varepsilon)\pi\sqrt{(\varphi + k + \mu)(\delta + \mu + \phi_1)}}{(\delta + \mu + \phi_2)[(\mu + \gamma + (1-\varepsilon)\beta]}, \quad E^* = \frac{\beta(1-\varepsilon)(\phi_2 + \gamma + \mu)}{\sqrt{(\gamma + k + \mu)(\delta + \mu + \alpha)}}$$

$$I^* = \frac{(1-\varepsilon)[\pi + (\mu + \gamma + \varphi)\sqrt{(k + \phi_1 + \mu)(\delta + \mu + \gamma)}]}{[\mu^2(\delta + \mu + \gamma)]},$$

$$T^* = \frac{(\mu + \gamma + k)}{(\delta + \mu + \alpha)[(\mu + k + \phi_2]} + \frac{\sqrt{(k + \varphi + \phi_1)(\delta + \mu + \delta)}}{(\gamma + \mu + k)} \tag{16}$$

$$R^* = \frac{(\mu + \alpha + \phi_1)}{[\mu^2(\varphi + \mu) + (1-\varepsilon)]} + \sqrt{\frac{(\mu + \varphi + k) + \mu^2}{(k + \alpha)(\gamma + \mu + k)(\varepsilon + \mu + \delta)}}$$

2.7. Basic Reproduction Number

The basic reproduction number $R_\bullet$ measures cholera spread by calculating secondary infections using next-generation matrices for new infections and transitions. Let

$R_\bullet = \rho(G - \lambda I |)$ where $G = F \times V^{-1}$ and ρ is the spectral radius of the matrix $|G - \lambda I|$. Thus,

the $R_\bullet$ is obtained as it is defined that $F_i = \left(\dfrac{\partial f_i(x_i)}{\partial x_j}\right), V_i = \left(\dfrac{\partial v_i(x_i)}{\partial x_j}\right)$. Such that

$f = \begin{pmatrix} \beta I S_0 + (1-\varepsilon)\beta I V_0 \\ 0 \end{pmatrix}$ and $v = \begin{pmatrix} (k+\mu)E \\ -kE + (\alpha+\mu+\gamma+\phi_2)I \end{pmatrix}$, the transmission matrix for

the disease and its transition compartmentally for the disease spread is obtained below in Eqn. (17)

$$F = \begin{pmatrix} 0 & \dfrac{\pi[(1-\varepsilon)\beta + \mu + \phi_1]}{(\phi_1 - \delta + \mu)(1-\varepsilon)\beta + \mu} \\ 0 & 0 \end{pmatrix} V = \begin{pmatrix} (k+\varepsilon) & 0 \\ -k & (\alpha+\mu+\gamma+\phi_2) \end{pmatrix} \qquad (17)$$

$$FV^{-1} = \frac{1}{(k+\mu)(\alpha+\mu+\gamma+\phi_2)} \begin{pmatrix} 0 & \dfrac{\pi[(1-\varepsilon)\beta + \mu + \phi_1]}{(\phi_1 + \mu)(1-\varepsilon)\beta + \mu} \\ 0 & 0 \end{pmatrix} \begin{pmatrix} (\alpha+\mu+\gamma+\phi_2) & 0 \\ -k & (k+\mu) \end{pmatrix}.$$

Resolving the above matrix respectively with their eigenvalues being independent factors of the leading variables, the basic reproduction number for Eqn. (17) is obtained in Eqn. (18) as discussed in [10]

$$R_\bullet = \frac{\pi[(1-\varepsilon)\beta + \mu + \phi_1]}{[(\phi_1 - \delta + \mu)(1-\varepsilon)\beta + \mu](\alpha+\mu+\gamma+\phi_2)} \qquad (18)$$

2.8. Quantitative Analysis of R_*

Here, we conduct a quantitative analysis of R_ε to assess its metric progression concerning each intervention method. By excluding the values of intervention parameters, we assess Eqn. (18) using the baseline values provided in Table 1, subsequently resulting in Eqns. (19)-(22). The outcomes of these calculations are presented in Table 3.

$$R_\bullet = \frac{\pi[(1-0.028726)\beta + 0.0087363 + 0.5263532\phi_1]}{[(1.27364 - 09377847 + 0.38736\alpha)(1-0.7653\varepsilon)\beta + 0.872625](0.9972 + 0.5243436\phi_2)}$$

$$R_\varepsilon = f(\phi_1)\big|_{\delta=0,\phi_2=0} = -1.7363526\phi_1 + 1.459137886\phi_2 \qquad (19)$$

$$R_\varepsilon = f(\varphi)\big|_{\alpha=0,\rho_1=0} = 0.005728262500 + 0.0000133\varphi + 0.0039257856\alpha \qquad (20)$$

$$R_\varepsilon = f(\phi_2)\big|_{c=0,\phi_2=0} = 0.093762(0.09756 + 0.54\phi_1) + 0.137747\phi_2 + 0.018\phi \tag{21}$$

$$R_\varepsilon = f(\varepsilon)\big|_{\rho_1=0,\tau=0} = 1.38947804 - 1.9276424\varepsilon \tag{22}$$

Table 3: Standalone metric of vaccination and general awareness on R_ε.

A						B					C				
s/n	ϕ_1	β	ϕ_2	ε	R_ε	s/n	ϕ_1	β	ϕ_2	ε	s/n	ϕ_1	β	ϕ_2	ε
1	0	0	0	0	1.4591378	0	0	0	0	1.45913788	0	0	0	0	1.45913788
2	0.2	0	0	0	1.1964930	0	0.2	0	0	1.16731030	0	0	0.2	0	0.25434513
3	0.4	0	0	0	0.93384824	0	0.4	0	0	0.87548273	0	0	0.4	0	0.20246410
4	0.6	0	0	0	0.67120342	0	0.6	0	0	0.58365515	0	0	0.6	0	0.18416303

2.9. Local Stability for Disease Free Equilibrium

Theorem 2.9.1. The disease-free state of the model is locally asymptotically stable if the threshold of the disease spread $R_* < 1$ and unstable whenever it is of the form $R_* > 1$.

Proof. The disease-free equilibrium is obtained using the Jacobian matrix approach from next generation matrix of the resulting eigenvalues of respective parameters as of the system of Eqn. (1) and evaluated at the disease free state using the linearization method thus;

$$J_{(E_1)} = \begin{pmatrix} -(\beta+\mu+\phi_1+\delta) & 0 & 0 & \beta & 0 & 0 \\ \phi_1 & -[(1-\varepsilon)\beta+\mu] & 0 & (1-\varepsilon)\beta & 0 & 0 \\ \beta & (1-\varepsilon)\beta & -(k+\mu) & (1-\varepsilon)\beta & 0 & 0 \\ 0 & 0 & k & -(\alpha+\mu+\gamma+\phi_2) & 0 & 0 \\ 0 & 0 & 0 & \phi_2 & -(\varphi+\mu) & 0 \\ 0 & 0 & 0 & \gamma & \varphi & -(\delta+\mu) \end{pmatrix} \tag{23}$$

Computing for the eigenvalues from the characteristic equation as $|J_{E_1} - \lambda_i I| = 0$, we then have

$$\begin{vmatrix} a-\lambda & 0 & 0 & \beta & 0 & 0 \\ \phi_1 & b-\lambda & 0 & (1-\varepsilon)\beta & 0 & 0 \\ \beta & (1-\varepsilon)\beta & c-\lambda & (1-\varepsilon)\beta & 0 & 0 \\ 0 & 0 & k & d-\lambda & 0 & 0 \\ 0 & 0 & 0 & \phi_2 & e-\lambda & 0 \\ 0 & 0 & 0 & \gamma & \varphi & f-\lambda \end{vmatrix} = 0$$

$a = -(\beta + \mu + \phi_1 + \delta), \quad b = -[(1-\varepsilon)\beta + \mu], \quad c = -(k+\mu), \quad d = -(\alpha + \mu + \gamma + \phi_2),$

$e = -(\varphi + \mu), \; f = -(\delta + \mu)$ as obtained from Eqn. (23) the respective eigen vales are deduced in Eqn. (24) below:

$$\lambda = -(v+\mu), \lambda = -(\alpha_2 + \mu), \lambda = -\mu, \begin{vmatrix} -(\alpha + \mu + \gamma + \phi_2) - \lambda & 0 \\ \phi_2 & -(\varphi + \mu) - \lambda \end{vmatrix}, \lambda_3 = -(\alpha + \mu + \gamma + \phi_2), \lambda = -(\varphi + \mu) \Bigg\}$$

(24)

Respective eigenvalues are negatively invariant in the region $\mathfrak{R}_+^6$, indicating a biological implication that there will be a decrease in the spread over time if necessary control measures as indicated are strictly adhered to. Hence it is asymptomatically stable $\forall \lambda_n < 0, n = 1,2\ldots6, t > 0$.

3. Regional Resilience for Persistence Equilibrium State

Theorem 3.1. The local stability of the persistent equilibrium of the model is ensured that if $R_\bullet < 1,$ invariantly and otherwise, it is unstable if $R_\bullet > 1$ is in the modification of the model equation as discussed in Eqn. (1).

Proof. Suppose

$$S = x + S^*, V = y + V^*, E = z + E^*, I = a + I^*, T = b + T^*, R = c + R^* \tag{25}$$

Linearizing Eqn. (1), is then obtained as from Eqn. (26) for respective sensitive parameters for each state variable that are

$$\frac{dS}{dt} = \pi - \beta(x + S^*)(a + I^*) - (\phi_1 + \mu)(x + S^*) + \delta(x + R^*)$$

$$\frac{dV}{dt} = \phi_1(x + S^*) - (1-\varepsilon)\beta(a + I^*)(y + V^*) - \mu(y + V^*)$$

$$\frac{dE}{dt} = (1-\varepsilon)\beta(a + I^*)(y + V^*) + \beta(x + S^*)(a + I^*) - (k+\mu)(z + E^*) \tag{26}$$

$$\frac{dI}{dt} = k(z + E^*) - (\alpha + \mu + \gamma + \phi_2)(a + I^*)$$

$$\frac{dT}{dt} = \phi_2(a + I^*) - (\varphi + \mu)(b + T^*)$$

$$\frac{dR}{dt} = \varphi(b + T^*) + \gamma(a + I^*) - (\delta + \mu)(c + R^*)$$

Linearizing Eqn. (25), it is then obtained that each

$$\frac{dx}{dt} = -\beta ax - (\phi_1 + \mu)x - \delta x + \text{higher order} + \text{non-linear terms...}$$

$$\frac{dy}{dt} = \phi_1 x - (1 - \varepsilon)\beta ay - \mu y + \text{higher order} + \text{non-linear terms...}$$

$$\frac{dz}{dt} = (1 - \varepsilon)\beta ay + \beta ax - (k + \mu)z + \text{higher order} + \text{non-linear terms...} \tag{27}$$

$$\frac{da}{dt} = kz - (\alpha + \mu + \gamma + \phi_2)a + \text{higher order} + \text{non-linear terms...}$$

$$\frac{db}{dt} = \phi_2 a - (\varphi + \mu)b + \text{higher order} + \text{non-linear terms...}$$

$$\frac{dc}{dt} = \varphi b + a\gamma - (\delta + \mu) + \text{higher order} + \text{non-linear terms...}$$

The characteristic equation obtained from its Jacobian matrix is;

$$\begin{vmatrix} A - \lambda & 0 & 0 & -\beta ax & 0 & 0 \\ \phi_1 x & -[(1-\varepsilon)\beta ay + \mu)]y - \lambda & 0 & (1-\varepsilon)\beta ay & 0 & 0 \\ \beta ax & (1-\varepsilon)\beta ay & B - \lambda & \beta ax & 0 & 0 \\ 0 & 0 & kz & C - \lambda & 0 & 0 \\ 0 & 0 & 0 & a\phi_2 & -(\varphi + \mu) - \lambda & 0 \\ 0 & 0 & 0 & a\gamma & \varphi b & (\delta + \mu)c \end{vmatrix} = 0 \tag{28}$$

Denoting that $A = -(\beta a + \mu + \phi_1)x, B = -[\beta ax - (k + \mu)z], C = -(\alpha + \mu + \gamma + \phi_2)$ the resulting eigenvalues of the above matrix are obtained as;

$$\lambda^6 - \left(x + (a + y) + (c + b)\right)\lambda^5 + \left((x + c)(y + s) + az + by\right)(1 + b)\lambda^4 - \left(ab(c + z) + bc(a + y)\right)(1 + z)\lambda^3$$

$$+ y\left(cz(a + b) + xb(a + y)\right)\lambda^2 - (a + c)(x + y)\lambda + abcxyz = 0. \tag{29}$$

With the invariance of the eigen values it is said to be locally asymptotically stable because all are of negative results.

3.1. Global Stability of Disease-Free Equilibrium

We employ the Lyapunov's function approach to establish the global asymptotic stability of the model solution for Eqn. (1) and ta disease free equilibrium, utilizing the Lyapunov algorithm for the model state variables, this is deduced in Eqn. (30) thus;

$$\Phi(t, S, V, E, I, T, R) = C_1 I_1 + C_2 I_2 + C_3 I_3 \tag{30}$$

$$\frac{d\Phi}{dt} = C_1 I_1^{\bullet} + C_2 I_2^{\bullet} + C_3 I_3^{\bullet}$$

$$= C_1 \big((1-\varepsilon)\beta I_2 V + \beta I_2 S - (k+\mu) I_1 \big) + C_2 \big(k I_1 - (\alpha + \gamma + \phi_2 + \mu) I_2 \big)$$
$$+ C_2 \big(\phi_2 I_2 - (\varphi_2 + \mu) I_3 \big)$$

$$= C_2 k I_1 - C_1 (k+\mu) I_1 + C_1 (1-\varepsilon)\beta I_2 V + C_1 \beta I_2 S - C_2 (\alpha + \gamma + \phi_2 + \mu) I_2$$
$$+ C_3 \phi_2 I_2 - C_3 (\varphi_2 + \mu) I_3$$

$$\leq \big(C_2 k - C_1 (k+\mu) \big) I_1 + \big(C_1 (1-\varepsilon)\beta V_0 + C_1 \beta S_0 - C_2 (\alpha + \gamma + \phi_2 + \mu) + C_3 \phi_2 \big) I_2$$
$$- C_3 (\varphi_2 + \mu) I_3$$

$$S_0 = \frac{\pi}{(\phi_1 + \mu)}, V_0 = \frac{\pi\phi_1}{(\phi_1 - \delta + \mu)(1-\varepsilon)\beta + \mu}, E_0 = 0, I_0 = 0, T_0 = 0, R_0 = 0 \tag{31}$$

$$S_0 = S_0 = \frac{\pi}{(\phi_1 + \mu)}, V_0 = \frac{\pi\phi_1}{(\phi_1 - \delta + \mu)(1-\varepsilon)\beta + \mu}, C_1 = \frac{1}{(k+\mu)},$$

$$C_2 = \left(\frac{(\phi_i + \mu - \delta)(1-\varepsilon) + \alpha + \beta}{\pi(\phi_2 + \mu + \delta + \gamma)(\alpha + \mu)} \right)$$

$$\frac{d\Phi}{dt} \leq C_1 \left(\frac{\pi(1-\varepsilon)\beta + \pi\mu + \pi\phi_1}{[(\phi_1 - \delta + \mu)(1-\varepsilon)} - \frac{(k+\mu)}{(k+\mu)} \right) I_1 - \left(\frac{\pi(\gamma + \mu + \delta)(1-\varepsilon)\beta + \mu}{(\phi_1 + \mu)(\gamma + \mu + \delta)(1-\varepsilon)} - \frac{\pi(\gamma + \mu + \delta)(1-\varepsilon)\beta + \mu}{(\phi_1 + \mu)(\gamma + \mu + \delta)(1-\varepsilon)} \right) I_2$$

$$\frac{d\Phi}{dt} \leq \psi(R_* - 1) \tag{32}$$

It is pertinent to observe that when time of the disease spread is simultaneously increasing at $t \to \infty$ and the constant of $C_1 < 1$, substituting into the model Eqn. (31), it is revealed that,

based on Lasalle's invariance principle $\Phi^{\bullet}=0$, is globally asymptotically stable whenever $R_* > 1$ as seen in Eqn. (32), because the basics reproduction number of the model system of Eqn. (1) is independent of the deiseal state eigen parameters.

3.2. Global Stability of Disease Endemic Equilibrium

Theorem 3.2.1 The Dulac criterion is a method used in dynamical systems to determine the absence of periodic orbits in a given region of the phase plane, which can be extended to analyze the global stability of an equilibrium point.

Proof. For a dynamical system described by the differential equations, i. e

$$\frac{dx}{dt} = f(x, y) \iff \frac{dy}{dt} = g(x, y) \tag{33}$$

The Dulac criterion states that if there exists a continuously differentiable function $B(x, y)$ (called the Dulac function) such that the expression in Eqn. (33) gives the equation below;

$$\frac{\partial}{\partial x}\big(B(x, y)f(x, y)\big) + \frac{\partial}{\partial x}\big(B(x, y)g(x, y)\big) \tag{34}$$

Which is either strictly positive or strictly negative throughout a simply connected region D of the phase plane. Then, there are no closed trajectories (periodic orbits) contained entirely within D. To apply this to determine the global stability of an endemic equilibrium (x^*, y^*) of a mathematical model, the endemic equilibrium point (x^*, y^*), which is also defined by the Dulac function $B(x, y)$ gives the equation below

$$\frac{\partial}{\partial x}\big(B(x, y)f(x, y)\big) + \frac{\partial}{\partial x}\big(B(x, y)g(x, y)\big) \text{ as } B(x, y)g(x, y) \tag{35}$$

This indicates that the equation has a constant sign (either strictly positive or strictly negative) in the region of interest. If such a Dulac function $B(x, y)$ can be found, the system has no periodic orbits in that region, suggesting the global stability of the endemic equilibrium if no other attractors exist. Hence, if $\exists B(x, y) \in C^1$ is such that

$$\frac{\partial}{\partial x}\big(B(x, y)f(x, y)\big) + \frac{\partial}{\partial x}\big(B(x, y)g(x, y)\big) \neq 0 \text{ in } D. \tag{36}$$

Then, there are no closed trajectories in D. This criterion is useful in proving the global stability of the endemic equilibrium when combined with other stability analysis techniques.

We then employ this concept of Dulac's criterion. Let, $X = (S, V, E, I, T, R)$ define the Dulac's function, i. E if $G = \dfrac{1}{SI}$. The following system of equations are derived.

$$G\frac{dS}{dt} = \frac{1}{SI}\left\{\pi - \beta SI - (\phi_1 + \mu)S + \delta R\right\}$$

$$G\frac{dV}{dt} = \frac{1}{SI}\left\{\phi_1 S - (1-\varepsilon)\beta IV - \mu V\right\}$$

$$G\frac{dE}{dt} = \frac{1}{SI}\left\{(1-\varepsilon)\beta IV + \beta SI - (k+\mu)E\right\} \tag{37}$$

$$G\frac{dI}{dt} = \frac{1}{SI}\left\{kE - (\alpha + \mu + \gamma + \phi_2)I\right\}$$

$$G\frac{dT}{dt} = \frac{1}{SI}\left\{\phi_2 I - (\varphi + \mu)T\right\}$$

$$G\frac{dR}{dt} = \frac{1}{SI}\left\{\varphi T + \gamma I - (\delta + \mu)R\right\}$$

The above system of equations then results to;

$$G\frac{dS}{dt} = \left\{\frac{\pi}{SI} - \beta - \frac{(\phi_1 + \mu)}{I} + \frac{\delta R}{SI}\right\}$$

$$G\frac{dV}{dt} = \left\{\frac{\phi_1}{I} - \frac{(1-\varepsilon)\beta}{S} - \frac{\mu}{S}\right\}$$

$$G\frac{dE}{dt} = \left\{\frac{(1-\varepsilon)\beta}{S} + \beta - \frac{(k+\mu)E}{S}\right\} \tag{38}$$

$$G\frac{dI}{dt} = \left\{\frac{kE}{SI} - \frac{(\alpha + \mu + \gamma + \phi_2)}{I}\right\}$$

$$G\frac{dT}{dt} = \left\{\frac{\phi_2}{S} - \frac{(\varphi + \mu)T}{SI}\right\}$$

$$G\frac{dR}{dt} = \left\{\frac{\varphi T}{SI} + \frac{\gamma}{S} - \frac{(\delta + \mu)R}{SI}\right\}$$

At an initial time, $t > 0$ orbital resolution of the system of equations is given by $\dfrac{d(GX)}{dt}$ which are obtained below compartmentally for each state variable and resolved descriptively to have,

$$\frac{d(GX)}{dt} = \frac{\partial}{\partial S}\left\{G\frac{dS}{dt}\right\} + \frac{\partial}{\partial V}\left\{G\frac{dV}{dt}\right\} + \frac{\partial}{\partial E}\left\{G\frac{dE}{dt}\right\} + \frac{\partial}{\partial I}\left\{G\frac{dI}{dt}\right\} + \frac{\partial}{\partial T}\left\{G\frac{dT}{dt}\right\}$$
$$+ \frac{\partial}{\partial R}\left\{G\frac{dR}{dt}\right\}$$

$$\frac{d(GX)}{dt} = \frac{\partial}{\partial S}\left\{\frac{\pi}{SI} - \beta - \frac{(\phi_1 + \mu)}{I} + \frac{\delta R}{SI}\right\} + \frac{\partial}{\partial V}\left\{\frac{\phi_1}{I} - \frac{(1-\varepsilon)\beta}{S} - \frac{\mu}{S}\right\}$$
$$+ \frac{\partial}{\partial E}\left\{\frac{(1-\varepsilon)\beta}{S} + \beta - \frac{(k+\mu)E}{S}\right\}$$

$$+ \frac{\partial}{\partial I}\left\{\frac{kE}{SI} - \frac{(\alpha + \mu + \gamma + \phi_2)}{I}\right\} + \frac{\partial}{\partial T}\left\{\frac{\phi_2}{S} - \frac{(\varphi + \mu)T}{SI}\right\} + \frac{\partial}{\partial R}\left\{\frac{\varphi T}{SI} + \frac{\gamma}{S} - \frac{(\delta + \mu)R}{SI}\right\} \quad (39)$$

$$\frac{d(GX)}{dt} = \left\{-\frac{[\pi + \beta + (\phi_1 + \mu) + \delta]}{SI}\right\} + \frac{\partial}{\partial V}\left\{-\frac{\phi_1 + (1-\varepsilon)\beta + \mu}{SI}\right\}$$
$$+ \frac{\partial}{\partial E}\left\{-\frac{(1-\varepsilon)\beta + \beta + (k+\mu)}{S}\right\}$$

$$+ \frac{\partial}{\partial I}\left\{-\frac{k + (\alpha + \mu + \gamma + \phi_2)}{SI}\right\} + \frac{\partial}{\partial T}\left\{-\frac{\phi_2 + (\varphi + \mu)}{S}\right\} + \frac{\partial}{\partial R}\left\{-\frac{\varphi + \gamma + (\delta + \mu)}{SI}\right\}$$

$$\frac{d(GX)}{dt} = -\left\{\begin{array}{l}\dfrac{A(1-v) + [(1-\rho) + \rho\beta] + (m+\mu)}{SI} + \dfrac{m + (1-\rho) - (\rho\beta + \mu)}{I} \\[2mm] + \dfrac{(1-\rho)\beta + (\delta + \mu)}{I} + \dfrac{\delta + \rho\beta + ((\gamma + \mu + d))}{SI} + \dfrac{Av + \gamma - \mu}{SI}\end{array}\right\} \quad (40)$$

$$\frac{d(GX)}{dt} = -\left\{\frac{[2(1-\rho)^2 + 3\rho\beta^2] + \sqrt{\gamma[2m^2 + m(1-\rho) - v^2(\rho\beta + \mu)]}}{SI}\right\} < 0 \quad (41)$$

This implies that the system has no closed orbit. It therefore portrays epidemiologically that, no existence of a periodic orbit which implies that there are fluctuations in the number of infective, which makes it obvious that in allocation of resources for the control of the disease, vaccination will help to eradicate the rapid spread of cholera with time.

3.3. Sensitivity Analysis

The primary aim is to assess the sensitivity of the basic reproduction number by computing its derivatives concerning all relevant parameters. This analysis will result in the determination of the normalized forward sensitivity index which is denoted as $\Gamma_Z^{R_\bullet} = \frac{\partial R_\bullet}{\partial Z} \times \frac{Z}{R_\bullet}$. Here we investigate the influence of various factors that affects the dynamic progression of cholera disease dynamics. Hence, the respective equations depicting the influence on cholera spread is obtained in Eqn. (42) and its values are illustrated in Table 4 below.

$$\frac{\partial R_*}{\partial \beta} = \frac{\partial R_*}{\partial \beta} \times \frac{\beta}{R_*} = 1.002863633, \frac{\partial R_*}{\partial \phi_1} = \frac{\partial R_*}{\partial \phi_1} \times \frac{\phi_1}{R_*} = 0.001307654,$$

$$\frac{\partial R_*}{\partial \phi_2} = \frac{\partial R_*}{\partial \phi_2} \times \frac{\phi_2}{R_*} = 1.1096546, \frac{\partial R_*}{\partial \mu} = \frac{\partial R_*}{\partial \mu} \times \frac{\mu}{R_*} = 0.15356728, \tag{42}$$

$$\frac{\partial R_*}{\partial \varphi} = \frac{\partial R_*}{\partial \varphi} \times \frac{\varphi}{R_*} = 0.765438, \frac{\partial R_*}{\partial \pi} = \frac{\partial R_*}{\partial \pi} \times \frac{\pi}{R_*} = 0.564321$$

The above results generated descriptively are depicted in Table 3 below.

Table 4: Sensitivity analysis of parameter and indices.

Parameters	Sensitivity indices
β	1.002863633
ϕ_1	0.001307654
ϕ_2	1.1096546
μ	0.15356728
φ	0.765438
π	0.564321

Table 4 above shows that the sensitivity indices are positively invariant in $\mathfrak{R}_6^+$. The sensitivity indices depend on the values of each parameter of R_* and this brings about changes in the values that will affect the behavior of the threshold on the spread or vanity of cholera disease. Based on the Table 3, above, we can conclude that parameter ε is the most sensitive to the basic reproduction number of the cholera disease. Particularly, increasing the value of ε will result in a 80.86% increase in R_*, while increasing the value of k will lead to a 91.52% decrease in R_*.

3.4. Numerical Simulation

Numerical simulation was conducted on the cholera model by creating the following iterative scheme of Laplace Adomian Decomposition Method for the model equation. The (LADM) was employed to computationally analyze the epidemic model. Also, Maple 18 software

facilitated the generation of iteration formulas for each compartment. These formulars were then iteratively solved which enables the numerical evaluation of the model's dynamics and providing insights into the epidemic's behavior and progression. Taking the (LADM) transforms from both sides of the system of Eqn. (1) to the form of Eqn. (43) below.

$$L\left[\frac{dS}{dt}\right] = L[\pi] - L[\beta SI - (\phi_1 + \mu)S + \delta R]$$

$$L\left[\frac{dV}{dt}\right] = L[\phi_1 S] - L[(1-\varepsilon)\beta IV - \mu V]$$

$$L\left[\frac{dE}{dt}\right] = L[(1-\varepsilon)\beta IV] - L[\beta SI - (k+\mu)E] \quad (43)$$

$$L\left[\frac{dI}{dt}\right] = L[kE] - L[(\alpha + \mu + \gamma + \phi_2)I]$$

$$L\left[\frac{dT}{dt}\right] = L[\phi_2 I] - L[(\varphi + \mu)T]$$

$$L\left[\frac{dR}{dt}\right] = L[\varphi T] - L[\gamma I - (\delta + \mu)R]$$

Substituting from Eqn. (1) into Eqn. (43) above to yield

$$mL[S(t)] = S(0) + \pi + L[-\alpha[SI] - \pi - \beta SI - (\phi_1 + \mu)S + \delta R]$$

$$mL[V(t)] = V(0) + L[\beta_1 S] - L[\phi_1 S - (1-\varepsilon)\beta IV - \mu V]$$

$$mL[E(t)] = E(0) + L[\alpha SI] - L[(1-\varepsilon)\beta IV + \beta SI - (k+\mu)E]$$

$$mL[I(t)] = I(0) + L[kE] - L[(\alpha + \mu + \gamma + \phi_2)I]$$

$$mL[T(t)] = I(0) + L[\phi_2 I] - L[(\varphi + \mu)T] \quad (44)$$

$$mL[R(t)] = R(0) + L[\varphi T] - L[\gamma I - (\delta + \mu)R]$$

Where at initial values of each state variables, $S(0) = s_0$, $V(0) = v_0$, $E(0) = e_0$, $I(0) = i_0$, $R(0) = r_0$, the resulting iteration from Eqn. (44) gives that in Eqn. (45) below

$$L[S(t)] = \frac{s_0}{m} + \frac{\pi}{m^2} + \frac{1}{m}L[-\alpha[SI] - \beta SI - (\phi_1 + \mu)S + \delta R]$$

$$L[V(t)] = \frac{v_0}{m} + \frac{1}{m}L[\phi_1 S] - L[(1-\varepsilon)\beta IV - \mu V]$$

$$L[E(t)] = \frac{e_0}{m} + \frac{1}{m} + L[(1-\varepsilon)\beta I] - L[\beta SI - (k+\mu)E] \tag{45}$$

$$L[I(t)] = \frac{i_0}{m} + \frac{1}{m} + L[kE] - L[(\alpha + \mu + \gamma + \phi_2)I]$$

$$mL[T(t)] = \frac{r_0}{m} + \frac{1}{m} + L[\phi_2 I] - L[(\varphi + \mu)T]$$

$$mL[R(t)] = \frac{r_0}{m} + \frac{1}{m} + L[\varphi T] - L[\gamma I - (\delta + \mu)R]$$

Letting the non-linear terms in the above iteration and substitutes by taking the inverse Laplace transform of both sides, we have

$$S(t) = s_0 + \pi t + L^{-1}\left(\frac{1}{m}L[\pi - \beta SI - (\phi_1 + \mu)S + \delta R]\right)$$

$$V(t) = v_0 + L^{-1}\left(\frac{1}{m}L[\phi_1 S] - L[(1-\varepsilon)\beta IV - \mu V]\right)$$

$$E(t) = e_0 + L^{-1}\left(\frac{1}{m} + L[(1-\varepsilon)\beta] - L[\beta SI - (k+\mu)E]\right) \tag{46}$$

$$I(t) = i_0 + L^{-1}\left(\frac{1}{m} + L[kE] - L[(\alpha + \mu + \gamma + \phi_2)I]\right)$$

$$T(t) = i_0 + L^{-1}\left(\frac{1}{m} + L[\phi_2 I] - L[(\varphi + \mu)T]\right)$$

$$R(t) = r_0 + L^{-1}\left(\frac{1}{m}L[\varphi T] - L[\gamma I - (\delta + \mu)R]\right)$$

Subsequently, iteration results obtained from the above Eqn. (46) which is deduced from the general iterative series in Eqn. (47) below as,

$$\sum_{k=0}^{\infty} S_n(t) = s_0 + \pi t + L^{-1}\left(\frac{1}{m}L\left[-\alpha\sum_{k=0}^{\infty}\pi_n - \phi_1\sum_{k=0}^{\infty}S_n + \phi_2\sum_{k=0}^{\infty}V_n - \mu\sum_{k=0}^{\infty}S_n\right]\right)$$

$$\sum_{k=0}^{\infty} V_n(t) = v_0 + \pi t + L^{-1}\left(\frac{1}{m}L\left[-\sum_{k=0}^{\infty}((1-\varepsilon)\beta) - \beta_1\sum_{k=0}^{\infty}V_n + \beta_2\sum_{k=0}^{\infty}V_n - \mu\sum_{k=0}^{\infty}V_n\right]\right)$$

$$\sum_{k=0}^{\infty} E_n(t) = e_0 + L^{-1}\left(\frac{1}{m} + L\varphi\sum_{k=0}^{\infty}\varepsilon_n - L[\beta - (k+\mu)]\sum_{k=0}^{\infty}E_n\right)$$

$$\sum_{k=0}^{\infty} I_n(t) = i_0 + L^{-1}\left(\frac{1}{m} + L\delta\sum_{k=0}^{\infty}E_n - L[(\alpha+\mu+\gamma+\phi_2)]\sum_{k=0}^{\infty}I_n\right) \tag{47}$$

$$\sum_{k=0}^{\infty} T_n(t) = i_0 + L^{-1}\left(\frac{1}{m} + L\alpha\sum_{k=0}^{\infty}E_n - L[(\varphi+\mu)]\sum_{k=0}^{\infty}T_n\right)$$

$$\sum_{k=0}^{\infty} R_n(t) = i_0 + L^{-1}\left(\frac{1}{m} + L\phi_2\sum_{k=0}^{\infty}E_n - L[(\delta+\mu)]\sum_{k=0}^{\infty}R_n\right)$$

The initial approximations of each class are given by Eqn. (44). Comparing the coefficients at $n = 1$, using the recurrence relations obtained from the iterations in Eqn. (47). Compartmentally, we obtained that

$$S_1(t) = (\pi i_0 s_0 - \mu s_0 - \beta s_0 + \phi_1 v_0)t + \left(-\frac{1}{2}\alpha i_0\varepsilon - \frac{1}{2}\mu\pi - \frac{1}{2}\delta\varphi_1\right)t^2$$

$$V_1(t) = \left(-\mu s_0 + \varphi i_1 s_0 - \beta v_0 + (1-\varepsilon)\varepsilon e_0\right)t + \frac{1}{2}\varepsilon\beta_1 t^2$$

$$E_1(t) = \left(\varphi i_0 s_0 - \mu e_0 - \delta e_0\right)t + \frac{1}{2}\alpha\pi i_1 t^2$$

$$I_1(t) = kE - (\alpha+\mu+\gamma+\phi_2)I\left(-\delta i_0 - \alpha + \mu + \gamma + \phi_2 e_0 i_0 + \sigma e_0\right)t$$

$$T_1(t) = \left(-\mu r_0 + \phi_2 s_0 v_0 + (\varphi+\mu)i_0\right)t$$

$$R_1(t) = \frac{1}{3}\varphi\phi_2\left(-\varphi + \mu r_0 + \frac{1}{2}(\delta+\mu)i_0\right)t \tag{48}$$

Further iterations are done to obtain successive iterative terms at n = 2 which gives Eqn. (49) below

$$S_2(t) = \left(\frac{1}{2}\alpha^2 i^2 s_0 + \frac{1}{2}\alpha i s_0 + \frac{1}{3}\alpha i s_0\mu_0 + \frac{1}{2}\alpha i s_0\rho_0 - \frac{1}{2}\alpha i s_0 e_0 + \frac{1}{2}\alpha i s_0\beta_1 - \frac{1}{2}\alpha i s_0\beta_2\right)t$$

$$+ \left(\frac{1}{2}\mu^2 s_0 + \beta_1\mu s_0 + \beta_1\mu v_0 + \frac{1}{2}\beta^2 s_0 + \frac{1}{2}\beta_1\right)t^2 + \left(\frac{1}{6}\alpha^2 i^2\theta + \frac{1}{3}\alpha i_0\pi\delta + \frac{2}{3}\alpha i_0\pi\mu\right)t^3$$

$$V_2(t) = -\frac{1}{2}\left(\alpha i s_0 \beta_1 + \frac{1}{2}\mu^2 v_0 - \beta_1 \mu s_0 + \beta_2 \mu s_0 - \frac{1}{2}\beta_1 \beta_2 v_0 + \frac{1}{2}\beta_2^2 v_0\right)t^2$$
$$-\left(\frac{1}{6}\alpha i_0 \pi \beta_1 - \frac{1}{3}\beta_1 \mu \pi - \frac{1}{6}\beta_1^2 \pi + \frac{1}{6}\beta_2 \pi \beta_1\right)t^3$$

$$E_2(t) = \left(-\frac{1}{6}\alpha^2 i^2 - \frac{1}{3}\alpha i_0 \delta - \frac{2}{3}\alpha i_0 \mu - \frac{1}{3}\alpha i_0 \rho + \frac{1}{3}\alpha e_0 \sigma_1 - \frac{1}{6}\mu^2 - \frac{1}{6}\alpha i_0 \pi \beta_1\right)t^3$$
$$-\left(\frac{1}{2}\alpha^2 i^2 s_0 - \sigma i s_0 - \frac{2}{3}\alpha i s_0 \mu_0 - \frac{1}{3}\alpha i s_0 \rho_0 - \mu^2 i e_0 \beta_1 + \frac{1}{2}\alpha i e_0 \sigma^2\right)t^2$$

$$I_2(t) = -\frac{1}{6}\alpha^2 + \left(\sigma \alpha i s_0 + \frac{1}{2}\delta^2 i_0 + \delta \mu i_0 - \delta \sigma i e_0 + \mu^2 i_0 - \mu \rho i_0\right)t - \left(\mu \sigma i_0 + \frac{1}{2}\rho^2 i_0\right)t^2$$

$$T_2(t) = \left(\frac{1}{2}\sigma \alpha i s_0 + \frac{1}{2}\delta^2 i_0 + \delta \mu i_0 - \frac{1}{2}\delta \sigma i e_0 + \frac{1}{2}\mu^2 i_0 - \mu \rho i_0\right)t$$
$$+\left(\mu \sigma i_0 + \frac{1}{2}\rho^2 i_0 - \frac{1}{2}\rho \sigma i e_0\right)t^2$$

$$R_2(t) = \left(-\frac{1}{2}\delta \rho i_0 + \frac{1}{2}\mu^2 r_0 - \mu \sigma i_0 - \frac{1}{2}\rho^2 i_0 + \frac{1}{2}\phi 1 \varphi e_0\right)t^2$$

and so on. This can be further resolved untived until the desired number of iterations is obtained. Thus, the obtained raw solution to each model compartment is summarily expressed in some form as shown in Eqn. (49) below:

$$S(t) = \sum_{k=0}^{3} s_k(t), V(t) = \sum_{k=0}^{3} v_k(t), E(t) = \sum_{k=0}^{3} e_k(t), I(t) = \sum_{k=0}^{3} i_k(t), R(t) = \sum_{k=0}^{3} r_k(t) \quad (49)$$

Evaluating these series results using the corresponding variables and parameter values, gives:

$$S(t) = 500.012 - 30.4440t + 1.1315290300t^2 - 0.05075029853t^3$$
$$-3.509616000x10^{-13}t^5 - 5.179149070x10^{-7}t^4$$

$$V(t) = 120 - 1.5060t - 0.01591470000t^2 + 0.001033697580t^3$$
$$+9.015111000 \times 10^{-9}t^4$$

$$E(t) = 65 + 18.1785t - 1.171778775t^2 + 0.04929560765t^3$$
$$+5.087939775 \times 10^{-7}t^4$$

$$I(t) = 23.0.9 - 60t + 0.0292567500t^2 - 0.0008440367798t^3$$
$$-4.378044000 \times 10^{-9}t^4$$

$$(50)$$

$$T(t) = 23.0.9 - 60t + 0.0292567500t^2 - 0.0008440367798t^3$$
$$- 4.378044000 \times 10^{-9} t^4$$

$$R(t) = 14 - 0.0155t - 0.005054500000t^2 + 0.0001458242541t^3$$
$$+ 2.473075000 \times 10^{-10} t^4$$

Hence, from the results of successive iterations in Eqn. (50), the comparison of control intervention effects on sub-populations in its graphical illustration is depicted as shown in Table 5 below.

Table 5: Comparison of parameters ϕ_1 and ϕ_2 values for ε at $\varepsilon = 0, 0.2, ..0.5$.

Variables	Description	at $\varepsilon = 0.1, 0.25, 0.5$
E(t)	exposed population	0.5, 0.25, 0.125
I(t)	infected population	0.5, 0.25
R(t)	recovered population	0.1, 0.25...0.5
ϕ_1	treatmen tintervention	0.1, 0.2,... 0.5
ϕ_2	Vaccination intervention	0.1, 0.2,... 0.5

4. Iterative Results

Graphical illustration of the resulting iterations is thus shown below:
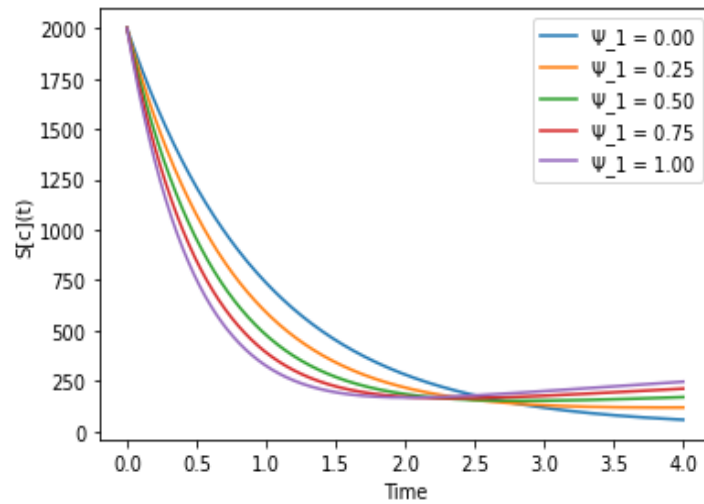
Figure 2: Effect of treatment rate on susceptible individuals.
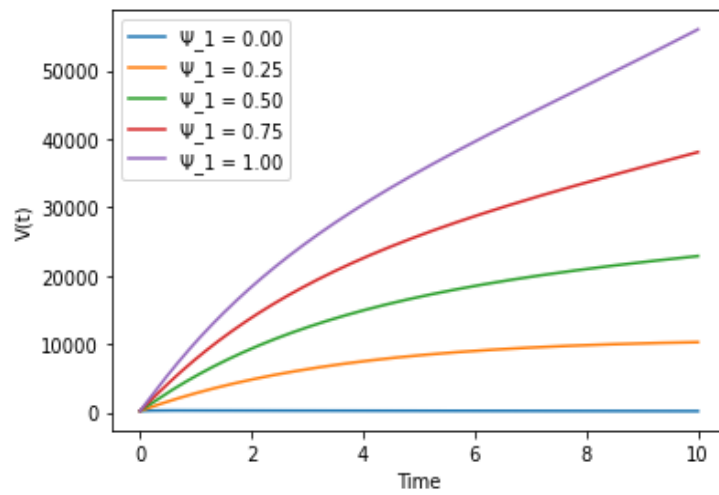
Figure 3: Adverse effect of treatment rate on the population of vaccinated individuals.
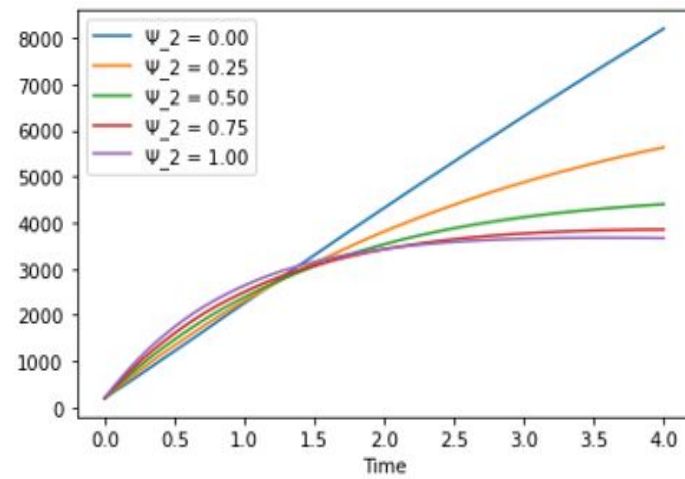
Figure 4: Adverse Increase of vaccination efficacy on individuals in the recovered population.
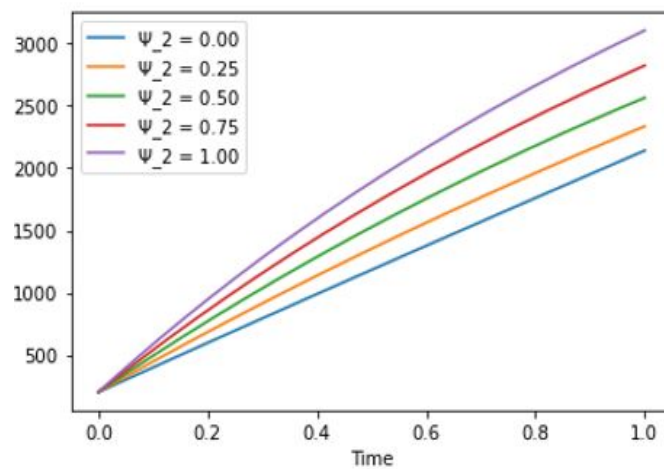
Figure 5: Increase in vaccination rate on exposed population.
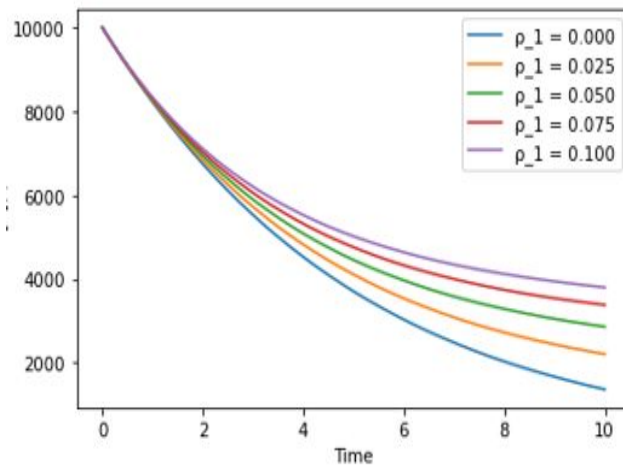
Figure 6: Effect of treatment rate on infected population.
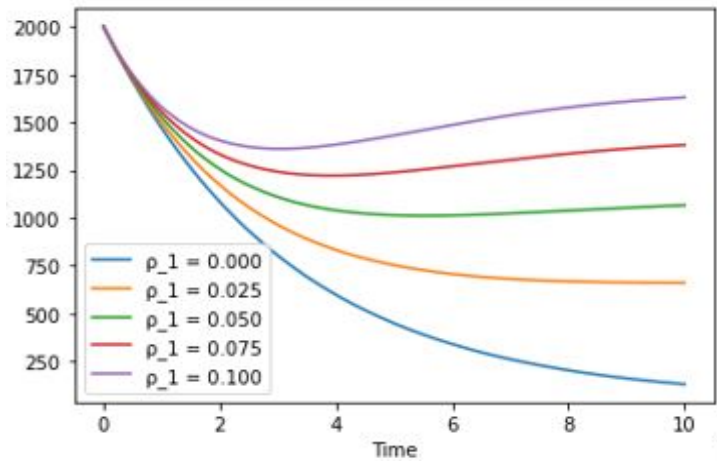
Figure 7: Effect of treatment rate on infected population.

5. Discussion of Graphical Results

From results obtained, Fig. 2 and Fig. 3, depicts that the effect of treatment ϕ_2 and vaccination rate ϕ_1 on the population of susceptible, infected, exposed and recovered is vital to the control of cholera disease as this brings about a rise in its efficacy and steep-slope in the spread of the viral disease in the disease compartments. In Fig. 4 shows the effect of vaccination rate on the population of the recovered individuals, as a rise the vaccination rate increases the population of the susceptible and rescored population which leads to a drastic fall in the exposed and infected population. Consequently, Fig. 5 and Fig. 6 depicts that an increases in treatment rate of exposed individuals will lead to an increase in the population of non-diseases classes. However, comparison of the control policies of on the infected population of Fig. 7 came with a rise in treatment and vaccination rate increases bring about drastic fall in the wide spread of cholera

disease in the disease population. Lastly, from the susceptible population of Fig. 8, the adverse effect of vaccination and treatment on this population brings about a rapid influx of non-disease class of individuals who reunite into the population free of the deadly diseases. This implies that, vaccination and treatment rate are vital control measures to eradicating the wide spread of cholera from the populace. The effect of vaccination and treatment brings about convergence to the spread of cholera disease in the exposed and infected population respectively.

6. Conclusion

The study explains that combining rapid treatment, and vaccination will significantly aid in the control of the spread of cholera. These interventions reduce infection rates and mitigate the disease's impact in endemic regions. It is imperative for healthcare personnel to prioritize and adhere to these measures to assist in controlling cholera outbreaks effectively. Prompt treatment and widespread vaccination should be an integral component of public health strategies to combat this persistent and potentially devastating disease. It is therefore recommended that adequate awareness, environmental sanitation in lieu of water treatment, and antibiotics can also be looked into in the future to study towards curtailing the spread of this disease. We can achieve substantial progress in managing and eventually controlling the spread of cholera.

Acknowledgements

References

[1] Babalola, O.O, Adebisi, A.F, Odeyemi, K.A., *Numerical Solution for Linear Integro-Differential Equations using Shifted Legendre Basis Functions*, Jurnal Diferensial, Indonesia, 7, 55–72, 2025.

[2] Olaosebikan, M.L., Kolawole, M.K., Bashiru, K.A., *Transmission Dynamics of Tuberculosis Model with Control Strategies*, Jambura Journal of Biomathematics, *4*(2), 110–118, 2023.

[3] Dere Z.O, Oladapo, A.O., *Mathematical (Seirb) Model Analysis for Evaluating Cholera Control Strategies in Remote Dry Season Region,* Jurnal Diferensial, 6, 142–169, 2024.

[4] Harpring, R., Maghsoudi, A., Fikar, C., Piotrowicz, W.D., *An Analysis of compounding factors of Epidemics in Complex Emergencies: a System Dynamics Approach*, Journal of Humanitarian Logistics and Supply Chain Management, 11, 198–226, 2021.

[5] Oladapo, A.O., Olayiwola, M.O., Adedokun, K.A., Alaje, I.A., Adedeji, J.A., Kabiru, K.O., *Optimal Control Analysis on Mathematical Model of Dynamical Transmission of Hiv-Malaria Co-Infection,* Journal of Southwest Jiaotong University, 58, 124–148, 2023.

[6] Oladapo, A.O., Olayiwola, M.O., Adedokun, K.A., Adedapo, A.I., Adedeji, J.A., Kabiru, K.O., et al., *Mathematical Analysis of Sensitive Parameters on the Dynamical Transmission of HIV-Malaria Co-Infection*, Jambura Journal of Biomathematics, 4, 37–45, 2023.

[7] Bhandari, M., Rathnayake, I.U., Huygens, F., *Genomic and Evolutionary insights into Asutralian Toxigenic Vibrio Cholerae 01 Strains*, Microbiology Spectrum, 17, 20–27, 2024.

[8] Hoefer, A., Pampaka, D., Herrera-Leon, S., Peiro, S., Varona, N., *Molecular and Epidemiological Characterization of Toxigenic and non-toxigenic Corynebacterium Diphtheriae, Corynebacterium Belfanti, Corynebacterium Rouxii*, Tanzania journal of sciences, 59, 32–48, 2025.

[9] Eftimie, R., Gillard, J.J., Cantrell, D.A., *Mathematical Models for Immunology: Current State of the Art and Future Research Directions*, Bulletin of Mathematical Biology, 78, 2091–2134, 2023.

[10] Engerman, S., Sokolloff, K., *Factor Endowments, Inequality, and Paths of Development among New World Economics*, Ethiopia Journal of Computational and Vatural Sciences, 3, 234–256, 2025.

[11] Feldman W.E., *Relation of Concentrations of Bacteria and Bacterial Antigen in Cerebrospinal Fluid to Prognosis in Patients with Bacterial Meningitis*, National England Journal of Medicine; 29, 433–35, 2023.

[12] Fing, C.H., Fitter, D.L., Borse, R.H., Meltzer, M.I., Tappero, J.W., *Modeling the Effect of Water, Sanitation, and Hygiene and Oral Cholera Vaccine Implementation in Haiti*, American Journal of Tropical Medicine and Hygiene, *89*, 633–640, 2024.

[13] Hanney, S.R., Gonzalez-Block, M.A., Buxton, M.J., Kogan, M., *The Utilisation of Health Research in Policy-Making Concepts, Examples and Methods of Assessment*, Health Research Policy and Systems, 1, 23–38, 2023.

[14] Mojtaba, M.E., Adam, S.O., A *Mathematical Model for Meningitis Disease*, Red Sea University Journal of Basic and Applied Science, 2, 467– 472, 2024.

[15] Asamoah, J.K., Nyabadza, F., Seidu, B., Chand, B., Dutta, H., *Mathematical Modeling of Bacterial Meningitis Transmission Dynamics with Control Measures*, Computational and Mathematical Methods in Medicine, 2, 29-41, 2023.

[16] Audrey, S., Abel, J., Blazeby, J.M., Falk, S., Campbell, R., *What Oncologists tell Patients about Survival Benefits of Palliative Chemotherapy and Implications for Informed Consent: Qualitative Study*, Bio-Medical Journal of Sciences, 3, 182–105, 2024.

[17] Azman, A.S., Lessler, J., *Reactive Vaccination in the Presence of Disease Hotspots*, Proceedings of the Royal Society of Biological Sciences, 282, 20–38, 2024.

[18] Baleanu, D., Aydogan, M., Mohammadi, H., Rezapour, S., *On Modeling of Epidemic Childhood Diseases with the Caputo-Fabrizio Derivative by using the Laplace Adomian Decomposition Method*, Alexandria Engineering Journal, *59*, 3029–3039, 2023.

[19] Agrawal, R., Murmu, J., Kanungo, S., Pati, S., *Nigeria on Alert: Diphtheria Outbreaks Require Urgent Action - A Critical Look at the Current Situation and Potential Solutions*, New Microbes and New Infections, *52*, 10–27, 2023.

[20] Akra-Ismail, M., Makki, R.F., Chmaisse, H.N., Kazma, A., Zgheib, N.K., *Association between Angiotensin-Converting Enzyme Insertion/Deletion Genetic Polymorphism and Hypertension in a Sample of Lebanese Patients*, Genetic Testing and Molecular Biomarkers, 14, 787–792, 2024.

[21] Ahmed, J., Halvorson, G.W., Gates, J.R., *Measles-like Disease and Measles Antibody Titers in an Adult Population*. Military Medicine, 144, 672–676, 2024.

[22] Aniji, K., Chiu, Y.L., Wilkin, T., *Measles, Mumps, and Rubella Serostatus and Response to MMR Vaccination among HIV-Infected Adults*, *AIDS Patient Care and STDs*, 29, 461–464, 2024.

[23] Asaboyi, J.L., Nashair, B.S., Bashaei, M.K., *Executive Summary of the Third Report of the National Cholesterol Education Program (NCEP) Expert Panel on Detection, Evaluation, and Treatment of High Blood Cholesterol in Adults (Adult Treatment Panel III)*, JAMA, 19, 86–97, 2024.

[24] Biggins, S.W., Angeli, P., Garcia-Tsao, G., Ginès, P., Ling, S.C., *Diagnosis, Evaluation and Management of Ascites, Spontaneous Bacterial Peritonitis and Hepatorenal Syndrome*, American Journal of Bio-Mathematics, 34, 29–40, 2024.

[25] Celen, O., *Factors Influencing Outcome of surgery for primary Aldosteronism*, Archives of Surgery, 6, 64–76, 2024.

[26] John, F., Castillo, C., Feng, Z., Huang, W., *On the computation of basic reproduction number and its role in global stability in mathematical approaches for emerging and reemerging infectious diseases*, Decision Analytics, 25, 229–250, 2023.

Some Properties of the Generalization of the p-Adic Factorial and the p-Adic Gamma Function

Rafik BELHADEF[1],[*], Nour Elhouda SAHALI[2]

[1]*University of Jijel, Faculty of Exact Sciences and Computer Science, Department of Mathematics, Laboratory of Pure and Applied Mathematics, BP98, Jijel, Algeria*
Belhadef_rafik@univ-jijel.dz, ORCID: 0000-0003-1523-9439
[2]*University of Jijel, Faculty of Exact Sciences and Computer Science, Department of Mathematics, BP98, Jijel, Algeria*
hodasahali2000@gmail.com, ORCID: 0009-0001-9931-7512

Abstract

In this work, we investigate several properties of the generalized p-adic gamma function Γ_q. We demonstrate remarkable identities and special values of Γ_q. We also derive a novel representation of Γ_q via its Mahler expansion and establish relationships among the coefficients within this expansion. To simplify this study, we introduce the definition of the q-adic factorial and establish its properties. In addition, some congruences are derived for this new concept.

Keywords: Mahler expansions; p-adic gamma function; p-adic factorial; p-adic number.

p-Adik Faktöriyelin ve p-Adik Gama Fonksiyonunun Genellemesinin Bazı Özellikleri

Öz

Bu çalışmada, genelleştirilmiş p-adik gama fonksiyonu Γ_q'nun çeşitli özelliklerini araştırıyoruz. Γ_q'nun dikkate değer özdeşliklerini ve özel değerlerini gösteriyoruz. Ayrıca Γ_q'nun Mahler açılımı aracılığıyla yeni bir gösterimini türetiyor ve bu açılımdaki katsayılar arasında ilişkiler kuruyoruz. Bu çalışmayı basitleştirmek için q-adik faktöriyel tanımını tanıtıyor ve özelliklerini belirliyoruz. Ek olarak, bu yeni kavram için bazı kongrüanslar türetiyoruz.

Anahtar Kelimeler: Mahler açılımı; p-adik gama fonksiyonu; p-adik faktöriyel; p-adik sayı.

1. Introduction

In 1897, Kurt Hensel introduced the p-adic numbers, which are an extension of the rational numbers for a given prime number p. These numbers have become essential in modern mathematics, due to their wide applications in number theory, analysis, mathematical physics, and cryptography. The unique representation of the p-adic numbers is given by the infinite series:

$$x = \sum_{j=m}^{+\infty} x_j p^j \quad , \qquad \text{where } x_j \in \{0, 1, \dots, p-1\} \text{ and } m \in \mathbb{Z}.$$

The p-adic gamma function Γ_p is the p-adic analog of the classical gamma function. In 1975, Morita [1] defined Γ_p as a unique continuous extension of the following sequence:

$$\Gamma_p(n+1) = (-1)^{n+1} \prod_{\substack{k=1 \\ (p,k)=1}}^{n} k \quad , \qquad \text{where } n \in \mathbb{N}.$$

Several generalizations of the p-adic gamma function have been proposed (see [2-5]), one of which was presented by Kaori Ota in 1994 [4]. To facilitate the study of the generalized p-adic hypergeometric function, Ota defined the generalized p-adic gamma function Γ_q, where $q = p^t$ and t is a positive integer, by the formula:

$$\Gamma_q(\alpha + 1) = \Gamma_p(h_\ell(\alpha) + 1).$$

such that $\alpha = \sum_{j=0}^{+\infty} \alpha_j p^j$ and $h_\ell(\alpha) = \sum_{j=\ell}^{+\infty} \alpha_j p^{j-\ell}$ for $\ell \in \mathbb{N}$.

The representation of generalized hypergeometric functions in terms of generalized gamma functions is particularly important. Such representations consistently yield results of notable mathematical significance, especially in applied contexts. The profound utility of these relationships manifests across multiple disciplines, including quantum field theory, analytic number theory, and cryptography.

N. Koblitz [3] proposed another extension of the p-adic gamma function, using the same notation Γ_q for his modified function. However, this shared notation does not lead to confusion. Both Koblitz's and Ota's generalized p-adic gamma functions were presented without complete characterizations of their properties.

In this paper, we introduce the concept of a q-adic factorial and establish several congruences and inequalities related to this new construct (see Definition 3.1, Lemma 3.3, Proposition 3.6, Proposition 3.7, Corollary 3.8, and Corollary 3.9). Furthermore, we present a definition of the generalized p-adic gamma function Γ_q and we demonstrate some of its combinatorial properties, similar to those of the p-adic gamma function (see Proposition 3.15, Proposition 3.16, and Corollary 3.17). Additionally, we propose a Mahler expansion for Γ_q and prove the relationships between its coefficients (see Proposition 3.18). Finally, we provide several numerical examples to illustrate our results (see Examples 3.4 and 3.13). These results offer new insights into the combinatorial and analytic structure of p-adic special functions and paving the way for further developments.

2. Preliminaries

2.1. Notations

In this work, we use the following concepts: $p \in \{2,3,5,7,11,13,17,\dots\}$ is a prime number, $\mathbb{Z}$ denotes the set of integers, $\mathbb{Z}_-$ (resp. $\mathbb{Z}_+$) represents the set of negative integers (resp. the positive integers), $\mathbb{Z}^*$ is the set of non-zero integers. The set of non-negative integers is denoted by $\mathbb{N}$, the field of rational numbers is $\mathbb{Q}$, and $\mathbb{R}$ is the field of real numbers. The absolute value in $\mathbb{R}$ is denoted by $|.|$, and the real integer part is denoted by $[.]$.

The p-adic valuation is defined as $v_p(0) = +\infty$ and for $n \in \mathbb{Z}^*$ by $v_p(n) = \max\{r \in \mathbb{Z} / p^r \text{ divides } n\}$. For $\frac{n}{m} \in \mathbb{Q}$, the p-adic valuation is given by $v_p\left(\frac{n}{m}\right) = v_p(n) - v_p(m)$.

The p-adic absolute value of an element in $\mathbb{Q}$ is given as

$$|a|_p = \begin{cases} p^{-v_p(a)} & \text{if } a \neq 0 \\ 0 & \text{if } a = 0 \end{cases}.$$

The completion of $\mathbb{Q}$ with respect to the p-adic absolute value $|.|_p$ yields a field, known as the field of p-adic numbers, denoted by $\mathbb{Q}_p$. The p-adic absolute value on $\mathbb{Q}_p$ is the extension of that on $\mathbb{Q}$. The set of p-adic integers, denoted $\mathbb{Z}_p$, contains the p-adic numbers that satisfy $|a|_p \leq 1$. For more details about p-adic numbers, we refer to the classical book of Gouvêa [6].

2.2. The p-adic Factorial and the p-adic Gamma Function

In this part, we present the concept of the p-adic factorial and the p-adic gamma function, along with several fundamental properties.

Definition 2.1. [7] We define the p-adic factorial by $0!_p = 1$, and for $n \in \mathbb{N}$ is given by

$$n!_p = \prod_{\substack{m=1 \\ p \nmid m}}^{n} m. \tag{1}$$

For more details and properties of this concept see [7].

The p-adic gamma function has found significant applications in dynamic systems and string theory. Various mathematicians [8-10] have utilized this function to explore properties of polynomials.

Definition 2.2. [1] The p-adic gamma function is a function $\Gamma_p : \mathbb{Z}_p \to \mathbb{Z}_p$ that extends the following sequence: $\Gamma_p(n+1) = (-1)^{n+1} n!_p$, for $n \in \mathbb{Z}_+$. Which we have, for $x \in \mathbb{Z}_p$:

$$\Gamma_p(x) = \lim_{n \to x} \Gamma_p(n).$$

Here, we cite the properties of Γ_p that we will give their analogue for the generalization of Γ_p in the next section.

Proposition 2.3. [11] The function Γ_p holds the following properties

1. $\Gamma_p(0) = 1$, $\Gamma_p(1) = -1$, $\Gamma_p(2) = 1$.

2. $\Gamma_p(n+1) = (-1)^{n+1} n!_p$, $\forall n \in \mathbb{N}$.

Proposition 2.4. [11] Let $n \geq 1$ be a positive integer with its p-adic expansion given by $\sum_{j=0}^{\ell} n_j p^j$ and we suppose the sum of digits is $S_n = \sum_{j=0}^{\ell} n_j$. Then,

For $\mu = \left[\frac{n}{p}\right]$, we have $\Gamma_p(n+1) = \frac{(-1)^{n+1}\, n!}{\mu!\, p^\mu}$. In particular $\Gamma_p(p^k) = \frac{(-1)^p\, p^{k}!}{p^{k-1}!\, p\, p^{k-1}}$,

1. For $m \in \mathbb{N}$ such that $0 \le \lambda < p$, we have

$$\Gamma_p(np + \lambda + 1) = \frac{(-1)^{np+\lambda+1}\,(np+\lambda)!}{n!\, p^n}.$$

2. We have the relation between $n!$ and Γ_p

$$n! = (-1)^{n+1-\ell}(-p)^{\frac{n-S_n}{p-1}} \prod_{i=0}^{\ell} \Gamma_p\left(\left[\frac{n}{p^i}\right]+1\right).$$

Theorem 2.5. [11] (Mahler Expansion of Γ_p)

For $x \in \mathbb{Z}_p$, let the Mahler expansion of Γ_p be given by the series $\Gamma_p(x+1) = \sum_{k=0}^{+\infty} \alpha_k \binom{x}{k}$, where the symbol $\binom{x}{\eta}$ is defined by $\binom{x}{0} = 1$ and $\binom{x}{\eta} = \frac{x(x-1)\dots(x-\eta+1)}{\eta!}$, $\eta = 1,2,\dots$

Then, the coefficients α_k satisfy the following relationship

$$\exp\left(x + \frac{x^p}{p}\right)\frac{1-x^p}{1-x} = \sum_{k=0}^{+\infty}(-1)^{k+1}\alpha_k\frac{x^k}{k!}. \tag{2}$$

3. Main Results and Proofs

Drawing on the work presented in [7], we will introduce a q-adic factorial and establish a few congruences and inequalities related to this new concept. We also provide a definition for the generalization of the p-adic gamma function and demonstrate some of its properties, including the Mahler expansion. Throughout this section, we consider $q = p^t$, where t is a positive integer.

3.1. The q-adic Factorial

Definition 3.1. The q-adic factorial is defined by $0!_q = 1$ and for $n > 1$ is equal to

$$n!_q = \prod_{\substack{k=1 \\ q \nmid k}}^{n} k. \tag{3}$$

Remark 3.2. If $1 \le n \le q-1$, then for all $1 \le k \le n$ we have $q \nmid k$. So, $n!_q = n!$.

Lemma 3.3. For $\delta \ge 1$, we have $(q\delta)!_q = (q\delta - 1)!_q$.

Proof. We observe that q divides $q\delta$, it means that

$$(q\delta)!_q = \prod_{\substack{k=1 \\ q\nmid k}}^{q\delta} k = \prod_{\substack{k=1 \\ q\nmid k}}^{q\delta-1} k = (q\delta - 1)!_q .$$

Example 3.4. In Tables 1, 2, and 3 we compute the q-adic factorials of a given positive integer, specifically for $q = 2^2, 2^3, 3^2$.

Table 1: For $q = 2^2$.

n	0	1	2	3	4	5	6	7	8	9	10	11
$n!_{2^2}$	1	1	2	6	6	30	180	1260	1260	11340	113400	1247400

Table 2: For $q = 2^3$.

n	0	1	2	3	4	5	6	7	8	9	10	11
$n!_{2^3}$	1	1	2	6	24	120	720	5040	5040	45360	453600	4989600

Table 3: For $q = 3^2$.

n	0	1	2	3	4	5	6	7	8	9	10	11
$n!_{3^2}$	1	1	2	6	24	120	720	5040	40320	40320	403200	4435200

A q-generalization of the Wilson congruence is given in the following theorem, which is necessary to prove the Proposition 3.6.

Theorem 3.5. Let $a \in \mathbb{Z}$ and $s > t$. Then

1. For p odd,

$$\prod_{\substack{j=a \\ q\nmid j}}^{a+p^s-1} j \equiv - \prod_{\substack{j=a \\ p\mid j}}^{a+p^s-1} j \ (\mathrm{mod}\ p^s).$$

2. For $p = 2$,

$$\prod_{\substack{j=a \\ q\nmid j}}^{a+2^s-1} j \equiv \prod_{\substack{j=a \\ j\ \text{even}}}^{a+2^s-1} j \ (\mathrm{mod}\ 2^s).$$

Proof. We have

$$\prod_{\substack{j=a \\ q\nmid j}}^{a+p^s-1} j = \left(\prod_{\substack{j=a \\ p\mid j}}^{a+p^s-1} j \right) \left(\prod_{\substack{j=a \\ p\nmid j}}^{a+p^s-1} j \right)$$

By generalizing the Wilson congruence, we obtain the result. For $p = 2$ is the same. From the previous, we get the following congruence.

Proposition 3.6. Let $n \in \mathbb{N}$ and $s > t$. Then

1. For p odd, we have $\dfrac{(n+p^s)!_q}{n!_q} \equiv -\prod_{\substack{j=n+1 \\ p\mid j}}^{n+p^s} j \pmod{p^s}$.

2. For p = 2, we have $\dfrac{(n+2^s)!_q}{n!_q} \equiv \prod_{\substack{j=n+1 \\ j \text{ even}}}^{n+2^s} j \pmod{2^s}$.

Proof. We calculate the quotient, we get

$$\frac{(n+p^s)!_q}{n!_q} = \prod_{\substack{j=n+1 \\ q\nmid j}}^{n+p^s} j \,.$$

Now, we take $a = n + 1$ in Case 1 of Theorem 3.5, we derive the congruence for p odd. Similarly, we obtain the result for $p = 2$, from case 2.

More generally, we establish the following proposition along with its immediate corollaries:

Proposition 3.7. Let $n, m, s \in \mathbb{Z}_+$ where $s > t$. Then

1. For p odd, we have

$$\frac{(n+mp^s)!_q}{n!_q} \equiv (-1)^m \prod_{\substack{j=n+1 \\ p\mid j}}^{n+mp^s} j \pmod{p^s}.$$

2. For p = 2 and s ≥ 3, we have

$$\frac{(n+m2^s)!_q}{n!_q} \equiv \prod_{\substack{j=n+1 \\ j \text{ even}}}^{n+2^s} j \pmod{2^s}.$$

Proof. This is proved by induction on m. Indeed, about the case $p \geq 3$ we have:

For $m = 1$ is true. We assume that the property is true at rank m and we demonstrate it at rank $m + 1$. We write

$$\frac{(n + (m + 1)p^s)!_q}{n!_q} = \frac{(n + mp^s)!_q}{n!_q} \cdot \prod_{\substack{j=n+mp^s+1 \\ q \nmid j}}^{n+(m+1)p^s} j$$

On the other hand

$$\frac{(n + mp^s)!_q}{n!_q} \equiv (-1)^m \prod_{\substack{j=n+1 \\ p \mid j}}^{n+mp^s} j \,(\mathrm{mod}\, p^s)$$

and

$$\prod_{\substack{j=n+mp^s+1 \\ q \nmid j}}^{n+(m+1)p^s} j \equiv - \prod_{\substack{j=n+mp^s+1 \\ p \mid j}}^{n+(m+1)p^s} j \,(\mathrm{mod}\, p^s)$$

So

$$\frac{(n + (m + 1)p^s)!_q}{n!_q} \equiv \left((-1)^m \prod_{\substack{j=n+1 \\ p \mid j}}^{n+mp^s} j \right) \left(- \prod_{\substack{j=n+mp^s+1 \\ p \mid j}}^{n+(m+1)p^s} j \right) \,(\mathrm{mod}\, p^s)$$

$$\equiv (-1)^{m+1} \prod_{\substack{j=n+1 \\ p \mid j}}^{n+(m+1)p^s} j \,(\mathrm{mod}\, p^s)$$

Then the property is true for all m. For $p = 2$ is the same.

The following corollaries follow from Proposition 3.6 and are presented here without proof.

Corollary 3.8. For $p \geq 3$, $n \in \mathbb{N}$ and $s \in \mathbb{Z}_+$ where $s > t$, we have

$$\left| (n + p^s)!_q + n!_q \prod_{\substack{j=n+1 \\ p \mid j}}^{n+p^s} j \right|_p \leq \frac{1}{p^s}.$$

Corollary 3.9. For p = 2, n ∈ ℕ and s ∈ ℤ₊ and s ≥ 3 where s > t, we have

$$\left| (n + 2^s)!_q - n!_q \prod_{\substack{j=n+1 \\ j \text{ even}}}^{n+2^s} j \right|_2 \leq \frac{1}{2^s}.$$

3.2. Generalized *p*-adic Gamma Function

In this important subsection, we present the definition of the generalized *p*-adic gamma function, which was originally introduced by Kaori Ota in [4], and we also explore in depth several of its significant properties. Moreover, we establish new properties of this function that were not covered in Ota's original work. For other references on this subject, see [12-13].

Definition 3.10. [4] Let $x \in \mathbb{Z}_p$ be given by its *p*-adic expansion $\sum_{j=0}^{+\infty} x_j p^j$, where $x_0 \neq 0$ and $x_j \in \{0, 1, \cdots, p - 1\}$ for all $j \in \mathbb{N}$. Ota define a map h_ℓ for $\ell \in \mathbb{N}$ by a formula

$$h_\ell(x) = \sum_{j=\ell}^{+\infty} x_j p^{j-\ell}. \tag{4}$$

Furthermore, we have

$$x = \sum_{j=0}^{\ell-1} x_j p^j + p^\ell h_\ell(x). \tag{5}$$

Definition 3.11. [4] The generalized *p*-adic gamma function is defined from $\mathbb{Z}_p$ to $\mathbb{Z}_p$ by:

$$\Gamma_q(x + 1) = \prod_{\ell=0}^{t-1} \Gamma_p(h_\ell(x) + 1). \tag{6}$$

Remark 3.12. For $t = 1$ the function Γ_q coincides with Γ_p, i.e.

$$\Gamma_q(x + 1) = \Gamma_p(h_0(x) + 1) = \Gamma_p(x + 1).$$

Example 3.13. For $t = 2$, we have $q = p^2$ so

$$\Gamma_q(x + 1) = \Gamma_p(h_0(x) + 1)\Gamma_p(h_1(x) + 1)$$

$$= \Gamma_p(h_0(x) + 1)\Gamma_p(h_1(x) + 1).$$

according to the relationship Eqn. (5) we have $x = x_0 + ph_1(x)$, hence

$$h_1(x) = \frac{x - x_0}{p}.$$

Therefore

$$\Gamma_q(x + 1) = \Gamma_p(x + 1)\Gamma_p\left(\frac{x - x_0}{p} + 1\right).$$

For example, if $x = 3$, $p = 3$ and $t = 2$, so $q = 3^2$. Then, $\Gamma_9(4) = \Gamma_3(4)\Gamma_3(2) = 2$.

In his paper [4], Ota presented some properties of the generalized p-adic gamma function. Among them, the following property is especially remarkable.

Proposition 3.14. [4]

1. For a positive integer n, we have

$$\Gamma_q(n + 1) = (-1)^{A_n} p^{-B_n} n!_q \tag{7}$$

where

$$A_n = t + \sum_{i=0}^{t-1} t\left[\frac{n}{p^i}\right] \quad \text{and} \quad B_n = \sum_{i=1}^{t}\left[\frac{n}{p^i}\right] - t\left[\frac{n}{p^t}\right].$$

2. For p odd and $x \in \mathbb{Z}_p$, the complement formula is given by

$$\Gamma_q(x)\Gamma_q(1 - x) = (-1)^{t-1+R_t(x)}, \tag{8}$$

where $R_t(x) \in \{1, 2, \ldots, q\}$ is the representative of x modulo $q\mathbb{Z}_p$.

Next, we present our results concerning the combinatorial properties of the generalized p-adic gamma function and the coefficients of its Mahler expansion.

Proposition 3.15. The following statements are verified by the function Γ_q:

1. For a positive integer n and $\xi = \left[\frac{n}{q}\right]$, we have

$$\Gamma_q(n + 1) = \frac{(-1)^{A_n} p^{-B_n} n!}{\xi! \; q^{\xi}}. \tag{9}$$

2. For a positive integer m and $\lambda \in \{0, 1, \cdots, q - 1\}$, we have

$$\Gamma_q(mq + \lambda + 1) = \frac{(-1)^{A_{m,\lambda}} p^{-B_{m,\lambda}}(mq + \lambda)!}{m! \; q^m}. \tag{10}$$

where $A_{m,\lambda} = t + \lambda + mq + v_p(\lambda!)$ and $B_{m,\lambda} = m\left(\frac{q-1}{p-1}\right) - tm - t\left[\frac{\lambda}{q}\right] + v_p(\lambda!)$.

3. For $s \in \mathbb{N}$ we have

$$\Gamma_q(q^s) = \frac{(-1)^{A_{q^s-1}} p^{-B_{q^s-1}}(q^s-1)!}{q^{s-1}! \; q^{q^{s-1}}}.$$

(11)

where

$$A_{q^s-1} = t - 1 + \sum_{i=0}^{t-1} p^{ts-i} \quad \text{and} \quad B_{q^s-1} = \sum_{i=1}^{t} p^{ts-i} - tq^{s-1}.$$

Proof.

1. We know that

$$n! = \prod_{k=1}^{n} k = \left(\prod_{\substack{k=1 \\ q|k}}^{n} k\right)\left(\prod_{\substack{k=1 \\ q \nmid k}}^{n} k\right) = \left(\prod_{\substack{k=1 \\ q|k}}^{n} k\right) n!_q.$$

(12)

On the other hand, we know that card $\{1 \le k \le n/\; q|k\} = \left[\frac{n}{q}\right]$. Thus,

$$\prod_{\substack{k=1 \\ q|k}}^{n} k = \prod_{j=1}^{\left[\frac{n}{q}\right]} (jq) = \left[\frac{n}{q}\right]! \; q^{\left[\frac{n}{q}\right]}.$$

Therefore, by the Proposition 3.14, we get

$$\Gamma_q(n+1) = (-1)^{A_n} p^{-B_n} n!_q = \frac{(-1)^{A_n} p^{-B_n} n!}{\xi! \; q^\xi}.$$

2. The Euclidean division gives $n = mq + \lambda$, where $\lambda \in \{0, 1, \cdots, q-1\}$. So,

$$\left[\frac{n}{q}\right] = m + \left[\frac{\lambda}{q}\right] = m.$$

Substituting this into Eqn. (9), we obtain

$$\Gamma_q(mq + \lambda + 1) = \frac{(-1)^{A_{mq+\lambda}} p^{-B_{mq+\lambda}} n!}{m! \; q^m}.$$

(13)

Such that $A_{mq+\lambda}$ and $B_{mq+\lambda}$ are calculated as follows:

- For $A_{mq+\lambda}$, we have

$$A_{mq+\lambda} = t + \sum_{i=0}^{t-1} \left[\frac{mq+\lambda}{p^i}\right] = t + mq + \lambda + mq \sum_{i=1}^{t-1} \left(\frac{1}{p}\right)^i + \sum_{i=1}^{t-1} \left[\frac{\lambda}{p^i}\right]. \tag{14}$$

We know that $v_p(\lambda!) = \sum_{i=0}^{t-1} \left[\frac{\lambda}{p^i}\right]$. Since the sum $\sum_{i=0}^{t-1} \left(\frac{1}{p}\right)^i$ is even, it comes that

$$(-1)^{\sum_{i=0}^{t-1}\left(\frac{1}{p}\right)^i} = 1.$$

Then, $(-1)^{A_{mq+\lambda}} = (-1)^{t+\lambda+mq+v_p(\lambda!)}$. Finally, we obtain $A_{m,\lambda} = t + \lambda + mq + v_p(\lambda!)$.

- For $B_{mq+\lambda}$, we have

$$B_{mq+\lambda} = \sum_{i=1}^{t} \left[\frac{mq+\lambda}{p^i}\right] - t\left[\frac{mq+\lambda}{q}\right] = mq \sum_{i=1}^{t} \left(\frac{1}{p}\right)^i + \sum_{i=1}^{t-1} \left[\frac{\lambda}{p^i}\right] + \left[\frac{\lambda}{p^t}\right] - tm - t\left[\frac{\lambda}{q}\right]. \tag{15}$$

So $B_{m,\lambda} = m\left(\frac{q-1}{p-1}\right) - tm - t\left[\frac{\lambda}{q}\right] + v_p(\lambda!)$.

3. We simply need to substitute $n = q^s - 1$ into Eqn. (9) to determine the value of $\Gamma_q(q^s)$.

Proposition 3.16.

1. We have $\Gamma_q(0) = 1$ and $\left|\Gamma_q(x)\right|_p = 1$, for all $x \in \mathbb{Z}_p$.

2. For $p \geq 3$, let $x, y \in \mathbb{Z}_p$. We have

   - If $|x-y|_p = 1$, then $\left|\Gamma_q(x) - \Gamma_q(y)\right|_p \leq |x-y|_p$.
   - If $|x-y|_p = \frac{1}{p^s}$, with $\geq t$, then $\left|\Gamma_q(x) - \Gamma_q(y)\right|_p \geq |x-y|_p$.

Proof.

1. By the definition of Γ_q, we have $\Gamma_q(0) = \prod_{\ell=0}^{t-1} \Gamma_p(h_\ell(-1)+1)$. Furthermore, we have

$$-1 = \sum_{i=0}^{\ell-1} (p-1)p^i + p^\ell \sum_{i=0}^{+\infty} (p-1)p^i. \tag{16}$$

So, $h_\ell(-1) = -1$. Then, $\Gamma_q(0) = \prod_{\ell=0}^{t-1} \Gamma_p(0) = 1$.

For the second part $\left|\Gamma_q(x)\right|_p = 1$, we simply use the fact that $\left|\Gamma_p(x)\right|_p = 1$.

2. First, we prove the property for positive integers and then extend the result to p-adic

integers by taking the limit. For $m, n \in \mathbb{N}$, we consider the following cases:

- If $|n - m|_p = 1$. Then,

$$\left| \Gamma_q(n) - \Gamma_q(m) \right|_p \leq \max \left(\left| \Gamma_q(n) \right|_p, \left| \Gamma_q(m) \right|_p \right) \leq 1 = |n - m|_p. \tag{17}$$

- If $n > m$ and $|n - m|_p = \frac{1}{p^s}$, with $s \geq t$. Then, there exists $\mu \in \mathbb{N}$ such that $n = m + \mu p^s$ and $p \nmid \mu$. Therefore, by applying the Eqn. (7), we get

$$\Gamma_q(n) = \Gamma_q(m + \mu p^s) = (-1)^{A_n} p^{-B_n} \prod_{\substack{k=1 \\ q \nmid k}}^{m + \mu p^s - 1} k$$

$$= (-1)^{A_n} p^{-B_n} \left(\prod_{\substack{k=1 \\ q \nmid k}}^{m-1} k \right) \left(\prod_{\substack{k=m \\ q \nmid k}}^{m + \mu p^s - 1} k \right). \tag{18}$$

Now, since $s \geq t$ we must have $A_n = A_1 + A_2$ and $B_n = B_1 + B_2$, with

$$A_1 = t + \sum_{i=0}^{t-1} \left[\frac{m}{p^i} \right] \quad , \quad A_2 = \sum_{i=0}^{t-1} \mu p^{s-i}.$$

$$B_1 = \sum_{i=1}^{t} \left[\frac{m}{p^i} \right] - t \left[\frac{m}{q} \right] \quad , \quad B_2 = \sum_{i=1}^{t} \mu p^{s-i} - t \mu p^{s-t}.$$

Therefore

$$\Gamma_q(n) = \left((-1)^{A_1} p^{-B_1} \prod_{\substack{k=1 \\ q \nmid k}}^{m-1} k \right) \left((-1)^{A_2} p^{-B_2} \prod_{\substack{k=m \\ q \nmid k}}^{m + \mu p^s - 1} k \right)$$

$$= \Gamma_q(m) \left((-1)^{A_2} p^{-B_2} \prod_{\substack{k=m \\ q \nmid k}}^{m + \mu p^s - 1} k \right). \tag{19}$$

Hence

$$\left| \Gamma_q(n) - \Gamma_q(m) \right|_p = \left| \Gamma_q(m) \right|_p \left| \left((-1)^{A_2} p^{-B_2} \prod_{\substack{k=m \\ q \nmid k}}^{m+\mu p^s - 1} k \right) - 1 \right|_p. \tag{20}$$

Now, rewriting the product as follows

$$\prod_{\substack{k=m \\ q \nmid k}}^{m+\mu p^s - 1} k = \left(\prod_{\substack{k=m \\ q \nmid k}}^{m+p^s - 1} k \right) \left(\prod_{\substack{k=m+p^s \\ q \nmid k}}^{m+2p^s - 1} k \right) \cdots \left(\prod_{\substack{k=m+(\mu-1)p^s \\ q \nmid k}}^{m+\mu p^s - 1} k \right). \tag{21}$$

By Theorem 3.5, we have for all $\theta \in \{1, 2, \ldots, \mu\}$

$$\prod_{\substack{k=m+(\theta-1)p^s \\ q \nmid k}}^{m+\theta p^s - 1} k \equiv - \prod_{\substack{j=m+(\theta-1)p^s \\ p \mid j}}^{m+\theta p^s - 1} k \pmod{p^s}.$$

We know that the fact $p \mid k$ implies that $k = \lambda_\theta p^{\ell_\theta}$ with $p \nmid \lambda_\theta$ and $\ell_\theta \in \mathbb{N}$. Thus

$$\prod_{\substack{k=m \\ q \nmid k}}^{m+\mu p^s - 1} k \equiv (-1)^\mu \left(\prod_{\substack{\theta=1 \\ p \nmid \lambda_\theta}}^{\mu} \lambda_\theta \right) \left(\prod_{\theta=1}^{\mu} p^{\ell_\theta} \right) \pmod{p^s}. \tag{22}$$

which implies

$$(-1)^{A_2} p^{-B_2} \prod_{\substack{k=m \\ q \nmid k}}^{m+\mu p^s - 1} k \equiv (-1)^{\mu+A_2} p^{\sum_{\theta=1}^{\mu} \ell_\theta - B_2} \prod_{\substack{\theta=1 \\ p \nmid \lambda_\theta}}^{\mu} \lambda_\theta \pmod{p^s}. \tag{23}$$

On the other hand, we have

$$\mu + A_2 = \mu \left(1 + p^{s+1-t} \frac{p^t - 1}{(p-1)} \right) \quad , \quad B_2 = \mu p^s \left(\frac{p^t - 1}{(p-1)p^{t-1}} - t p^{-t} \right).$$

So, we get

$$\left((-1)^{A_2} p^{-B_2} \prod_{\substack{k=m \\ q \nmid k}}^{m+\mu p^s - 1} k \right) \equiv p^{\sum_{\theta=1}^{\mu} \ell_\theta - B_2} \prod_{\substack{\theta=1 \\ p \nmid \lambda_\theta}}^{\mu} \lambda_\theta \pmod{p^s}. \tag{24}$$

Thus

$$\left| \left((-1)^{A_2} p^{-B_2} \prod_{\substack{k=m \\ q\nmid k}}^{m+\mu p^s-1} k \right) - 1 \right|_p = \max\left\{ p^{B_2 - \sum_{\theta=1}^{\mu} \ell_\theta}, p^{-s}, 1 \right\} \geq \frac{1}{p^s}. \tag{25}$$

Which yields the result $\left| \Gamma_q(n) - \Gamma_q(m) \right|_p \geq |n-m|_p$.

By passing to the limit, we conclude that the property holds for all elements of $\mathbb{Z}_p$.

Corollary 3.17. For p odd, we have

$$\Gamma_q^2 \left(\frac{1}{2} \right) = (-1)^t.$$

Proof. According to the complements Eqn. (8), for p odd and $x = \frac{1}{2}$ we have

$$\Gamma_q \left(\frac{1}{2} \right) \Gamma_q \left(\frac{1}{2} \right) = \Gamma_q^2 \left(\frac{1}{2} \right) = (-1)^{t-1+R_t\left(\frac{1}{2}\right)}, \tag{26}$$

with $R_t \left(\frac{1}{2} \right) \in \{1,2,\dots,q\}$ is the representative of $\frac{1}{2}$ modulo $q\mathbb{Z}_p$. In fact, we know that

$$\frac{1}{2} = \frac{p+1}{2} + \sum_{i=1}^{+\infty} \frac{p-1}{2} p^i = \frac{p+1}{2} + \frac{p-1}{2} \sum_{i=1}^{t-1} p^i + \sum_{i=t}^{+\infty} \frac{p-1}{2} p^i, \tag{27}$$

which implies that

$$\frac{1}{2} = \frac{q+1}{2} + q \sum_{i=1}^{+\infty} \frac{p-1}{2} p^i, \tag{28}$$

thus $R_t \left(\frac{1}{2} \right) = \frac{q+1}{2}$, which is even, so $(-1)^{-1+R_t\left(\frac{1}{2}\right)} = 1$. Hence, the result follows.

Proposition 3.18. (Mahler expansion of Γ_q)

Let the Mahler expansion of $\Gamma_q(x+1)$ be given by

$$\Gamma_q(x+1) = \sum_{\eta=0}^{+\infty} a_\eta \binom{x}{\eta}.$$

For $x \in \mathbb{Z}_p$. So, the coefficients a_η in this expansion satisfy the following relation

$$\exp_p\left(p^{\frac{q-1}{p-1}}x^q + x\right) = \frac{1}{\delta_q}\sum_{\eta=0}^{+\infty}(-1)^\eta \alpha_\eta \frac{x^\eta}{\eta!}, \tag{29}$$

where

$$\delta_q = \sum_{\lambda=0}^{q-1}(-1)^{t+v_p(\lambda!)}p^{t\left[\frac{\lambda}{q}\right]-v_p(\lambda!)}(-x)^\lambda.$$

Proof. The coefficients a_η satisfy the generating function relation

$$\sum_{\eta=0}^{+\infty}\alpha_\eta\frac{x^\eta}{\eta!} = e^{-x}\sum_{\eta=0}^{+\infty}\Gamma_q(\eta+1)\frac{x^\eta}{\eta!}. \tag{30}$$

The aim is to find an expression for the generating series of $\left(\Gamma_q(n+1)\right)_{n\in\mathbb{N}}$ given by

$$f(x) = \sum_{\eta=0}^{+\infty}\Gamma_q(\eta+1)\frac{x^\eta}{\eta!}.$$

To achieve this, we'll first decompose the index η in the sum according to its residue modulo q. Let $\eta = mq + \lambda$ where $m \geq 0$ and $\lambda \in \{0, 1, \dots, q-1\}$.

By separating the sum based on the possible values of λ, we can express $f(x)$ as

$$f(x) = \sum_{\lambda=0}^{q-1}\sum_{m=0}^{+\infty}\frac{\Gamma_q(mq+\lambda+1)}{(mq+\lambda)!}x^{mq+\lambda}. \tag{31}$$

We now use relation (10) to derive an explicit form of the generating series f

$$f(x) = \sum_{\lambda=0}^{q-1}\sum_{m=0}^{+\infty}\frac{(-1)^{t+\lambda+mq+v_p(\lambda!)}\,p^{-m\left(\frac{q-1}{p-1}\right)+tm+t\left[\frac{\lambda}{q}\right]-v_p(\lambda!)}}{m!\,q^m}x^{mq+\lambda}$$

$$= \sum_{\lambda=0}^{q-1}(-1)^{t+v_p(\lambda!)}p^{t\left[\frac{\lambda}{q}\right]-v_p(\lambda!)}(-x)^\lambda\sum_{m=0}^{+\infty}\left(\frac{(-1)^q\,x^q}{q}\right)^m\frac{1}{m!}$$

$$= \delta_q\exp\left(p^{\frac{q-1}{p-1}}(-x)^q\right), \tag{32}$$

where

$$\delta_q = \sum_{\lambda=0}^{q-1} (-1)^{t+v_p(\lambda!)}\, p^{t\left[\frac{\lambda}{q}\right]-v_p(\lambda!)}(-x)^\lambda$$

Hence

$$e^{-x}f(x) = \delta_q \exp\left(p^{\frac{q-1}{p-1}}(-x)^q - x\right). \tag{33}$$

Then

$$\sum_{\eta=0}^{+\infty} \alpha_\eta \frac{x^\eta}{\eta!} = \delta_q \exp\left(p^{\frac{q-1}{p-1}}(-x)^q - x\right). \tag{34}$$

By replacing $-x$ with x, we obtain

$$\sum_{\eta=0}^{+\infty} (-1)^\eta \alpha_\eta \frac{x^\eta}{\eta!} = \delta_q \exp\left(p^{\frac{q-1}{p-1}}x^q + x\right).$$

This completes the proof.

4. Conclusion

In this work, we introduced and systematically studied the q-adic factorial $n!_q$, establishing its fundamental properties, including several novel congruences and inequalities. Building on this foundation, we reformulated the generalized p-adic gamma function Γ_q given by Ota through the q-adic factorial, revealing new combinatorial identities. In addition, we proposed the Mahler expansion of Γ_q and proved the relationships between its coefficients. These results collectively advance the theory of p-adic special functions and open new avenues for further research in p-adic analysis and its applications.

Acknowledgements

References

[1] Morita, Y.A., *A p-adic Analogue of the Gamma Function*, Journal of the Faculty of Science, the University of Tokyo, Sect. 1 A, Mathematics, 22(2), 255–266, 1975.

[2] Asakura, M., *New p-adic Hypergeometric Functions and Syntomic Regulators,* Journal de Théorie des Nombres de Bordeaux, 35(2), 393–451, 2023.

[3] Koblitz, N., *q-Extension of the p-adic Gamma Function*, Transactions of the American Mathematical Society, 260(2), 449–457, 1980.

[4] Ota, K., *On special values of generalized p-adic hypergeometric functions*, Acta Arithmetica, 67(2), 141–163, 1994.

[5] Duran, U., Acikgoz, M., *A study on Novel Extensions for the p-adic Gamma and p-adic Beta Functions*, Mathematical and Computational Applications, 24(2), 53, 2019.

[6] Gouvêa, F.Q., *p-adic Numbers, An introduction*, Springer, 2 ed., 1997.

[7] Belhadef, R., *A Generalization of p-adic Factorial*, Journal of New Theory, 39, 94–103, 2022.

[8] Young, P.T., *Apery numbers, Jacobi sums, and special values of generalized p-adic hypergeometric functions*, Journal of Number Theory, 41(2), 231–255, 1992.

[9] Çolakoğlu Havare, Ö., Menken, H., *On the p-adic Gamma Function and Changhee Polynomials*, Turkish Journal of Analysis and Number Theory, 6(4), 120–123, 2018.

[10] Duran, U., Açikgöz, M., *On p-adic Gamma Function Related to q-Daehee Polynomials and Numbers*, Proyecciones (Antofagasta), 38(4), 799–810, 2019.

[11] Robert, A.M., *A Course in p-adic Analysis*. Springer-Verlag, Graduate Texts in Mathematics, 2000.

[12] Chang, T.W., *Geometric Gauss Sums and Gross-Koblitz Formulas over Function Fields*, arXiv: 2502.01109, 2025.

[13] Sulakashna, Barman, R., *p-adic hypergeometric functions and certain weight three newforms*, Journal of Mathematical Analysis and Applications, 542(1), 128763, 2025.

Determination of Radiation Characteristics of Samarium and Boron Doped Indium Oxide Thin Film by Simulation Method

Mehmet Murat YAŞAR[1,*], Mehmet KOŞAL[2], Ali SÜT[3]

[1]*Harran University, Vocational School of Health Services, Department of Medical Services and Techniques, 63000, Şanlıurfa, Türkiye*
muratyasar@harran.edu.tr, ORCID: 0000-0001-6211-0350
[2]*Harran University, Faculty of Arts and Sciences, Department of Physics, 63000, Şanlıurfa, Türkiye*
kosal@harran.edu.tr, ORCID: 0000-0002-3224-5569
[3]*Harran University, Faculty of Arts and Sciences, Department of Physics, 63000, Şanlıurfa, Türkiye*
alisutmra@gmail.com, ORCID: 0009-0009-0600-5746

Abstract

In this study, the addition of samarium (Sm) and boron (B) to indium oxide (In_2O_3) thin films at rates of 5%, 10%, and 20% was investigated, and radiation properties were determined using the Monte Carlo N-Particle (MCNP6.2) simulation program. The reason for choosing In_2O_3 in the study is that In_2O_3 has high chemical stability, optical transparency, excellent electrical properties, and semiconductor properties. It is also widely used in various applications, including displays, solar cells, and sensors. Since In_2O_3 is used in sensors, it is aimed to be investigated for integration into radiation detector systems. At this point, it will provide a new idea. The simulation results obtained were compared with the values in the National Institute of Standards and Technology (NIST-XCOM) database, and it was observed that the simulation gave efficient results. According to the simulation analyses, it was observed that Sm provided better radiation shielding properties than B.

Keywords: Boron; Thin film; Indium oxide; MCNP; Radiation; Samarium.

Samaryum ve Bor Katkılı İndiyum Oksit İnce Filmin Radyasyon Karakteristiklerinin Simülasyon Yöntemiyle Belirlenmesi

Öz

Bu çalışmada, indiyum oksit (In_2O_3) ince filmine %5, %10 ve %20 oranlarında samaryum (Sm) ve bor (B) katkılanarak radyasyon özellikleri Monte Carlo N-Particle (MCNP6.2) simülasyon programıyla belirlenmeye çalışılmıştır. Çalışmada In_2O_3'ün seçilmesinin sebebi; In_2O_3'ün yüksek kimyasal kararlılığa, optik şeffaflığa, mükemmel elektriksel özelliklere ve yarı iletken özelliklere sahip olmasıdır. Aynı zamanda ekran, güneş pilleri ve sensörler gibi birçok alanda yaygın olarak kullanılmaktadır. In_2O_3'ün sensörlerde kullanıldığı için radyasyon dedektör sistemlerine entegrasyonu amacıyla araştırılması amaçlanmaktadır. Bu noktada yeni bir fikir sunmuş olacaktır. Elde edilen simülasyon sonuçları Ulusal Standartlar ve Teknoloji Enstitüsü (NIST-XCOM) veri tabanındaki değerlerle karşılaştırılarak yapılan simülasyonun verimli sonuçlar verdiği gözlenmiştir. Simülasyon analizlerine göre Sm'nin B'den daha iyi radyasyon zırhlama özelliği kazandırdığı gözlenmiştir.

Anahtar Kelimeler: Bor; İnce film; İndiyum oksit; MCNP; Radyasyon; Samaryum.

1. Introduction

Today, it is important to minimize the effects of radiation in environments where radiation is used. For this purpose, there are intensive studies on technological developments in various sectors, such as medicine, materials science, and energy, in order to protect against radiation or to utilize radiation more efficiently. One of these is the design and improvement of thin films. In some studies, different elemental additives can be used to improve the physical properties of thin films. Radiation and particles, including electromagnetic waves and transmissions from nuclear inter-level transitions, are a pervasive and fundamental aspect of our time. These radiation and particles are emitted from a variety of sources, both natural and artificial, and play a crucial role in people's lives, particularly in scientific, industrial, and medical practices. The need for protection has necessitated extensive research into materials that can reduce the harmful effects of radiation. Ionizing radiation, with its ability to remove tightly bound electrons from atoms, can also cause unwanted damage to the cell structures of living organisms. The necessity to protect against these potential hazards has led to the research and development of materials that function as shielding [1–4].

Natural sources of ionizing radiation include external cosmic rays. In addition, terrestrial radiation from the Earth's crust, radioactive isotopes in the environment, and artificial sources

used for diagnostic purposes in medicine are also in this category [5]. On the other hand, industrial processes and nuclear energy production also involve the use of ionizing radiation. Of course, in energy production, concrete and lead are used for shielding structures. However, transparent materials with high MAC (mass attenuation coefficient) (non-toxic like lead) are of interest to researchers [6–9]. Glass compositions play a very important role in various industrial applications, especially in the field of radiation protection due to specific properties of the materials [10]. One of them is the MAC values for glass compositions, which are crucial for optimizing glass in radiation protection applications [11]. On the other hand, numerous questions remain unanswered regarding the use of transparent materials for this purpose, and further studies are needed in these areas. This study aims to utilize glass as an alternative and environmentally friendly material for gamma radiation shielding applications.

Indium oxide (In_2O_3), studied as a thin film, is an n-type semiconductor with a bandgap of 3.5-3.7 eV [12]. It also has high electrical conductivity and outstanding optical transparency [13]. In_2O_3 thin films can be synthesized using various techniques, including sol-gel dip coating, RF and DC sputtering, chemical vapor deposition, and spray pyrolysis [14]. Of these, the spray pyrolysis method is easy, low-cost, and suitable for industry as large areas can be coated with this method. In addition, the phase, size, and morphology of the thin film can be controlled [15]. It is crucial to obtain ultrafine powders with high purity, high porosity, and a large surface area through spray pyrolysis [16]. The electrical resistance and optical transmission of this film have been studied [17]. The physical properties of In_2O_3 thin film have been reported to be extensively improved by iron doping [18]. In_2O_3 is widely preferred in thin film designs due to its high semiconductor properties. At the same time, some physical properties can be created by doping various elements to In_2O_3. In thin film designs, it is also important for it to be transparent for use in sensors and detectors. For example, molybdenum element is doped into In_2O_3 to increase its conductivity and transparency properties [19].

Various elements are being tested to increase the physical properties of devices used in nuclear technologies. One of these is Sm. Since Sm is a high-purity element, it is the focus of the studies [20]. Stainless steels are also used for radiation protection in nuclear applications. According to the researches, Sm doping has also been tried to strengthen the shielding properties of stainless steel used in radiation shielding processes. The results indicate that Sm has positive contributions to radiation shielding [21]. There are also studies on the radiation properties of Sm-doped compounds. In one of these studies, radiation permeability coefficients were investigated Sm doped zinc bismuth silicate. The change in radiation shielding properties under the influence of silica at low photon energies was investigated [22].

Another element widely used in research on the radiation properties of compounds is B. Boron has a positive effect in slowing down radiation types such as thermal neutrons. Therefore, when examining studies on B-containing compounds, it is evident that high performance is achieved in terms of radiation shielding [23]. When we examine the studies investigating the radiation properties of alloys composed of iron and B, it has been observed that there is a positive correlation between the photon shielding property and the amount of B. This shows that B-containing samples can be used for radiation shielding [24].

The main objective of this study is to determine the radiation protection properties of In_2O_3 thin films by obtaining other parameters, such as MAC, LAC, and HVL for different types of glasses produced by doping In_2O_3 thin films with different proportions of Sm and B at 5%, 10% and 20%. The reason for choosing In_2O_3 is that it has high chemical stability, optical transparency, excellent electrical properties, and semiconductor properties. Due to these properties, it offers the opportunity to be used in nuclear applications. Sm, one of the elements doped in In_2O_3, provides a high density to In_2O_3. At the same time, it increases its high-purity feature. The other element doped in In_2O_3, B, contributes to the increase in radiation shielding feature.

2. Materials and Methods

In this study, Indium oxide doped with different ratios of Sm and B was investigated as a radiation shielding material. The individual doping rates of Sm and B materials were decided as 5%, 10%, and 20%. The values of the related shielding materials are given in Table-1.

Table 1: Percentage ratios and densities of the samples.

Sample Name	Doped Material	Main Material	Density (g/cm^3)
	Sm (%)	In_2O_3 (%)	(g/cm^3)
sm1	0	100	7.13
sm2	5	95	7.12
sm3	10	90	7.09
sm4	20	80	7.00
Sample Name	Doped Material	Main Material	Density (g/cm^3)
	B (%)	In_2O_3 (%)	(g/cm^3)
b1	0	100	7.13
b2	5	95	6.92
b3	10	90	6.70
b4	20	80	6.30

The Monte Carlo N-Particle (MCNP6.2) simulation program, a Monte Carlo-based tool, was utilized in this study. MCNP is a radiation transport program that is frequently used and preferred in radiation modeling in the scientific world. Input files were prepared, and calculations

were performed using the experimental setup shown in Fig. 1. The experimental setup consists of a source emitting radiation at various energy levels (0.284 MeV, 0.347 MeV, 0.511 MeV, 0.662 MeV, 0.826 MeV, 1.17 MeV, 1.33 MeV, and 2 MeV), 0.0002 cm-thick thin film samples, and a detector system that detects gamma rays passing through the samples. f4 (Average photon flux n/cm2) was used for the detector tally card. The simulation was performed with 10 million stories for each sample and each energy value.
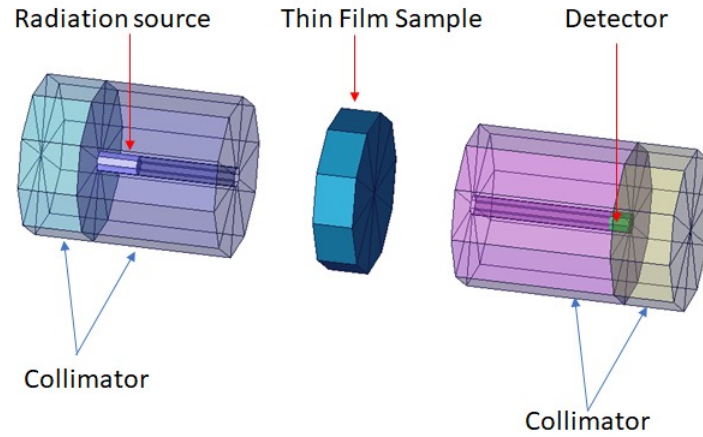
Figure 1: MCNP experimental setup.

The Linear Attenuation Coefficient (LAC) (Eqn. (2)), Mass Attenuation Coefficient (MAC) (Eqn. (3)), Mean Free Path (MFP) (Eqn. (4)), Half Value Layer (HVL) (Eqn. (5)) and Tenth Value Layer (TVL) (Eqn. (6)) values of each sample were calculated according to the Beer-Lambert Law stated in Eqn. (1) using the data in the outputs obtained from the simulation [25]. These equations represent the radiation characteristics of the respective samples [26].

$$I = I_0 e^{-\mu x} \tag{1}$$

Where I_0 is the intensity from the radiation source, I is the intensity detected by the detector, x is the sample thickness and μ is the LAC.

$$LAC = \mu \ (1/cm) \tag{2}$$

$$MAC = {}^{\mu}/_{\rho} \left(\frac{cm^2}{g} \right) \tag{3}$$

Here ρ is the density of the sample.

$$MFP = \frac{1}{LAC} = \frac{1}{\mu} (cm) \tag{4}$$

$$HVL = \frac{\ln(2)}{LAC} = \frac{\ln(2)}{\mu} \ (cm) \qquad (5)$$

$$TVL = \frac{\ln(10)}{LAC} = \frac{\ln(10)}{\mu} \ (cm) \qquad (6)$$

The LAC, MAC, MFP, HVL, and TVL values were compared with the NIST-XCOM data using the data from the simulation outputs [27]. This study is simulation-based and experimental results are not available. Therefore, to verify the accuracy of the simulations, the results obtained were compared with NIST-XCOM values. The NIST-XCOM program is utilized for calculating mass attenuation coefficients and cross sections of interaction for different elements, compounds, and mixtures in the energy range 1 keV–100 GeV [28,29]. According to the comparison results, the simulation was found to be efficient.

3. Results and Discussion

3.1. Results for Sm Doped In$_2$O$_3$ Samples

The LAC, MAC, MFP, HVL and TVL results obtained using MCNP6.2 simulation program for Sm doped In$_2$O$_3$ thin film are given in Figs. 2–6, respectively.

LAC (1/cm)				
Energy (MeV)	sm1	sm2	sm3	sm4
0.284	1.17824	1.17824	1.21751	1.25679
0.347	0.94257	0.94257	0.94257	0.98184
0.511	0.66763	0.66763	0.66763	0.66763
0.662	0.54981	0.54981	0.54981	0.54981
0.826	0.47126	0.47126	0.47126	0.47126
1.17	0.39271	0.39271	0.39271	0.39271
1.33	0.35344	0.35344	0.35344	0.35344
2	0.31417	0.31417	0.2749	0.2749

Figure 2: LAC values of Sm doped In$_2$O$_3$ samples.

MAC (cm^2/g)				
Energy (MeV)	sm1	sm2	sm3	sm4
0.284	0.16525	0.16548	0.17172	0.17726
0.347	0.1322	0.13238	0.13294	0.13848
0.511	0.09364	0.09377	0.09417	0.09417
0.662	0.07711	0.07722	0.07755	0.07755
0.826	0.0661	0.06619	0.06647	0.06647
1.17	0.05508	0.05516	0.05539	0.05539
1.33	0.04957	0.04964	0.04985	0.04985
2	0.04406	0.04412	0.03877	0.03877
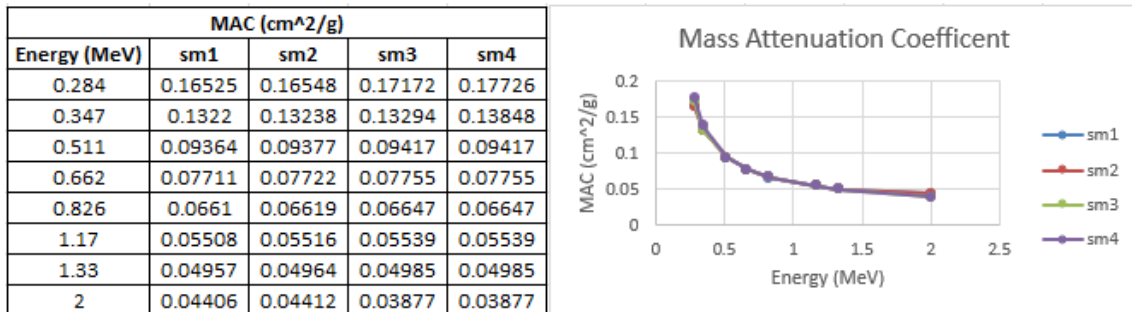
Figure 3: MAC of Sm doped In$_2$O$_3$ samples.

MFP (cm)				
Energy (MeV)	sm1	sm2	sm3	sm4
0.284	0.84873	0.84873	0.82135	0.79567
0.347	1.06093	1.06093	1.06093	1.01849
0.511	1.49783	1.49783	1.49783	1.49783
0.662	1.81881	1.81881	1.81881	1.81881
0.826	2.12197	2.12197	2.12197	2.12197
1.17	2.54638	2.54638	2.54638	2.54638
1.33	2.82932	2.82932	2.82932	2.82932
2	3.183	3.183	3.63773	3.63773
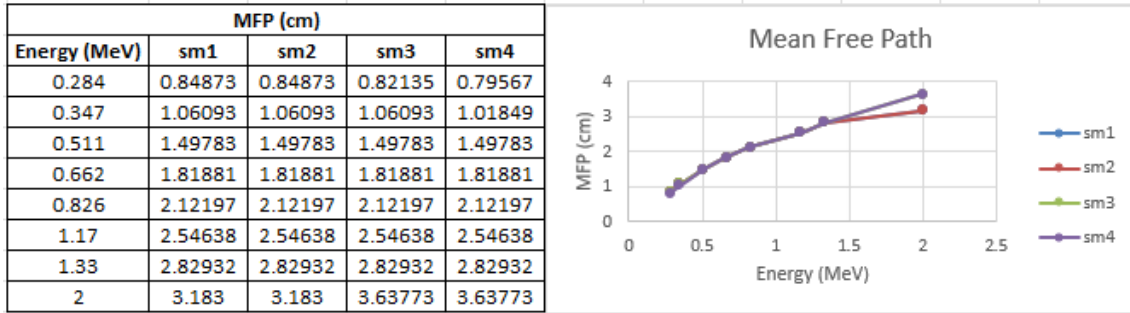
Figure 4: MFP of Sm doped In$_2$O$_3$ samples.

HVL (cm)				
Energy (MeV)	sm1	sm2	sm3	sm4
0.284	0.58829	0.58829	0.56931	0.55152
0.347	0.73538	0.73538	0.73538	0.70596
0.511	1.03822	1.03822	1.03822	1.03822
0.662	1.26071	1.26071	1.26071	1.26071
0.826	1.47084	1.47084	1.47084	1.47084
1.17	1.76502	1.76502	1.76502	1.76502
1.33	1.96114	1.96114	1.96114	1.96114
2	2.20629	2.20629	2.52148	2.52148
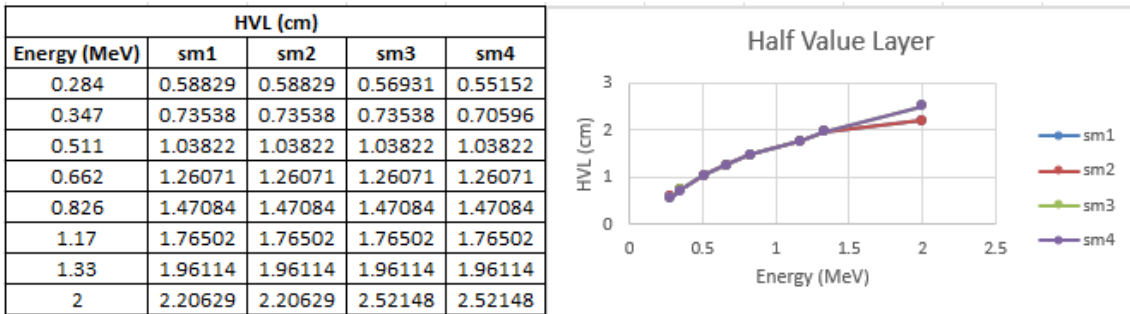
Figure 5: HVL of Sm doped In$_2$O$_3$ samples.

TVL (cm)				
Energy (MeV)	sm1	sm2	sm3	sm4
0.284	1.95427	1.95427	1.89122	1.83211
0.347	2.44289	2.44289	2.44289	2.34516
0.511	3.44888	3.44888	3.44888	3.44888
0.662	4.18797	4.18797	4.18797	4.18797
0.826	4.88601	4.88601	4.88601	4.88601
1.17	5.86326	5.86326	5.86326	5.86326
1.33	6.51476	6.51476	6.51476	6.51476
2	7.32913	7.32913	8.37618	8.37618
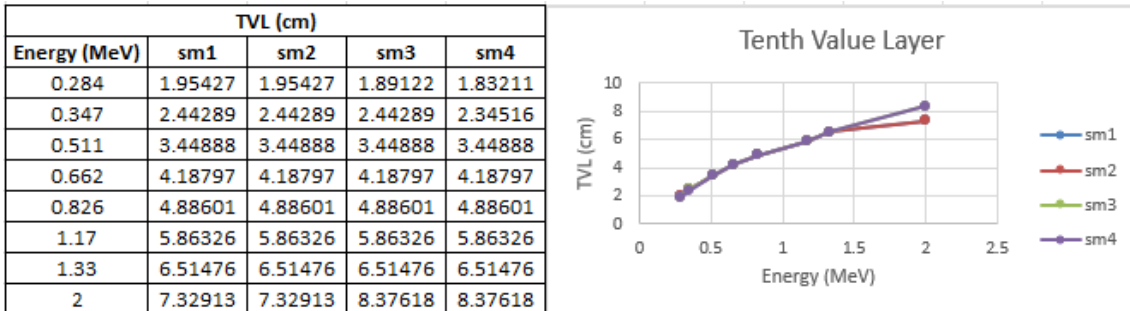
Figure 6: TVL of Sm doped In$_2$O$_3$ samples.

When the LAC values of the Sm-doped In$_2$O$_3$ samples were examined, it was observed that the LAC values increased as the doping ratio increased. Only at an energy of 2 MeV, a deviation was observed in the LAC values of the sm3 and sm4 coded samples. For this reason, Sm-doped In$_2$O$_3$ thin films do not give the desired results at very high energies. When the obtained results are compared with XCOM, the fact that the error rates are higher than the others support this situation. When the MFP values are examined, it is seen that the values deviate as the doping ratio increases at high energies. Since the MFP values of the samples express the amount of radiation passing through the substance without interacting, these results show that Sm-doped In$_2$O$_3$ thin films are not efficient at high energies.

3.2. Results for B Doped In₂O₃ Samples

LAC, MAC, MFP, HVL and TVL results obtained using MCNP6.2 simulation program for B doped In₂O₃ thin film are given in Figs. 7–11, respectively.
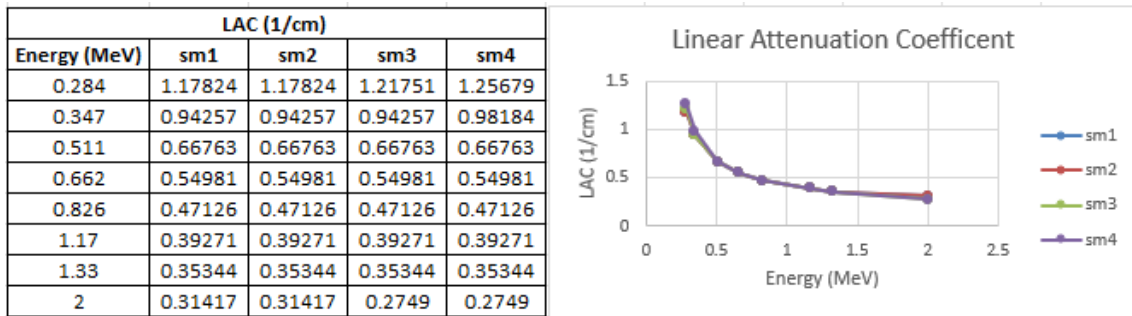
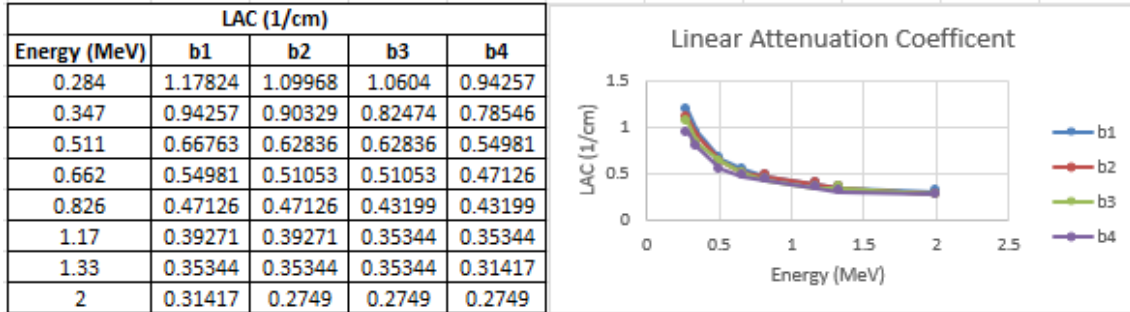| LAC (1/cm)				
Energy (MeV)	b1	b2	b3	b4
0.284	1.17824	1.09968	1.0604	0.94257
0.347	0.94257	0.90329	0.82474	0.78546
0.511	0.66763	0.62836	0.62836	0.54981
0.662	0.54981	0.51053	0.51053	0.47126
0.826	0.47126	0.47126	0.43199	0.43199
1.17	0.39271	0.39271	0.35344	0.35344
1.33	0.35344	0.35344	0.35344	0.31417
2	0.31417	0.2749	0.2749	0.2749

Figure 7: LAC of B doped In₂O₃ samples.

MAC (cm^2/g)				
Energy (MeV)	b1	b2	b3	b4
0.284	0.16525	0.15891	0.15827	0.14961
0.347	0.1322	0.13053	0.12309	0.12468
0.511	0.09364	0.0908	0.09378	0.08727
0.662	0.07711	0.07378	0.0762	0.0748
0.826	0.0661	0.0681	0.06448	0.06857
1.17	0.05508	0.05675	0.05275	0.0561
1.33	0.04957	0.05108	0.05275	0.04987
2	0.04406	0.03972	0.04103	0.04363
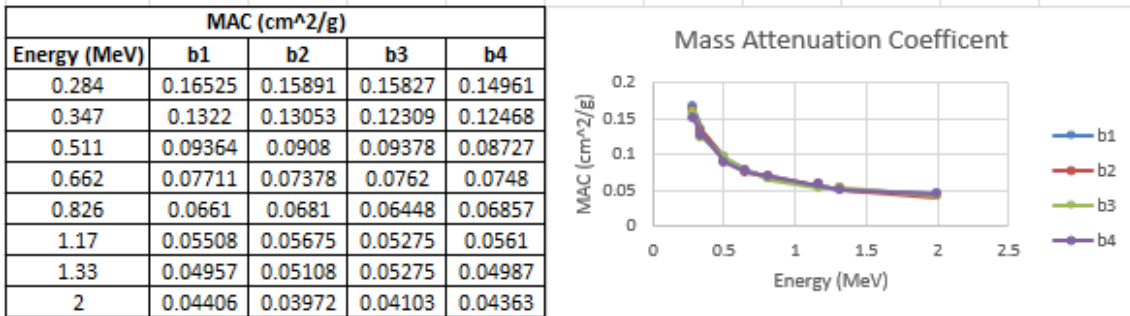
Figure 8: MAC of B doped In₂O₃ samples.

MFP (cm)				
Energy (MeV)	b1	b2	b3	b4
0.284	0.84873	0.90936	0.94304	1.06093
0.347	1.06093	1.10707	1.21251	1.27314
0.511	1.49783	1.59145	1.59145	1.81881
0.662	1.81881	1.95873	1.95873	2.12197
0.826	2.12197	2.12197	2.31488	2.31488
1.17	2.54638	2.54638	2.82932	2.82932
1.33	2.82932	2.82932	2.82932	3.183
2	3.183	3.63773	3.63773	3.63773
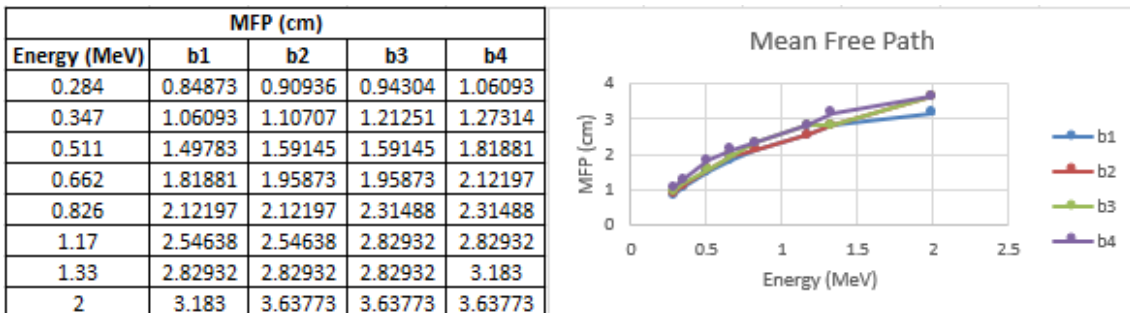
Figure 9: MFP of B doped In₂O₃ samples.

HVL (cm)				
Energy (MeV)	b1	b2	b3	b4
0.284	0.58829	0.63032	0.65367	0.73538
0.347	0.73538	0.76736	0.84045	0.88247
0.511	1.03822	1.10311	1.10311	1.26071
0.662	1.26071	1.35769	1.35769	1.47084
0.826	1.47084	1.47084	1.60455	1.60455
1.17	1.76502	1.76502	1.96114	1.96114
1.33	1.96114	1.96114	1.96114	2.20629
2	2.20629	2.52148	2.52148	2.52148
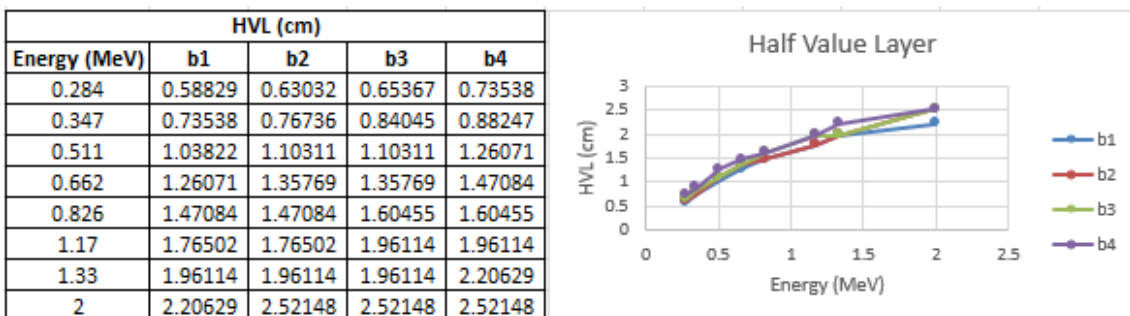
Figure 10: HVL of B doped In₂O₃ samples.

TVL (cm)				
Energy (MeV)	b1	b2	b3	b4
0.284	1.95427	2.09387	2.17143	2.44289
0.347	2.44289	2.54911	2.79191	2.93151
0.511	3.44888	3.66445	3.66445	4.18797
0.662	4.18797	4.51014	4.51014	4.88601
0.826	4.88601	4.88601	5.33021	5.33021
1.17	5.86326	5.86326	6.51476	6.51476
1.33	6.51476	6.51476	6.51476	7.32913
2	7.32913	8.37618	8.37618	8.37618
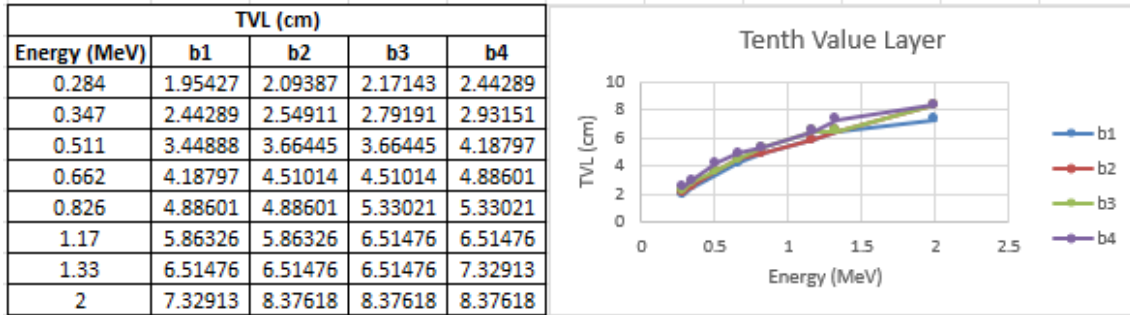
Figure 11: TVL of B doped In_2O_3 samples.

When the LAC values of the B-doped In_2O_3 samples were examined, it was observed that the LAC values decreased as the B ratio increased. This situation demonstrates that doping with B did not have a positive effect on the radiation properties. When compared with the XCOM values, it was seen that the error rates were below 5%. This situation demonstrates that the simulation outputs were not erroneous and that doping B into In_2O_3 did not contribute to the radiation shielding properties. Similarly, when the MFP values were examined, it was seen that the values for each sample at each energy increased.

According to the results obtained in this study, if a comparison is desired between Sm and B, it can be said that Sm is more efficient in radiation shielding due to its higher density than B.

4. Conclusion

In this simulation-based study, an attempt was made to obtain data for the most frequently used energy values in nuclear applications. It can be considered a study that is recommended for glass forms suitable for use in nuclear applications. When the MAC values obtained in the study are compared with the NIST-XCOM data, the difference rates do not exceed 5%. These difference rates indicate that the simulation is efficient (available upon request). In this study, Sm has a higherdensity when compared with B. Therefore, it is seen that Sm is more efficient in terms of radiation shielding. Additionally, Sm can be preferred for glass components worldwide due to its abundant presence. Upon examining the literature, it becomes apparent that numerous studies have been conducted on samples in glass form. The study conducted is simulation-based only and cannot be compared with experimental data. At this point, experimental studies can be recommended for Sm-doped In_2O_3 glass samples. In addition, experimental studies of other elements with high densities, electrical and optical properties, such as Sm, are also recommended.

References

[1] Saeed, J.J., Jasim Hasan, M., Hala, A.R., Ajmi, D.R.N., & Ati, E.M., *The dangers of ionizing radiation that affect human safety and the environment: A review Article*, Texas Journal of Medical Science, 26, 151–160, 2023.

[2] Tasnim, A., Sahadath, M.H., & Islam Khan, M.N., *Development of high-density radiation shielding materials containing $BaSO_4$ and investigation of the gamma-ray attenuation properties*, Radiation Physics and Chemistry, 189, 109772, 2021.

[3] Alshahrani, B., Olarinoye, I.O., Mutuwong, C., Sriwunkum, C., Yakout, H.A., Tekin, H.O., et al., *Amorphous alloys with high Fe content for radiation shielding applications*, Radiation Physics and Chemistry, 183, 109386, 2021.

[4] Sayyed, M.I., Mhareb, M.H.A., Alajerami, Y.S.M., Mahmoud, K.A., Imheidat, M.A., Alshahri, F., et al., *Optical and radiation shielding features for a new series of borate glass samples*, Optik, 239, 166790, 2021.

[5] Charles, M., *UNSCEAR Report 2000: Sources and effects of ionizing radiation*, Journal of Radiological Protection, 21(1), 83–86, 2021.

[6] Al-Buriahi, M.S., Alrowaili, Z.A., Alomairy, S., Olarinoye, I.O., & Mutuwong, C., *Optical properties and radiation shielding competence of Bi/Te-BGe glass system containing B_2O_3 and GeO_2*, Optik, 257, 168883, 2022.

[7] Alharshan, G.A., Eke, C., Al-Buriahi, M.S., *Radiation-transmission and self-absorption factors of P_2O_5–SrO–Sb_2O_3 glass system*, Radiation Physics and Chemistry, 193, 109938, 2022.

[8] Alothman, M.A., Kurtulus, R., Olarinoye, I.O., Kavas, T., Mutuwong, C., Al-Buriahi, M.S., *Optical, elastic, and radiation shielding properties of Bi_2O_3-PbO-B_2O_3 glass system: a role of SnO_2 addition*, Optik, 248, 168047, 2021.

[9] Sekhar, K.C., Hameed, A., Narsimlu, N., Alzahrani, J.S., Alothman, M.A., Olarinoye, I.O., et al., *Synthesis,optical,structural, and radiation transmission properties of PbO/Bi_2O_3/B_2O_3/Fe_2O_3 glasses: An experimental and in silico study*, Optical Materials, 117, 111173, 2021.

[10] Karpuz, N., *Radiation shielding properties of glass composition,* Journal of Radiation Research and Applied Sciences, 16(4), 100689, 2023.

[11] Eid, M.S., Bondouk, I., Saleh, H.M., Omar, K.M., Sayyed, M., El-Khatib, A.M., et al., *Implementation of waste silicate glass into composition of ordinary cement for radiation shielding applications*, Nuclear Engineering and Technology, 54(4),1456–1463, 2022.

[12] Sudha, A., Sharma, S.L., and Gupta, A.N., *Achieving sensitive and stable indium oxide thin films for gamma radiation monitoring*, Sensors and Actuators A: Physical, 285, 378–385, 2019.

[13] Yan, C., Su, Z., Zhao, Z., & Zhou, Y., *Abrasion-resistant, transparent, conductive In_2O_3@ SiO_2 films*, Ceramics International, 49(22), 35316–35322, 2023.

[14] Deokate, R.J., *Influence of spray solution quantity on microstructural and optical properties of In_2O_3 thin films prepared by spray pyrolysis*, Macromolecular Symposia, 392, 1900152, 2020.

[15] Patil, S.P., Patil, V.L., Shendage, S.S., Harale, N.S., Vanalakar, S.A., Kim, J.H., et al., *Spray pyrolyzed indium oxide thick films as NO_2 gas sensor*, Ceramics International, 42, 16160–16168, 2016.

[16] Gavrilovic, T.V., Jovanovic, D.J., and Dramicanin, M.D., *Synthesis of Multifunctional Inorganic Materials: From Micrometer to Nanometer Dimensions*, Nanomaterials for Green Energy, 55–81,2018.

[17] El Hichou, A., Addou, M., Mansori, M., and Eboth´E, J., *Structural, optical and luminescent characteristics of sprayed fluorine-doped In₂O₃ thin films for solar cells*, Solar Energy Materials and Solar Cells, 93, 609–612, 2009.

[18] Beji, N., Souli, M., Ajili, M., Azzaza, S., Alleg, S., and Turki, N.K., *Effect of iron doping on structural, optical and electrical properties of sprayed In₂O₃ thin films*, Superlattices and Microstructures, 81, 114–128, 2015.

[19] Meng, Y., Yang, X.L., Chen, H.X., Shen, J., Jiang, Y.M., Zhang, Z.J., et al., *Molybdenum-doped indium oxide transparent conductive thin films,* Journal of Vacuum Science & Technology A: Vacuum, Surfaces, and Films, 20(1), 288–290, 2002.

[20] Sokkalingam, R., Panghal, A., Roy, S.S., Sankaran, E.M., & Sonachalam, A., *Impact of shockwaves on the structural and morphological characteristics of the Sm₂O₃ compound for wastewater treatment,* Journal of the Taiwan Institute of Chemical Engineers, 106105, 2025.

[21] Yayla, N., Albayrak, M.G., Güler, Ö., Sen Baykal, D., Alkarrani, H., ALMisned, G., et al., *Enhanced Radiation Shielding and Structural Modifications in Samarium (III) Oxide-Reinforced Type 316L Stainless Steel Composites for Nuclear Applications:A Comprehensive Evaluation of Physical, Structural, Mechanical, Gamma-Ray, and Neutron Attenuation Properties,* Nuclear Technology, 1–21, 2025.

[22] Iliyasu, U., Bature, M., Umar, M., Abubakar, U., & Shehu, A., *Photon attenuation properties of samarium-doped zinc bismuth silicate glass: A study using Cs-137, Co-60, and Na-22 Radiation Sources,* Caliphate Journal of Science and Technology, 6(3), 281–288, 2024.

[23] Shin, J.W., Lee, J.W., Yu, S., Baek, B.K., Hong, J.P., Seo, Y., et al., *Polyethylene/boron-containing composites for radiation shielding,* Thermochimica Acta, 585, 5–9, 2014.

[24] Levet, A., Kavaz, E., & Özdemir, Y., *An experimental study on the investigation of nuclear radiation shielding characteristics in iron-boron alloys,* Journal of Alloys and Compounds, 819, 152946, 2020.

[25] Eskalen, H., Kavun, Y., Kerli, S., Eken, S., *An investigation of radiation shielding properties of boron doped ZnO thin films,* Optical Materials, 105, 109871, 2020.

[26] Mirji, R., & Lobo, B., *Computation of the mass attenuation coefficient of polymeric materials at specific gamma photon energies*, Radiation Physics and Chemistry, 135, 32–44, 2017.

[27] Hubbell, J.H., Gimm, H.A., & Verbo, I.O., *Pair, triplet, and total atomic cross sections (and mass attenuation coefficients) for 1 MeV-100 GeV photons in elements Z= 1 to 100*, Journal of Physical and Chemical Reference Data, 9(4), 1023–1148, 1980.

[28] Gerward, L., Guilbert, N., Jensen, K.B., Levring, H., *WinXCom-a program for calculating X-ray attenuation coefficients,* Radiation Physics and Chemistry, 71(3–4), 653–654, 2004.

[29] El-bashir, B.O., Sayyed, M.I., Zaid, M.H.M., Matori, K.A., *Comprehensive study on physical, elastic and shielding properties of ternary BaO-Bi₂O₃-P₂O₅ glasses as a potent radiation shielding material,* Journal of Non-Crystalline Solids, 468, 92–99,2017.